

**HIGH-ORDER ACCURATE PARTITIONED SCHEMES
FOR CONJUGATE HEAT TRANSFER
WITH ADVECTION-DIFFUSION EQUATIONS**

Sijia Huang

Submitted in Partial Fulfillment of the Requirements
for the Degree of

DOCTOR OF PHILOSOPHY

Approved by:
Donald Schwendeman, Chair
Jeffrey Banks, Co-Advisor
William Henshaw, Co-Advisor
Ashwani Kapila
Onkar Sahni



Department of Mathematical Sciences
Rensselaer Polytechnic Institute
Troy, New York

[August 2022]
Submitted July 2022

© Copyright 2022
by
Sijia Huang
All Rights Reserved

CONTENTS

LIST OF TABLES	v
LIST OF FIGURES	vii
LIST OF ALGORITHMS	xi
ACKNOWLEDGMENT	xii
ABSTRACT	xiii
1. INTRODUCTION	1
2. HIGH-ORDER ACCURATE PARTITIONED SCHEMES FOR CONJUGATE HEAT TRANSFER WITH DIFFUSION EQUATIONS	11
2.1 A Brief Introduction	11
2.2 Governing Equations and Model Problem Specification	11
2.3 Derivation of the CHAMP Interface Conditions	14
2.3.1 A Brief Review on Optimized Schwarz Algorithm for Domain Decom- position Problems	14
2.3.2 CHAMP Conditions for a 4th-Order Accurate Scheme	15
2.3.3 CHAMP Condition for a pth-Order Accurate Scheme	19
2.4 Partitioned Algorithms Using the CHAMP Conditions	21
2.5 Application of the CHAMP Conditions on a Spatial Grid	24
2.6 Analysis of the CHAMP Schemes	26
2.6.1 Model Problem Analysis of the CHAMP Iteration	26
2.6.2 Analysis of the Un-Iterated CHAMP Time-Stepping Scheme	33
2.6.3 Accuracy of the Un-iterated CHAMP Time-stepping Scheme	42
2.7 CHAMP Interface Conditions for a Curvilinear Grid	48
2.8 An Adaptive Variable Sub-Iteration Algorithm for the CHAMP Scheme	52
2.9 Numerical Results	54
2.9.1 Numerical Results for Two Steady State Problems	54
2.9.2 Verification with Exact Solutions for Time Dependent Problems	57
2.9.2.1 Adjacent Rectangles	57
2.9.2.2 Concentric Annuli	60
2.9.3 Verification Using Manufactured Solutions on Various Geometries	63
2.9.3.1 Rotated Squares	65
2.9.3.2 Sheared Squares	66

2.9.3.3	Wavy Geometry with Orthogonal Grid at the Interface . . .	69
2.9.3.4	Wavy Geometry with Non-Orthogonal Grid at the Interface	72
2.9.4	Large Time-Step Study for Adaptive CHAMP Algorithm	74
2.9.5	Four-Disks-in-a-Square Geometry	77
2.10	Conclusions	79
3.	HIGH-ORDER ACCURATE PARTITIONED SCHEMES FOR CONJUGATE HEAT TRANSFER WITH ADVECTION-DIFFUSION EQUATIONS	81
3.1	A Brief Introduction	81
3.2	Governing Equations and Model Problem	81
3.3	Derivation of the CHAMP Operators for a pth-Order Accurate Scheme . . .	84
3.4	The Partitioned Conjugate Heat Transfer Algorithm Using CHAMP Conditions	88
3.5	Analysis of the CHAMP Schemes	90
3.5.1	Model Problem Analysis of the CHAMP Iteration	92
3.5.2	Constraints on Velocities for the CHAMP Conditions	95
3.5.3	Analysis of the Un-iterated CHAMP Time-stepping Scheme	99
3.6	The CHAMP Interface Conditions on Curvilinear Grids	103
3.7	Numerical Results	108
3.7.1	Verification with Exact Solutions for Time Dependent Problems . . .	109
3.7.1.1	Adjacent Rectangles	109
3.7.1.2	Concentric Annuli	112
3.7.2	Verification Using Manufactured Solutions on Various Geometries . .	116
3.7.2.1	Rotated Squares	117
3.7.2.2	Sheared Squares	117
3.7.2.3	Wavy Geometry with Orthogonal Grid at Interface	120
3.7.2.4	Wavy Geometry with Non-Orthogonal Grid at Interface . .	122
3.8	Conclusions	124
4.	CONCLUSIONS AND FUTURE WORK	127
	REFERENCES	130
	APPENDICES	142
	A. PROOF OF LEMMA 1	142
	B. DERIVATION OF THE INTERFACE PROJECTION	145
	C. A POWER-METHOD-LIKE APPROACH FOR COMPUTING COMPLEX AM- PLIFICATION FACTORS	149

LIST OF TABLES

2.1	Values of α_ℓ and β_0 for BDF schemes of order $p = 2, 4, 6$	22
2.2	CHAMP iteration: A_{CI} and corresponding optimal p_L and p_R for a 4 th -order accurate CHAMP conditions with various choices of material parameters $K_{LR} = \frac{K_L}{K_R}$, $D_{LR} = \frac{D_L}{D_R}$, $\lambda_{DL} = \frac{tD_L}{h^2}$	33
2.3	A convergence study for a annulus-annulus domain at $t_{\text{nal}} = 0.5$ using the steady state solution.	57
2.4	Selected eigenvalues s and coefficients A_L, A_R for two selected cases on a double-rectangle domain.	59
2.5	A convergence study for the double-rectangle problem using the time-dependent exact solution with selected thermal parameters.	60
2.6	Selected eigenvalues s and coefficients for three selected cases on a double-annulus domain.	62
2.7	A convergence study for the double-annulus problem using the time-dependent exact solution with selected thermal parameters.	64
2.8	Constants in manufactured solutions used for rotated-square geometry.	66
2.9	A convergence study for the un-iterated CHAMP scheme on a rotated-square domain using the trigonometric manufactured solution with various choices of material parameters.	67
2.10	Constants in manufactured solutions used for sheared-square geometry.	69
2.11	A convergence study for the un-iterated CHAMP scheme on a stretched-square domain using the trigonometric manufactured solution with various choices of material parameters.	70
2.12	Constants in manufactured solutions used for wiggled geometry.	71
2.13	A convergence study for the un-iterated CHAMP scheme on a wiggled-cos domain using the trigonometric manufactured solution with various choices of material parameters.	72
2.14	A convergence study for the un-iterated CHAMP scheme on a wiggled-sin domain using the trigonometric manufactured solution with various choices of material parameters.	75
2.15	A convergence study for the CHAMP scheme on a curvilinear domain using one or two sub-iterations.	76
2.16	Material coefficients and coupling parameters used for the four-disks-in-a-box problem.	78

2.17	A convergence study for a multi-domain problem using the adaptive CHAMP algorithm.	80
3.1	Selected eigenvalues s and coefficients for two selected cases on double-rectangle domain.	111
3.2	A convergence study for the double-rectangle problem using the time-dependent exact solution with selected thermal parameters.	113
3.3	Selected eigenvalues s_ν of the exact solutions for three selected cases on double-annulus domain.	115
3.4	A convergence study for the double-annulus problem using the time-dependent exact solution with selected thermal parameters.	116
3.5	Constants in manufactured solutions used for rotated-square geometry.	117
3.6	A convergence study for the un-iterated CHAMP scheme on a rotated-square domain using the trigonometric manufactured solution with various choices of material parameters.	119
3.7	Constants in manufactured solutions used for sheared-square geometry.	120
3.8	A convergence study for the un-iterated CHAMP scheme on a stretched-square domain using the trigonometric manufactured solution with various choices of material parameters.	122
3.9	Constants in manufactured solutions used for wiggled geometry.	123
3.10	A convergence study for the un-iterated CHAMP scheme on a wiggled domain defined by the cos function using the trigonometric manufactured solution with various choices of material parameters.	124
3.11	A convergence study for the un-iterated CHAMP scheme on a wiggled domain defined by the sin function using the trigonometric manufactured solution with various choices of material parameters.	126

LIST OF FIGURES

1.1	Left: sample computational domains for monolithic schemes. Right: sample computational domains for partitioned schemes.	2
1.2	Flow charts for monolithic scheme and partitioned scheme.	3
1.3	A schematic diagram for a phase change problem.	10
2.1	A schematic diagram for a sample conjugate heat transfer problem. The entire domain consists of four sub-regions, one rectangle with material properties (K_1, D_1) and three disks with material properties (K_2, D_2) , (K_3, D_3) and (K_4, D_4) respectively. The interfaces between various domains are labeled with $l_{1,2}, l_{1,3}, l_{1,4}$	12
2.2	Simplified model problem geometry. Domains are labeled with Ω_L, Ω_R , and are assumed to be semi-infinite in x	13
2.3	A sample computational grid for a 4 th -order accurate scheme with two ghost points at each domain.	24
2.4	Comparison of the CHAMP iteration convergence rate to Optimized Schwarz for the problem with equal material parameters and different overlap width.	31
2.5	CHAMP iteration: A versus $\kappa = kh$ for selected optimal p_L and p_R for orders 2, 4, and 6 ($h = 10^{-3}$).	32
2.6	CHAMP iteration: A_{CI} and corresponding optimal p_L and p_R for orders 2, 4, and 6 ($h = 10^{-3}$) with various choices of material parameters $K_{LR} = \frac{K_L}{K_R}, D_{LR} = \frac{D_L}{D_R}, \lambda_{DL} = \frac{tD_L}{h^2}$	34
2.7	CHAMP time-stepping: A_{CT} and corresponding optimal p_L and p_R for a 4 th -order accurate schemes with various choices of material parameters $K_{LR} = \frac{K_L}{K_R}, D_{LR} = \frac{D_L}{D_R}, \lambda_{DL} = \frac{tD_L}{h^2}$	41
2.8	Computational domain for the square-square geometry.	55
2.9	Physical domain for the annulus-annulus geometry.	57
2.10	Numerical results for the double-rectangle problem. Left: a sample computational grid for a double-rectangle geometry. Middle: CHAMP4 solution for Case 1 at $t_{\text{nal}} = 5$ on grid $G_{dr}^{(8)}$. Right: error for Case 1 at $t_{\text{nal}} = 5$ on the same grid.	61
2.11	Numerical results for the double-annulus problem. Left: a sample computational grid for a double-annulus geometry. Middle: CHAMP4 solution for Case 3 at $t_{\text{nal}} = 0.5$ on grid $G_{dr}^{(4)}$. Right: error for Case 3 at $t_{\text{nal}} = 0.5$ on the same grid.	63

2.12	Rotated-square results. Left: a sample grid for a rotated-square geometry. Middle: CHAMP4 solution at $t_{\text{nal}} = 0.2$ for Case 1 on grid $G^{(8)}$. Right: error at $t_{\text{nal}} = 0.2$ for Case 1 on the same grid.	66
2.13	Convergence plots for rotated-square geometry. Left: max-norm errors for Case 1 at $t_{\text{nal}} = 0.2$ using CHAMP2 and CHAMP4 schemes. Right: max-norm errors for Case 2 at $t_{\text{nal}} = 0.2$ using CHAMP2 and CHAMP4 schemes.	68
2.14	Sheared-square results. Left: a sample grid for a stretched-square geometry. Middle: CHAMP4 solution at $t_{\text{nal}} = 0.2$ for Case 1 on grid $G^{(8)}$. Right: error at $t_{\text{nal}} = 0.2$ for Case 1 on the same grid.	68
2.15	Convergence plots for sheared-square geometry. Left: max-norm errors for Case 1 at $t_{\text{nal}} = 0.2$ using CHAMP2 and CHAMP4 schemes. Right: max-norm errors for Case 2 at $t_{\text{nal}} = 0.2$ using CHAMP2 and CHAMP4 schemes.	69
2.16	Curvilinear-grid results. Left: a sample grid for a wiggled-cos geometry. Middle: CHAMP4 solution at $t_{\text{nal}} = 0.2$ for Case 2 on grid $G^{(8)}$. Right: error at $t_{\text{nal}} = 0.2$ for Case 2 on the same grid.	71
2.17	Convergence plots for wiggled-cos geometry. Left: max-norm errors for Case 1 at $t_{\text{nal}} = 0.2$ using CHAMP2 and CHAMP4 schemes. Right: max-norm errors for Case 2 at $t_{\text{nal}} = 0.2$ using CHAMP2 and CHAMP4 schemes.	71
2.18	Curvilinear-grid results. Left: a sample grid for a wiggled-sin geometry. Middle: CHAMP4 solution at $t_{\text{nal}} = 0.2$ for Case 1 on grid $G^{(8)}$. Right: error at $t_{\text{nal}} = 0.2$ for Case 1 on the same grid.	73
2.19	Convergence plots for wiggled-sin geometry. Left: max-norm errors for Case 1 at $t_{\text{nal}} = 0.2$ using CHAMP2 and CHAMP4 schemes. Right: max-norm errors for Case 2 at $t_{\text{nal}} = 0.2$ using CHAMP2 and CHAMP4 schemes.	74
2.20	Adaptive CHAMP algorithm. Left: average number of sub-iterations as a function of λ_{DL} for different CHAMP tolerance. Right: optimal weighting parameters p_L and p_R for different λ_{DL}	77
2.21	Four disks in a box. Left: a schematic diagram showing five sub-domains. Middle: a sample overset grid used for the calculations. Right: amplified grid showing different components of the overset grid.	79
2.22	Four disks in a box results. Left: max-norm errors at $t_{\text{nal}} = 0.5$ using CHAMP2 and CHAMP4 scheme. Middle: CHAMP4 solution at $t_{\text{nal}} = 0.5$ on grid $G^{(4)}$. Right: error at $t_{\text{nal}} = 0.5$ on the same grid.	79
3.1	An example of a conjugate heat transfer problem. The entire domain consists of four sub-regions, one large disk with material properties (K_1, D_1) and three smaller disks with material properties (K_2, D_2) , (K_3, D_3) and (K_4, D_4) respectively. The interfaces between various domains are labeled with $l_{1,2}$, $l_{1,3}$, $l_{1,4}$	82

3.2	The geometry for the model problems. The solution is assumed to be 2π -periodic in the y -direction.	90
3.3	CHAMP iteration for advection-diffusion: A_{CI} and corresponding optimal p_L and p_R for orders 2 and 4 ($h = 10^{-3}$) with various choices of material parameters $K_{LR} = \frac{K_L}{K_R}$, $D_{LR} = \frac{D_L}{D_R}$, $\lambda_{DL} = \frac{tD_L}{h^2}$	95
3.4	CHAMP iteration for advection-diffusion: A_{CI} and corresponding optimal p_L and p_R for orders 2 and 4 ($h = 10^{-2}$) for various choices of material parameters $K_{LR} = \frac{K_L}{K_R}$, $D_{LR} = \frac{D_L}{D_R}$, $\lambda_{DL} = \frac{tD_L}{h^2}$. Here λ_{DL} are chosen to be 10^6 , 10^4 and 10^3	96
3.5	Double-rectangle results. Left: a sample grid for the double-rectangle geometry. Middle: BDF4 solution at $t_{\text{nal}} = 5$ for Case 1 on grid $G^{(4)}$. Right: error at $t_{\text{nal}} = 5$ on grid $G^{(4)}$ for the same case.	112
3.6	Double-annulus results. Left: a sample grid for the double-annulus geometry. Middle: BDF4 solution at $t_{\text{nal}} = 2$ for Case 2 on grid $G^{(4)}$. Right: error at $t_{\text{nal}} = 2$ on grid $G^{(4)}$ for the same case.	115
3.7	Rotated-square results. Left: a sample grid for a rotated-square geometry. Middle: BDF4 solution at $t_{\text{nal}} = 0.1$ for Case 1 on grid $G^{(8)}$. Right: error at $t_{\text{nal}} = 2$ on grid $G^{(8)}$ for the same case.	118
3.8	Convergence plots for rotated-square geometry. Left: max-norm errors as a function of mesh spacing for Case 1 at $t_{\text{nal}} = 0.1$. Right: max-norm errors as a function of mesh spacing for Case 2 at $t_{\text{nal}} = 0.1$	118
3.9	Stretched-square results. Left: a sample grid for a stretched-square geometry. Middle: BDF4 solution at $t_{\text{nal}} = 0.1$ on grid $G^{(8)}$ for Case 1. Right: error at $t_{\text{nal}} = 0.1$ on grid $G^{(8)}$ for the same case.	120
3.10	Convergence plots for stretched-square geometry. Left: max-norm errors as a function of mesh spacing for Case 1 at $t_{\text{nal}} = 0.1$. Right: max-norm errors as a function of mesh spacing for Case 2 at $t_{\text{nal}} = 0.1$	121
3.11	Wiggled domain results. Left: a sample grid for a wiggled geometry. Middle: BDF4 solution at $t_{\text{nal}} = 0.1$ on grid $G^{(8)}$ for Case 2. Right: error at $t_{\text{nal}} = 0.1$ on grid $G^{(8)}$ for the same case.	121
3.12	Convergence plots for a wiggled geometry. Left: max-norm errors as a function of mesh spacing for Case 1 at $t_{\text{nal}} = 0.1$. Right: max-norm errors as a function of mesh spacing for Case 2 at $t_{\text{nal}} = 0.1$	123
3.13	Wiggled domain results. Left: a sample grid for a wiggled geometry. Middle: BDF4 solution at $t_{\text{nal}} = 0.1$ on grid $G^{(8)}$ for Case 1. Right: error at $t_{\text{nal}} = 0.1$ on grid $G^{(8)}$ for the same case.	125

3.14 Convergence plots for a wiggled geometry. Left: max-norm errors as a function of mesh spacing for Case 1 at $t_{\text{nal}} = 0.1$. Right: max-norm errors as a function of mesh spacing for Case 2 at $t_{\text{nal}} = 0.1$ 125

LIST OF ALGORITHMS

1	CHAMP partitioned conjugate heat transfer solver for heat equations.	23
2	Un-iterated CHAMP time-stepping algorithm.	35
3	Transforming polynomial system to a single high-degree polynomial.	40
4	CHAMP adaptive conjugate heat transfer solver.	53
5	A sample MAPLE code that defines x -derivatives of T_R for advection-diffusion equations.	87
6	A sample MAPLE code that forms the fourth-order accurate CHAMP conditions for advection-diffusion equations.	88
7	CHAMP partitioned conjugate heat transfer solver for advection-diffusion equations.	89
8	Un-iterated CHAMP time-stepping algorithm for advection-diffusion equation.	99
9	A sample MAPLE code that computes $G(A)$ for the time-stepping amplification factor of the advection-diffusion equation.	103

ACKNOWLEDGMENT

I would like to express my deepest appreciation to all my thesis committee members. A special thanks go to Professor Schwendeman, Professor Henshaw, and Professor Banks for their invaluable expertise and immense knowledge in the area. Many thanks to Professor Banks for his treasured support that inspired my initial interest in this subject. Special thanks to Professor Henshaw and Professor Schwendeman for their patience and guidance that carried me through all the stages of completing this research project. I would particularly like to thank my academic advisor, Professor Kovacic, who has supported my academic goals and has a profound belief in my abilities.

I would also like to thank my friends, Yiqing and Dong, for their accompany and encouragement. Finally, I would like to thank my mom and dad and my best friend Yulu and Zeren for their love and guidance throughout my study. The completion of my dissertation would not have been possible without their support.

ABSTRACT

This thesis presents a high-order accurate partitioned scheme for the solution of conjugate heat transfer (CHT) problems. The scheme is based on special second-order accurate CHAMP (Conjugate Heat transfer Advanced Multi-domain Partitioned) interface conditions, and extended here to high-order accuracy and to the advection-diffusion equations. The solutions in each material domain are advanced independently with an implicit method, and domains are coupled at the interface using the new CHAMP interface conditions. These conditions are based on usual interface matching conditions involving continuity of temperature and heat flux, together with additional compatibility conditions derived from the governing equations. The new CHAMP conditions are implemented numerically using an optimized Schwarz approach, with a Taylor expansion leading to an effective domain overlap, which significantly improves the convergence rate. The partitioned time-stepping schemes are found to be stable with none or just a few sub-time-step iterations for a wide class of CHT problems.

The first part of this thesis focuses on the conjugate heat transfer problem for the diffusion equations and extends the current second-order accurate CHAMP schemes to higher-order accuracy. A detailed fourth-order accurate derivation is given to demonstrate the approach, with a general discussion on deriving a p th-order accurate method. The scheme is then analyzed to determine the optimal coupling coefficients in the CHAMP condition based on solving an optimization problem. The CHAMP iteration is studied in isolation while keeping the time-step fixed, and the iteration amplification factor of the CHAMP scheme is compared to the optimized Schwarz scheme with different overlap widths. The CHAMP time-stepping scheme is then studied for the case where no sub-iteration is taken. The un-iterated CHAMP time-stepping scheme is analyzed to show the overall fourth-order accuracy when a fourth-order accurate CHAMP interface condition is applied. The CHAMP condition is also derived for general curvilinear grids. Numerical results using manufactured solutions on curvilinear grids are given showing the accuracy and stability of the un-iterated CHAMP schemes. To solve problems with large time steps, an adaptive variable sub-iteration CHAMP algorithm is proposed. The new algorithm chooses the number of sub-iterations adaptively based on a measure of the residual for the CHAMP conditions at each time step. A large time step study using the new adaptive algorithm is given to show the robustness of

the method.

The second part of this thesis generalizes the approach to solving the conjugate heat transfer problems with advection-diffusion equations, also to higher-order. Involving the advective terms in the governing equations and interface conditions complicates the analysis. The p th-order accurate method is derived first, followed by a presentation of the complete CHAMP time-stepping algorithm. A detailed second-order accurate analysis is presented to describe the approach, with a general discussion on analyzing a p th-order accurate method. The CHAMP iteration amplification factor for the advection-diffusion equations is computed numerically using some numerical software packages. The coupling parameters in the CHAMP condition are calculated by solving an optimization problem based on the convergence factor of the sub-iterations. The iteration amplification factors for the CHAMP schemes using the optimal coupling parameters with different orders of accuracy are presented and compared. The convergence factor of a p th-order accurate un-iterated CHAMP time-stepping scheme is also derived and analyzed. Finally, the accuracy of the scheme is verified using several numerical examples.

CHAPTER 1

INTRODUCTION

Conjugate heat transfer (CHT) arises in many scientific and engineering applications. Such CHT problems include modeling of aerothermodynamic processes [10], thermal management of lithium-ion cells [82], thermal energy storage for power plants [80], simulation of heat transfer in turbine engines [22, 53, 87, 91], modeling of phase change [63], and more. The general CHT problem involving a solid body and a surrounding fluid was analyzed by Perelman [83] and Luikov [68], among others; see the review article in [57]. Since thermal coupling generally involves an interaction between multiple domains, exact solutions are often unavailable or difficult to obtain. Thus a significant effort has been made to solve CHT problems using efficient and accurate numerical schemes. A difficulty for CHT problems with coupled domains involves the accurate treatment of the matching conditions at material interfaces. Applying discrete interface conditions to approximate the matching conditions in numerical solvers is a very important component in modeling heat transfer for multi-domain systems, and the primary goal of the current work is to develop high-order accurate numerical methods for the solution of such problems.

In the present work, a high-order accurate partitioned scheme is developed for the solution of CHT problems. The scheme is based on the innovative CHAMP (Conjugate Heat transfer Advanced Multi-domain Partitioned) approach developed in [75]. This original approach was described for CHT problems governed by diffusion only and for second-order accurate numerical approximations. The principal advances described in this thesis involve an extension of the CHAMP approach to higher-order accuracy and to problems governed by diffusion with and without advection. In particular, problems with non-zero advection velocity at the interface are considered, with materials either gained or lost at the interface. Such a situation will be denoted by CHT-AI (Conjugate Heat Transfer Active Interface) in later discussions.

A sample CHT-AI problem is depicted in Figure 1.1, where the domain consists of three sub-domains joined at two material interfaces. Such a problem includes, for example, the classical Stephan problem describing the material undergoing a phase change, or an ablation problem modeling the surface ablation of a given material [32]. The physical domains for these types of problems would include multiple fluid and solid subdomains, and

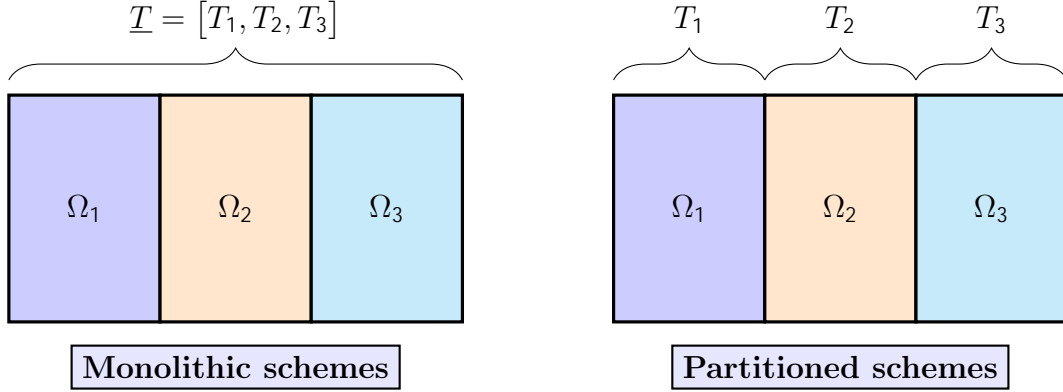


Figure 1.1: Left: sample computational domains for monolithic schemes.
 Right: sample computational domains for partitioned schemes.

the matching conditions at the interfaces require continuity of temperature and heat flux across the interfaces. The behavior of the material in each subdomain obeys some governing equations, along with the interface conditions and physical boundary conditions. To solve this problem numerically, one approach would be to construct a large coupled system that involves discrete approximations of the governing equations as well as the boundary conditions and interface conditions [16], and then advance the solution together in time. This is often referred to as a monolithic approach. The plot on the left of Figure 1.1 presents a sample computational domain for a typical monolithic scheme. The composite solution \underline{T} is formed for the entire domain $\Omega = \Omega_1 \llcorner \Omega_2 \llcorner \Omega_3$, and the updating matrix for a time-stepping scheme contains all of the information of the system. At each time step, the matrix equation for \underline{T} is solved, and the sub-domain solutions are advanced together. If the problem is nonlinear, then a matrix system would be obtained from a linearization of the problem in an iterative scheme such as Newton's method. Figure 1.2 provides a simplified monolithic algorithm.

An alternative approach, and the focus of the work in this thesis, is a partitioned approach. In a partitioned scheme, during each time step, the interface conditions are applied for each domain in a segregated fashion with some number of sub-time-step iterations taken. The solution in each sub-domain is then advanced in time using some time-stepping method along with the domain solver for that subdomain. The right plot in Figure 1.1 illustrates a sample computational domain used for a partitioned scheme. For each subdomain Ω_i , $i = 1, 2, 3$, an updating matrix that includes the interface coupling is formed, and solutions T_i , $i = 1, 2, 3$ for each sub-domain are solved sequentially through some iterative technique.

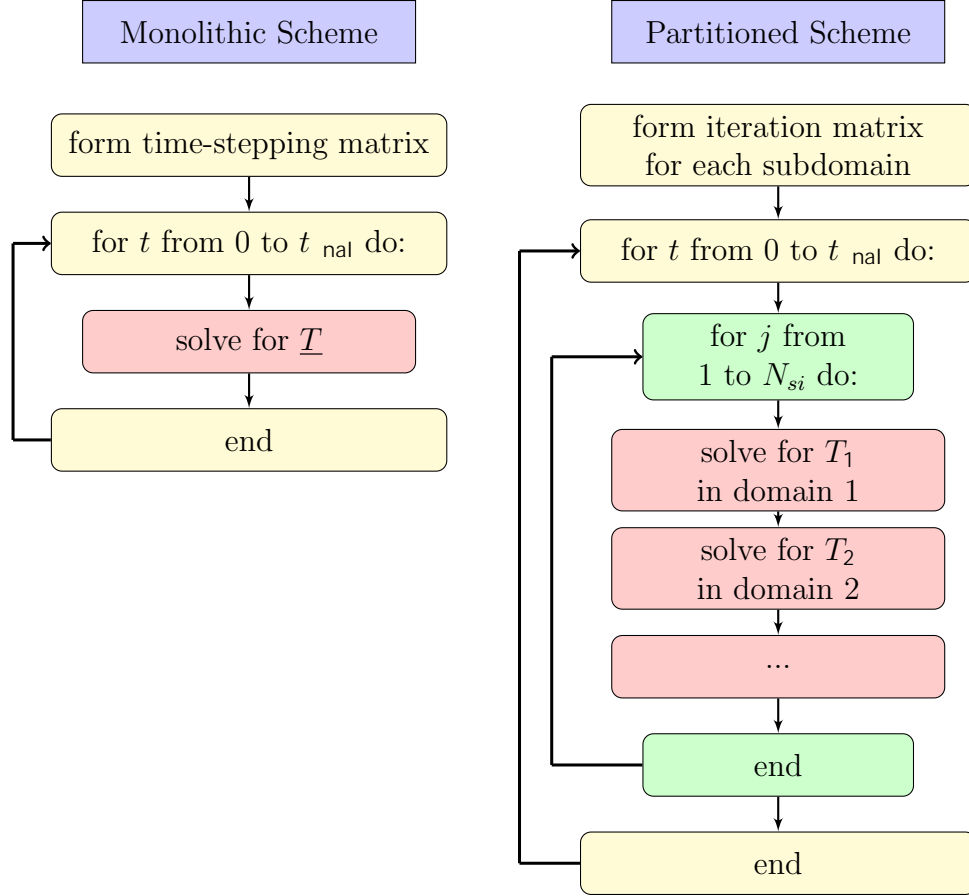


Figure 1.2: Flow charts for monolithic scheme and partitioned scheme.

A crucial element of the partitioned scheme is how the information is transmitted between adjacent subdomains, and the choice of this interface coupling has a major impact on the overall performance of the scheme.

If the underlying physical systems can be discretized directly, monolithic schemes are, in general, very effective as they typically have favorable stability properties when appropriate time integration methods are chosen [49, 59]. However, a monolithic scheme typically involves a large linear system that needs to be solved at each time step. Often this is done using some preconditioned iterative solver, but if the subdomains involve different fluid and solid systems, then deriving an effective preconditioner for such a matrix can be challenging. Partitioned solvers, on the other hand, can take advantage of efficient single-domain solvers that have been developed over the years for different types of fluid or solid equations specifically [50, 52, 93]. There are other benefits of using partitioned schemes. For example, one can have disparate time scales in different subdomains [48, 76], and from an implementation

point of view, the approach can be easier to generalize to problems with more complicated domains. A potential disadvantage is that the stability and accuracy of the entire algorithm can be an issue, and this requires careful investigation. In the present study, the stability and accuracy of the CHAMP algorithm are analyzed and verified, and we consider CHT problems that are modeled by diffusion, with or without advection, but with no fluid flow.

For a partitioned scheme, the traditional interface treatment is the Dirichlet-Neumann (DN) coupling conditions. For problems involving both fluid and solids, the temperature information from the solid domain is applied as a Dirichlet condition to the fluid domain, and the flux information from the fluid domain is applied as a Neumann boundary condition to the solid domain. Giles [43], for example, investigated the stability of the DN coupling for a simplified one-dimensional fluid-structure interaction problem. He found that the scheme is stable, provided that the Neumann boundary conditions are applied for the solid domain and the Dirichlet boundary conditions are applied for the fluid domain along the interface. Roe [85] pointed out that the traditional Dirichlet-Neumann treatment suffers from a strict stability constraint. To improve the stability limit, he developed a new coupling scheme that imposes an additional equation at the interface. This equation is derived from taking the time derivative of the temperature continuity equations, and the time dependence is replaced using the governing equations. The new combined interface boundary condition (CIBC) method was shown to have a larger stability region and improved accuracy. Henshaw and Chand [51] proposed some weakly coupled algorithms to solve transient and steady-state CHT problems with various discretizations of the interface equations. They showed that when the time-step is advanced implicitly, the convergence of the sub-time-step iterations of the scheme depends on the relative sizes of material properties in each sub-domain. They also proved that for the case when an explicit time-stepping method is used, their scheme is stable and second-order accurate regardless of the relative material parameters in different domains.

In related work, Errera [25] considered Dirichlet-Robin interface conditions for a one-dimensional CHT problem. A normal mode stability analysis [45] was presented to derive an exact expression for the amplification factor, which was used to formulate the optimal coupling coefficients that provide the fastest convergence rate for the Dirichlet-Robin scheme. Based on this formulation, analysis of the coupling coefficients for the Dirichlet-Neumann, Dirichlet-Robin, and Neumann-Robin interface conditions are extended to more general CHT

problems by Errera in [24, 26, 27, 29], and to three-dimensional applications by Khoury and Errera in [23]. Analysis of the stability of the Dirichlet-Robin coupling was also investigated by Joshi [58]. Verstraete and Scholl [94] studied the stability for different coupling approaches based on how the boundary information is passed between solid and fluid domains for a simplified one-dimensional steady CHT problem. Based on their work, Scholl [88] extended the stability analysis to more general Robin-Robin conditions and presented new coupling approaches. Moretti [79] presented a detailed analysis of the stability of a Dirichlet-Robin condition and a Neumann-Robin condition for steady CHT problems. The exact form of the temporal and spatial convergence factors are derived based on a normal mode analysis for a simplified model problem involving the Navier-Stokes equations for the fluid domain and a steady diffusion equation in the solid domain, and a numerical Biot number emerges that characterizes the strength of the fluid-structure interaction, with a high value indicating strong thermal interaction between the fluid and solid domains. Optimal coupling parameters are derived based on the Biot number and the convergence factors, and the results show that the optimal Dirichlet-Robin conditions are effective for problems with low and moderate values of the Biot number, whereas the Neumann-Robin conditions work better for strong fluid-structure interactions.

For more general CHT simulations, Gelatin [41] investigated the Dirichlet-Neumann interface coupling applied to problems involving high-speed flow around a supersonic vehicle. Zhang [97] considered structural heat transfer and hypersonic flow behavior using a finite element method solver with the interface loosely coupled with the D-N interface conditions. More simulations using the D-N coupling are performed and analyzed in [13, 28, 46, 47, 66, 77]. Extension to Neumann-Neumann, Dirichlet-Robin, Neumann-Robin, or Robin-Robin interface conditions for general CHT problems are investigated in [30, 44, 78]. In particular, Kazemi-Kamyab [62] investigated a second-order accurate loosely coupled partitioned scheme of the time-dependent CHT problem with the Dirichlet-Neumann coupling at the interface. He derived a stability constraint in terms of time-step, mesh spacing, and material coefficients for each subdomain when the Crank-Nicolson scheme is used for temporal integration. For the same Dirichlet-Neumann interface coupling, Kazemi-Kamyab [60, 61] also studied the stability of a high-order accurate loosely coupled implicit-explicit (IMEX) Runge-Kutta scheme and a strongly coupled explicit first-stage singly diagonally implicit Runge-Kutta (ESDIRK) scheme for the time-dependent CHT problem with various mate-

rial coefficients. He showed that the IMEX scheme converges faster than the Crank-Nicolson scheme for time-accurate solutions, and the ESDIRK scheme is more efficient than the IMEX scheme in terms of computational efficiency.

For CHT problems involving complex geometry, Costa [18] proposed a high-order accurate finite volume method that uses the Dirichlet-Neumann and Neumann-Neumann interface treatments for a two-dimensional steady-state model problem with discontinuous thermal coefficients. Li [65] proposed a new lattice Boltzmann equation method based on a Dirichlet-Neumann interface treatment. The new scheme is proved to be second-order accurate for both steady and unsteady advection-diffusion equations with a planar interface. More work on the lattice Boltzmann model is investigated by Yue [96] for solving general CHT problems and by Esfahani [31] for problems involving incompressible flows.

Other researchers have studied monolithic methods for CHT problems. Pan, Li and Choi [81], for example, proposed a monolithic approach to solve a time-dependent CHT problem involving both convection and conduction and the thermal interaction at the interface. The globally coupled system is discretized spatially using a second-order accurate finite difference formula and integrated in time using a Crank-Nicolson scheme. The method is shown to be stable and second-order accurate for a two-dimensional model problem. A comparison between a monolithic solver and a partitioned solver for problems involving fluid-structure interaction is studied by [19].

For CHT-AI problems involving advection through the interfaces, Roe [84] extended the work of Giles [43] to investigate the stability of a coupled fluid-structure interaction problem with a moving interface. He showed that with the usual interface jump conditions, the stability for the coupled scheme depends on both the interface velocities and the relative heat capacity of each sub-domain. He also showed that a smaller time step must be taken when domains have larger interface velocities for the Dirichlet-Neumann iteration to be stable. The analysis follows a Godunov–Ryabenkii [45] normal mode approach for the advection-diffusion equation, which was also studied by Sousa [92] for linear parabolic equations. Lindstrom [67] analyzed a weakly coupled one-dimensional CHT problem involving heat transfer between a fluid and solid, with the interface conditions derived from the energy method. Kutluay [63] considered different explicit finite difference approximations to solve the classic one-dimensional melting ice problem. He formulated the problem using an interface-fixed coordinate system. Such a procedure generates more accurate numerical

results in terms of the temperature distribution than treating the moving interface directly using a variable space grid method (VSG). In a VSG method, the total number of grid points is kept fixed, and the mesh spacing would change at each time step so that the location of the moving boundary on the mesh space always has the same grid index. Zhao [98] also investigated the numerical stability of a moving interface problem in fluid-structure interaction with Dirichlet-Robin interface coupling through a Goudonov-Ryabenkii normal mode analysis. The results prove that for a given velocity, the coupling coefficients in the Dirichlet-Robin conditions can be chosen so that the resulting scheme is stable and accurate.

A subclass of CHT problems is the domain-decomposition problem, where the material coefficients are the same across the interface. Many numerical schemes have been developed to solve these types of problems specifically [90, 14]. For example, Achdou [2] proposed a Robin-Robin algorithm to solve the advection-diffusion equation on a partitioned domain. Roux [86] developed a Dirichlet-Robin condition and a Robin-Robin condition for the domain-decomposition problem and showed that they have better stability properties than the D-N iteration. He indicated that the optimal coupling parameters for the Robin conditions are generally hard to compute, but can be obtained by some approximation methods. Another commonly used approach is the classical Schwarz method, which involves splitting the domain into sub-domains and solving the problem on each sub-domain separately. The results are then combined to form the general solution of a boundary-value problem [95]. Gander [33] presented a new type of interface coupling conditions for a model two-domain domain-decomposition problem. The new method, called the optimized Schwarz (OS) method, employs a domain overlap and two coupling parameters, and it was shown to converge uniformly faster than the classical Schwarz method. The convergence factor of the new scheme can be derived by seeking solutions to the Fourier transformed system to obtain a function in terms of the domain parameters and transformed frequencies. The performance of the method can be further improved by solving an optimization problem based on the convergence factor to obtain optimal coupling parameters that minimize the convergence factor over all frequencies. For schemes without overlap, Gander [37] studied a new type of optimized Schwarz method for Helmholtz problems. He presented new types of transmission conditions where the optimal parameters are chosen such that the convergence of the scheme is optimized. Dubois [21] investigated optimized Schwarz methods with Robin transmission conditions for both overlapping and non-overlapping domain-decomposition problems with

advection-diffusion equations. He found that the new schemes are less sensitive to mesh spacing than traditional Robin conditions. Japhet [56] presented a new Schwarz-like method that uses a Dirichlet to Neumann mappings in the interface condition. The new method is shown to converge faster than the classical Schwarz method for solving domain decomposition problems. Other methods that extended the Schwarz-like algorithm for domain decomposition problems are studied in [20, 40, 71].

Another well-known technique to solve the domain-decomposition problem is the waveform relaxation method, which is an iterative method based on a domain partitioning, with coupling terms replaced by solutions from the previous iteration. Gander [35], based on the work of Lelarsmee [64], extended the waveform relaxation method to include a Schwarz-like iteration [38], and proposed new transmission conditions so that the overlapping Schwarz waveform relaxation algorithm is stable and converges faster than classic Schwarz waveform relaxation algorithm. Martin [73] also studied the convergence of the Schwarz waveform relaxation algorithm for a two-dimensional advection-diffusion equation. The resulting scheme is very efficient when using optimal coupling parameters that are chosen based on the minimization of the convergence rate. Mandal [72] presented a new waveform relaxation algorithm based on the Dirichlet-Neumann coupling on a one-dimensional model problem consisting of heat equations. Other works on waveform relaxation algorithms are studied in [12].

The challenge remains to extend the Schwarz-like approach to general CHT problems. Including a domain overlap in the domain-decomposition problem provides an important grid overlapping parameter in the stability analysis, which can be used to improve the convergence rate of the resulting scheme. But for problems with discontinuous coefficients, the idea of including a domain overlap becomes less obvious. Gander [34], for example, investigated the non-overlapping optimized Schwarz method for a steady-state two-domain diffusion problem with different material properties. Optimal coupling parameters for the corresponding schemes can be determined by analyzing the convergence factor of the Fourier transformed system, and the resulting scheme is very effective in solving problems with discontinuous coefficients. Hoang [54] proposed an implicit time-stepping method that uses the optimized Schwarz waveform relaxation (OSWR) algorithm with Robin transmission conditions at the interface to solve advection-diffusion equations. The convergence of the algorithm only weakly depends on mesh spacing, and the scheme is able to solve the problem with a jump in thermal coefficients. Blayo [15] proposed an optimized Schwarz waveform

relaxation algorithm for solving advection-diffusion equations with discontinuous material coefficients. A non-overlapping Schwarz waveform relaxation method was also investigated by Gander [36] to solve a one-dimensional advection-diffusion-reaction equation. Other extensions of Schwarz like methods to problems involving discontinuous parameters are investigated in [11, 39, 42, 55, 69, 70].

Of particular interest for the work in this thesis is the Robin interface condition for CHT problems developed by Meng [75]. This interface condition involves a weighted combination of a generalized Dirichlet operator and a generalized Neumann operator, and it incorporates a domain overlap. The new condition combines the idea of overlapping optimized Schwarz methods together with Robin coupling conditions that have been developed in recent papers [3, 4, 5, 6, 7, 8, 9, 89]. A simplified two-dimensional model problem involving just the heat equation is formed, and the new scheme, called CHAMP, is able to include an effective domain overlap via suitable Taylor expansions of the temperature and heat flux in each subdomain at a distance equal to the overlap width about the interface. The CHAMP scheme was implemented using second-order accurate finite difference approximations, and it was shown to be accurate in space and time using just one sub-time-step iteration for a wide range of thermal coefficients. It was also proved to converge uniformly faster than traditional D-N schemes. For the case when the material coefficients are the same, CHAMP is shown to perform better than the optimized Schwarz scheme with one grid-cell overlap, and it behaves as well as the OS scheme with doubled overlap width. For harder problems that need large time steps or very fine grids, the CHAMP scheme may require additional sub-iterations for the scheme to be stable, and for a majority of problems, two sub-iterations are sufficient.

The primary goal of the current work is to extend and analyze the previously developed second-order accurate CHAMP scheme to higher-order and also extend to advection-diffusion equations. As a motivating example, consider a sublimation process whereby a solid material undergoes a phase change directly to a gas, e.g., conversion of solid carbon dioxide (i.e., dry ice) into CO_2 gas at atmospheric temperatures and pressures. While the full Stefan problem would involve incompressible fluid flow, solid mechanics, moving interfaces, heat transfer, etc., the present study focuses specifically on the coupled heat transfer portion of the problem. The conversion of material from solid to gas along the front implies that at any point on the interface, the solid and gas velocities do not necessarily match. Therefore, spatially

dependent divergence-free velocity fields in either domain are considered. Finally, because the interface evolves slowly, it is appropriate to consider the interface geometry as fixed in time, and for convenience, all further discussion will be with respect to this fixed reference frame. Such a scenario is depicted schematically in Figure 1.3, which illustrates a geometrically complex interface separating solid and gas phases, each with its own divergence-free velocity field.

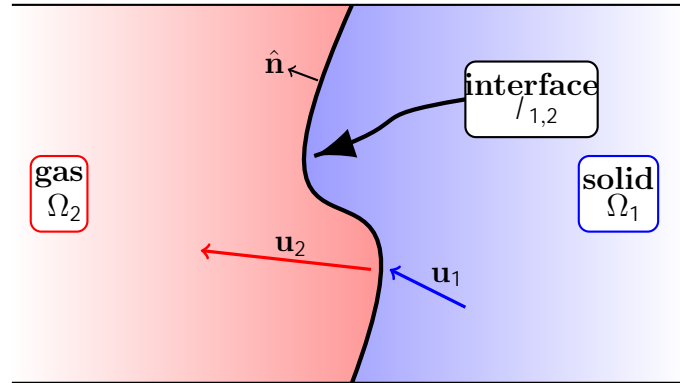


Figure 1.3: A schematic diagram for a phase change problem.

This thesis is organized as follows. In Chapter 2, a higher-order accurate CHAMP scheme for the diffusion equation is derived and analyzed. A simplified model problem is presented, and the interface stability analysis is carried out. The convergence of the model problem using an un-iterated CHAMP time-stepping scheme across all domains is also investigated. The accuracy of the CHAMP scheme is verified by computing numerical solutions to problems on various domains with different thermal properties. In Chapter 3, the method is extended to a two-dimensional model problem involving advection-diffusion equations. Analysis of sub-time-step iterations is given for arbitrary p th-order accurate CHAMP conditions, and an iteration convergence factor is derived to determining the optimal weighting parameters. Numerical approximations for the simulation of CHT problems are presented to verify the accuracy and stability of the un-iterated CHAMP time-stepping scheme. Some concluding remarks are given in Chapter 4.

CHAPTER 2

HIGH-ORDER ACCURATE PARTITIONED SCHEMES FOR CONJUGATE HEAT TRANSFER WITH DIFFUSION EQUATIONS

2.1 A Brief Introduction

In this chapter, a high-order accurate partitioned scheme, called CHAMP scheme, for solving conjugate heat transfer problems with diffusion equations is developed. The methodology discussed in this chapter is an extension to the previous work on second-order accurate CHAMP schemes [75]. The concept is generalized from a second-order accurate method, first to fourth-order, then to an arbitrarily p^{th} -order accurate method.

The remainder of this chapter is organized as follows. In Section 2.2, the model problem and the governing equations are described. In Section 2.3, a detailed derivation to the fourth-order accurate CHAMP conditions is given, followed by a generalization to derive a p^{th} -order accurate condition. In Section 2.4 the complete conjugate heat transfer solver for the model problem is introduced, with a brief discussion on the implementation of the CHAMP schemes. In Section 2.6.1, the convergence of the CHAMP sub-time step iteration is analyzed. In Section 2.6.2 the stability of the un-iterated CHAMP time-stepping scheme is studied, and a detailed analysis of the accuracy of the fourth-order accurate un-iterated CHAMP time-stepping scheme is presented in Section 2.6.3. In Section 2.7 the method is applied to general mapped domains. In Section 2.8, an adaptive CHAMP algorithm is proposed. Results from numerical simulations are presented in Section 2.9 and some concluding remarks are given in Section 2.10.

2.2 Governing Equations and Model Problem Specification

Consider a physical domain, denoted by Ω , that is partitioned into N subdomains $\Omega_m, m = 1, 2, 3, \dots, N$, each consisting of a different material. Let $T(\mathbf{x}, t)$ denote the temperature for $\mathbf{x} \in \Omega$ and for time $t \in [0, t_{\text{nal}}]$, and let $\rho(\mathbf{x})$, $C(\mathbf{x})$ and $K(\mathbf{x})$ denote the density, specific heat at constant pressure and heat conductivity, respectively. Define $T_m(\mathbf{x}, t)$ to be the temperature in each subdomain Ω_m , and let ρ_m , C_m and K_m be the properties of the material in Ω_m all assumed to be constant. The corresponding thermal diffusivity in Ω_m

is constant and given by $D_m = K_m/(\rho_m C_m)$. The interface between domains m_1 and m_2 is denoted by l_{m_1, m_2} , with $m_1, m_2 = 1, 2, \dots, N$, $m_1 < m_2$. An example of the problem configuration is depicted in Figure 2.1, where the physical domain Ω is divided into four sub-regions, each with their own thermal parameters.

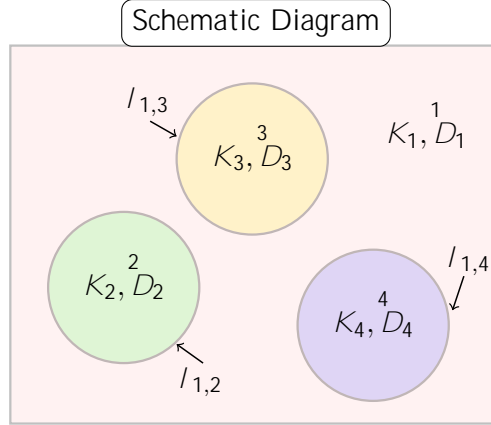


Figure 2.1: A schematic diagram for a sample conjugate heat transfer problem. The entire domain consists of four sub-regions, one rectangle with material properties (K_1, D_1) and three disks with material properties (K_2, D_2) , (K_3, D_3) and (K_4, D_4) respectively. The interfaces between various domains are labeled with $l_{1,2}$, $l_{1,3}$, $l_{1,4}$.

The temperature $T(\mathbf{x}, t)$ is assumed to be governed by the heat (diffusion) equation

$$\rho C \partial_t T = r - (K \nabla \cdot \nabla T), \quad \mathbf{x} \in \Omega, \quad t \in [0, t_{\text{nal}}], \quad (2.1)$$

where ∂_t denotes a partial derivative with respect to time, and with spatial derivatives similarly defined. Initial conditions and boundary conditions are taken to be

$$T(\mathbf{x}, 0) = T^{\text{IC}}(\mathbf{x}), \quad \mathbf{x} \in \Omega, \quad (2.2a)$$

$$a(\mathbf{x}, t)T + b(\mathbf{x}, t)\mathbf{n} \cdot \nabla T = h(\mathbf{x}, t), \quad \mathbf{x} \in \partial\Omega, \quad t \in [0, t_{\text{nal}}], \quad (2.2b)$$

where T^{IC} , a , b and h are given functions and where \mathbf{n} is the outward unit normal on the boundary $\partial\Omega$. The matching conditions involving continuity of temperature and heat flux

at a generic interface l between two materials are given by

$$[T]_l = 0, \quad \mathbf{x} \in l, \quad (2.3a)$$

$$[K\mathbf{n} \cdot \mathbf{T}]_l = 0, \quad \mathbf{x} \in l, \quad (2.3b)$$

where $[f(\mathbf{x}, t)]_l$ denotes the jump in a function f across l and \mathbf{n} is defined to be the unit normal pointing outward from the domain with the higher index.

The conjugate heat transfer (CHT) problem given by (2.1)–(2.3b) is solved numerically using a partitioned scheme. In general, the temperature in each subdomain is solved independently using a method of lines approach together with an implicit time-stepping method. The subdomain solvers are coupled at interfaces using discrete approximations to the original matching conditions. These coupling conditions are the basis of the CHAMP approach, and they are derived later in Section 2.3.

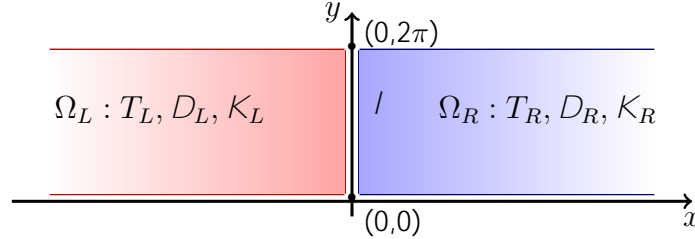


Figure 2.2: Simplified model problem geometry. Domains are labeled with Ω_L, Ω_R , and are assumed to be semi-infinite in x .

To study the accuracy and the stability of the partitioned scheme, a model CHT problem is considered for an infinite strip, $\Omega = \{(x, y) \mid -1 < x < 1, 0 < y < 2\pi\}$. The strip consists of two material subdomains, denoted by Ω_L and Ω_R , on either side of an interface l located at $x = 0$ as shown in Figure 2.2. Solutions are assumed to be 2π -periodic in the y -direction, and $T(x, y, t)$ decays to zero as $|x| \rightarrow 1$. For this configuration, the system to be analyzed is

$$\partial_t T_m = D_m \Delta T_m, \quad \text{for } (x, y) \in \Omega_m, \quad (2.4a)$$

$$[T]_l = 0, \quad \text{for } y \in (0, 2\pi), \quad (2.4b)$$

$$[K \partial_x T]_l = 0, \quad \text{for } y \in (0, 2\pi), \quad (2.4c)$$

$$T(x, y, t) \rightarrow 0, \quad \text{for } |x| \rightarrow 1, \quad (2.4d)$$

$$T_m(\mathbf{x}, 0) = T_m^{\text{IC}}(\mathbf{x}), \quad \text{for } (x, y) \in \Omega_m, \quad (2.4e)$$

where $m = L$ and R indicate the left and right domain, respectively, and the thermal properties D_m and K_m are constant in each subdomain (as mentioned previously). The ratios of thermal conductivities and diffusivities are defined as

$$K_{LR} \stackrel{\text{def}}{=} \frac{K_L}{K_R}, \quad D_{LR} \stackrel{\text{def}}{=} \frac{D_L}{D_R}, \quad (2.5)$$

and these non-dimensional parameters are used later in the derivation and analysis of the CHAMP coupling conditions.

2.3 Derivation of the CHAMP Interface Conditions

In this section, the CHAMP interface conditions are derived for the model CHT problem described in (2.4), where the domain consists of two adjacent rectangles with a planar interface located at $x = 0$. In order to motivate the derivation of the CHAMP conditions, a brief discussion on the optimized Schwarz approach for a domain decomposition problem is given. A derivation of 4th-order accurate CHAMP interface conditions is given next, followed by a general approach to obtain a p^{th} -order accurate method. For a 4th-order accurate scheme, explicit forms for the CHAMP operators can be expressed compactly and these form are presented below.

2.3.1 A Brief Review on Optimized Schwarz Algorithm for Domain Decomposition Problems

Let us first consider the heat equation defined on a domain with uniform material properties. A numerical approach for the approximate solution of the temperature can be considered in which the heat equation is advanced in time using an implicit time-stepping scheme. The system of equations implied by the implicit time-stepping scheme can be solved at each time step using a Schwarz approach for domain decomposition. Such an approach involves partitioning the domain into a set of subdomains, often with an overlap, and then solving the system of equations on each subdomain separately using matching conditions at the boundaries with adjacent subdomains (as well as any physical boundary conditions). Typically, the approach involves an iteration of the solvers on each subdomain until the solutions on all subdomains converge to the solution of the equations implied by the implicit time-stepping scheme for the full domain. A key aspect of this approach is the rate of

convergence of the iteration, and an optimized Schwarz approach uses matching conditions that give the fastest rate of convergence.

The optimized Schwarz approach proposed by Gander [33] employs matching conditions involving a weighted combination of a Dirichlet condition and a Neumann condition. In the context of the model problem in (2.4), assuming equal material properties in the left and right subdomains, the matching conditions are

$$\partial_x T_L^{(j)}(h, y) + \mathbf{S}_L T_L^{(j)}(h, y) = \partial_x T_R^{(j-1)}(h, y) + \mathbf{S}_L T_R^{(j-1)}(h, y), \quad (2.6a)$$

$$\partial_x T_R^{(j)}(0, y) - \mathbf{S}_R T_R^{(j)}(0, y) = \partial_x T_L^{(j)}(0, y) - \mathbf{S}_R T_L^{(j)}(0, y). \quad (2.6b)$$

Here, $T_L^{(j)}$ and $T_R^{(j)}$ are j th iterates of the temperatures in the left and right subdomain, respectively, and h measures the overlap between the two subdomains. This overlap, which often corresponds to a grid spacing, is introduced here for the purpose of speeding up the convergence of the optimized Schwarz approach. The weightings between the Dirichlet and Neumann terms in (2.6a) are given by \mathbf{S}_L and \mathbf{S}_R . Optimal weights are chosen by an analysis of the iteration in Fourier space, becoming pseudo differential operators in physical space, see [33].

The derivation of the CHAMP interface conditions leverages several key ideas from the optimized Schwarz approach for domain decomposition encapsulated in (2.6a). A nonzero overlap is key for the convergence of the optimized Schwarz approach. For a CHT problem, however, the material properties can jump at the interface and so no physical overlap is available. Nevertheless, it is possible to construct an effective overlap into the CHAMP interface conditions using suitable Taylor series expansions of the solution at a distance h from the interface as is described below. Another key idea is combining Dirichlet and Neumann conditions in the matching conditions, and this is done in CHAMP by combining generalized Dirichlet and Neumann operators obtained from the Taylor expansions and compatibility conditions. Finally, an optimal choice is needed for weights \mathbf{S}_L and \mathbf{S}_R and this done in CHAMP by solving a min-max problem. Details are given in the next sections.

2.3.2 CHAMP Conditions for a 4th-Order Accurate Scheme

A detailed derivation of the 4th-order accurate CHAMP interface conditions for the CHT model problem in (2.4) is given in this section. As discussed in Section 2.3.1, the

CHAMP condition uses a Taylor series approach to build in an effect of domain overlap following the optimized Schwarz algorithm for domain decomposition problems. Starting with the temperature T_R in the right domain at a distance h_R from the interface, a Taylor series expansion is performed about the interface $x = 0$ to get

$$T_R(h_R, y) = T_R + h_R \partial_x T_R + \frac{h_R^2}{2} \partial_x^2 T_R + \frac{h_R^3}{6} \partial_x^3 T_R + \frac{h_R^4}{24} \partial_x^4 T_R + O(h_R^5), \quad (2.7)$$

where the terms on the right-hand side are evaluated at $x = 0$. The time t is fixed and omitted from the argument of T_R for notational convenience. The expansion is truncated at $\partial_x^4 T_R$, and all of the higher-order terms in (2.7) will be dropped. The choice of this truncation is justified later in Section 2.6.3. Terms involving T_R and its derivatives on the right-hand side of (2.7) are now replaced by ones only involving T_L and its derivatives using the interface conditions and the heat equations. The first two terms can be replaced directly using the primary interface conditions (2.4b) and (2.4c). To replace the term involving second derivatives, an interface compatibility condition is derived by taking the time derivative of (2.4b) and using (2.4a) to yield

$$[D\Delta T]_I = 0. \quad (2.8)$$

Since the continuity of temperature (2.4b) applies for all y , we can take two derivatives with respect to y to give

$$[\partial_y^2 T]_I = 0. \quad (2.9)$$

The conditions in (2.8) and (2.9) give

$$\partial_x^2 T_R = (D_{LR} \partial_x^2 + (D_{LR} - 1) \partial_y^2) T_L = L_{D_{LR}} T_L, \quad (2.10)$$

where

$$L_{D_{LR}} \stackrel{\text{def}}{=} D_{LR} \partial_x^2 + (D_{LR} - 1) \partial_y^2. \quad (2.11)$$

To replace the term involving a third derivative, take the time derivative of (2.4c) and use (2.4a) to give

$$[K\partial_x D\Delta T]_I = 0. \quad (2.12)$$

Since the continuity of heat flux in (2.4c) holds for all y , it follows that

$$[K\partial_x \partial_y^2 T]_I = 0. \quad (2.13)$$

Now solve for $\partial_x^3 T_R$ yields

$$\partial_x^3 T_R = (D_{LR} K_{LR} \partial_x^3 + (D_{LR} K_{LR} - K_{LR}) \partial_x \partial_y^2) T_L = K_{LR} L_{DLR} (\partial_x T_L). \quad (2.14)$$

To replace the term in (2.7) involving $\partial_x^4 T_R$, equation (2.4b) is differentiated twice with respect to time to yield

$$[D^2 \Delta^2 T]_I = [D^2 (\partial_x^4 T + 2\partial_x^2 \partial_y^2 T + \partial_y^4 T)]_I = 0. \quad (2.15)$$

The y -derivatives of T_R can be expressed as

$$\partial_x^2 T_R = L_{DLR} T_L \quad) \quad \partial_x^2 \partial_y^2 T_R = L_{DLR} \partial_y^2 T_L, \quad (2.16)$$

and

$$[T]_I = 0 \quad) \quad [\partial_y^4 T]_I = 0, \quad (2.17)$$

which gives

$$\partial_x^4 T_R = (D_{LR}^2 \partial_x^4 + (2D_{LR}^2 - 2D_{LR}) \partial_x^2 \partial_y^2 + (D_{LR}^2 - 2D_{LR} - 1) \partial_y^4) T_L = (L_{DLR})^2 T_L. \quad (2.18)$$

Substituting (2.10), (2.14), (2.18) and the primary interface conditions into (2.7) gives the operator

$$\mathbf{D}_{LR}[T_L] \stackrel{\text{def}}{=} \left(1 + K_{LR} h_R \partial_x + \frac{h_R^2}{2} L_{DLR} + \frac{h_R^3}{6} K_{LR} L_{DLR} \partial_x + \frac{h_R^4}{24} L_{DLR}^2 \right) T_L, \quad (2.19)$$

with $D_{LR} = \frac{D_L}{D_R}$, and $K_{LR} = \frac{K_L}{K_R}$ as before. The operator $\mathbf{D}_{LR}[T_L]$ in (2.19) can be interpreted as a generalized Dirichlet condition for the left domain.

A similar approach is used to derive a Neumann operator for the left domain. For this case, the starting point is a Taylor series expansion of $\partial_x T_R(h_R, y)$ about the interface at $x = 0$ which gives

$$\partial_x T_R(h_R, y) = \partial_x T_R(0, y) + h_R \partial_x^2 T_R(0, y) + \frac{h_R^2}{2} \partial_x^3 T_R(0, y) + \frac{h_R^3}{6} \partial_x^4 T_R(0, y) + O(h_R^4). \quad (2.20)$$

where the terms on the right-hand side are evaluated at $x = 0$ as before. Terms involving T_R and its derivatives on the right-hand side of (2.20) are replaced with terms involving T_L and its derivatives following similar steps as before to give

$$\mathbf{N}_{LR}[T_L] \stackrel{\text{def}}{=} \left(K_{LR} \partial_x + h_R L_{DLR} + \frac{h_R^2}{2} K_{LR} L_{DLR} \partial_x + \frac{h_R^3}{6} L_{DLR}^2 \right) T_L. \quad (2.21)$$

The operator $\mathbf{N}_{LR}[T_L]$ defines a generalized Neumann condition for the left domain.

A differential operator, \mathbf{S}_L , is used to combine the generalized Dirichlet operator (2.19) and the Neumann operator (2.21) together. This operator \mathbf{S}_L is a scalar function in Fourier space, and it provides a weighted combination of the generalized Dirichlet and Neumann conditions. A more detailed discussion on how to determine the value of \mathbf{S}_L is given in Section 2.6.1. The new 4th-order accurate CHAMP interface conditions for the left domain is expressed as

$$(\mathbf{N}_{LR} + \mathbf{S}_L \mathbf{D}_{LR}) [T_L(0, y)] = (\partial_x + \mathbf{S}_L) T_R(h_R, y). \quad (2.22)$$

Generalized Dirichlet and Neumann conditions for the right domain can be derived in a similar manner by taking Taylor series expansions of T_L and $\partial_x T_L$ at a distance h_L to the interface, which gives

$$\mathbf{D}_{LR} T_R \stackrel{\text{def}}{=} \left(1 \quad K_{RL} h_L \partial_x + \frac{h_L^2}{2} L_{DRL} \quad \frac{h_L^3}{6} K_{RL} L_{DRL} \partial_x + \frac{h_L^4}{24} L_{DRL}^2 \right) T_R, \quad (2.23a)$$

$$\mathbf{N}_{LR} T_R \stackrel{\text{def}}{=} \left(K_{RL} \partial_x \quad h_L L_{DRL} + \frac{h_L^2}{2} K_{RL} L_{DRL} \partial_x \quad \frac{h_L^3}{6} L_{DRL}^2 \right) T_R, \quad (2.23b)$$

where

$$K_{RL} \stackrel{\text{def}}{=} \frac{K_R}{K_L}, \quad D_{RL} \stackrel{\text{def}}{=} \frac{D_R}{D_L}, \quad (2.24)$$

are reciprocals of the ratios K_{LR} and D_{LR} defined previously. Combing these two conditions together using the coupling parameter \mathbf{S}_R gives the 4th-order accurate CHAMP interface condition for the right domain as

$$(\mathbf{N}_{RL} \quad \mathbf{S}_R \mathbf{D}_{RL}) [T_R(0, y)] = (\partial_x \quad \mathbf{S}_R) T_L(h_L, y). \quad (2.25)$$

The complete 4th-order accurate CHAMP conditions are summarized in the following theorem:

Theorem 1 *The 4th-order accurate CHAMP conditions for the heat equations in (2.4a) with matching conditions in (2.4b) and (2.4c) are*

$$(\mathbf{N}_{LR} + \mathbf{S}_L \mathbf{D}_{LR}) [T_L(0, y)] = (\partial_x + \mathbf{S}_L) T_R(h_R, y), \quad (2.26a)$$

$$(\mathbf{N}_{RL} \quad \mathbf{S}_R \mathbf{D}_{RL}) [T_R(0, y)] = (\partial_x \quad \mathbf{S}_R) T_L(h_L, y), \quad (2.26b)$$

where the operators \mathbf{D}_{LR} , \mathbf{N}_{LR} , \mathbf{D}_{RL} and \mathbf{N}_{RL} are defined by (2.19), (2.21), (2.23a) and (2.23b), respectively.

2.3.3 CHAMP Condition for a p th-Order Accurate Scheme

The general approach to derive CHAMP interface conditions for a p th-order accurate scheme follows by extension of the derivations of the 2nd-order accurate conditions in [75] and the 4th-order accurate conditions above. The first step involves suitable Taylor expansions of $T_R(h_R, y)$ and $\partial_x T_R(h_R, y)$ about the interface $x = 0$. For a p th-order accurate scheme the following expansions are used

$$T_R(h_R, y) = \sum_{\ell=0}^p \frac{h_R^\ell}{\ell!} \partial_x^\ell T_R(0, y) + O(h_R^{p+1}), \quad (2.27a)$$

$$\partial_x T_R(h_R, y) = \sum_{\ell=0}^{p-1} \frac{h_R^\ell}{\ell!} \partial_x^{\ell+1} T_R(0, y) + O(h_R^p). \quad (2.27b)$$

Note that one less term is retained in the expansion for $\partial_x T_R(h_R, y)$ following the previous derivations. As before, the goal is to replace terms involving x -derivatives of T_R on the right-hand sides of (2.27) with ones involving the x and y -derivatives of T_L . To start this process the interface matching conditions in (2.4b) and (2.4c) are used to give the relations

$$T_R(0, y) = T_L(0, y) \stackrel{\text{def}}{=} L_0 T_L(0, y), \quad (2.28a)$$

$$\partial_x T_R(0, y) = K_{LR} \partial_x T_L(0, y) \stackrel{\text{def}}{=} L_1 T_L(0, y), \quad (2.28b)$$

where the differential operators $L_0 = I$ and $L_1 = K_{LR} \partial_x$ are introduced. Compatibility conditions are used to obtain expressions for higher x -derivatives of T_R at $x = 0$. Taking q time derivatives of the matching conditions in (2.4b) and (2.4c), and then using the heat equations to replace time derivatives with spatial derivatives leads to the compatibility interface conditions,

$$[D^q \Delta^q T]_I = 0, \quad q = 0, 1, 2, 3, \dots, \quad (2.29a)$$

$$[K D^q \partial_x \Delta^q T]_I = 0, \quad q = 0, 1, 2, 3, \dots \quad (2.29b)$$

Using (2.29a) with $q = 1$, for example, leads to an expression for the second x -derivative of T_R on the interface,

$$\partial_x^2 T_R(h_R, y) = D_{LR} \Delta T_L(0, y) \quad \partial_y^2 L_0 T_L(0, y) \stackrel{\text{def}}{=} L_2 T_L(0, y), \quad (2.30)$$

where the use of y -derivatives of (2.28a) was made. Using (2.29) leads to conditions for an arbitrary x -derivative of T_R on the interface,

$$\partial_x^{2q} T_R(0, y) = \left[D_{LR}^q \Delta^q \sum_{\ell=0}^{q-1} \binom{q}{\ell} \partial_y^{2(q-\ell)} L_{2\ell} \right] T_L(0, y) \stackrel{\text{def}}{=} L_{2q} T_L(0, y), \quad (2.31a)$$

$$\partial_x^{2q+1} T_R(0, y) = \left[K_{LR} D_{LR}^q \Delta^q \partial_x \sum_{\ell=0}^{q-1} \binom{q}{\ell} \partial_y^{2(q-\ell)} L_{2\ell+1} \right] T_L(0, y) \stackrel{\text{def}}{=} L_{2q+1} T_L(0, y), \quad (2.31b)$$

for $q = 0, 1, 2, \dots$. Here, the operators L_ℓ are defined recursively and give $\partial_x^\ell T_R(h_R, y) = L_\ell T_L(0, y)$, $\ell = 0, 1, 2, \dots$. Each operator L_ℓ can be written in terms of powers of ∂_x and ∂_y ,

and the notation $L_\ell[\partial_x, \partial_y]$ is used to expose this dependence. For example,

$$L_0[\partial_x, \partial_y] = I, \quad (2.32a)$$

$$L_1[\partial_x, \partial_y] = K_{LR}\partial_x, \quad (2.32b)$$

$$L_2[\partial_x, \partial_y] = D_{LR}(\partial_x^2 + \partial_y^2) \quad \partial_y^2, \quad (2.32c)$$

$$L_3[\partial_x, \partial_y] = K_{LR}D_{LR}\partial_x(\partial_x^2 + \partial_y^2) \quad K_{LR}\partial_y^2\partial_x, \quad (2.32d)$$

$$L_4[\partial_x, \partial_y] = D_{LR}^2(\partial_x^2 + \partial_y^2)^2 \quad \partial_y^4 \quad 2\partial_y^2(D_{LR}(\partial_x^2 + \partial_y^2) \quad \partial_y^2). \quad (2.32e)$$

The CHAMP Dirichlet and Neumann operators can now be defined using (2.31) in the Taylor expansions (2.27). The result is summarized in the following Theorem.

Theorem 2 *The Dirichlet and Neumann operators for the p^{th} -order accurate CHAMP conditions for the heat equations in (2.4a) with matching conditions in (2.4b) and (2.4c) are*

$$\mathbf{D}_{LR}^{(p)}[\partial_x, \partial_y] \stackrel{\text{def}}{=} \sum_{\ell=0}^p \frac{h_R^\ell}{\ell!} L_\ell[\partial_x, \partial_y], \quad (2.33a)$$

$$\mathbf{N}_{LR}^{(p)}[\partial_x, \partial_y] \stackrel{\text{def}}{=} \sum_{\ell=0}^{p-1} \frac{h_R^\ell}{\ell!} L_{\ell+1}[\partial_x, \partial_y], \quad (2.33b)$$

where the operators $L_\ell[\partial_x, \partial_y]$ are defined by (2.31). Here the notation $L_\ell[\partial_x, \partial_y]$ indicates that L_ℓ is a differential operator which depends on the powers of ∂_x and ∂_y .

Note that p^{th} -order accurate CHAMP conditions are given by the conditions in (2.26) with the operators \mathbf{D}_{LR} and \mathbf{N}_{LR} replaced by the corresponding ones in (2.33), and with similar conditions replacing the operators \mathbf{D}_{RL} and \mathbf{N}_{RL} .

2.4 Partitioned Algorithms Using the CHAMP Conditions

The partitioned algorithms using the CHAMP conditions for the model problem introduced in Section 2.2 is described in this section. The model problem is solved numerically on a uniform grid with equal grid spacing and matched grid lines on either side of the interface. The numerical domain consists of two adjacent rectangles and a vertical interface located at $x = 0$. To present the CHAMP time-stepping algorithm, the spatial coordinates are left continuous, but the solutions in each subdomain are stepped discretely in time. The overall

algorithm is given in Algorithm 1. Solution are time-stepped in an implicit manner using a backward differentiation formula (BDF), which at p^{th} -order accuracy takes the form

$$\sum_{\ell=0}^p \alpha_{\ell} T_m^{n+1-\ell} = \beta_0 H_m(T_m^{n+1}), \quad (2.34)$$

for known constants α_{ℓ} and β_0 depending on the order p . Table 2.1 provides values for α_{ℓ} and β_0 for $p = 2, 4, 6$; values for other orders of accuracy can be found in [1]. Here T_m^n denotes the approximate solution at time $t^n = n\Delta t$ and

$$H_m \stackrel{\text{def}}{=} D_m \Delta, \quad (2.35)$$

denotes the diffusion operator.

Table 2.1: Values of α_{ℓ} and β_0 for BDF schemes of order $p = 2, 4, 6$.

p	β_0	α_0	α_1	α_2	α_3	α_4	α_4	α_6
2	$\frac{2}{3}$	1	$\frac{4}{3}$					
4	$\frac{12}{25}$	1	$\frac{48}{25}$	$\frac{36}{25}$	$\frac{16}{25}$	$\frac{3}{25}$		
6	$\frac{60}{147}$	1	$\frac{360}{147}$	$\frac{450}{147}$	$\frac{400}{147}$	$\frac{225}{147}$	$\frac{72}{147}$	$\frac{10}{147}$

The semi-discrete solution T_m^0 is initialized using the initial condition. The superscript without the parenthesis indicate the time level, so that T_m^0 is the semi-discrete solution set equal to T_m^{IC} at $t = 0$. At each time-step for $t \geq [0, t_{\text{nal}}]$, a linear combination of the discrete temperature values at past time steps in the BDF scheme are defined in $F_m(\mathbf{x})$ for each subdomain. To initialize the CHAMP iteration, an initial guess for the temperature on the right domain is needed, and here a p th-order accurate extrapolation formula is used to obtain a value for the temperature from past time values. This initial value is denoted by $T_R^{(0)}$, where the superscript with the parenthesis now indicates the number of iterations. With this initial value, the CHAMP conditions are then applied iteratively for each subdomain. Using the temperature information from the other subdomain, the CHAMP condition and the boundary conditions are applied to the current domain, and an implicit solve is performed to get an updated solution. The other subdomain will use this updated solution to apply the CHAMP condition and the boundary conditions, and another implicit solve is

Algorithm 1: CHAMP partitioned conjugate heat transfer solver for heat equations.

```

1: DiffusionSolver( $\Omega, t_{\text{nal}}$ )
2:  $t = 0, n = 0$ ;
3:  $T_m^0(\mathbf{x}) = T_m^{\text{IC}}(\mathbf{x}), \quad \mathbf{x} \in \Omega_m, \quad m = L, R;$  ▷ Initial conditions
4: Evaluate past time values as needed by BDF schemes.
5: // Time stepping loop
6: while  $t < t_{\text{nal}}$  do
7:    $F_m(\mathbf{x}) = \sum_{\ell=1}^p \alpha_\ell T_m^{n-\ell}(\mathbf{x}), \quad \mathbf{x} \in \Omega_m, \quad m = L, R;$  ▷ Assign RHS for BDF scheme
8:    $T_R^{(0)} = \sum_{i=1}^{p+1} \binom{p+1}{i} (-1)^{i+1} T_R^{n+1-i};$  ▷ Extrapolate in time for initial guess
9:   for  $j = 1, \dots, N_{\text{sj}}$  do ▷ Sub-time-step iterations
10:    // Solve for  $T_L^{(j)}$  given  $T_R^{(j-1)}$ 
11:     $T_L^{(j)} - \beta_0 \Delta t D_L \Delta T_L^{(j)} = F_L, \quad \mathbf{x} \in \Omega_L;$ 
12:     $(\mathbf{N}_{LR} + \mathbf{S}_L \mathbf{D}_{LR}) T_L^{(j)}(\mathbf{x}) = (\partial_n + \mathbf{S}_L) T_R^{(j-1)}(\mathbf{x} + h_R), \quad \mathbf{x} \in I;$  ▷ CHAMP
13:     $B_L(T_L^{(j)}) = g(\mathbf{x}, t + \Delta t), \quad \mathbf{x} \in \partial\Omega_L;$  ▷ Physical BCs.
14:    // Solve for  $T_R^{(j)}$  given  $T_L^{(j)}$ 
15:     $T_R^{(j)} - \beta_0 \Delta t D_R \Delta T_R^{(j)} = F_R, \quad \mathbf{x} \in \Omega_R;$ 
16:     $(\mathbf{N}_{RL} + \mathbf{S}_R \mathbf{D}_{RL}) T_R^{(j)}(\mathbf{x}) = (\partial_n + \mathbf{S}_R) T_L^{(j)}(\mathbf{x} + h_L), \quad \mathbf{x} \in I;$  ▷ CHAMP
17:     $B_R(T_R^{(j)}) = g(\mathbf{x}, t + \Delta t), \quad \mathbf{x} \in \partial\Omega_R;$  ▷ Physical BCs.
18:     $\text{error}^{(j)} = \max_I \{|T_L^{(j)} - T_R^{(j)}|\};$  ▷ Error in iteration
19:    If  $|\text{error}^{(j)} - \text{error}^{(j-1)}| < \text{tol}$  then break; ▷ Converged
20:  end for
21:   $T_m^{n+1} = T_m^{(j)}, \quad m = L, R;$  ▷ Solution at new time
22:   $t = t + \Delta t, n = n + 1;$ 
23: end while

```

performed. The collection of these steps, starting with the *for* loop, completes an iteration of the CHAMP scheme for a particular time step.

To satisfy the matching conditions in (2.4b) and (2.4c), the CHAMP conditions are iterated at each time-step inside the *for* loop. The loop stops when the temperatures match at the interface. The residual of the CHAMP interface conditions at the j^{th} iteration is defined to be

$$\text{Res}^{(j)} = \max_{\mathbf{x} \in I} \left\{ |T_L^{(j)} - T_R^{(j)}| \right\}, \quad (2.36)$$

where the maximum norm over the interface is taken. The convergence rate of the CHAMP iteration is measured by an amplification factor A_1^c given by

$$A_1^c = \frac{\text{Res}^{(j)}}{\text{Res}^{(j-1)}}, \quad (2.37)$$

where $j = 1, \dots, N_{si}$ denotes the iteration number. For the iteration to converge, the maximum iteration number N_{si} is required to satisfy the condition

$$j\text{Res}^{(N_{si})} - \text{Res}^{(N_{si}-1)}j < \text{tol}. \quad (2.38)$$

where tol is taken to be 10^{-13} .

2.5 Application of the CHAMP Conditions on a Spatial Grid

This section discusses the application of the CHAMP conditions on a spatial grid. Ghost points are used to facilitate the discretization of a high-order accurate scheme near the boundaries and the interface. A spatially 4th-order accurate scheme is considered as a representative example, and various approaches are presented to specify the ghost points. In particular, two different methods are introduced to specify values at ghost points near the interface for the CHAMP scheme. Numerical experiments show that both methods give accurate and stable results, and the major difference between the two schemes comes from the implementation, which will be discussed next.

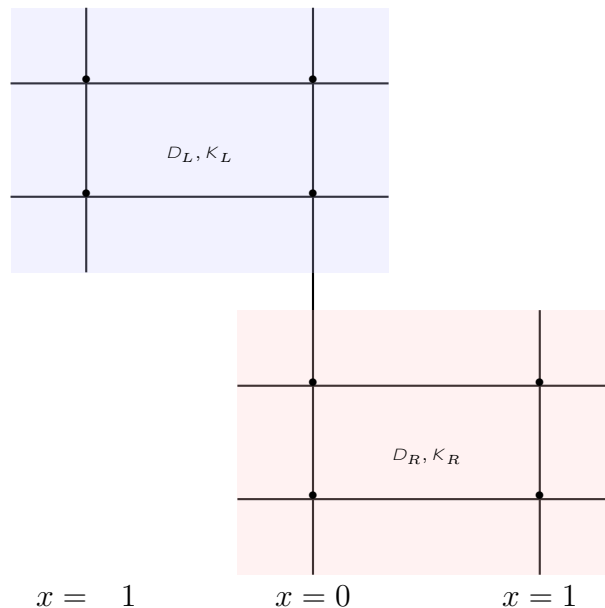


Figure 2.3: A sample computational grid for a 4th-order accurate scheme with two ghost points at each domain.

For a 4th-order accurate scheme, two ghost cells are required at each boundary and

interface for both the left and right domains. A computational grid for this case is depicted in Fig 2.3. The first ghost point can be solved using a high-order extrapolation formula in space. For the second ghost point at far left and far right boundaries in the x direction, a compatibility boundary condition is derived using the governing equations and the original boundary conditions. Taking a time derivative of the original boundary conditions and then substituting in the governing equations gives a new equation to solve for the first ghost value. These conditions are

$$\partial_t T_{mj\partial} = D_m (\partial_x^2 + \partial_y^2) T_{mj\partial} = 0. \quad (2.39)$$

Equation (2.39) is discretized using a second order centered difference formula.

For ghost points in the y direction, periodic boundary conditions are applied. For the first ghost points at the interface, the CHAMP interface conditions are discretized using a 4th-order accurate centered difference method. There are several choices to fill in the equation for the second ghost cells at the interface, and here two possible approaches are presented.

The first method derives the compatibility boundary conditions based from the second-order accurate CHAMP interface conditions, which gives two more equations to be applied at the second ghost points. Differentiating the second-order accurate CHAMP interface conditions with respect to t gives

$$\text{LHS} = \left(\mathbf{N}_{LR}^{(2)} + \mathbf{S}_L \mathbf{D}_{LR}^{(2)} \right) [\partial_t T_L^{(j)}(\mathbf{x})] = \left(\mathbf{N}_{LR}^{(2)} + \mathbf{S}_L \mathbf{D}_{LR}^{(2)} \right) \left(D_L \Delta T_L^{(j)}(\mathbf{x}) \right), \quad \mathbf{x} \geq l, \quad (2.40a)$$

$$\text{RHS} = (\partial_x + \mathbf{S}_L) \partial_t T_R^{(j-1)}(\mathbf{x} + h_R) = (\partial_x + \mathbf{S}_L) \left(D_R \Delta T_R^{(j-1)}(\mathbf{x} + h_R) \right), \quad \mathbf{x} \geq l, \quad (2.40b)$$

where $\mathbf{N}_{LR}^{(2)}, \mathbf{D}_{LR}^{(2)}$ are the second-order accurate CHAMP operators, given by

$$\mathbf{D}_{LR}^{(2)} = T_L(\mathbf{x}) + K_{LR} h_R \partial_x T_L(\mathbf{x}) + \frac{h_R^2}{2} L_2 T_L(\mathbf{x}), \quad \mathbf{x} \geq l, \quad (2.41a)$$

$$\mathbf{N}_{LR}^{(2)} = K_{LR} \partial_x T_L(\mathbf{x}) + h_R L_2 T_L(\mathbf{x}), \quad \mathbf{x} \geq l, \quad (2.41b)$$

and L_2 is defined in (2.32). Detailed derivations can be found in Section 2.3.3. Equation (2.40a) and (2.40b) provides two equations to be applied at the second ghost point at the interface for the left domain. Similar expression can be obtained for the right domain, and details are omitted here.

The second method evaluates the RHS of the CHAMP condition at a distance $2h_m$, $m = L, R$ to the left and right of the interface to obtain two different equations for the second ghost cells. This is given by

$$\left(\mathbf{N}_{LR}^{(4)} + \mathbf{S}_L \mathbf{D}_{LR}^{(4)}\right) [T_L^{(j)}(\mathbf{x})] = (\partial_x + \mathbf{S}_L) T_R^{(j-1)}(\mathbf{x} + 2h_R), \quad \mathbf{x} \geq l, \quad (2.42a)$$

$$\left(\mathbf{N}_{RL}^{(4)} - \mathbf{S}_R \mathbf{D}_{RL}^{(4)}\right) [T_R^{(j)}(\mathbf{x})] = (\partial_x - \mathbf{S}_R) T_L^{(j-1)}(\mathbf{x} - 2h_L), \quad \mathbf{x} \geq l, \quad (2.42b)$$

where $\mathbf{N}_{LR}^{(4)}, \mathbf{D}_{LR}^{(4)}, \mathbf{N}_{RL}^{(4)}, \mathbf{D}_{RL}^{(4)}$ are the 4th-order CHAMP operator defined in Section 2.3.3. Notice that the LHS of these equations remain the same as the original CHAMP conditions, only the RHS are evaluated at different grid points. Unlike the first method where a new set of operators needs to be derived, this method uses the same CHAMP operators as the original CHAMP conditions, which saves some time in terms of the derivation.

2.6 Analysis of the CHAMP Schemes

In this section, the p^{th} -order accurate CHAMP scheme as described in Algorithm 1 for the CHT model problem in (2.4) is studied and analyzed. The convergence of the CHAMP iteration for a given time-step is studied first in Section 2.6.1, followed by an analysis of the complete time-stepping scheme in Section 2.6.2. Finally in Section 2.6.3 the accuracy of a fourth-order accurate CHAMP scheme is verified using a modified equation approach.

2.6.1 Model Problem Analysis of the CHAMP Iteration

In this section, the CHAMP scheme is analyzed by considering the iteration described in Algorithm 1 in isolation. At each time-step, the CHAMP condition is applied iteratively at the interface. For the model problem described in Section 2.2 consisting of two rectangles that meet at a vertical interface at $x = 0$, the convergence factor of the CHAMP sub-time-step iteration is now derived and studied.

Start by expanding the solution in a Fourier series in y ,

$$T_m(\mathbf{x}, t) = \sum_{k=-\infty}^{\infty} \hat{T}_m(x, k, t) e^{iky}, \quad (2.43)$$

so that the CHT model problem in (2.4) becomes

$$\partial_t \hat{T}_L = D_m(\partial_x^2 - k^2) \hat{T}_L, \quad x \in (-1, 0), \quad (2.44a)$$

$$\partial_t \hat{T}_R = D_m(\partial_x^2 - k^2) \hat{T}_R, \quad x \in (0, +1), \quad (2.44b)$$

$$[\hat{T}]_{x=0} = 0, \quad (2.44c)$$

$$[K \partial_x \hat{T}]_{x=0} = 0, \quad (2.44d)$$

$$k \hat{T}_m(\cdot, k, t) k_2 < 1, \quad (2.44e)$$

$$\hat{T}_m(x, 0) = \hat{T}_m^{\text{IC}}(x). \quad (2.44f)$$

Discretize in time using the BDF scheme in (2.34) and use the CHAMP interface conditions to give

$$\left[I - \Delta t \beta_0 (D_L(\partial_x^2 - k^2)) \right] \hat{T}_L^{n+1} = \sum_{j=1}^p \alpha_j \hat{T}_L^{n-j} \stackrel{\text{def}}{=} F_L^n, \quad x \in (-1, 0), \quad (2.45a)$$

$$\left[I - \Delta t \beta_0 (D_R(\partial_x^2 - k^2)) \right] \hat{T}_R^{n+1} = \sum_{j=1}^p \alpha_j \hat{T}_R^{n-j} \stackrel{\text{def}}{=} F_R^n, \quad x \in (0, +1), \quad (2.45b)$$

$$\left(\mathbf{N}_{LR}[\partial_x] + \mathbf{S}_L \mathbf{D}_{LR}[\partial_x] \right) \hat{T}_L^{n+1}(0) = \left(+\partial_x + \mathbf{S}_L \right) \hat{T}_R^{n+1}(+h), \quad (2.45c)$$

$$\left(\mathbf{N}_{RL}[\partial_x] + \mathbf{S}_R \mathbf{D}_{RL}[\partial_x] \right) \hat{T}_R^{n+1}(0) = \left(\partial_x + \mathbf{S}_R \right) \hat{T}_L^{n+1}(-h), \quad (2.45d)$$

$$k \hat{T}_m^{n+1} k_2 < 1, \quad (2.45e)$$

$$\hat{T}_m^0(x) = \hat{T}_m^{\text{IC}}(x), \quad (2.45f)$$

where $\mathbf{N}_{LR}[\partial_x]$, $\mathbf{D}_{LR}[\partial_x]$, $\mathbf{N}_{RL}[\partial_x]$ and $\mathbf{D}_{RL}[\partial_x]$ are the linearized and Fourier transformed CHAMP Dirichlet and Neumann operators. It is assumed that $h_L = h_R = h$.

Let $\hat{T}_m^{(j)}$ \hat{T}_m^{n+1} denote the j^{th} iterate in a fixed-point iteration of (2.45) to compute

\hat{T}_L^{n+1} and \hat{T}_R^{n+1} . This fixed-point iteration is given by

$$\left[I \quad \Delta t \beta_0 (D_L(\partial_x^2 - k^2)) \right] \hat{T}_L^{(j)} = F_L^n, \quad x \in (-1, 0), \quad (2.46a)$$

$$\left(\mathbf{N}_{LR}[\partial_x] + \mathbf{S}_L \mathbf{D}_{LR}[\partial_x] \right) \hat{T}_L^{(j)}(0) = \left(\partial_x + \mathbf{S}_L \right) \hat{T}_R^{(j-1)}(+h), \quad (2.46b)$$

$$k \hat{T}_L^{(j)} k_2 < 1, \quad (2.46c)$$

$$\left[I \quad \Delta t \beta_0 (D_R(\partial_x^2 - k^2)) \right] \hat{T}_R^{(j)} = F_R^n, \quad x \in (0, +1), \quad (2.46d)$$

$$\left(\mathbf{N}_{RL}[\partial_x] + \mathbf{S}_R \mathbf{D}_{RL}[\partial_x] \right) \hat{T}_R^{(j)}(0) = \left(\partial_x + \mathbf{S}_R \right) \hat{T}_L^{(j)}(-h), \quad (2.46e)$$

$$k \hat{T}_R^{(j)} k_2 < 1, \quad (2.46f)$$

with an initial value for $\hat{T}_R^{(0)}$ obtained by extrapolation in time. The errors $\hat{E}_m^{(j)} = \hat{T}_m^{(j)} - \hat{T}_m^{n+1}$, $m = L, R$ satisfy the homogeneous equations in (2.46) with $F_m^n = 0$. Therefore, from now on in this section, $F_m^n = 0$ is taken in (2.46) and $\hat{T}_m^{(j)}$ is interpreted as the error in the j th iterate.

For the problem described in (2.46), a p^{th} -order accurate spatial approximations is used to discretize the CHAMP Dirichlet and Neumann operators, with the order of accuracy in time left open. The general solution of (2.46) (with zero forcing) subject to the far-field boundary conditions is given as

$$\hat{T}_L^{(j)}(x, k) = c^L A^j e^{\xi_L x}, \quad (2.47a)$$

$$\hat{T}_R^{(j)}(x, k) = c^R A^j e^{-\xi_R x}, \quad (2.47b)$$

with

$$\xi_m \stackrel{\text{def}}{=} \sqrt{\frac{1}{\beta_0 D_m \Delta t} + k^2}, \quad (2.48)$$

where c^L and c^R are constants and A is the amplification factor for the CHAMP sub-time iteration. Substituting (2.47a) and (2.47b) into the CHAMP interface conditions (2.46b) and (2.46e) gives

$$\left(\mathbf{N}_{LR}[\xi_L] + \mathbf{S}_L \mathbf{D}_{LR}[\xi_L] \right) c^L A^j = \left(-\xi_R + \mathbf{S}_L \right) c^R A^{j-1} e^{-\xi_R h}, \quad (2.49)$$

$$\left(\mathbf{N}_{RL}[\xi_R] + \mathbf{S}_R \mathbf{D}_{RL}[\xi_R] \right) c^R A^j = \left(\xi_L + \mathbf{S}_R \right) c^L A^j e^{\xi_L h}. \quad (2.50)$$

This is a system of two homogeneous equations for the two unknowns c^L and c^R . For nontrivial solutions the determinant of the corresponding 2×2 coefficient matrix must be zero. This leads to the following result.

Theorem 3 (CHAMP iteration, diffusion equation) *The iteration amplification factor when using p^{th} -order accurate spatial approximations to the CHAMP interface conditions for the diffusion equation is*

$$A_{CI} = \frac{(\xi_R + \mathbf{S}_L) e^{-\xi_R h}}{(\mathbf{N}_{RL}^{(p)}[\xi_R] + \mathbf{S}_R \mathbf{D}_{RL}^{(p)}[\xi_R])} \frac{(\xi_L + \mathbf{S}_R) e^{-\xi_L h}}{(\mathbf{N}_{LR}^{(p)}[\xi_L] + \mathbf{S}_L \mathbf{D}_{LR}^{(p)}[\xi_L])}. \quad (2.51)$$

For example, here are the forms of the symbols of the Dirichlet and Neumann operators for orders of accuracy two, four and six,

$$\mathbf{D}_{LR}^{(2)}[\xi_L] = 1 + K_{LR} z_L + \frac{z_R^2}{2}, \quad (2.52a)$$

$$h \mathbf{N}_{LR}^{(2)}[\xi_L] = K_{LR} z_L + z_R^2, \quad (2.52b)$$

$$\mathbf{D}_{LR}^{(4)}[\xi_L] = 1 + K_{LR} z_L + \frac{1}{2} z_R^2 + \frac{1}{6} K_{LR} z_L z_R^2 + \frac{1}{24} z_R^4, \quad (2.52c)$$

$$h \mathbf{N}_{LR}^{(4)}[\xi_L] = K_{LR} z_L + z_R^2 + \frac{1}{2} K_{LR} z_L z_R^2 + \frac{1}{6} z_R^4, \quad (2.52d)$$

$$\mathbf{D}_{LR}^{(6)}[\xi_L] = 1 + K_{LR} z_L + \frac{1}{2} z_R^2 + \frac{1}{6} K_{LR} z_L z_R^2 + \frac{1}{24} z_R^4 + \frac{1}{120} K_{LR} z_L z_R^4 + \frac{1}{720} z_R^6, \quad (2.52e)$$

$$h \mathbf{N}_{LR}^{(6)}[\xi_L] = K_{LR} z_L + z_R^2 + \frac{1}{2} K_{LR} z_L z_R^2 + \frac{1}{6} z_R^4 + \frac{1}{24} K_{LR} z_L z_R^4 + \frac{1}{120} z_R^6, \quad (2.52f)$$

where

$$z_m \stackrel{\text{def}}{=} \xi_m h, \quad m = L, R. \quad (2.53)$$

Note that all of the terms in $\mathbf{D}_{LR}^{(p)}[\xi_L]$ and $\mathbf{N}_{LR}^{(p)}[\xi_L]$ are positive which will be important for the convergence of the iteration. In (2.51), if $\mathbf{S}_L = \xi_R$ or $\mathbf{S}_R = \xi_L$, then $A_{CI} = 0$ and the iteration converges in one step, regardless of the material properties, grid size and the time step. This is the optimal result, but $\mathbf{S}_L, \mathbf{S}_R$ are operators in the Fourier space, and to implement the CHAMP scheme one would need to transform them back to real space. Since ξ_L and ξ_R contains square root functions, it will result in a global operator. In practice, local operators

are always preferred, and for simplicity here $\mathbf{S}_L, \mathbf{S}_R$ are chosen to be scaled constants, i.e.

$$\mathbf{S}_L = \frac{p_L}{h}, \quad \mathbf{S}_R = \frac{p_R}{h} \quad (2.54)$$

for constants p_L and p_R (independent of the mesh spacing h). The amplification factor A_{CI} can be written in a non-dimensional form by introducing

$$p_L \stackrel{\text{def}}{=} h\mathbf{S}_L, \quad p_R \stackrel{\text{def}}{=} h\mathbf{S}_R, \quad \kappa \stackrel{\text{def}}{=} kh, \quad \lambda_{DL} \stackrel{\text{def}}{=} \frac{\Delta t D_L}{h^2}, \quad \lambda_{DR} \stackrel{\text{def}}{=} \frac{\Delta t D_R}{h^2}, \quad (2.55)$$

(note that $\lambda_{DR} = \lambda_{DL}/\mathbf{D}_{LR}$) which implies

$$z_L = \sqrt{\frac{1}{\beta_0} \frac{1}{\lambda_{DL}} + \kappa^2}, \quad z_R = \sqrt{\frac{1}{\beta_0} \frac{1}{\lambda_{DR}} + \kappa^2}, \quad (2.56)$$

and then $A_{CI} = A_{CI}(K_{LR}, \mathbf{D}_{LR}, \lambda_{DL}, \kappa, p_L, p_R)$ is given by

$$A_{CI}(K_{LR}, \mathbf{D}_{LR}, \dots) = \frac{(z_R + p_L) e^{-z_R}}{(h \mathbf{N}_{RL}^{(p)}[z_R] + p_R \mathbf{D}_{RL}^{(p)}[z_R])} \frac{(z_L + p_R) e^{-z_L}}{(h \mathbf{N}_{LR}^{(p)}[z_L] + p_L \mathbf{D}_{LR}^{(p)}[z_L])}. \quad (2.57)$$

In a similar manner to [75], it can be shown that parameters p_L and p_R always exist such that $jA_{CI}j < 1$ and the iteration converges. In particular it is straightforward to show that $jA_{CI}j < 1$ when $p_L = p_R = 0$, i.e. when the Neumann condition in CHAMP is used alone. Similarly, $jA_{CI}j < 1$ when the Dirichlet operator is used alone. Therefore the iteration converges when using either the pure Dirichlet or pure Neumann CHAMP interface conditions.

To find p_L and p_R that minimize the magnitude of the amplification factor A_{CI} for all wavenumbers κ , the following min-max problem must be solved,

$$A_{CI} = \min_{p_L, p_R} \left[\max_{\kappa \in [\kappa_{min}, \kappa_{max}]} jA_{CI}j \right], \quad (2.58)$$

where κ_{min} and κ_{max} are bounds on the frequency range, $[\kappa_{min}, \kappa_{max}] = [\pi, \pi]$. The optimal values for p_L and p_R can be found by precomputing terms in the expression for A_{CI} that depend on κ but do not depend on p_L and p_R . A minimization algorithm such as `fminsearch` from Matlab [74] can then be used to find p_L and p_R .

Figure 2.4 compares the convergence rates for the CHAMP iteration to those for optimized Schwartz (OS) for a domain decomposition problem where the material parameters

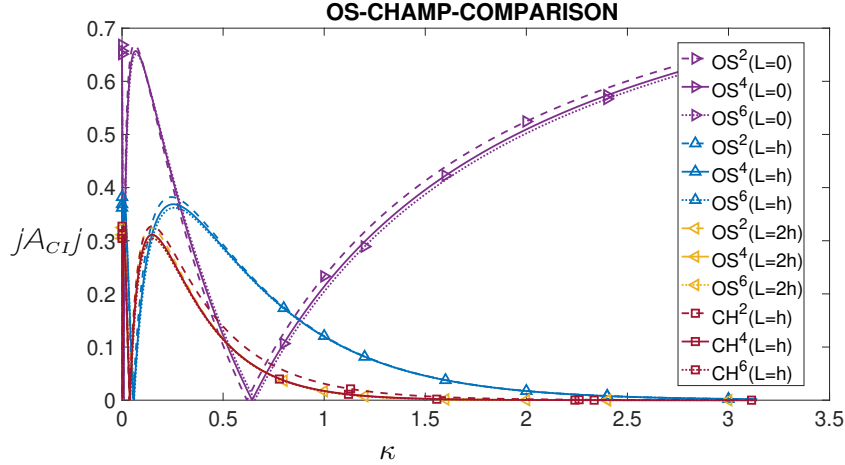


Figure 2.4: Comparison of the CHAMP iteration convergence rate to Optimized Schwarz for the problem with equal material parameters and different overlap width.

are the same in the two subdomains, i.e. $K_{LR} = 1$, $D_{LR} = 1$. Here $\lambda_{DL} = 10^6$ is chosen (which corresponds to a very large explicit time step). Results are shown for orders of accuracy $p = 2, 4, 6$. Optimized Schwarz results are given for domain overlaps of $L = 0$, $L = h$ and $L = 2h$. For each case, optimized values of the coupling parameters are chosen. As expected, the OS results improve with increasing overlap. The CHAMP results, which are similar for all orders of accuracy, are very close to the OS results with $L = 2h$. These results show that the CHAMP algorithm incorporates an effective overlap, and this applies even for CHT problems where the material properties are not equal across the interface between adjacent subdomains.

Figure 2.5 shows A_{CI} versus κ using the optimal p_L and p_R for various values λ_{DL} . As seen in the graph, the curves $A_{CI}(\kappa)$ have three extrema, two maxima and one minimum, for all orders of accuracy shown. The curves compress near $\kappa = 0$ as λ_{DL} increases due to the exponential terms in (2.51). Note that when using the optimal values p_L and p_R , the magnitudes of the three extrema of A_{CI} are equal. Also note that the shapes of the curves are very similar for all orders of accuracy.

Table 2.2 gives some values for A_{CI} and the corresponding values for p_L and p_R obtained using the optimization procedure described above. Figure 2.6 shows graphs of A_{CI} versus K_{LR} and D_{LR} for different cases of $\lambda_{DL} = 10^6$. Also shown are the optimal values of p_L and p_R obtained for each case. The plot on the top left shows the iteration amplification factor

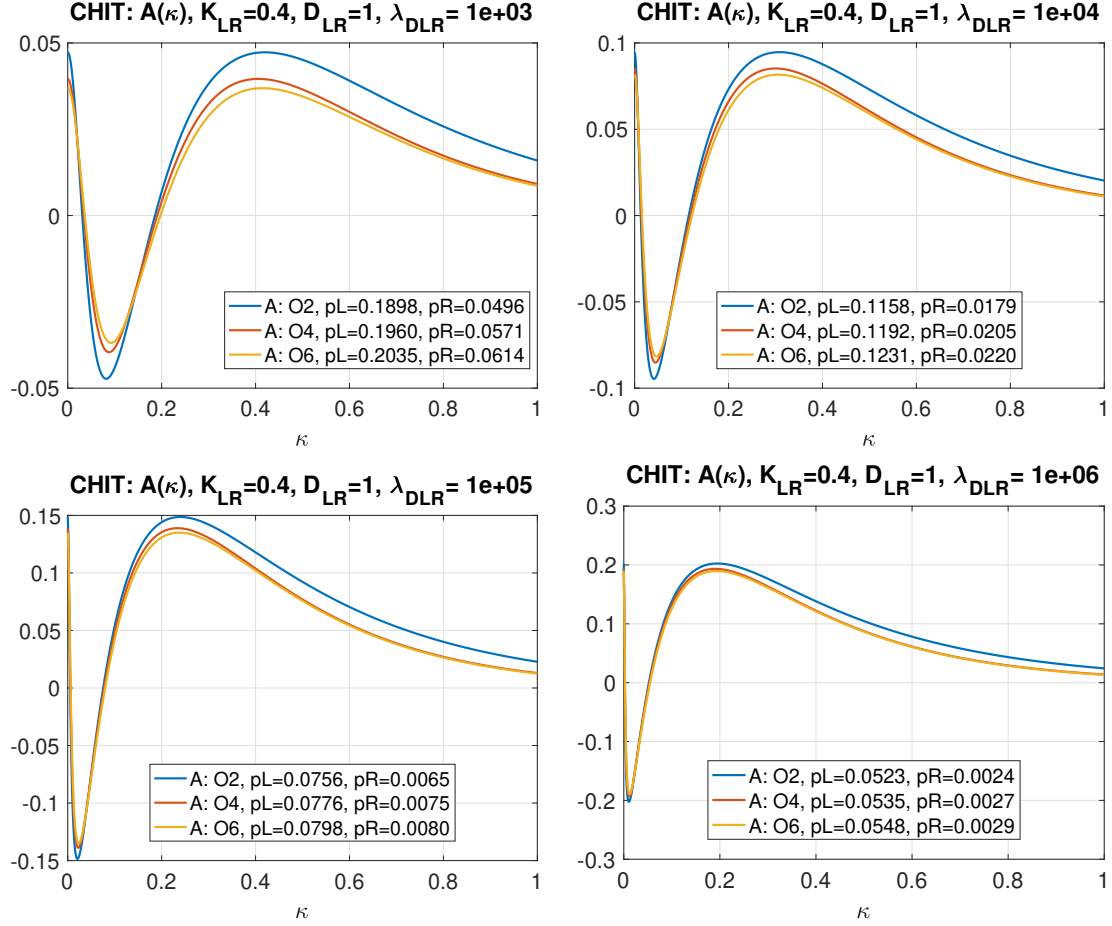


Figure 2.5: CHAMP iteration: A versus $\kappa = kh$ for selected optimal p_L and p_R for orders 2, 4, and 6 ($h = 10^{-3}$).

A_{CI} as a function of K_{LR} ranging from 10^{-2} to 10^2 , with the order of accuracy increasing from 2 to 6. The curve for the amplification factor is symmetric about the line $K_{LR} = 1$, and is also maximal there. The plots on the bottom left show the behavior of A_{CI} as D_{LR} varies from 10^{-2} to 10^2 , also with increasing orders of accuracy. As D_{LR} increases, A_{CI} decreases slowly at first, and after passing $D_{LR} = 1$ it starts to decrease rapidly.

Table 2.2: CHAMP iteration: A_{CI} and corresponding optimal p_L and p_R for a 4th-order accurate CHAMP conditions with various choices of material parameters $K_{LR} = \frac{K_L}{K_R}$, $D_{LR} = \frac{D_L}{D_R}$, $\lambda_{DL} = \frac{tD_L}{h^2}$.

CHAMP Iteration					
λ_{DL}	D_{LR}	K_{LR}	p_L	p_R	A_{CI}
1.00e+06	1.00e+00	1.00e-02	8.18e-02	2.42e-03	6.49e-03
1.00e+06	1.00e+00	4.64e-02	7.79e-02	2.45e-03	2.93e-02
1.00e+06	1.00e+00	2.15e-01	6.38e-02	2.60e-03	1.20e-01
1.00e+06	1.00e+00	1.00e+00	3.87e-02	2.91e-03	3.11e-01
1.00e+06	1.00e+00	4.64e+00	2.60e-03	6.38e-02	1.20e-01
1.00e+06	1.00e+00	2.15e+01	2.44e-03	7.79e-02	2.94e-02
1.00e+06	1.00e+00	1.00e+02	2.42e-03	8.19e-02	6.49e-03
λ_{DL}	D_{LR}	K_{LR}	p_L	p_R	A_{CI}
2.00e+07	1.00e+00	1.00e+00	2.73e-02	7.42e-04	3.84e-01
1.00e+07	1.00e+00	1.00e+00	2.84e-02	1.04e-03	3.75e-01
5.00e+06	1.00e+00	1.00e+00	3.03e-02	1.43e-03	3.62e-01
2.50e+06	1.00e+00	1.00e+00	3.29e-02	1.96e-03	3.44e-01
1.25e+06	1.00e+00	1.00e+00	3.70e-02	2.65e-03	3.20e-01
6.25e+05	1.00e+00	1.00e+00	4.34e-02	3.52e-03	2.89e-01
3.12e+05	1.00e+00	1.00e+00	5.20e-02	4.64e-03	2.55e-01
λ_{DL}	D_{LR}	K_{LR}	p_L	p_R	A_{CI}
1.00e+06	1.00e-02	1.00e+00	3.45e-02	2.30e-03	3.34e-01
1.00e+06	4.64e-02	1.00e+00	3.50e-02	2.39e-03	3.31e-01
1.00e+06	2.15e-01	1.00e+00	3.61e-02	2.56e-03	3.25e-01
1.00e+06	1.00e+00	1.00e+00	3.87e-02	2.91e-03	3.11e-01
1.00e+06	4.64e+00	1.00e+00	4.87e-03	5.24e-02	2.53e-01
1.00e+06	2.15e+01	1.00e+00	9.15e-03	6.79e-02	2.02e-01
1.00e+06	1.00e+02	1.00e+00	1.78e-02	9.46e-02	1.44e-01

2.6.2 Analysis of the Un-Iterated CHAMP Time-Stepping Scheme

The time-stepping scheme incorporating the CHAMP interface conditions was given in Algorithm 1. In general, N_{si} iterations of the CHAMP conditions are used at each time step. Since each iteration requires the solution of a linear system associated with the BDF implicit time-stepping scheme for each subdomain, it is desirable to use as few iterations as possible.

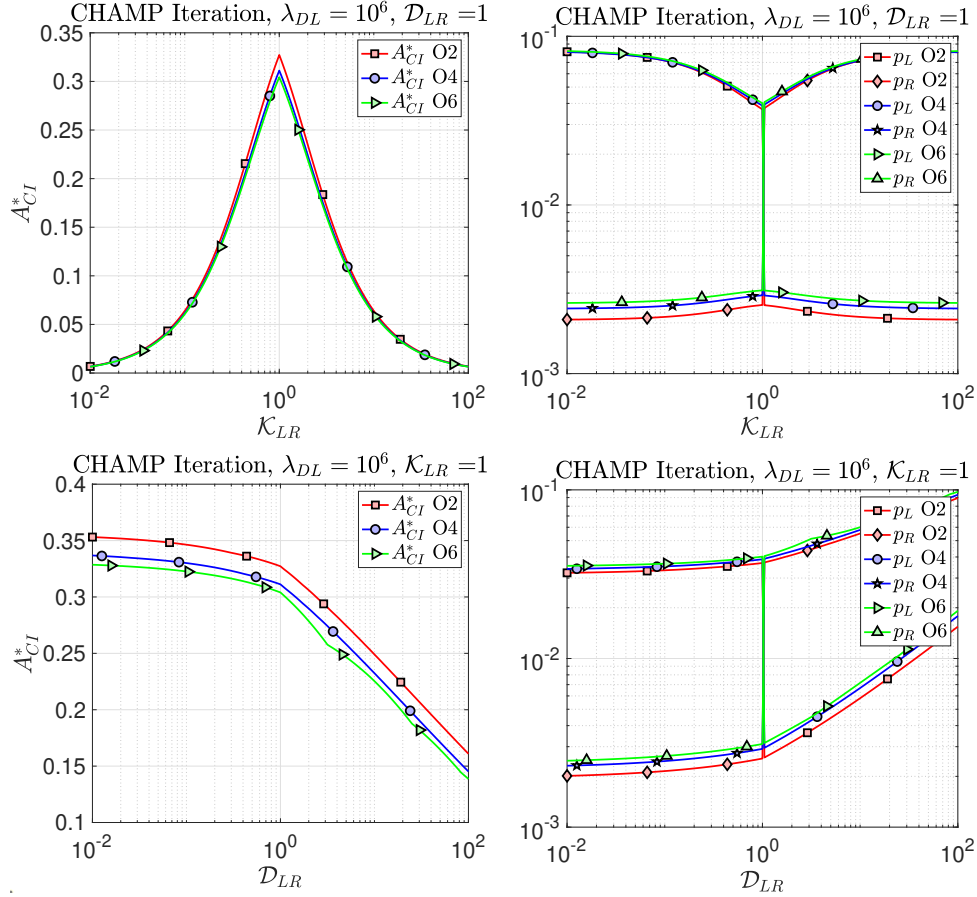


Figure 2.6: CHAMP iteration: A_{CI} and corresponding optimal p_L and p_R for orders 2, 4, and 6 ($h = 10^{-3}$) with various choices of material parameters $\mathcal{K}_{LR} = \frac{\mathcal{K}_L}{\mathcal{K}_R}$, $\mathcal{D}_{LR} = \frac{\mathcal{D}_L}{\mathcal{D}_R}$, $\lambda_{DL} = \frac{t\mathcal{D}_L}{h^2}$.

In fact, it is possible to use just one iteration, i.e. $N_{si} = 1$, for many CHT simulations, and this scheme is called the un-iterated CHAMP time-stepping scheme. This section is devoted to an analysis of this scheme.

A sample un-iterated time-stepping algorithm is given in Algorithm 2. After Fourier

Algorithm 2: Un-iterated CHAMP time-stepping algorithm.

- 1: $t = 0, n = 0;$
 - 2: $T_m^0(\mathbf{x}) = T_m^{\text{IC}}(\mathbf{x}), \quad \mathbf{x} \in \Omega_m, \quad m = L, R;$ ▷ Initial conditions
 - 3: Evaluate past time values as needed by BDF schemes.
 - 4: // *Time stepping loop*
 - 5: **for** $t = 1, \dots, t_{\text{final}}$ **do**
 - 6: $F_m(\mathbf{x}) = \sum_{j=1}^p \alpha_j T_m^{n+1-j}(\mathbf{x}), \quad \mathbf{x} \in \Omega_m, \quad m = L, R;$ ▷ Assign RHS for BDF scheme
 - 7: $T_R^{(0)} = \sum_{i=1}^{p+1} \binom{p+1}{i} (-1)^{i+1} T_R^{n+1-i};$ ▷ Extrapolate in time for initial guess
 - 8: // *Solve for T_L^{n+1} given $T_R^{(0)}$:*
 - 9: $T_L^{n+1} - \beta_0 \Delta t D_L \Delta T_L^{n+2} = F_L, \quad \mathbf{x} \in \Omega_L;$
 - 10: $(\mathbf{N}_{LR} + \mathbf{S}_L \mathbf{D}_{LR}) T_L^{n+1}(\mathbf{x}) = (\partial_n + \mathbf{S}_L) T_R^{(0)}(\mathbf{x} + h_R \mathbf{n}_{LR}), \quad \mathbf{x} \in \Gamma; \quad \triangleright \text{CHAMP}$
 - 11: $B_L(T_L^{n+1}) = g(\mathbf{x}, t + \Delta t), \quad \mathbf{x} \in \partial\Omega_L; \quad \triangleright \text{Physical BCs.}$
 - 12: // *Solve for T_R^{n+1} given T_L^{n+1} :*
 - 13: $T_R^{n+1} - \beta_0 \Delta t D_R \Delta T_R^{n+1} = F_R, \quad \mathbf{x} \in \Omega_R;$
 - 14: $(\mathbf{N}_{RL} + \mathbf{S}_R \mathbf{D}_{RL}) T_R^{n+1}(\mathbf{x}) = (\partial_n + \mathbf{S}_R) T_L^{n+1}(\mathbf{x} + h_L \mathbf{n}_{RL}), \quad \mathbf{x} \in \Gamma; \quad \triangleright \text{CHAMP}$
 - 15: $B_R(T_R^{n+1}) = g(\mathbf{x}, t + \Delta t), \quad \mathbf{x} \in \partial\Omega_R; \quad \triangleright \text{Physical BCs.}$
 - 16: $t = t + \Delta t, n = n + 1;$
 - 17: **end for**
-

transforming the equations, the time-step update to determine \hat{T}_L^{n+1} and \hat{T}_R^{n+1} is given by

$$\hat{T}_R^{(0)} = \text{extrapolate}(\hat{T}_R^n, \hat{T}_R^{n-1}, \dots) \quad (2.59a)$$

$$\left[I - \Delta t \beta_0 (D_L (\partial_x^2 - k^2)) \right] \hat{T}_L^{n+1} = F_L^n, \quad x \in (-1, 0), \quad (2.59b)$$

$$\left(\hat{\mathbf{N}}_{LR} + \mathbf{S}_L \hat{\mathbf{D}}_{LR} \right) \hat{T}_L^{n+1}(0) = \left(\partial_x + \mathbf{S}_L \right) \hat{T}_R^{(0)}(+h), \quad (2.59c)$$

$$k \hat{T}_L^{n+1} k_2 < 1, \quad (2.59d)$$

$$\left[I - \Delta t \beta_0 (D_R (\partial_x^2 - k^2)) \right] \hat{T}_R^{n+1} = F_R^n, \quad x \in (0, 1), \quad (2.59e)$$

$$\left(\hat{\mathbf{N}}_{RL} + \mathbf{S}_R \hat{\mathbf{D}}_{RL} \right) \hat{T}_R^{n+1}(0) = \left(\partial_x + \mathbf{S}_R \right) \hat{T}_L^{n+1}(-h), \quad (2.59f)$$

$$k \hat{T}_R^{n+1} k_2 < 1, \quad (2.59g)$$

with an initial guess for $\hat{T}_R(0)$ obtained by extrapolation to $(p+1)$ -order in time,

$$\hat{T}_R^{(0)} = \text{extrapolate}(\hat{T}_R^n, \hat{T}_R^{n-1}, \dots) = \sum_{\ell=1}^{p+1} \binom{p+1}{\ell} (-1)^{\ell+1} \hat{T}_R^{n+1-\ell}. \quad (2.60)$$

A BDF scheme is used to discretize the equations in time, with the formula given in (2.34).

The parameters for the fourth-order accurate BDF scheme can be found in Table 2.1.

With the Assumption that the IVP for each heat equation on an infinite or on a periodic domain is stable, a GKS normal mode analysis is carried out to study the stability of the time step given in (2.59). One looks for normal mode solutions in each domain of the form

$$\hat{T}_L^n = A^n e^{\xi_L x}, \quad \hat{T}_R^n = A^n e^{-\xi_R x}, \quad (2.61)$$

where A is the amplification factor of the time-stepping scheme. (Note that A must be the same for both subdomains in order to satisfy the interface conditions.) Substitution of the normal mode ansatz into (2.59b) or (2.59e) gives the characteristic equations the characteristic equations

$$\sum_{\mu=0}^p \alpha_\mu A^{p-\mu} = \beta_0 \Delta t D_m (\xi_m^2 + k^2) A^p, \quad m = L, R, \quad (2.62)$$

which results in two possible roots for both ξ_L , and ξ_R given by

$$\xi_m = \sqrt{\frac{1}{\beta_0 \Delta t D_L} \frac{\sum_{\mu=1}^p \alpha_\mu A^{p-\mu}}{A^p} + k^2}, \quad m = L, R. \quad (2.63)$$

The scheme is stable provided that there are no nontrivial solutions to the homogeneous equations in (2.59) with $|jAj| > 1$. As is usual with GKS analysis, provided the Cauchy problem for the heat equation is stable, then unstable modes that grow in time with $|jAj| > 1$ will decay in space with the corresponding ξ having $\text{Re}(\xi) \neq 0$. This result is encompassed in the following lemma. The proof is given in A.

Lemma 1 *If $\text{Re}(\xi_m) = 0$ then $|jAj| = 1$. Furthermore $|jAj| = 1$ only when $\xi_m = 0$ and $k = 0$, in which case $A = 1$ is a simple root. Thus solutions with $|jAj| > 1$ will have $\text{Re}(\xi_m) \neq 0$.*

Lemma 1 shows that all solutions to (2.59) corresponding to pure imaginary values of ξ_m are stable. Therefore our analysis can be reduced to the situation when ξ_m has a nonzero real part. For this case one solution ξ_m from (2.63) has a positive real part and the other has a negative real part. To satisfy the far-field boundary conditions in (2.59d) and (2.59g) only one of the two roots in (2.63) is retained for each domain, leading to the solutions of

the form

$$\hat{T}_L^n = c_L A^n e^{\xi_L x}, \quad \hat{T}_R^n = c_R A^n e^{-\xi_R x}, \quad (2.64)$$

where the principal branch of the square root in (2.63) is assumed so that the real part of ξ_m is nonnegative.

Substituting the solution in (2.64) into the CHAMP interface conditions (2.33), and using the extrapolation formula (2.60) yields

$$\begin{aligned} & c^L A^{n+1} \left(\mathbf{N}_{LR}^{(p)}[\xi_L, k] + \mathbf{S}_L \mathbf{D}_{LR}^{(p)}[\xi_L, k] \right) \\ &= c^R \left\{ \sum_{\ell=1}^{p+1} \binom{p+1}{\ell} (-1)^{\ell+1} A^{n+1-\ell} \right\} (\xi_R + \mathbf{S}_L) e^{-\xi_R h}, \end{aligned} \quad (2.65a)$$

$$c^R A^{n+1} \left(\mathbf{N}_{RL}^{(p)}[\xi_R, k] + \mathbf{S}_R \mathbf{D}_{RL}^{(p)}[\xi_R, k] \right) = c^L A^{n+1} (\xi_L + \mathbf{S}_R) e^{\xi_L h}. \quad (2.65b)$$

Here, $\mathbf{D}_{LR}^{(p)}[\partial_x, \partial_y]$ and $\mathbf{N}_{LR}^{(p)}[\partial_x, \partial_y]$ denote the p^{th} -order CHAMP Dirichlet and Neumann operators as functions of ∂_x and ∂_y , respectively, and Fourier transforming in y replaces ∂_y^2 in these operators with $-k^2$. The dependence on k is noted as $\mathbf{D}_{LR}^{(p)}[\partial_x, k]$, for example. The conditions in (2.65) define two equations for two unknowns c^L and c^R . For non-trivial solutions the determinant of the corresponding matrix must equal to zero which implies

$$\begin{aligned} & A \left(\mathbf{N}_{LR}^{(p)}[\xi_L, k] + \mathbf{S}_L \mathbf{D}_{LR}^{(p)}[\xi_L, k] \right) \left(\mathbf{N}_{RL}^{(p)}[\xi_R, k] + \mathbf{S}_R \mathbf{D}_{RL}^{(p)}[\xi_R, k] \right) \\ &= (\xi_L + \mathbf{S}_R) e^{\xi_L h} (\xi_R + \mathbf{S}_L) e^{-\xi_R h} \left\{ \sum_{\ell=1}^{p+1} \binom{p+1}{\ell} (-1)^{\ell+1} A^{-\ell} \right\} \end{aligned} \quad (2.66)$$

This leads to the following result.

Theorem 4 *The p^{th} -order accurate un-iterated CHAMP time-stepping scheme is stable provided there are no solutions A with $|A| > 1$ to $G(A) = 0$ where*

$$\begin{aligned} G(A) \stackrel{\text{def}}{=} & \frac{A^{p+1}}{\sum_{\ell=1}^{p+1} \binom{p+1}{\ell} (-1)^{\ell+1} A^{p-\ell}} \\ & \frac{(\xi_L + \mathbf{S}_R) e^{\xi_L h}}{\left(\mathbf{N}_{LR}^{(p)}[\xi_L, k] + \mathbf{S}_L \mathbf{D}_{LR}^{(p)}[\xi_L, k] \right)} \frac{(\xi_R + \mathbf{S}_L) e^{-\xi_R h}}{\left(\mathbf{N}_{RL}^{(p)}[\xi_R, k] + \mathbf{S}_R \mathbf{D}_{RL}^{(p)}[\xi_R, k] \right)}, \end{aligned} \quad (2.67)$$

Here, $\xi_L(A)$ and $\xi_R(A)$ are given by

$$\xi_m(A) = \sqrt{\frac{1}{\beta_0 \Delta t D_L} \frac{\sum_{\mu=0}^p \alpha_\mu A^{p-\mu}}{A^p} + \kappa^2}, \quad m = L, R, \quad (2.68)$$

with $\text{Re}(\xi_m) > 0$. This must be true for all $kh \in [2\pi, \pi]$.

The function $G(A)$ defined above also depends parametrically on the non-dimensional parameters given previously in (2.55), which implies values for z_L and z_R now given by

$$z_L = \sqrt{\frac{1}{\beta_0} \frac{1}{\lambda_{DL}} \frac{\sum_{\mu=0}^p \alpha_\mu A^{p-\mu}}{A^p} + \kappa^2}, \quad z_R = \sqrt{\frac{1}{\beta_0} \frac{1}{\lambda_{DR}} \frac{\sum_{\mu=0}^p \alpha_\mu A^{p-\mu}}{A^p} + \kappa^2}, \quad (2.69)$$

and then $G(A) = G(A, \mathbf{K}_{LR}, \mathbf{D}_{LR}, \lambda_{DL}, \kappa, p_L, p_R, z_L, z_R)$ can be expressed as

$$G(A) = \frac{A^{p+1}}{\sum_{\ell=1}^{p+1} \binom{p+1}{\ell} (1)^\ell A^{p-\ell}} \frac{(z_L + p_L) e^{z_L}}{\left(\mathbf{N}_{LR}^{(p)}[z_L] + p_L \mathbf{D}_{LR}^{(p)}[z_L] \right)} \frac{(z_R + p_R) e^{z_R}}{\left(\mathbf{N}_{RL}^{(p)}[z_R] + p_R \mathbf{D}_{RL}^{(p)}[z_R] \right)}. \quad (2.70)$$

Based on (2.70), the optimal parameters $\mathbf{S}_L = p_L h$ and $\mathbf{S}_R = p_R h$ can be determined such that the scheme is stable for each choice of the material parameters. Thus a min-max problem needs to be solved, which is given by

$$A_{CT} \stackrel{\text{def}}{=} \min_{p_L, p_R} \left[\max_{\kappa_{min}, \kappa, \kappa_{max}} \left\{ |jA| : G(A, \kappa, p_L, p_R) = 0 \right\} \right]. \quad (2.71)$$

The function $G(A)$ in (2.67) is a transcendental function of A due to the terms involving the exponential of $\xi_m h$. To simplify the process of finding roots in (2.71) these exponential terms are replaced by a Taylor series approximation. It is found that a linear approximation given by

$$e^{z_m} \approx 1 + z_m. \quad (2.72)$$

is sufficient. Once the optimal parameters are found, one can double check that, with these parameters, the original $G(A)$ satisfies the stability condition through an application of the argument principle [75].

With the Taylor series approximations, (2.70) can be written as

$$\begin{aligned} \tilde{G}(A) = (A^{p+1}) \left(\mathbf{N}_{LR}^{(p)}[z_L] + p_L \mathbf{D}_{LR}^{(p)}[z_L] \right) \left(\mathbf{N}_{RL}^{(p)}[z_R] + p_R \mathbf{D}_{RL}^{(p)}[z_R] \right) \\ \left(\sum_{\ell=1}^{p+1} \binom{p+1}{\ell} (1)^{\ell+1} A^{p-\ell} \right) \left((z_L + p_L) e^{z_L} \right) \left((z_R + p_R) e^{z_R} \right) \stackrel{\text{def}}{=} 0, \end{aligned} \quad (2.73)$$

which results in a polynomial involving A , z_L and z_R . Also, rewrite $z_m, m = L, R$ as

$$h_L(A) \stackrel{\text{def}}{=} z_L^2 = \frac{1}{\beta_0} \frac{1}{\lambda_{DL}} \frac{\sum_{\mu=0}^p \alpha_{\mu} A^{p-\mu}}{A^p} + \kappa^2, \quad (2.74a)$$

$$h_R(A) \stackrel{\text{def}}{=} z_R^2 = \frac{1}{\beta_0} \frac{1}{\lambda_{DR}} \frac{\sum_{\mu=0}^p \alpha_{\mu} A^{p-\mu}}{A^p} + \kappa^2. \quad (2.74b)$$

Equations (2.73), (2.74a) and (2.74b) form a polynomial system involving A , z_L and z_R . To simplify the problem, this polynomial system is transformed into a single polynomial so that only one unknown, A , is involved. The steps involved in this transformation are given in Algorithm 3 for a 2nd-order scheme. Briefly, equation (2.73) can be used to solve for z_L in terms of A and z_R . Squaring both sides of the equation and using (2.74a) to remove the z_L dependency gives a polynomial in A and z_R . Following a similar approach, z_R can be solved in terms of A and (2.74b) is used to remove the z_R dependency. The final polynomial formed only contains a single unknown variable A , and can be solved using some polynomial solvers. The entire optimization problem can then be evaluated using a minimization algorithm such as `fminsearch` from Matlab[74] to find p_L and p_R .

Algorithm 3: Transforming polynomial system to a single high-degree polynomial.

Step 1) Expand $G(A)$ and squaring z_L, z_R :

$$\begin{aligned}\tilde{G}(A) &= f(A) + g_1(A)z_L + g_2(A)z_R + g_3(A)z_Lz_R = 0 \\ z_L^2 &= h_L(A) \\ z_R^2 &= h_R(A)\end{aligned}$$

Step 2) Using $G(A)$, solve for z_L in terms of A and z_R

$$z_L = \frac{G(A) - f(A) - g_2(A)z_R}{g_1(A) + g_3(A)z_R}$$

Step 3) Squaring both sides to get rid of z_L

$$z_L^2 = h_L(A) = \left(\frac{G(A) - f(A) - g_2(A)z_R}{g_1(A) + g_3(A)z_R} \right)^2 = \frac{\hat{G}(A) + \hat{g}_1(A)z_R + \hat{g}_2(A)z_R^2}{\hat{f}_1(A) + \hat{f}_2(A)z_R + \hat{f}_3(A)z_R^2}$$

Step 4) Substitute in z_R^2

$$h_L(A) = \frac{\hat{G}(A) + \hat{g}_1(A)z_R + \hat{g}_2(A)h_R(A)}{\hat{f}_1(A) + \hat{f}_2(A)z_R + \hat{f}_3(A)h_R(A)}$$

Step 5) Solve for z_R

$$z_R = \tilde{G}^\theta(A).$$

Step 6) Square both sides and get rid of z_R^2

$$h_R(A) = \tilde{G}^\theta(A)^2 = G(A).$$

All dependence on z_L and z_R have been removed.

Figure 2.7 shows graphs for A_{CT} versus K_{LR} , D_{LR} and λ_{DL} for a 4th-order CHAMP scheme. Corresponding optimal values of p_L and p_R are also presented. The plot on top left shows the time-stepping amplification factor A_{CT} as a function of K_{LR} , with λ_{DL} and D_{LR} fixed. Similar to Figure 2.6, the curve is symmetric about $K_{LR} = 1$, and as K_{LR} changes from 10^{-2} to 10^2 , A_{CT} first increases until reaches the maxima at $K_{LR} = 1$, then decreases. The maximal value of A_{CT} for $\lambda_{DL} = 10^3$ is about 0.9 which is still below 1, so it is possible to increase the time step further and still have a stable scheme. The middle plot at left shows how A_{CI} changes as D_{LR} varies from 10^{-2} to 10^2 . The time-stepping amplification factor decreases as D_{LR} increases, so for D_{LR} large, the scheme can generally run with larger time step. The plot on the bottom left shows the time-stepping amplification factor A_{CT} as a function of λ_{DL} , with $K_{LR} = 1$ and $D_{LR} = 1$. For this hard case, the scheme is still stable with $\lambda_{DL} = 10^{3.5}$. So with the optimal parameters chosen, even for case with large time-steps, the un-iterated CHAMP time-stepping scheme is stable for a wide range of material parameters.

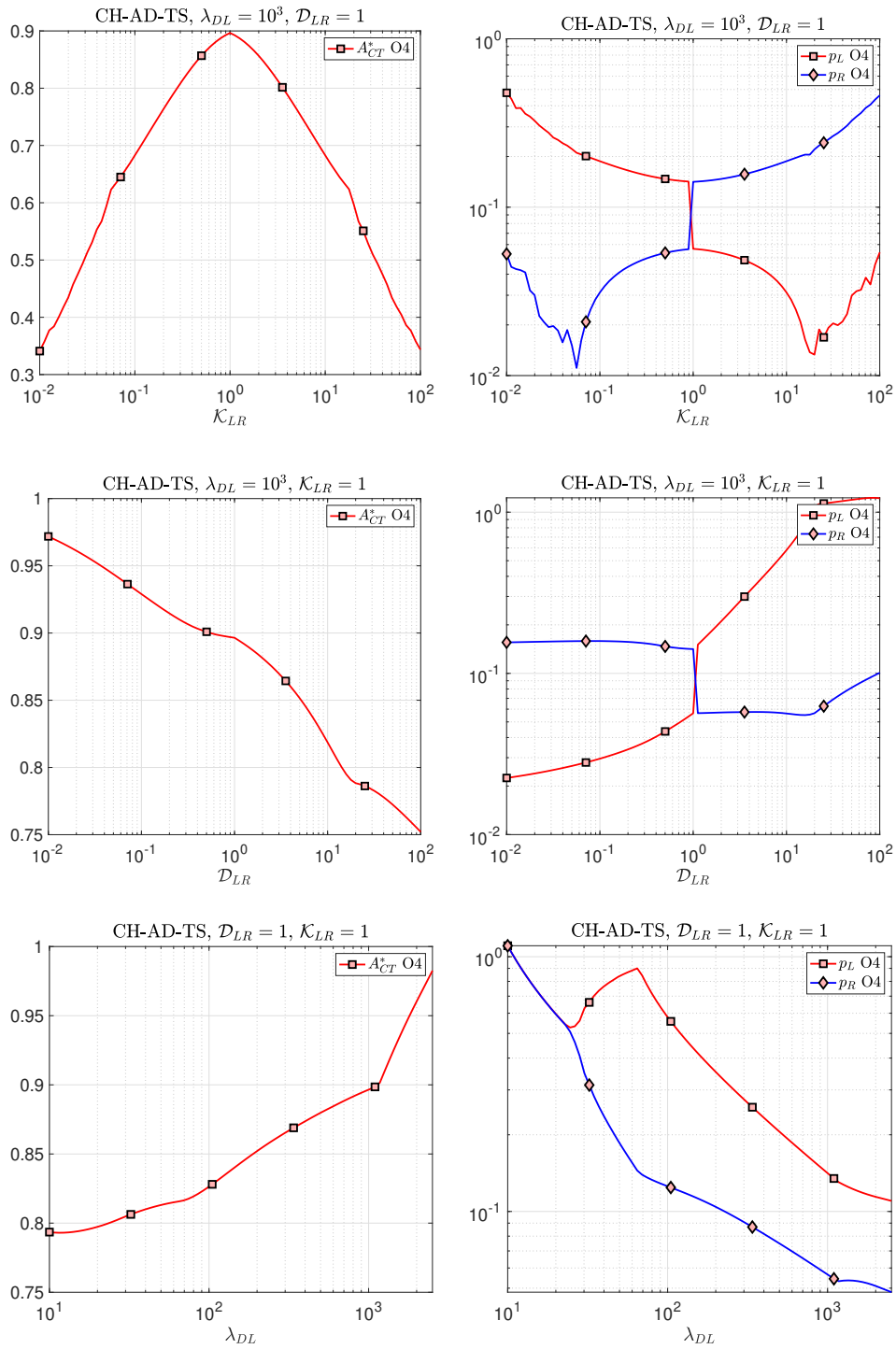


Figure 2.7: CHAMP time-stepping: A_{CT} and corresponding optimal p_L and p_R for a 4th-order accurate schemes with various choices of material parameters $\mathcal{K}_{LR} = \frac{K_L}{K_R}$, $\mathcal{D}_{LR} = \frac{D_L}{D_R}$, $\lambda_{DL} = \frac{tD_L}{h^2}$.

2.6.3 Accuracy of the Un-iterated CHAMP Time-stepping Scheme

In this section, the accuracy of the un-iterated CHAMP time-stepping scheme is analyzed. The main task is to verify the order of accuracy for an un-iterated time-stepping scheme when a p^{th} -order accurate CHAMP condition is applied at the interface. As part of this analysis, the order of the time-extrapolation formula to initialize the CHAMP iteration at each time step is shown to be at least $p + 1$. Questions related to the accuracy of the truncated Taylor series expansions in the derivation of the CHAMP operators are also addressed in the analysis.

To give a concrete presentation, the case of a fourth-order accurate BDF scheme and CHAMP conditions ($p = 4$) is chosen. To further simplify the analysis a one-dimensional CHT problem with a bounded domain $x \in [-1, 1]$ is considered, given by

$$\partial_t T_m - D_m \partial_x^2 T_m = f_m(x, t), \quad \text{for } x \in \Omega_m, \quad t > 0, \quad (2.75a)$$

$$[T]_I = 0, \quad \text{for } t > 0, \quad (2.75b)$$

$$[K \partial_x T]_I = 0, \quad \text{for } t > 0, \quad (2.75c)$$

$$T_L(-1, t) = 0, \quad T_R(1, t) = 0, \quad \text{for } t > 0, \quad (2.75d)$$

$$T_m(x, 0) = T_m^{IC}(x), \quad \text{for } x \in \Omega_m, \quad (2.75e)$$

for $m = L, R$. Here, $\Omega_L = [-1, 0]$ and $\Omega_R = [0, 1]$ with the interface located at $x = 0$ as before. The error between the discrete approximation of (2.75) and the continuous problem is determined using a modified equation approach assuming $f_m(x, t)$ and $T_m^{IC}(x)$ are smooth functions. The temporal domain is discretized with a fixed time-step Δt , and the spatial domain is discretized uniformly with grid spacing h . Fourth-order central divided difference formulas are used for spatial discretization, and the discrete solution is denoted by $\hat{T}_{m,j}^n$, $m = L, R$, which approximates the exact solution $T_m(x_j, t^n)$ at time $t_n = n\Delta t$ and position $x_j = jh$ for a grid defined by $j = -N, -N + 1, \dots, 0, 1, \dots, N$, where $j = 0$ denotes the interface.

Some standard difference formulas for discretizing the equations in space are provided

below,

$$D_+ \hat{u}_j \stackrel{\text{def}}{=} \frac{\hat{u}_{j+1} - \hat{u}_j}{h}, \quad D \hat{u}_j \stackrel{\text{def}}{=} \frac{\hat{u}_j - \hat{u}_{j-1}}{h}, \quad D_0 \hat{u}_j \stackrel{\text{def}}{=} \frac{\hat{u}_{j+1} - \hat{u}_{j-1}}{2h}, \quad (2.76a)$$

$$\hat{D}_0 \hat{u}_j \stackrel{\text{def}}{=} \left[D_0 - \frac{h^2}{6} (D_0 D_+ D) \right] \hat{u}_j, \quad (2.76b)$$

$$\hat{D}_+ \hat{D} \hat{u}_j \stackrel{\text{def}}{=} \left[D_+ D - \frac{\Delta x^2}{12} (D_+ D)^2 \right] \hat{u}_j, \quad (2.76c)$$

where \hat{D}_0 and $\hat{D}_+ \hat{D}$ denote fourth-order accurate difference approximations and \hat{u}_j is a discrete solution that approximates $u(x_j)$. Representing the discrete CHAMP Dirichlet and Neumann operators by $\tilde{\mathbf{D}}$ and $\tilde{\mathbf{N}}$, respectively, the discrete error in the associated CHAMP operators for the left domain, for example, are given by

$$\begin{aligned} \mathbf{D}_{LR} - \tilde{\mathbf{D}}_{LR} &= K_{LR} h \left(\partial_x - \hat{D}_0 \right) + \frac{h^2}{2} D_{LR} \left(\partial_x^2 - \hat{D}_+ \hat{D} \right) \\ &+ \frac{h^3}{6} K_{LR} D_{LR} \left(\partial_x^3 - D_0 (D_+ D) \right) + \frac{h^4}{24} D_{LR}^2 \left(\partial_x^4 - (D_+ D)^2 \right) = O(h^5), \end{aligned} \quad (2.77a)$$

$$\begin{aligned} \mathbf{N}_{LR} - \tilde{\mathbf{N}}_{LR} &= K_{LR} \left(\partial_x - \hat{D}_0 \right) + h D_{LR} \left(\partial_x^2 - \hat{D}_+ \hat{D} \right) \\ &+ \frac{h^2}{2} K_{LR} D_{LR} \left(\partial_x^3 - D_0 D_+ D \right) + \frac{h^3}{6} D_{LR}^2 \left(\partial_x^4 - (D_+ D)^2 \right) = O(h^4), \end{aligned} \quad (2.77b)$$

where the standard truncation error formulas are used. The coupling parameter \mathbf{S}_L and \mathbf{S}_R are assumed to be positive constants, and with a typical choice of $\Delta t = O(h)$, it is reasonable to assume

$$S_m = O(h^{-p}), \quad 0 \leq p \leq 1, \quad m = L, R \quad (2.78)$$

An accurate initial temperature is needed from the solution in the right domain to initialize the CHAMP iteration starting in the left domain at each time step. One approach to do this is to use a time extrapolation formula of order q . For fourth-order, consider formulas for $q = 4, 5$, which are given by

$$\hat{T}_{\text{guess}}^{(q)}(\hat{T}_{R,j}^{n+1}) = \begin{cases} 4\hat{T}_{R,j}^n - 6\hat{T}_{R,j}^{n-1} + 4\hat{T}_{R,j}^{n-2} - \hat{T}_{R,j}^{n-3}, & \text{for } q = 4, \\ 5\hat{T}_{R,j}^n - 10\hat{T}_{R,j}^{n-1} + 10\hat{T}_{R,j}^{n-2} - 5\hat{T}_{R,j}^{n-3} + \hat{T}_{R,j}^{n-4}, & \text{for } q = 5. \end{cases} \quad (2.79)$$

Using the discrete solutions to (2.75), the fully discrete un-iterated CHAMP time-stepping

scheme can be expressed as,

$$\frac{\sum_{\ell=1}^4 \alpha_\ell \hat{T}_m^{n-\ell}}{\beta_0 \Delta t} D_m(\hat{D}_+ \hat{D}_-) \hat{T}_{m,j}^{n+1} = f_{m,j}^{n+2}, \quad \text{for } n \geq 0, \quad (2.80a)$$

$$(\tilde{\mathbf{N}}_{LR} + \mathbf{S}_L \tilde{\mathbf{D}}_{LR}) \hat{T}_{L,0}^{n+1} - (\hat{D}_0 + \mathbf{S}_L) T_{\text{guess}}^{(q)}(\hat{T}_{R,0}^{n+1}) = 0, \quad \text{for } n \geq 0, \quad (2.80b)$$

$$(\tilde{\mathbf{N}}_{RL} - \mathbf{S}_R \tilde{\mathbf{D}}_{RL}) \hat{T}_{R,0}^{n+1} - (\hat{D}_0 - \mathbf{S}_R) \hat{T}_{L,1}^{n+1} = 0, \quad \text{for } n \geq 0, \quad (2.80c)$$

$$\hat{T}_{L,N}^{n+1} = 0, \quad \hat{T}_{R,N}^{n+1} = 0, \quad \text{for } n \geq 0, \quad (2.80d)$$

$$\hat{T}_{m,j}^0 = T_m^{IC}(x_j), \quad j \geq \tilde{\Omega}_{m,h}. \quad (2.80e)$$

Note that $\tilde{\Omega}_{m,h}$ is used to denote the computational grid that also includes the ghost points. Assuming all past time values are correctly determined, and f_m is zero at the interface. The modified-equation CHT problem corresponding to the discretization in (2.80), to the leading order, is given by

$$\partial_t \tilde{T}_m - D_m \partial_x^2 \tilde{T}_m = \tau^{(4)}, \quad (2.81a)$$

$$(\mathbf{N}_{LR} + \mathbf{S}_L \mathbf{D}_{LR}) \tilde{T}_L(0, t) - (\partial_x + \mathbf{S}_L) \tilde{T}_R(h, t) = \tau^{(4)} + \mathbf{S}_L \tau^{(5,q)}, \quad (2.81b)$$

$$(\mathbf{N}_{RL} - \mathbf{S}_R \mathbf{D}_{RL}) \tilde{T}_R(0, t) - (\partial_x - \mathbf{S}_R) \tilde{T}_L(-h, t) = \tau^{(4)} + \mathbf{S}_R \tau^{(5)}, \quad (2.81c)$$

$$\tilde{T}_L(-1, t) = 0, \quad \tilde{T}_R(1, t) = 0, \quad (2.81d)$$

$$\tilde{T}_m(x, 0) = T_m^{IC}(x), \quad (2.81e)$$

where $\mathbf{D}_{\nu,\mu}$ and $\mathbf{N}_{\nu,\mu}$, $\nu, \mu = L, R$ are the original CHAMP operators. The truncation error terms, generically denoted by τ , are given by

$$\tau^{(4)} = O(h^4 + \Delta t^4) = O(h^4), \quad (2.82a)$$

$$\tau^{(5)} = O(h^5), \quad (2.82b)$$

$$\tau^{(5,q)} = O(h^5 + \Delta t^q) = O(h^5 + h^q). \quad (2.82c)$$

A key step here is to rearrange the CHAMP interface conditions (2.81b)–(2.81c) using a

Taylor series expansion for $\tilde{T}_R(h, t)$ and $\tilde{T}_L(h, t)$ about $x = 0$, which gives

$$\begin{aligned}
& (\mathbf{N}_{LR} + \mathbf{S}_L \mathbf{D}_{LR}) \tilde{T}_L(0, t) - (\partial_x + \mathbf{S}_L) \tilde{T}_R(h, t) \\
&= \mathbf{S}_L \tilde{T}_L(0, t) + K_{LR} (1 + \mathbf{S}_L h) \partial_x \tilde{T}_L(0, t) + h D_{LR} (1 + \mathbf{S}_L \frac{h^2}{2}) \partial_x^2 \tilde{T}_L(0, t) \\
&\quad + \frac{h^2}{2} K_{LR} D_{LR} (1 + \mathbf{S}_L \frac{h}{3}) \partial_x^3 \tilde{T}_L(0, t) + \frac{h^3}{6} D_{LR}^2 (1 + \mathbf{S}_L \frac{h}{4}) \partial_x^4 \tilde{T}_L(0, t) \\
&\quad \mathbf{S}_L \tilde{T}_R(0, t) - (1 + \mathbf{S}_L h) \partial_x \tilde{T}_R(0, t) - h (1 + \mathbf{S}_L \frac{h}{2}) \partial_x^2 \tilde{T}_R(0, t) \\
&\quad \frac{h^2}{2} (1 + \mathbf{S}_L \frac{h}{3}) \partial_x^3 \tilde{T}_R(0, t) - \frac{h^3}{6} (1 + \mathbf{S}_L \frac{h}{4}) \partial_x^4 \tilde{T}_R(0, t) = \tau^{(4)} + \mathbf{S}_L \tau^{(5,g)}.
\end{aligned} \tag{2.83}$$

Using the definition

$$K_{LR} = \frac{K_L}{K_R}, \quad D_{LR} = \frac{D_L}{D_R}, \tag{2.84}$$

the LHS of (2.83) can be expressed as

$$\begin{aligned}
& \mathbf{S}_L [\tilde{T}]_I + \frac{1 + \mathbf{S}_L h}{K_R} [\tilde{\sigma}]_I + h (1 + \mathbf{S}_L \frac{h}{2}) \frac{1}{D_R} \partial_t [\tilde{T}]_I \\
&+ \frac{h^2}{2} (1 + \mathbf{S}_L \frac{h}{3}) \frac{1}{D_R K_R} \partial_t [\tilde{\sigma}]_I + \frac{h^3}{6} (1 + \mathbf{S}_L \frac{h}{4}) \frac{1}{D_R^2} \partial_t^2 [\tilde{T}]_I = \tau^{(4)} + \mathbf{S}_L \tau^{(5,g)},
\end{aligned} \tag{2.85a}$$

$$\begin{aligned}
& \mathbf{S}_R [\tilde{T}]_I - \frac{1 + \mathbf{S}_R h}{K_L} [\tilde{\sigma}]_I + h (1 + \mathbf{S}_R \frac{h}{2}) \frac{1}{D_L} \partial_t [\tilde{T}]_I \\
&\frac{h^2}{2} (1 + \mathbf{S}_R \frac{h}{3}) \frac{1}{D_L K_L} \partial_t [\tilde{\sigma}]_I + \frac{h^3}{6} (1 + \mathbf{S}_R \frac{h}{4}) \frac{1}{D_L^2} \partial_t^2 [\tilde{T}]_I = \tau^{(4)} + \mathbf{S}_R \tau^{(5)},
\end{aligned} \tag{2.85b}$$

where $[\cdot]_I$ denotes the jump at the interface, \tilde{T} denotes the temperature, and $\tilde{\sigma}$ denotes the heat flux. Let

$$a_m = \frac{1 + \mathbf{S}_L h}{K_R}, \quad b_m = \frac{1 + \mathbf{S}_L \frac{h}{2}}{D_R}, \quad c_m = \frac{1 + \mathbf{S}_L \frac{h}{3}}{K_R D_R}, \quad d_m = \frac{1 + \mathbf{S}_L \frac{h}{4}}{D_R^2}. \tag{2.86}$$

Since $\mathbf{S}_L, \mathbf{S}_R = O(h^{-p})$, for $0 < p < 1$, it follows that (a_m, b_m, c_m, d_m) , $m = L, R$, are all $O(1)$. Then (2.85a) and (2.85b) can be written as

$$\mathbf{S}_L [\tilde{T}]_I + a_L [\tilde{\sigma}]_I + h b_L \partial_t [\tilde{T}]_I + \frac{h^2}{2} c_L \partial_t [\tilde{\sigma}]_I + \frac{h^3}{6} d_L \partial_t^2 [\tilde{T}]_I = \tau^{(4)} + \mathbf{S}_L \tau^{(5,g)}, \tag{2.87a}$$

$$\mathbf{S}_R [\tilde{T}]_I - a_R [\tilde{\sigma}]_I + h b_R \partial_t [\tilde{T}]_I - \frac{h^2}{2} c_R \partial_t [\tilde{\sigma}]_I + \frac{h^3}{6} d_R \partial_t^2 [\tilde{T}]_I = \tau^{(4)} + \mathbf{S}_R \tau^{(5)}. \tag{2.87b}$$

Let

$$Y = \begin{bmatrix} y_1 \\ y_2 \\ y_3 \end{bmatrix}, \quad y_1 = [\tilde{T}]_I, \quad y_2 = \partial_t[\tilde{T}]_I, \quad y_3 = [\tilde{\sigma}]_I. \quad (2.88)$$

Then the above equations can be written as a system of first order ODEs,

$$\begin{bmatrix} 1 & 0 & 0 \\ 0 & \frac{h^3}{6}d_L & \frac{h^2}{2}c_L \\ 0 & \frac{h^3}{6}d_R & \frac{h^2}{2}c_R \end{bmatrix} \partial_t Y + \begin{bmatrix} 0 & 1 & 0 \\ \mathbf{S}_L & hb_L & a_L \\ \mathbf{S}_R & hb_R & a_R \end{bmatrix} Y = \begin{bmatrix} 0 \\ \tau^4 + \mathbf{S}_L \tau^{(5,q)} \\ \tau^4 + \mathbf{S}_R \tau^{(5)} \end{bmatrix}. \quad (2.89)$$

Rearranging the equation gives

$$\partial_t Y = AY + b, \quad (2.90)$$

where

$$A = \begin{bmatrix} 0 & 1 & 0 \\ \frac{6c_R \mathbf{S}_L + 6c_L \mathbf{S}_R}{h^3(c_L d_R + c_R d_L)} & \frac{6c_R b_L + 6c_L b_R}{h^2(c_L d_R + c_R d_L)} & \frac{6c_R a_L}{h^3(c_L d_R + c_R d_L)} \quad \frac{6c_L a_R}{h^3(c_L d_R + c_R d_L)} \\ \frac{2d_R \mathbf{S}_L}{h^2(c_L d_R + c_R d_L)} \quad \frac{2d_L \mathbf{S}_R}{h^2(c_L d_R + c_R d_L)} & \frac{2d_R b_L}{h(c_L d_R + c_R d_L)} \quad \frac{2d_L b_R}{h(c_L d_R + c_R d_L)} & \frac{2d_R a_L + 2d_L a_R}{h^2(c_L d_R + c_R d_L)} \end{bmatrix}, \quad (2.91a)$$

$$b = \begin{bmatrix} 0 \\ \frac{6c_L \tau^{(4)} + 6c_R \tau^{(5,q)}}{h^3(c_L d_R + c_R d_L)} \\ \frac{2d_L \tau^{(4)} + 2d_R \tau^{(5)}}{h^2(c_L d_R + c_R d_L)} \end{bmatrix}. \quad (2.91b)$$

The solution to (2.90) is

$$Y(t) = Y(0)e^{-At} + \int_0^t e^{-A(t-\tau)} b(\tau) d\tau \quad (2.92)$$

Since A is non-singular,

$$\int_0^t e^{At} dt = A^{-1}(e^{At} - I). \quad (2.93)$$

Apply integration by part twice to the solution (2.92) gives

$$\begin{aligned} Y(t) = & (Y(0) - A^{-1}b(0) + (A^{-1})^2 b^{(0)}(0)) e^{-At} + A^{-1}b(t) \\ & (A^{-1})^2 b^{(0)}(t) + (A^{-1})^2 \int_0^t e^{-A(t-\tau)} b^{(0)}(\tau) d\tau. \end{aligned} \quad (2.94)$$

Note that A has three distinct eigenvalues $\lambda_1, \lambda_2, \lambda_3$ and $\lambda_i = O(h^{-(1+\frac{1}{2}p)}, h^{-2})$ $\forall i$. Define $\hat{\lambda}_i$ to be the eigenvalues of A^{-1} . Then $\hat{\lambda}_i$ are also distinct, with $\hat{\lambda}_i = O(h^2, h^{2+\frac{1}{2}p})$ $\forall i$. If t is greater than a small time $t_0 = \max(\hat{\lambda}_i)$, then the exponential term e^{-At} is small so that (2.94) gives the estimate

$$Y(t) = A^{-1}b(t) = \begin{bmatrix} \frac{(\mathbf{S}_R \tau^5 + \tau^4)a_L + a_R(\mathbf{S}_L \tau^{5,q} + \tau^4)}{\mathbf{S}_L a_R + \mathbf{S}_R a_L} \\ 0 \\ \frac{(\tau^5 + \tau^{5,q})\mathbf{S}_R \mathbf{S}_L - \tau^4 \mathbf{S}_L + \tau^4 \mathbf{S}_R}{\mathbf{S}_L a_R + \mathbf{S}_R a_L} \end{bmatrix}, \quad (2.95)$$

which gives

$$[\tilde{T}]_I = \frac{(\mathbf{S}_R \tau^5 + \tau^4)a_L + a_R(\mathbf{S}_L \tau^{5,q} + \tau^4)}{\mathbf{S}_L a_R + \mathbf{S}_R a_L}, \quad (2.96a)$$

$$[\tilde{\sigma}]_I = \frac{(\tau^5 + \tau^{5,q})\mathbf{S}_R \mathbf{S}_L - \tau^4 \mathbf{S}_L + \tau^4 \mathbf{S}_R}{\mathbf{S}_L a_R + \mathbf{S}_R a_L}. \quad (2.96b)$$

Assuming $\mathbf{S}_L = O(h^{-p})$, $\mathbf{S}_R = O(h^{-p})$, then the jump in the heat flux $[\tilde{\sigma}]_I$ given in (2.96) is $O(h^4 + \Delta t^4)$ provided

$$\tau^{(5,q)} h^{-p} = O(h^4 + \Delta t^4), \quad (2.97)$$

which require

$$5 - p \geq 4, \quad q - p \geq 4. \quad (2.98)$$

If $0 < p \leq 1$ then $q = 5$. Also notice that from (2.96), the jump in temperature is given by

$$[\tilde{T}]_I = \tau^{(4+p)} = O(h^{4+p}), \quad 0 \leq p \leq 1. \quad (2.99)$$

Thus for $p = 1$, this jump would be fifth-order accurate. Following a similar truncation error analysis and energy estimate in [75], one concludes that the CHAMP scheme is fourth-order accurate provided a fifth-order accurate time-extrapolation is used for (2.80b), with $p > 0$ and $\mathbf{S}_m = O(h^{-p}), 0 \leq p \leq 1$.

2.7 CHAMP Interface Conditions for a Curvilinear Grid

This section considers a discretization of the CHT problem given in (2.4a)–(2.4e) for a two-dimensional domain consisting of two subdomains, each represented by a curvilinear grid. A curvilinear grid is defined by a smooth mapping function $\mathbf{x} = \mathbf{G}_g(\mathbf{r})$ from a parameter space $\mathbf{r} = (r_1, r_2)$ to physical space $\mathbf{x} = (x_1, x_2)$. The governing equations, the boundary conditions and the interface conditions are transformed from physical space to parameter space using the chain rule to convert \mathbf{x} -derivatives to \mathbf{r} -derivatives. For example, $\partial_{x_i} T(\mathbf{x})$ is expressed as

$$\frac{\partial T(\mathbf{x})}{\partial x_i} = \frac{\partial r_k}{\partial x_i} \frac{\partial T(\mathbf{r})}{\partial r_k}, \quad (2.100)$$

where the summation convention is used. The Laplacian operators in curvilinear coordinates is written as

$$\Delta_{r,m} = \sum_{i,j} A_{ij}^m(\mathbf{r}^m) \partial_{r_i}^m \partial_{r_j}^m + \sum_i c_i^m(\mathbf{r}^m) \partial_{r_i}^m, \quad (2.101)$$

where

$$A_{ij}^m = \sum_k (\partial_{x_k} r_i^m) (\partial_{x_k} r_j^m), \quad (2.102a)$$

$$c_i^m = \sum_k \partial_{x_k} \partial_{x_k} r_i^m. \quad (2.102b)$$

The normal derivative for a subdomain m is denoted by $\partial_{n,m}$. For deriving the CHAMP conditions for the left domain, the normal \mathbf{n}_L is pointing outward from the left domain, and

is written as

$$\partial_{n,m} = \mathbf{n}_L \cdot \mathbf{r}_{\mathbf{x},m} = \sum_i B_i^m(\mathbf{r}^m) \partial_{r_i^m}, \quad m = L, R, \quad (2.103)$$

where

$$B_i^m = (\mathbf{n}_L \cdot \mathbf{r}_{\mathbf{x},m}) r_i^n = \sum_k \frac{1}{j_j r_{\mathbf{x},m} r_i^L j_j} \frac{\partial r_i^L}{\partial x_k} \frac{\partial r_i^m}{\partial x_k}, \quad m = L, R. \quad (2.104)$$

The grid spacings in parameter space are Δr^L and Δr^R , and \mathbf{r}^L and \mathbf{r}^R are used to indicate a point at the interface for the left and right subdomain, respectively. To simplify the presentation the interface is assumed to be located at $r_1^L = 1$ for the left subdomain and $r_1^R = 0$ for the right subdomain. To derive the CHAMP interface conditions on curvilinear grids, one starts from the derivation of the general Dirichlet condition for the left domain using a Taylor expansion of the solution on the right domain at an overlap distance of Δr_1^R to get

$$T_R(\Delta r_1^R, r_2) = \sum_{\ell=0}^p \frac{(\Delta r_1^R)^\ell}{\ell!} \partial_{r_1}^\ell T_R(0, r_2) + O((\Delta r_1^R)^{p+1}), \quad (2.105a)$$

$$\partial_{r_1} T_R(\Delta r_1^R, r_2) = \sum_{\ell=0}^{p-1} \frac{(\Delta r_1^R)^\ell}{\ell!} \partial_{r_1}^{\ell+1} T_R(0, r_2) + O((\Delta r_1^R)^p), \quad (2.105b)$$

where one less term is kept in the expansion for $\partial_{r_1} T_R(\Delta r_1^R, r_2)$. Terms involving $T_R(\mathbf{r})$ and its derivatives on the RHS of the above expansions are replaced by terms involving $T_L(\mathbf{r})$ and its derivatives using the interface conditions and the governing equation. The form for $\partial_{r_1} T_R$ is derived directly from the flux interface conditions, given by

$$K_R \partial_{n,R} T_R(\mathbf{r}^R) = K_L \partial_{n,L} T_L(\mathbf{r}^L), \quad (\mathbf{r}^L, \mathbf{r}^R) \in \Gamma. \quad (2.106)$$

Rearranging the equation yields

$$B_1^R \partial_{r_1} T_R = \frac{K_L}{K_R} (B_2^L \partial_{r_2} - B_2^R \partial_{r_2}) T_L \stackrel{\text{def}}{=} Q_R^{(1)} T_L. \quad (2.107)$$

This gives an expression for the r_1 -derivative of T_R in terms of derivatives T_L . To derive an expression for $\partial_{r_1}^2 T_R$, the governing equation and the temperature jump condition are used

to derive an interface compatibility conditions,

$$[D\Delta T]_I = 0, \quad (2.108)$$

which gives

$$\begin{aligned} \partial_{r_1}^2 T_R &= \frac{1}{A_{11}^R} \left(\beta \Delta_L \quad \frac{c_1^R}{B_1^R} Q_R^{(1)} \quad c_2^R \partial_{r_2} \quad A_{22}^R \partial_{r_2}^2 \quad 2A_{12}^R \partial_{r_2} \left(\frac{1}{B_1^R} Q_R^{(1)} \right) \right) T_L, \\ &\stackrel{\text{def}}{=} \frac{1}{(B_1^R)^2} Q_R^{(2)} T_L. \end{aligned} \quad (2.109)$$

The third order derivative term can be obtained by deriving an interface compatibility condition using the governing equation and flux interface condition to get

$$[K(B_1 \partial_{r_1} + B_2 \partial_{r_2})(D\Delta T)]_I = 0, \quad (2.110)$$

and the fourth-order derivative term can be obtained by differentiating the temperature jump condition twice with respect to t to get

$$[D\Delta(D\Delta T)]_I = 0. \quad (2.111)$$

The detailed calculation for the higher order derivative terms are omitted here, and derivatives $\partial_{r_1}^3 T_R$ and $\partial_{r_1}^4 T_R$ are defined symbolically as $Q_R^{(3)}$, $Q_R^{(4)}$, i.e.

$$\partial_{r_1}^3 T_R \stackrel{\text{def}}{=} \frac{1}{(B_1^R)^3} Q_R^{(3)}, \quad \partial_{r_1}^4 T_R \stackrel{\text{def}}{=} \frac{1}{(B_1^R)^4} Q_R^{(4)}. \quad (2.112)$$

These derivatives can then be substituted back into the Taylor expansions of $T_R(\Delta r_1^R, r_2)$ to get the generalized Dirichlet operator for the left domain,

$$T_R(\Delta r_1^R, r_2) = \mathbf{D}_{LR}^c + O(h^{p+1}), \quad (2.113)$$

with

$$\mathbf{D}_{LR}^c \stackrel{\text{def}}{=} \left(1 + \sum_{\ell=1}^p \frac{1}{\ell!} \frac{(\Delta r_1^R)^\ell}{(B_1^R)^\ell} Q_R^{(\ell)} \right) T_R. \quad (2.114)$$

Similarly, the generalized Neumann operator can be obtained by substituting those derivatives back into the Taylor expansion of $\partial_{r_1} T_R(\Delta r_1^R, r_2)$ to get

$$\partial_{r_1} T_R(\Delta r_1^R, r_2) = \sum_{\ell=1}^{p-1} \frac{1}{(\ell-1)!} \frac{(\Delta r_1^R)^{\ell-1}}{(B_1^R)^\ell} Q_R^{(\ell)} T_R. \quad (2.115)$$

Multiply the above equation by B_1^R to match the formula with the Cartesian case, one obtains the generalized Neumann operator for the left domain

$$\mathbf{N}_{LR}^c \stackrel{\text{def}}{=} \sum_{\ell=1}^p \frac{1}{(\ell-1)!} \frac{(\Delta r_1^R)^{\ell-1}}{(B_1^R)^\ell} Q_R^{(\ell)} T_R. \quad (2.116)$$

Operators for the right domain are derived analogously, with a Taylor expansion about the solution on the left domain at a distance Δr_1^L to the interface. The Dirichlet and Neumann operators become

$$\mathbf{D}_{RL}^c \stackrel{\text{def}}{=} \left(1 + \sum_{\ell=1}^p \frac{1}{\ell!} \frac{(\Delta r_1^L)^\ell}{(B_1^L)^\ell} Q_L^{(\ell)} \right) T_L, \quad (2.117a)$$

$$\mathbf{N}_{RL}^c \stackrel{\text{def}}{=} \sum_{\ell=1}^p \frac{1}{(\ell-1)!} \frac{(\Delta r_1^L)^{\ell-1}}{(B_1^L)^\ell} Q_L^{(\ell)} T_L. \quad (2.117b)$$

Following a similar approach used for the case of a Cartesian grid, the generalized Dirichlet and Neumann conditions are then combined using the weighting operators \mathbf{S}_L^c and \mathbf{S}_R^c to give the new CHAMP interface conditions for the mapped domain. The results are summarized in the following theorem.

Theorem 5 *The p^{th} -order accurate CHAMP interface conditions on curvilinear grids are*

$$(\mathbf{N}_{LR}^c + \mathbf{S}_L^c \mathbf{D}_{LR}^c) [T_L(0, r_2)] = (B_1^R \partial_x + \mathbf{S}_L^c) T_R(+\Delta r_1^R, r_2), \quad (2.118a)$$

$$(\mathbf{N}_{RL}^c - \mathbf{S}_R^c \mathbf{D}_{RL}^c) [T_R(0, r_2)] = (B_1^L \partial_x - \mathbf{S}_R^c) T_L(-\Delta r_1^L, r_2), \quad (2.118b)$$

where the operators $\mathbf{N}_{LR}^c, \mathbf{D}_{LR}^c, \mathbf{N}_{RL}^c, \mathbf{D}_{RL}^c$ are given in (2.114), (2.116), (2.117a) and (2.117b), respectively.

2.8 An Adaptive Variable Sub-Iteration Algorithm for the CHAMP Scheme

The analysis in Section 2.6 shows that the amplification factor of the CHAMP scheme depends on λ_{DL} , which is a parameter related to a dimensionless time-step. For a diffusive problem using an explicit time-stepping scheme, the natural scaling of the time-step is in terms of the diffusivity and the mesh spacing squared so that the magnitude of λ_{DL} is of order 1. For an implicit calculation on a fine grid, one would like to take Δt proportional to Δx , and this effective λ_{DL} which is measuring an explicit time-step, can become large. As λ_{DL} gets larger, the convergence of the CHAMP scheme slows down, and the residual in the CHAMP interface condition tends to increase over time. So the focus here is to study the convergence of the CHAMP time-stepping scheme for the case when λ_{DL} is large, and consider a modification to the original algorithm to pick the number of sub-time-step iterations adaptively.

The original CHAMP scheme, given in Algorithm 1, specifies a fixed upper bound for the number of sub-iterations at each time step. The CHAMP conditions are iterated at each step until the residual in the interface condition involving the continuity of temperature reaches some tolerance or the upper bound given by N_{si} is reached. Based on this process, a modified adaptive CHAMP algorithm is proposed to include an additional adaptive checking at each iteration with a stopping criterion. The number of sub-iteration N_{si} is now chosen adaptively based on a measure of the convergence of the CHAMP conditions and a chosen tolerance at each time step. The new algorithm is given in Algorithm 4, with two main changes: the *for* loop that does the sub-time-step iteration is now replaced by a *while* loop in line 7, and an *if* statement is added in line 26 to the iteration to adaptively control the number of sub-iterations.

At each time-step, the CHAMP iteration is initialized as before. At iteration j , the new solutions after one implicit solve for each sub-domain are denoted by $T_m^{(j)}$, with $m = L, R$. These solutions are used to calculate the residual of the CHAMP conditions at the interface. The final CHAMP residual, ResCH, is determined by taking the maximum over Res $_m$, where Res $_L$ and Res $_R$ denote the CHAMP residuals in each sub-domain. If this maximum residual is smaller than the tolerance, then the iteration stops, and the solutions at the new time-step are updated. If, on the other hand, the maximum residual is greater than the tolerance, another sub-iteration is performed, and the process continues until the residuals of the interface

Algorithm 4: CHAMP adaptive conjugate heat transfer solver.

```

1: AdaptiveDiffusionSolver( $\Omega, t_{\text{nal}}$ )
2:  $t = 0, n = 0$ ;
3:  $T_m^0(\mathbf{x}) = T_m^{\text{IC}}(\mathbf{x}), \quad \mathbf{x} \in \Omega_m, \quad m = L, R;$  ▷ Initial conditions
4: Evaluate past time values as needed by BDF schemes.
5: // Time stepping loop
6:  $N_{\text{si}} = 0;$  ▷ Initialize counting
7: while  $t < t_{\text{nal}}$  do
8:    $F_m(\mathbf{x}) = \sum_{\ell=1}^p \alpha_{\ell} T_m^{n-\ell}(\mathbf{x}), \quad \mathbf{x} \in \Omega_m, \quad m = L, R;$  ▷ Assign RHS for BDF scheme
9:    $T_R^{(0)} = \sum_{i=1}^{p+1} \binom{p+1}{i} (-1)^{i+1} T_R^{n+1-i};$  ▷ Extrapolate in time for initial guess
10:  while  $|\text{error}^{(j)} - \text{error}^{(j-1)}| > \text{tol}$  do ▷ Sub-time-step iterations
11:    // Solve for  $T_L^{(j)}$  given  $T_R^{(j-1)}$ 
12:     $T_L^{(j)} - \beta_0 \Delta t D_L \Delta T_L^{(j)} = F_L, \quad \mathbf{x} \in \Omega_L;$ 
13:     $(\mathbf{N}_{LR} + \mathbf{S}_L \mathbf{D}_{LR}) T_L^{(j)}(\mathbf{x}) = (\partial_n + \mathbf{S}_L) T_R^{(j-1)}(\mathbf{x} + h_R), \quad \mathbf{x} \in l;$  ▷ CHAMP
14:     $B_L(T_L^{(j)}) = g(\mathbf{x}, t + \Delta t), \quad \mathbf{x} \in \partial\Omega_L;$  ▷ Physical BCs.
15:    // Solve for  $T_R^{(j)}$  given  $T_L^{(j)}$ 
16:     $T_R^{(j)} - \beta_0 \Delta t D_R \Delta T_R^{(j)} = F_R, \quad \mathbf{x} \in \Omega_R;$ 
17:     $(\mathbf{N}_{RL} + \mathbf{S}_R \mathbf{D}_{RL}) T_R^{(j)}(\mathbf{x}) = (\partial_n + \mathbf{S}_R) T_L^{(j)}(\mathbf{x} + h_L), \quad \mathbf{x} \in l;$  ▷ CHAMP
18:     $B_R(T_R^{(j)}) = g(\mathbf{x}, t + \Delta t), \quad \mathbf{x} \in \partial\Omega_R;$  ▷ Physical BCs.
19:    // Calculate error in iteration
20:     $\text{error}^{(j)} = \max_{m=L,R} \{k |T_m^{(j)} - T_m^{(j-1)}|_l\};$  ▷ Error in iteration *CHECK*
21:    // Calculate CHAMP residual
22:     $\text{Res}_L = k(\mathbf{N}_{LR} + \mathbf{S}_L \mathbf{D}_{LR}) T_L^{(j)}(\mathbf{x}) - (\partial_n + \mathbf{S}_L) T_R^{(j)}(\mathbf{x} + h_R) k, \quad \mathbf{x} \in l;$ 
23:     $\text{Res}_R = k(\mathbf{N}_{RL} + \mathbf{S}_R \mathbf{D}_{RL}) T_R^{(j)}(\mathbf{x}) - (\partial_n + \mathbf{S}_R) T_L^{(j)}(\mathbf{x} + h_L) k, \quad \mathbf{x} \in l;$ 
24:     $\text{ResCH} = \max(\text{Res}_L, \text{Res}_R);$  ▷ CHAMP residual
25:     $N_{\text{si}} = N_{\text{si}} + 1;$  ▷ Count
26:    If  $\text{ResCH} < \text{tol}_{\text{CH}}$  then break; ▷ Stopping criterion
27:  end while
28:   $T_m^{n+1} = T_m^{(j)}, \quad m = L, R;$  ▷ Solution at new time
29:   $t = t + \Delta t, n = n + 1;$ 
30: end while

```

conditions becomes sufficiently small. Notice that the CHAMP residual may need to be non-dimensionalized in line 26 by the norm of the solution.

There are possible advantages and disadvantages of the present adaptive algorithm. A possible disadvantage is that a choice must be made for the tolerance of the CHAMP residual. However, as it will be shown later in Section 2.9.4, the convergence of the CHAMP scheme does not depend strongly on this tolerance. In addition, as more sub-iterations are taken at each time-step, the CHAMP scheme becomes less sensitive to the choice of the weighting

parameters p_L and p_R , and this could be considered an advantage. For a large value of λ_{DL} , a value for N_{si} greater than 1, perhaps equal to 2 or 3, is required in the original CHAMP scheme, especially at higher order accuracy. By picking N_{si} adaptively, the new algorithm is possibly more efficient if smaller values of N_{si} can be used at some time steps over the full time integration of the scheme. Detailed results are presented in Section 2.9.4.

2.9 Numerical Results

Computational results are now presented to verify the accuracy and stability of a 4th-order accurate un-iterated CHAMP time-stepping scheme. In Section 2.9.1, the fourth-order spatial accuracy of the CHAMP scheme is demonstrated by comparing the numerical solution to the exact solution of two steady-state problems. In Section 2.9.2, the temporal and spatial accuracy of the CHAMP scheme is verified by computing numerical solutions to some time-dependent CHT problems where the exact solution is known. The analytical solution of problems on a double-rectangle domain is derived in Section 2.9.2.1, and the exact solution to problems of a double-annulus geometry is derived in Section 2.9.2.2. Numerical simulations are performed using various thermal coefficients on computational grids with increasing resolutions. In Section 2.9.3, the accuracy of the CHAMP scheme is verified using the method of manufactured solutions to problems with different geometries. A large time-step study for a steady-state problem using the adaptive CHAMP algorithm is given in Section 2.9.4, and finally, in Section 2.9.5, the un-iterated CHAMP time-stepping scheme is implemented on a multi-domain problem using the overlapping composite grids.

2.9.1 Numerical Results for Two Steady State Problems

Solutions of two steady state CHT problems can be used to verify the spatial accuracy of the un-iterated CHAMP scheme. The geometry of the first problem is illustrated in Figure 2.8. The domain contains two adjacent squares with a vertical interface at $x = x_l$. Dirichlet boundary conditions are chosen at $x = x_a$ and $x = x_b$, and periodic boundary conditions are applied in the y -direction. Assuming boundary data given by $T_L(x_a) = T_{x_a}^L$ and $T_R(x_b) = T_{x_b}^R$, the steady state solution of this problem is

$$T_L(x) = \frac{x_l - x}{x_l - x_a} T_{x_a}^L + \frac{x - x_a}{x_l - x_a} T_l, \quad T_R(x) = \frac{x_b - x}{x_b - x_l} T_l + \frac{x - x_l}{x_b - x_l} T_{x_b}^R, \quad (2.119)$$

where

$$T_I = \frac{T_{x_b}^R}{1 + K_{RL}} + \frac{T_{x_a}^L}{K_{LR} + 1}. \quad (2.120)$$

The steady state solution can be obtained via a long-time integration of the CHT problem assuming initial conditions given by

$$T_L(x, y, 0) = T_R(x, y, 0) = \frac{1}{2}(T_{x_a}^L + T_{x_b}^R). \quad (2.121)$$

Notice that the solution depends only on x . Computations are performed using a Cartesian grid for the domain defined by $x_a = -1$, $x_I = 0$, $x_b = 1$, $y_a = 0$ and $y_b = 1$. The material parameters are chosen to be $D_L = 1$, $D_R = 10$, $K_L = 10$ and $K_R = 1$, while the boundary values are taken to be $T_{x_b}^R = 1$ and $T_{x_a}^L = 5$. The scheme is run using $\Delta t = 3.1e-4$ to a sufficiently large final time, i.e. $t_{\text{nal}} = 10$, so that the solution can be considered at steady state. Since the exact solution is linear in x and the CHAMP scheme is fourth-order accurate, the numerical error is expected to be within round-off error. The actual computation shows that the maximum error for the computed solution is $1.07e-12$ which agrees with this expectation.

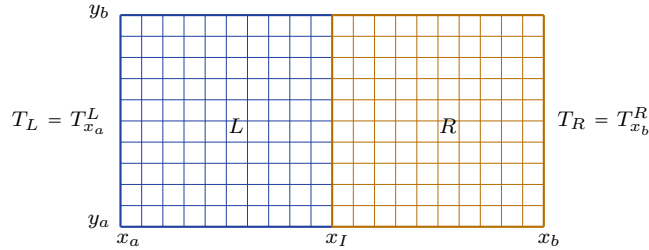


Figure 2.8: Computational domain for the square-square geometry.

The second problem involves two concentric annuli with an inner radius at r_a , an outer radius at r_b , and an interface at a radius $r_I \in (r_a, r_b)$. A sample grid for the domain is depicted in Figure 2.9. Boundary conditions are given as

$$T_L(r_a) = T_{r_a}^L, \quad T_R(r_b) = T_{r_b}^R. \quad (2.122)$$

For this setup, the steady state solution is given by

$$T_L(r) = \frac{\ln(r_I/r)}{\ln(r_I/r_a)} T_{r_a}^L + \frac{\ln(r/r_a)}{\ln(r_I/r_a)} T_I, \quad T_R(r) = \frac{\ln(r/r_I)}{\ln(r_b/r_I)} T_{r_b}^R + \frac{\ln(r_b/r)}{\ln(r_b/r_I)} T_I, \quad (2.123)$$

where

$$T_I = \frac{T_{r_b}^R}{1 + \mathcal{K}_{LR} \frac{\ln(r_b/r_I)}{\ln(r_I/r_a)}} + \frac{T_{r_a}^L}{1 + \mathcal{K}_{RL} \frac{\ln(r_I/r_a)}{\ln(r_b/r_I)}}. \quad (2.124)$$

As before, the steady state solution can be reached through a long-time integration of the CHT problem assuming initial conditions given by

$$T_L(r, \theta, 0) = T_R(r, \theta, 0) = \frac{1}{2}(T_{r_a}^L + T_{r_b}^R). \quad (2.125)$$

The computations for this second problem are performed using a curvilinear grid for the domain with $r_a = 0.2$, $r_I = 0.4$ and $r_b = 0.6$. The curvilinear grid is defined by a double-annulus mapping function given by

$$\mathbf{x} = \mathbf{G}_{\text{da}}(\mathbf{r}) = \begin{bmatrix} (\alpha + \beta r_1) \cos(\omega r_2) \\ (\alpha + \beta r_1) \sin(\omega r_2) \end{bmatrix}, \quad (2.126)$$

where α , β and ω are constants and $\mathbf{r} \in [0, 1]^2$. The grid for the calculation of T_L uses $\alpha = \beta = 0.2$ and $\omega = 2\pi$, while the grid for the calculation of T_R uses $\alpha = 0.4$, $\beta = 0.2$ and $\omega = 2\pi$. The material parameters are chosen to be $D_L = 1$, $D_R = 10$, $\mathcal{K}_L = 10$ and $\mathcal{K}_R = 1$. The temperatures at the boundaries are taken to be $T_{r_a}^L = 5$ and $T_{r_b}^R = 1$. A grid for the double annulus domain, denoted by $G_{\text{da}}^{(j)}$ for a resolution factor j , consists of two Cartesian grids in the computational space $\mathbf{r} = (r_1, r_2)$ with mesh spacings $h_{r_1}^{(j)} = 1/(10j)$ and $h_{r_2}^{(j)} = 1/(10j)$ in the mapped space corresponding to the radial and circumferential directions in physical space, respectively. The maximum error is computed at $t_{\text{nal}} = 10$ and the results are presented in Table 2.3. Since the steady state solution is no longer linear in r , the error is not expected to be at round-off. The rate of convergence is expected to be approximately equal to 4 as a fourth-order accurate scheme is implemented. Results in Table 2.3 shows that as the mesh spacing decreases by a factor of 2, the error decreases approximately by a factor of 16, which indicates a fourth-order convergence rate.

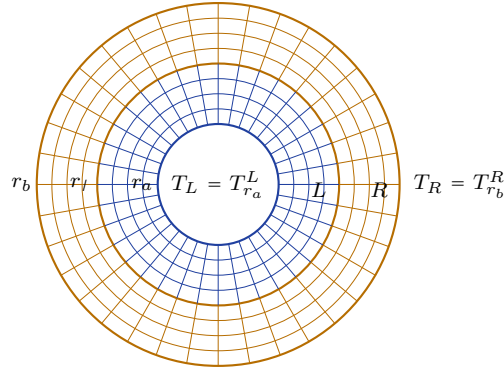


Figure 2.9: Physical domain for the annulus-annulus geometry.

Table 2.3: A convergence study for a annulus-annulus domain at $t_{\text{nal}} = 0.5$ using the steady state solution.

Annulus Geometry					
$D_{LR} = 0.1, K_{LR} = 10, t_{\text{nal}} = 0.5.$					
j	h_{r_1}	max error	ratio	rate	
2	5.00e 02	1.251e 06			
4	2.50e 02	7.555e 08	16.55	4.05	
8	1.25e 02	4.646e 09	16.26	4.02	

2.9.2 Verification with Exact Solutions for Time Dependent Problems

In this section, exact time-dependent solutions are used to verify both the temporal and spatial accuracy of the un-iterated CHAMP scheme. Computational results are compared to the exact solution derived from the model problem, and a grid refinement study is performed to verify the convergence rate for the CHAMP schemes. Numerical simulations for a problem on a double-rectangle domain are presented in Section 2.9.2.1, while the results for a problem on a double-annulus domain are presented in Section 2.9.2.2.

2.9.2.1 Adjacent Rectangles

Exact solutions of a CHT problem for a region consisting of two adjacent rectangles with a planar interface located at $x = 0$ is computed first. Let the left domain be the rectangle $\Omega_L = [x_a, 0] \times [y_a, y_b]$ and the right domain be the rectangle $\Omega_R = [0, x_b] \times [y_a, y_b]$.

The CHT problem is given by

$$\partial_t T_m = D_m \Delta T_m, \quad \text{for } \mathbf{x} \in \Omega_m, \quad m = L, R, \quad (2.127a)$$

$$[T]_l = 0, \quad \text{for } y \in [y_a, y_b], \quad x = 0, \quad (2.127b)$$

$$[K(\partial_x T)]_l = 0, \quad \text{for } y \in [y_a, y_b], \quad x = 0, \quad (2.127c)$$

$$T_L(x_a, y, t) = 0, \quad T_R(x_b, y, t) = 0, \quad \text{for } y \in [y_a, y_b], \quad (2.127d)$$

$$T_m(x, y, 0) = T_m^{\text{IC}}(x, y), \quad \text{for } \mathbf{x} \in \Omega_m, \quad m = L, R, \quad (2.127e)$$

where $m = L, R$ indicates the left or right domain. Separable solutions of the form

$$T_m(x, y, t) = e^{-s^2 t} \hat{T}_m(x) \sin(ky), \quad m = L, R, \quad (2.128)$$

can be found, where s is an eigenvalue and k is chosen such that $k(y_b - y_a) = 2\pi\nu$ for an integer ν . Solutions to $\hat{T}_m(x)$ that satisfy the Dirichlet boundary conditions at $x = x_a$ and $x = x_b$ are given as

$$\hat{T}_L(x) = A_L \sin(r_L(x - x_a)), \quad \hat{T}_R(x) = A_R \sin(r_R(x - x_b)), \quad (2.129)$$

where r_m is defined as

$$r_m = \sqrt{\frac{s^2}{D_m} - k^2}, \quad m = L, R, \quad (2.130)$$

and A_L and A_R are constants. Substituting the solutions in (2.129) into the matching conditions at the interface leads to a homogeneous system in terms of the constants A_L and A_R and the eigenvalue s , given by

$$\begin{bmatrix} \sin(r_L x_a) & \sin(r_R x_b) \\ K_L r_L \cos(r_L x_a) & K_R r_R \cos(r_R x_b) \end{bmatrix} \begin{bmatrix} A_L \\ A_R \end{bmatrix} = \begin{bmatrix} 0 \\ 0 \end{bmatrix}. \quad (2.131)$$

Non-trivial solutions exist if the coefficient matrix in (2.131) is singular, which leads to the determinant condition given by

$$K_L \sqrt{\frac{s^2}{D_L} - k^2} \tan \left(x_b \sqrt{\frac{s^2}{D_R} - k^2} \right) - K_R \sqrt{\frac{s^2}{D_R} - k^2} \tan \left(x_a \sqrt{\frac{s^2}{D_L} - k^2} \right) = 0, \quad (2.132)$$

which is a transcendental equation that defines s for a given choice for the integer ν . There is an infinite set of eigenvalues s for each ν that defines the wave number k in the y direction, and for the purpose of this test the smallest eigenvalue is picked. Once the eigenvalue satisfying (2.132) is found, nontrivial values for A_L and A_R that lie in the nullspace of the homogeneous system (2.131) can be computed. For the purpose of numerical calculations, two such solutions are picked and whose parameters are given in Table 2.4. Notice that here A_L is normalized to equal to 1 with A_R scaled accordingly. For Case 1, the root r_R is pure imaginary, which gives an imaginary value for A_R . The final combined solution would still be real.

Table 2.4: Selected eigenvalues s and coefficients A_L , A_R for two selected cases on a double-rectangle domain.

Adjacent Rectangles			
Case 1: $D_L = 1$, $K_L = 10$, $D_R = 10$, $K_R = 1$.			
ν	s	A_L	A_R
1	1.143	1	9.463i
Case 2: $D_L = 1$, $K_L = 1$, $D_R = 1$, $K_R = 1$.			
ν	s	A_L	A_R
1	1.118	1	1.000

Computations are performed on a grid defined by $x_a = 0$, $x_I = 0$, $x_b = \pi$, $y_a = 0$, $y_b = 2\pi$, and is denoted by $G_{\text{dr}}^{(j)}$ with a target mesh spacing approximately equals to $\Delta s^{(j)} = \pi/(10j)$ in both the x and y directions. The resolution factor j is chosen to be $j = 2, 4, 8$. A sample grid is provided in the left of Figure 2.10. The material parameters are chosen to be $D_L = 1$, $D_R = 10$, $K_L = 10$, $K_R = 1$ with $\nu = 1$ for the Case 1, and $D_L = 1$, $D_R = 1$, $K_L = 1$, $K_R = 1$ with $\nu = 1$ for Case 2. The scheme is run to a final time $t_{\text{nal}} = 5$ with Δt chosen to be proportional to the grid spacing Δs . Only one sub-iteration is performed at each time

step, and values for p_L and p_R are picked by solving the optimization problem described in Section 2.6.2. The exact solution provides the initial data and the information needed to start the multi-step scheme (BDF4 in this case). Results of a grid refinement study are presented in Table 2.5, where the maximum error at $t_{\text{nal}} = 5$ and the estimated convergence rate for each domain are computed. One can see that the error decreases by a factor of 16 as the mesh spacing decreases by a factor of 2, indicating fourth-order accurate convergence of the un-iterated CHAMP scheme. Contour plots of the solution and corresponding error for Case 1 on the finest grid at $t_{\text{nal}} = 5$ are shown in Figure 2.10. The error jumps at the interface, as expected, but is smooth in each sub-domain.

Table 2.5: A convergence study for the double-rectangle problem using the time-dependent exact solution with selected thermal parameters.

Adjacent Rectangles									
Case 1: $\nu = 1$, $D_L = 1$, $K_L = 10$, $D_R = 10$, $K_R = 1$, $t_{\text{nal}} = 5$, max-iteration = 1.									
j	Δs	λ_{DL}	max error left	ratio	rate	max error right	ratio	rate	
2	1.57e 02	6.33e+00	1.581e 07			1.558e 07			
4	7.85e 02	1.27e+01	8.256e 09	19.15	4.26	8.089e 09	19.26	4.27	
8	3.93e 02	2.55e+01	4.873e 10	16.94	4.08	4.760e 10	16.99	4.09	
Case 2: $\nu = 1$, $D_L = 1$, $K_L = 1$, $D_R = 1$, $K_R = 1$, $t_{\text{nal}} = 5$, max-iteration = 1.									
j	Δs	λ_{DL}	max error left	ratio	rate	max error right	ratio	rate	
2	1.57e 02	6.33e+00	6.453e 08			7.766e 08			
4	7.85e 02	1.27e+01	4.005e 09	16.11	4.01	4.332e 09	17.92	4.16	
8	3.93e 02	2.55e+01	2.744e 10	14.60	3.87	2.779e 10	15.59	3.96	

2.9.2.2 Concentric Annuli

In this section, numerical simulations are performed on a double-annulus domain to provide a second verification of both the temporal and spatial accuracy of the un-iterated CHAMP time-stepping scheme. The exact solution to the model problem is derived first, followed by a grid refinement study to verify the convergence rate for the CHAMP scheme.

Let the inner domain be the annulus $\Omega_L = \{r \in [r_a, r_l], \theta \in [0, 2\pi]\}$, and the outer domain be the annulus $\Omega_R = \{r \in [r_l, r_a], \theta \in [0, 2\pi]\}$. For this configuration, the

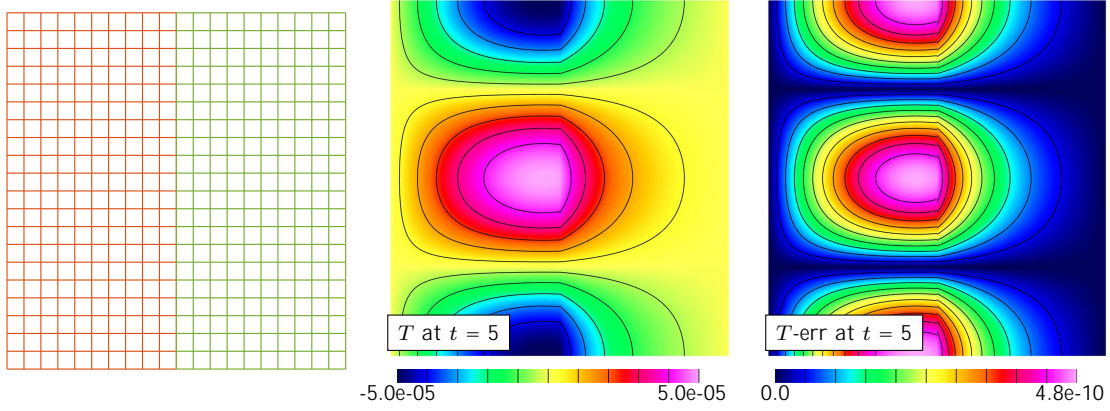


Figure 2.10: Numerical results for the double-rectangle problem. **Left:** a sample computational grid for a double-rectangle geometry. **Middle:** CHAMP4 solution for Case 1 at $t_{\text{nal}} = 5$ on grid $G_{dr}^{(8)}$. **Right:** error for Case 1 at $t_{\text{nal}} = 5$ on the same grid.

governing equations and the interface conditions are given by

$$\partial_t T_m = D_m \left(\frac{1}{r} \partial_r (r \partial_r T_m) + \frac{1}{r^2} \partial_\theta^2 T_m \right), \quad \text{for } \mathbf{r} \in \Omega_m, \quad m = L, R \quad (2.133a)$$

$$T_L(r_a, \theta, t) = 0, \quad T_R(r_b, \theta, t) = 0, \quad \text{for } \theta \in (0, 2\pi), \quad (2.133b)$$

$$[T]_I = 0, \quad \text{for } \theta \in (0, 2\pi), \quad (2.133c)$$

$$[K \partial_r T]_I = 0, \quad \text{for } \theta \in (0, 2\pi), \quad (2.133d)$$

$$T_m(r, \theta, 0) = T_m^{\text{IC}}(r, \theta), \quad \text{for } \mathbf{x} \in \Omega_m, \quad m = L, R, \quad (2.133e)$$

where $m = L, R$ indicates the inner or outer annulus. Separable solutions in each annular domain, satisfying the homogeneous Dirichlet conditions at $r = r_a$ and $r = r_b$, take the form

$$T_L(r, \theta, t) = C_L e^{-s^2 t} Q_L(r) \sin(\nu \theta), \quad r_a < r < r_I, \quad (2.134a)$$

$$T_R(r, \theta, t) = C_R e^{-s^2 t} Q_R(r) \sin(\nu \theta), \quad r_I < r < r_b, \quad (2.134b)$$

for $\nu = 0, 1, 2, \dots$, where

$$Q_L(r) = J_\nu(\beta_L r) Y_\nu(\beta_L r_a) - J_\nu(\beta_L r_a) Y_\nu(\beta_L r), \quad (2.135a)$$

$$Q_R(r) = J_\nu(\beta_R r) Y_\nu(\beta_R r_b) - J_\nu(\beta_R r_b) Y_\nu(\beta_R r). \quad (2.135b)$$

Here, C_L and C_R are constants, J_ν and Y_ν are Bessel functions of the first and second kind, respectively, and β_m is given by

$$\beta_m \stackrel{\text{def}}{=} \rho \frac{s}{D_m}, \quad m = L, R. \quad (2.136)$$

Imposing the interface conditions at $r = r_l$ leads to a homogeneous linear system whose coefficient matrix must be singular for non-trivial solutions to exist. This leads determinant conditions $R(s) = 0$ given by

$$R(s) \stackrel{\text{def}}{=} \sqrt{D_{LR}} Q_R^0(r_l) Q_L(r_l) - K_{LR} Q_L^0(r_l) Q_R(r_l) = 0. \quad (2.137)$$

For each $\nu = 0, 1, 2, \dots$ there are infinitely set of eigenvalues s . For given ν an eigenvalue s satisfying (2.137) is picked, and the coefficients in (2.134) are taken as

$$C_L = \gamma Q_R(r_l), \quad C_R = \gamma Q_L(r_l), \quad (2.138)$$

for some scaling γ . Table 2.6 gives selected eigenvalues and the corresponding coefficients of the exact solution for three choices of thermal parameters. Here C_L is normalized to equal to 1, with other coefficients scaled accordingly.

Table 2.6: Selected eigenvalues s and coefficients for three selected cases on a double-annulus domain.

Concentric Annuli				
Case 1: $D_L = 0.75, K_L = 0.5, D_R = 1, K_R = 1.$				
ν	s	γ	C_L	C_R
0	1.516	12.649	2.148	3.120
Case 2: $D_L = 1, K_L = 1, D_R = 1, K_R = 1.$				
ν	s	γ	C_L	C_R
1	1.636	18.922	3.077	5.587
Case 3: $D_L = 1, K_L = 10, D_R = 10, K_R = 1.$				
ν	s	γ	C_L	C_R
2	1.893	-5.474	1.484	1.787

Numerical simulation are performed on an annulus-annulus domain using an un-iterated

CHAMP time-stepping scheme. The inner radius is chosen to be $r_a = 1$ and the outer radius is chosen to be $r_b = 3$, with the interface located at $r_i = 2$. The double annulus grid is denoted by $G_{da}^{(j)}$, with resolution factor j , $j = 1, 2, 4$, and a target mesh spacing $\Delta s^{(j)} = 1/(5j)$ in both the circumferential and the radial directions. The mapping function is given in (2.126), with parameters chosen to be $\alpha = 1$, $\beta = 2$, $\omega = 2\pi$ for the left grid and $\alpha = 3$, $\beta = 2$, $\omega = 2\pi$ for the right grid. A sample grid for the double-annulus configuration is given in the left of Figure 2.11. Again the exact solution is used for the initial data, along with the past temperature values to start up the multi-step scheme. The scheme is run to a final time $t_{nal} = 0.5$, and the maximum error between the numerical solution and the exact solution is computed at t_{nal} . Table 2.7 provides results of a grid refinement study using various choices of material parameters. Only one sub-iteration is performed at each time step, and computational results show that the error decreases by a factor of 16 when the mesh spacing decreases by a factor of 2, indicating a fourth-order convergence rate for all the cases tested. Solution and error contours for Case 3 using the finest grid $G_{da}^{(4)}$ are plotted at t_{nal} in Figure 2.11.

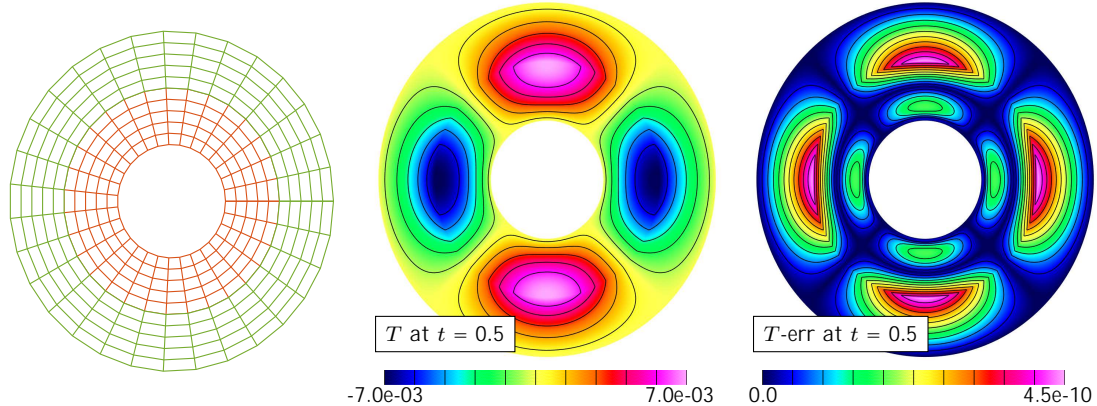


Figure 2.11: Numerical results for the double-annulus problem. Left: a sample computational grid for a double-annulus geometry. Middle: CHAMP4 solution for Case 3 at $t_{nal} = 0.5$ on grid $G_{dr}^{(4)}$. Right: error for Case 3 at $t_{nal} = 0.5$ on the same grid.

2.9.3 Verification Using Manufactured Solutions on Various Geometries

In this section, the accuracy of the un-iterated CHAMP scheme is verified by numerical simulations performed on various geometries. In particular, computations are performed on

Table 2.7: A convergence study for the double-annulus problem using the time-dependent exact solution with selected thermal parameters.

Concentric Annuli									
Case 1: $\nu = 0$, $D_L = 0.75$, $K_L = 0.5$, $D_R = 1$, $K_R = 1$, $t_{\text{nal}} = 0.5$, max-iteration = 1.									
j	Δs	λ_{DL}	max error left	ratio	rate	max error right	ratio	rate	
1	2.00e 01	7.50e 01	1.076e 07			4.599e 08			
2	1.00e 01	1.50e+00	5.725e 09	18.79	4.23	3.033e 09	15.17	3.92	
4	5.00e 02	3.00e+00	3.375e 10	16.96	4.08	2.041e 10	14.85	3.89	
Case 2: $\nu = 1$, $D_L = 1$, $K_L = 1$, $D_R = 1$, $K_R = 1$, $t_{\text{nal}} = 0.5$, max-iteration = 1.									
j	Δs	λ_{DL}	max error left	ratio	rate	max error right	ratio	rate	
1	2.00e 01	1.00e+00	1.695e 07			1.499e 07			
2	1.00e 01	2.00e+00	1.035e 089	16.38	4.03	9.726e 09	15.41	3.95	
4	5.00e 02	4.00e+00	6.617e 10	15.64	3.97	6.390e 10	15.22	3.93	
Case 3: $\nu = 2$, $D_L = 1$, $K_L = 10$, $D_R = 10$, $K_R = 1$, $t_{\text{nal}} = 0.5$, max-iteration = 1.									
j	Δs	λ_{DL}	max error left	ratio	rate	max error right	ratio	rate	
1	2.00e 01	1.00e+00	1.280e 07			1.463e 07			
2	1.00e 01	2.00e+00	7.412e 09	17.27	4.11	8.074e 09	18.12	4.18	
4	5.00e 02	4.00e+00	4.436e 10	16.71	4.06	4.657e 10	17.34	4.12	

curvilinear grids that are non-orthogonal. The grids introduced in Section 2.9.2.1 and 2.9.2.2 that involves rectangle or annulus are orthogonal everywhere, namely the grid lines intersect with each other at a 90-degree angle. This has the effect of eliminating certain terms in the governing equation and interface conditions. For example, the coefficient of the cross derivative terms A_{12}^m and A_{21}^m in (2.101) are zero for orthogonal grids, and B_{12}^m in (2.103) used for the normal derivative in the interface conditions also vanishes. Here the focus is on more complicated geometry so that some or all of the coefficients in the governing equations appear in the simulation. Two simple geometries involving rotated squares and sheared squares are presented in Section 2.9.3.1, and more complicated wavy-domain geometries are presented in Sections 2.9.3.3 and 2.9.3.4.

To verify the accuracy of the CHAMP scheme, the method of manufactured solutions is used. In this method, an exact solution is constructed by adding forcing functions to the governing equations and boundary/interface conditions so that the constructed solution satisfies the forced equations exactly. The error in the discrete solution can be calculated by

subtracting the numerical approximation from the constructed solutions. The trigonometric manufactured solutions used in this section are given by

$$T_m = a_m \sin(f_{m,x}x + \phi_{m,x}) \sin(f_{m,y}y + \phi_{m,y}) \sin(f_{m,t}t), \quad m = L, R, \quad (2.139)$$

for a set of constants $\bar{f}a_m, f_{m,x}, \phi_{m,x}, f_{m,y}, \phi_{m,y}, f_{m,t}g$ to be chosen later. The boundary conditions are chosen to be of Dirichlet type at all domain boundaries. Notice that the values for the CHAMP interface parameters p_L and p_R used in this section are determined by solving the optimization problem described in Section 2.6.2 with thermal properties adjusted based on the problem solved. Note that the values found are not globally optimal as the analysis does not apply exactly for the case of mapped grids. It of interest, then, to test the un-iterated CHAMP scheme with the approximate values for p_L and p_R for various material parameters. Numerical results presented in this section show good agreement with the theory.

2.9.3.1 Rotated Squares

The first example considers two adjacent rotated squares. The manufactured solution for this example is given in (2.139) with constants listed in Table 2.8. The mapping function for the problem domain is given as

$$\mathbf{x} = \mathbf{G}_{\text{dr},r}(\mathbf{r}) = \begin{bmatrix} \cos(\theta_0)(r_1 + \beta_0) & \sin(\theta_0)r_2 \\ \sin(\theta_0)(r_1 + \beta_0) + \cos(\theta_0)r_2 \end{bmatrix}, \quad (2.140)$$

where θ_0 is the angle of rotation, β_0 is a constant and (r_1, r_2) are the coordinates in the computational domain. The grid based on this mapping is denoted by $G_{\text{dr},r}^{(j)}$ with $j = 2, 4, 8$ being a resolution factor. The left plot in Figure 2.12 presents a sample grid with $\theta_0 = \pi/4$, $\beta_0 = 1$ for the left domain, and $\theta_0 = \pi/4$, $\beta_0 = 0$ for the right domain. Numerical simulations are carried out on grids with different resolutions for selected material parameters to a final time $t_{\text{nal}} = 0.2$ using both second-order accurate and fourth-order accurate CHAMP time-stepping schemes. Contour plots of the solution and error at t_{nal} are given in Figure 2.12 for a representative case with $D_L = 1$, $D_R = 1$, $K_L = 1$ and $K_R = 1$.

Figure 2.13 shows the errors as a function of Δs in log-log plots for various cases, and the slopes for each curve agree with their reference lines for second or fourth-order accuracy.

Table 2.8: Constants in manufactured solutions used for rotated-square geometry.

a_L	$f_{L,x}$	$f_{L,y}$	$\phi_{L,x}$	$\phi_{L,y}$	$f_{L,t}$	a_R	$f_{R,x}$	$f_{R,y}$	$\phi_{R,x}$	$\phi_{R,y}$	$f_{R,t}$
0.9	0.5	1.5	1.3	0.8	1	1.1	0.7	1.2	0.2	1.6	1

Table 2.9 lists the computed the maximum errors in the discrete solution at $t = t_{\text{nal}}$ and the corresponding estimated convergence rates for different grid resolutions. Note that as the mesh spacing decreases by a factor of 2, the error at t_{nal} decreases by a factor of 4 or 16, in agreement with the design accuracy of the CHAMP2 and CHAMP4 schemes.

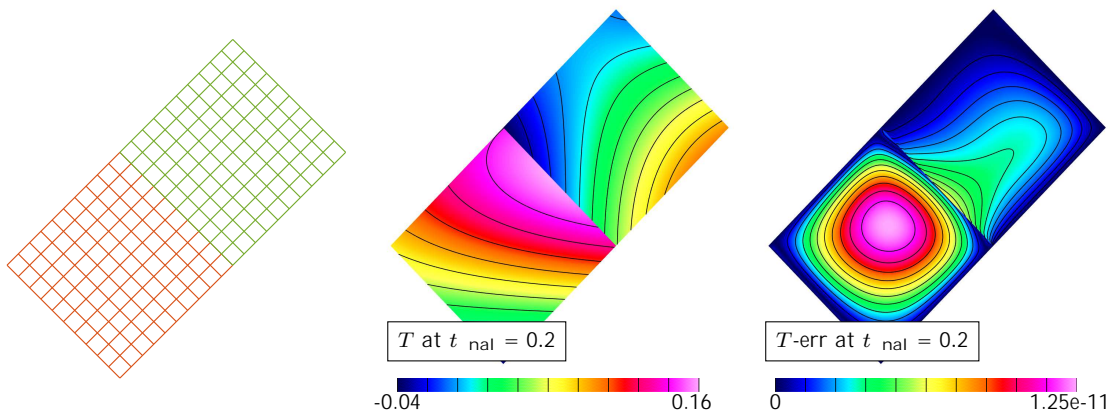


Figure 2.12: Rotated-square results. Left: a sample grid for a rotated-square geometry. Middle: CHAMP4 solution at $t_{\text{nal}} = 0.2$ for Case 1 on grid $G^{(8)}$. Right: error at $t_{\text{nal}} = 0.2$ for Case 1 on the same grid.

2.9.3.2 Sheared Squares

The second example consider two adjacent sheared squares as shown, for example, in Figure 2.14. The mapping function depicting for this problem is

$$\mathbf{x} = \mathbf{G}_{\text{dr},s}(\mathbf{r}) = \begin{bmatrix} r_1 + \beta_0 + \alpha_0 r_2 \\ r_2 \end{bmatrix}, \quad (2.141)$$

where α_0, β_0 are constants to be determined. Here α_0 is chosen to be 1, with $\beta_0 = 1$ for the left domain and $\beta_0 = 0$ for the right domain. The grid for this mapping is $G_{\text{dr},s}^{(j)}$ with

Table 2.9: A convergence study for the un-iterated CHAMP scheme on a rotated-square domain using the trigonometric manufactured solution with various choices of material parameters.

Rotated Squares									
Case 1: $D_L = 1, D_R = 1, K_L = 1, K_R = 1, t_{\text{nal}} = 0.2, \text{max-iteration} = 1.$									
CHAMP2 results									
j	Δs	λ_{DL}	max error left	ratio	rate	max error right	ratio	rate	
2	5.00e 02	2.00e+00	6.529e 06			3.327e 06			
4	2.50e 02	4.00e+00	1.407e 06	4.64	2.21	4.840e 07	6.87	2.78	
8	1.25e 02	8.00e+00	3.305e 07	4.26	2.09	7.671e 08	6.31	2.66	
CHAMP4 results									
j	Δs	λ_{DL}	max error left	ratio	rate	max error right	ratio	rate	
2	5.00e 02	2.00e+00	2.808e 09			3.246e 09			
4	2.50e 02	4.00e+00	1.915e 10	14.67	3.87	1.361e 10	23.85	4.58	
8	1.25e 02	8.00e+00	1.248e 11	15.34	3.94	6.334e 12	21.49	4.43	
Case 2: $D_L = 0.5, D_R = 10.3, K_L = 7.6, K_R = 0.2, t_{\text{nal}} = 0.2, \text{max-iteration} = 1.$									
CHAMP2 results									
j	Δs	λ_{DL}	max error left	ratio	rate	max error right	ratio	rate	
2	5.00e 02	1.00e+00	1.897e 05			1.471e 05			
4	2.50e 02	2.00e+00	4.754e 06	3.99	2.00	4.225e 06	3.48	1.80	
8	1.25e 02	4.00e+00	1.189e 06	4.00	2.00	1.123e 07	3.76	1.91	
CHAMP4 results									
j	Δs	λ_{DL}	max error left	ratio	rate	max error right	ratio	rate	
2	5.00e 02	1.00e+00	8.538e 09			1.043e 08			
4	2.50e 02	2.00e+00	5.479e 10	15.58	3.96	6.103e 10	17.09	4.10	
8	1.25e 02	4.00e+00	3.454e 11	15.86	3.99	3.65e 11	16.70	4.06	

resolution factor j chosen to be $j = 2, 4, 8$. Parameters for the manufactured solution is given in Table 2.10. Simulations are performed for two sets of material parameters given by $D_L = 1, D_R = 1, K_L = 1$ and $K_R = 1$ for Case 1 and $D_L = 1, D_R = 10, K_L = 10$ and $K_R = 1$ for Case 2. Both cases are run to a final time $t_{\text{nal}} = 0.2$. The maximum errors at t_{nal} for each grid resolution and the corresponding convergence rates are presented in Table 2.11. The ratio between the computed errors for nearby resolutions are approximately equal to 16, which indicates a fourth-order convergence rate. Contour plots of the solution

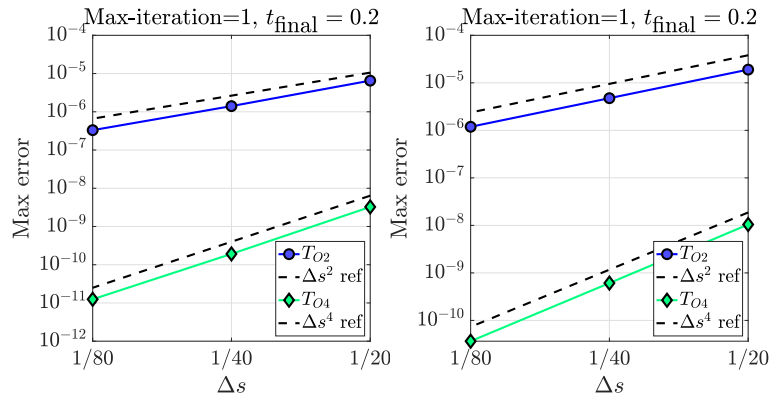


Figure 2.13: Convergence plots for rotated-square geometry. Left: max-norm errors for Case 1 at $t_{\text{nal}} = 0.2$ using CHAMP2 and CHAMP4 schemes. Right: max-norm errors for Case 2 at $t_{\text{nal}} = 0.2$ using CHAMP2 and CHAMP4 schemes.

and error at t_{nal} for Case 1 are shown in Figure 2.14. Convergence plots showing errors as a function of mesh spacing Δs are presented in Figure 2.15. Again the slopes for each curve agrees with their reference lines, which confirms second-order accuracy for CHAMP2 or fourth-order accuracy for CHAMP4.

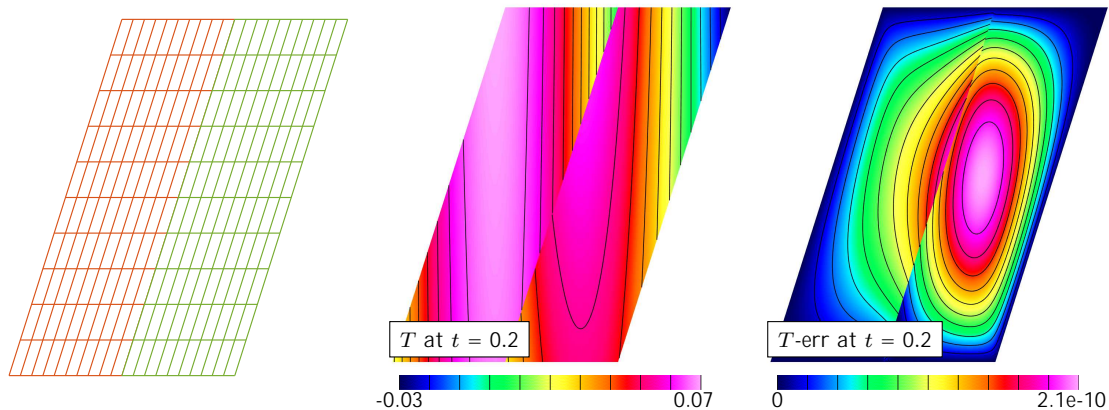


Figure 2.14: Sheared-square results. Left: a sample grid for a stretched-square geometry. Middle: CHAMP4 solution at $t_{\text{nal}} = 0.2$ for Case 1 on grid $G^{(8)}$. Right: error at $t_{\text{nal}} = 0.2$ for Case 1 on the same grid.

Table 2.10: Constants in manufactured solutions used for sheared-square geometry.

a_L	$f_{L,x}$	$f_{L,y}$	$\phi_{L,x}$	$\phi_{L,y}$	$f_{L,t}$	a_R	$f_{R,x}$	$f_{R,y}$	$\phi_{R,x}$	$\phi_{R,y}$	$f_{R,t}$
0.5	1.4	0.1	1.7	1.1	0.8	0.6	1.6	0.2	0.5	0.6	0.8

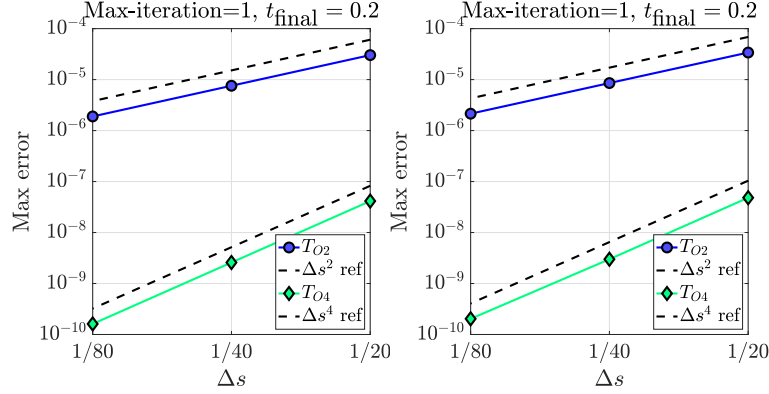


Figure 2.15: Convergence plots for sheared-square geometry. Left: max-norm errors for Case 1 at $t_{\text{nal}} = 0.2$ using CHAMP2 and CHAMP4 schemes. Right: max-norm errors for Case 2 at $t_{\text{nal}} = 0.2$ using CHAMP2 and CHAMP4 schemes.

2.9.3.3 Wavy Geometry with Orthogonal Grid at the Interface

The next problem geometry is a wavy domain consisting of curved boundaries defined by cosine functions. The mapping function is given as

$$\mathbf{x} = \mathbf{G}_{\text{dw,c}}(\mathbf{r}) = (1 - r_2)\mathbf{C}_{\text{top}}(r_1) + r_2\mathbf{C}_{\text{bot}}(r_1) \quad (2.142)$$

where

$$\mathbf{C}_{\text{top}}(r_1) = \begin{bmatrix} r_1 + b_1 \\ a_1 \cos(\delta_0 \pi (r_1 + b_1)) \quad a_1 \end{bmatrix}, \quad (2.143a)$$

$$\mathbf{C}_{\text{bot}}(r_1) = \begin{bmatrix} 2(r_1 + b_1) \\ a_2 \cos(\delta_0 \pi (r_1 + b_1)) + 1 \quad a_2 \end{bmatrix}. \quad (2.143b)$$

The mapping involves constants a_1 , a_2 , b_1 and δ_0 as yet to be specified. Note that the grid lines at the interface are still orthogonal to each other for this particular mapping function. A sample curvilinear grid is illustrated in the left plot of Figure 2.16, with $a_1 = 0.1$, $a_2 = 0.1$,

Table 2.11: A convergence study for the un-iterated CHAMP scheme on a stretched-square domain using the trigonometric manufactured solution with various choices of material parameters.

Stretched Squares									
Case 1: $D_L = 1, D_R = 1, K_L = 1, K_R = 1, t_{\text{nal}} = 0.2, \text{max-iteration} = 1.$									
CHAMP2 results									
j	Δs	λ_{DL}	max error left	ratio	rate	max error right	ratio	rate	
2	5.00e 02	2.00e+00	3.022e 05			2.938e 05			
4	2.50e 02	4.00e+00	7.570e 06	3.99	2.00	7.570e 06	3.94	1.98	
8	1.25e 02	8.00e+00	1.893e 06	4.00	2.00	1.879e 06	3.97	1.99	
CHAMP4 results									
j	Δs	λ_{DL}	max error left	ratio	rate	max error right	ratio	rate	
2	5.00e 02	2.00e+00	3.491e 08			4.138e 08			
4	2.50e 02	4.00e+00	2.214e 09	15.77	3.98	2.581e 09	16.03	4.00	
8	1.25e 02	8.00e+00	1.392e 10	15.90	3.99	1.611e 10	16.01	4.00	
Case 2: $D_L = 1, D_R = 10, K_L = 10, K_R = 1, t_{\text{nal}} = 0.2, \text{max-iteration} = 1.$									
CHAMP2 results									
j	Δs	λ_{DL}	max error left	ratio	rate	max error right	ratio	rate	
2	5.00e 02	2.00e+00	3.292e 05			3.393e 05			
4	2.50e 02	4.00e+00	8.183e 06	4.02	2.01	8.549e 06	3.97	1.99	
8	1.25e 02	8.00e+00	2.038e 06	4.01	2.01	2.144e 06	3.99	2.00	
CHAMP4 results									
j	Δs	λ_{DL}	max error left	ratio	rate	max error right	ratio	rate	
2	5.00e 02	2.00e+00	4.817e 08			4.707e 07			
4	2.50e 02	4.00e+00	2.948e 09	16.34	4.03	2.995e 09	15.72	3.97	
8	1.25e 02	8.00e+00	1.820e 10	16.20	4.02	2.029e 10	14.76	3.88	

$b_1 = 1, \delta_0 = 1$ for the left domain and $a_1 = 0.1, a_2 = 0.1, b_1 = 0, \delta_0 = 1$ for the right domain. The grid based on this mapping is denoted by $G_{\text{dw,c}}^{(j)}$ with the resolution factor j chosen to be $j = 2, 4, 8$. Parameters in manufactured solutions are given in Table 2.12. The CHAMP schemes are tested with various material parameters, and the results are presented in Table 2.13. Convergence plots for different cases are presented in Figure 2.17. Contours of the solution and the corresponding max-norm error for the case $D_L = 1, D_R = 10, K_L = 10, K_R = 1$ at $t_{\text{nal}} = 2$ are plotted in Figure 2.16. The grid refinement study shows that the

Table 2.12: Constants in manufactured solutions used for wiggled geometry.

a_L	$f_{L,x}$	$f_{L,y}$	$\phi_{L,x}$	$\phi_{L,y}$	$f_{L,t}$	a_R	$f_{R,x}$	$f_{R,y}$	$\phi_{R,x}$	$\phi_{R,y}$	$f_{R,t}$
0.9	0.5	0.1	0	0	0.8	0.8	0.6	0.2	0	0	0.8

CHAMP2 and CHAMP4 schemes, both using one sub-iteration, are stable and accurate for given choices of material parameters.

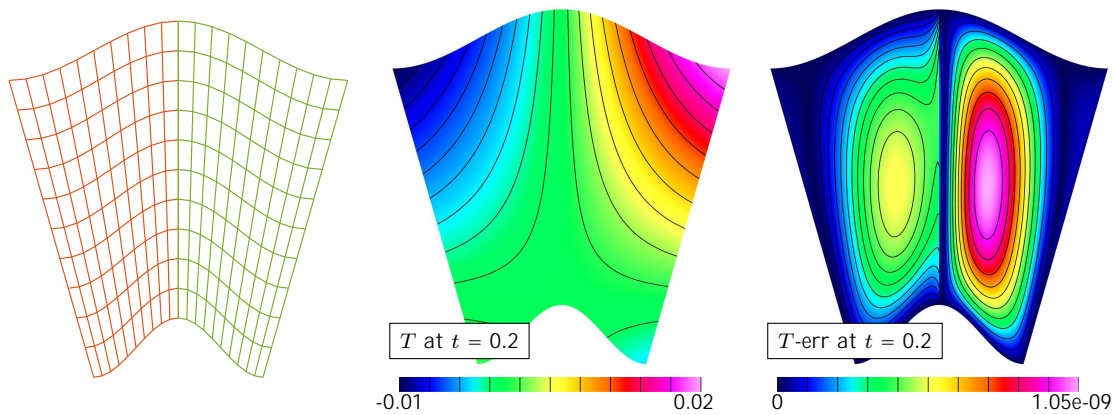


Figure 2.16: Curvilinear-grid results. Left: a sample grid for a wiggled-cos geometry. Middle: CHAMP4 solution at $t_{\text{nal}} = 0.2$ for Case 2 on grid $G^{(8)}$. Right: error at $t_{\text{nal}} = 0.2$ for Case 2 on the same grid.

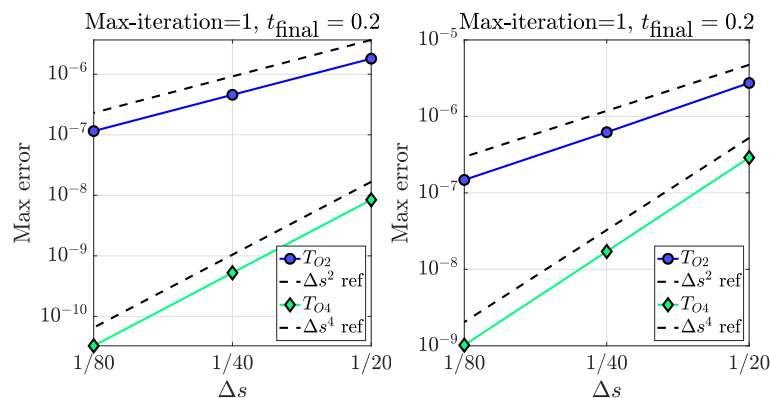


Figure 2.17: Convergence plots for wiggled-cos geometry. Left: max-norm errors for Case 1 at $t_{\text{nal}} = 0.2$ using CHAMP2 and CHAMP4 schemes. Right: max-norm errors for Case 2 at $t_{\text{nal}} = 0.2$ using CHAMP2 and CHAMP4 schemes.

Table 2.13: A convergence study for the un-iterated CHAMP scheme on a wiggled-cos domain using the trigonometric manufactured solution with various choices of material parameters.

Wiggled Cos									
Case 1: $D_L = 1$, $D_R = 1$, $K_L = 1$, $K_R = 1$, $t_{\text{nal}} = 0.2$, max-iteration = 1.									
CHAMP2 results									
j	Δs	λ_{DL}	max error left	ratio	rate	max error right	ratio	rate	
2	5.00e 02	2.00e+00	8.273e 07			1.806e 06			
4	2.50e 02	4.00e+00	2.133e 07	3.88	1.96	4.575e 07	3.95	1.98	
8	1.25e 02	8.00e+00	5.421e 08	3.93	1.98	1.151e 07	3.97	1.99	
CHAMP4 results									
j	Δs	λ_{DL}	max error left	ratio	rate	max error right	ratio	rate	
2	5.00e 02	2.00e+00	5.845e 09			8.421e 09			
4	2.50e 02	4.00e+00	2.715e 10	21.53	4.43	5.249e 10	16.04	4.00	
8	1.25e 02	8.00e+00	1.661e 11	16.35	4.03	3.268e 11	16.06	4.01	
Case 2: $D_L = 0.7$, $D_R = 2.9$, $K_L = 0.8$, $K_R = 1.6$, $t_{\text{nal}} = 0.2$, max-iteration = 1.									
CHAMP2 results									
j	Δs	λ_{DL}	max error left	ratio	rate	max error right	ratio	rate	
2	5.00e 02	1.40e+00	1.112e 06			2.735e 06			
4	2.50e 02	2.80e+00	4.077e 07	2.73	1.45	6.210e 07	4.40	2.14	
8	1.25e 02	5.60e+00	1.186e 07	3.44	1.78	1.478e 07	4.20	2.07	
CHAMP4 results									
j	Δs	λ_{DL}	max error left	ratio	rate	max error right	ratio	rate	
2	5.00e 02	1.40e+00	1.381e 07			2.893e 07			
4	2.50e 02	2.80e+00	1.209e 08	11.42	3.51	1.713e 08	16.89	4.08	
8	1.25e 02	5.60e+00	8.606e 10	14.04	3.81	1.021e 09	16.78	4.07	

2.9.3.4 Wavy Geometry with Non-Orthogonal Grid at the Interface

The last example in this section considers a completely non-orthogonal grid, with the curved boundaries in the domain defined by sine functions. The mapping function for this case is given by

$$\mathbf{x} = \mathbf{G}_{\text{dw},s}(\mathbf{r}) = (1 - r_2)\mathbf{C}_{\text{top}}(r_1) + r_2\mathbf{C}_{\text{bot}}(r_1) \quad (2.144)$$

with $\mathbf{r} = [r_1, r_2]^T$ and

$$\mathbf{C}_{\text{top}} = \begin{cases} x_1 = (r_1 + b_1) \\ x_2 = a_1 \sin(\delta_0 \pi (r_1 + b_1)) \end{cases} \quad a_1, \quad (2.145a)$$

$$\mathbf{C}_{\text{bot}} = \begin{cases} x_1 = 2(r_1 + b_1) \\ x_2 = a_2 \sin(2\delta_0 \pi (r_1 + b_1)) + 1 \end{cases} \quad a_2, \quad (2.145b)$$

and a_1, a_2, b_1 and δ_0 are constants to be determined. The grid corresponding to this particular mapping function is denoted by $G_{\text{dw},s}^{(j)}$, with $j = 2, 4, 8$ as before. A sample curvilinear grid is illustrated in Figure 2.18, with the parameters chosen to be $a_1 = 0.1, a_2 = 0.1, b_1 = 1, \delta_0 = 1$ for the left domain and $a_1 = 0.1, a_2 = 0.1, b_1 = 0, \delta_0 = 1$ for the right domain. Manufactured solutions given in (2.139) are used with parameters chosen in Table 2.12. The un-iterated CHAMP scheme is tested with two choices of material parameters. Solutions and error at $t_{\text{nal}} = 0.2$ for a selected case are plotted in Figure 2.18. The max-error and the convergence rate are computed at t_{nal} are listed in Table 2.14, and the results of the grid convergence studies are presented in Figure 2.19. The results again show second-order and fourth-order convergence for the CHAMP2 and CHAMP4 schemes, respectively.

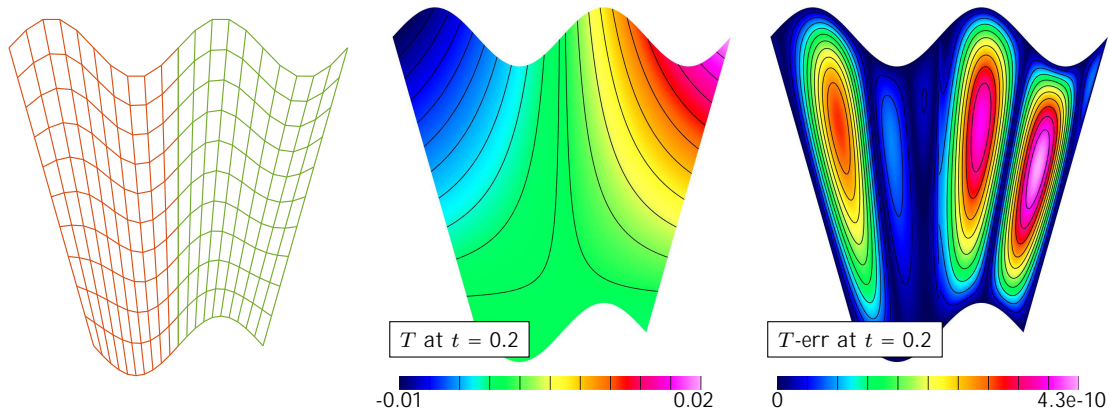


Figure 2.18: Curvilinear-grid results. Left: a sample grid for a wiggled-sin geometry. Middle: CHAMP4 solution at $t_{\text{nal}} = 0.2$ for Case 1 on grid $G^{(8)}$. Right: error at $t_{\text{nal}} = 0.2$ for Case 1 on the same grid.

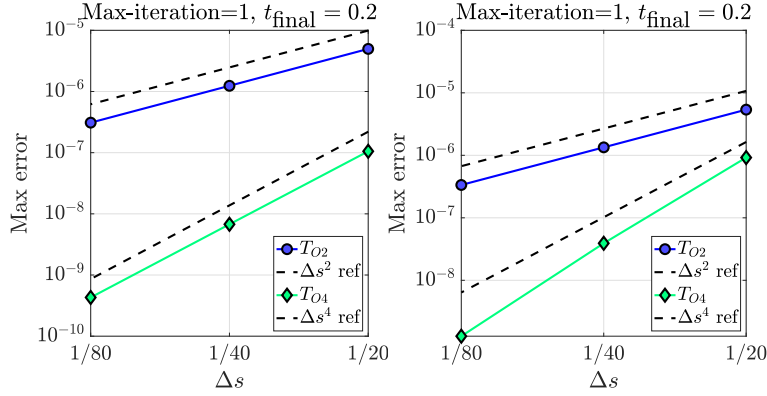


Figure 2.19: Convergence plots for wiggled-sin geometry. Left: max-norm errors for Case 1 at $t_{\text{nal}} = 0.2$ using CHAMP2 and CHAMP4 schemes. Right: max-norm errors for Case 2 at $t_{\text{nal}} = 0.2$ using CHAMP2 and CHAMP4 schemes.

2.9.4 Large Time-Step Study for Adaptive CHAMP Algorithm

In this section, the CHAMP scheme is tested for a time-dependent CHT problem when a large λ_{DL} is selected. The primary interest is to investigate the number of sub-iterations needed for the CHAMP scheme when a large time-step is taken. As an illustrating example, Table 2.15 provides results from a grid refinement study for a time-dependent CHT problem on a domain consisting of two curved domains. The mapping function is given in (2.142) and (2.143) with the material parameters chosen to be $a_1 = 0.1$, $a_2 = 0.1$, $b_1 = 1$, $\delta_0 = 1$ for the left domain and $a_1 = 0.1$, $a_2 = 0.1$, $b_1 = 0$, $\delta_0 = 1$ for the right domain. The manufactured solution used here is a simple trigonometric function given by

$$T(x, y, t) = \sin(x) \sin(y) \sin(t), \quad (2.146)$$

for both the left and right domain. The scheme is run with either one or no sub-iterations, and the maximal error at $t_{\text{nal}} = 10$ is calculated. When λ_{DL} is small, the un-iterated CHAMP time-stepping scheme is stable and fourth-order accurate for the chosen parameters. However, when λ_{DL} gets larger, the scheme becomes less accurate and the solution eventually blows up. By taking another sub-iteration at each time-step, the discrete errors in the solution settle down and the CHAMP scheme, with one sub-iteration, remains stable and fourth-order accurate to t_{nal} .

An adaptive algorithm was introduced in Section 2.8, and it is of interest to test this algorithm for a time-dependent version of the problem considered in Section 2.9.1 when a

Table 2.14: A convergence study for the un-iterated CHAMP scheme on a wiggled-sin domain using the trigonometric manufactured solution with various choices of material parameters.

Wiggled Sin									
Case 1: $D_L = 1$, $D_R = 1$, $K_L = 1$, $K_R = 1$, $t_{\text{nal}} = 0.2$, max-iteration = 1.									
CHAMP2 results									
j	Δs	λ_{DL}	max error left	ratio	rate	max error right	ratio	rate	
2	5.00e 02	2.00e+00	4.549e 06			4.971e 06			
4	2.50e 02	4.00e+00	1.150e 06	3.96	1.98	1.239e 06	4.01	2.00	
8	1.25e 02	8.00e+00	2.876e 07	4.00	2.00	3.095e 07	4.00	2.00	
CHAMP4 results									
j	Δs	λ_{DL}	max error left	ratio	rate	max error right	ratio	rate	
2	5.00e 02	2.00e+00	9.352e 08			1.053e 07			
4	2.50e 02	4.00e+00	5.976e 09	15.65	3.97	6.748e 09	15.60	3.96	
8	1.25e 02	8.00e+00	3.779e 10	15.81	3.98	4.297e 10	15.70	3.97	
Case 2: $D_L = 0.7$, $D_R = 2.9$, $K_L = 0.8$, $K_R = 1.6$, $t_{\text{nal}} = 0.2$, max-iteration = 1.									
CHAMP2 results									
j	Δs	λ_{DL}	max error left	ratio	rate	max error right	ratio	rate	
2	5.00e 02	1.40e+00	4.126e 06			5.380e 06			
4	2.50e 02	2.80e+00	1.045e 06	3.95	1.98	1.341e 06	4.01	2.00	
8	1.25e 02	5.60e+00	2.614e 07	4.00	2.00	3.352e 07	4.00	2.00	
CHAMP4 results									
j	Δs	λ_{DL}	max error left	ratio	rate	max error right	ratio	rate	
2	5.00e 02	1.40e+00	2.262e 07			9.198e 07			
4	2.50e 02	2.80e+00	1.146e 08	19.75	4.30	3.912e 08	23.51	4.56	
8	1.25e 02	5.60e+00	3.848e 10	29.77	4.90	1.276e 09	3.066	4.94	

large λ_{DL} is taken. A constant initial state is given in (2.121), with the boundary data chosen to be $T_{x_a}^L = 0.6$ and $T_{x_b}^R = 5.8$. The scheme is run using different values of λ_{DL} and for a fixed number of time steps, taken to be 100. This number is sufficient for the solution to be considered at steady state. Different tolerances are picked for the stopping criterion in the adaptive algorithm, and the average number of sub-iterations taken is determined after reaching the final time step. The optimal weighting parameters for each case is determined by solving the optimization problem described in Section 2.6.2. Plots of λ_{DL} as a function

Table 2.15: A convergence study for the CHAMP scheme on a curvilinear domain using one or two sub-iterations.

Cosine								
CHAMP4 results: $D_L = 1$, $D_R = 10$, $K_L = 10$, $K_R = 1$, $t_{\text{nal}} = 10$.								
			Un-iterated, max-iteration = 1			max-iteration = 2.		
j	Δs	λ_{DL}	max error	ratio	rate	max error	ratio	rate
1	1.00e 01	5.00e+02	4.253e 04			1.397e 04		
2	5.00e 02	1.00e+03	2.472e 05	17.21	4.10	9.521e 06	14.67	3.87
4	2.50e 02	2.00e+03	unstable	-	-	5.887e 07	16.17	4.02

of the average number of sub-iterations are presented in the left plot of Figure 2.20 for both the second-order and fourth-order adaptive CHAMP scheme. Note that since the schemes are run with a fixed number of time-steps, the final time is smaller when λ_{DL} is smaller. The average number of sub-iterations for small λ_{DL} would be close to 1 if the scheme is allowed to run longer. Also notice that as the tolerance decreases, the average number of sub-iterations for different λ_{DL} increases. Since the adaptive algorithm is based on how well the residuals of the interface conditions match at each iteration, when the tolerance in the adaptive scheme becomes stricter, more sub-iterations are required to meet the stopping criterion.

Another observation is that, even for λ_{DL} of magnitude $1e+8$, the fourth-order accurate CHAMP scheme only requires approximately 1.8 sub-iterations for the scheme to converge to a tolerance less than $1e-7$. This means that without the adaptive algorithm, for large λ_{DL} , one can pick $N_{\text{si}} = 2$ at each time-step to get a stable results for the fourth-order accurate CHAMP scheme. The resulting curve also shows that the fourth-order CHAMP scheme is more sensitive to the size of the time-step than the second order scheme. The right figure of Figure 2.20 presents plots of optimal weighting parameters p_L and p_R as a function of λ_{DL} . Both values decreases as λ_{DL} gets larger, which agrees with the theory.

Note that the results here have considered one problem, and they may not necessarily carry over to other more complicated cases. Nevertheless, the results here give some good insight about the capability of the CHAMP scheme, and the adaptive algorithm will be used in the next section.

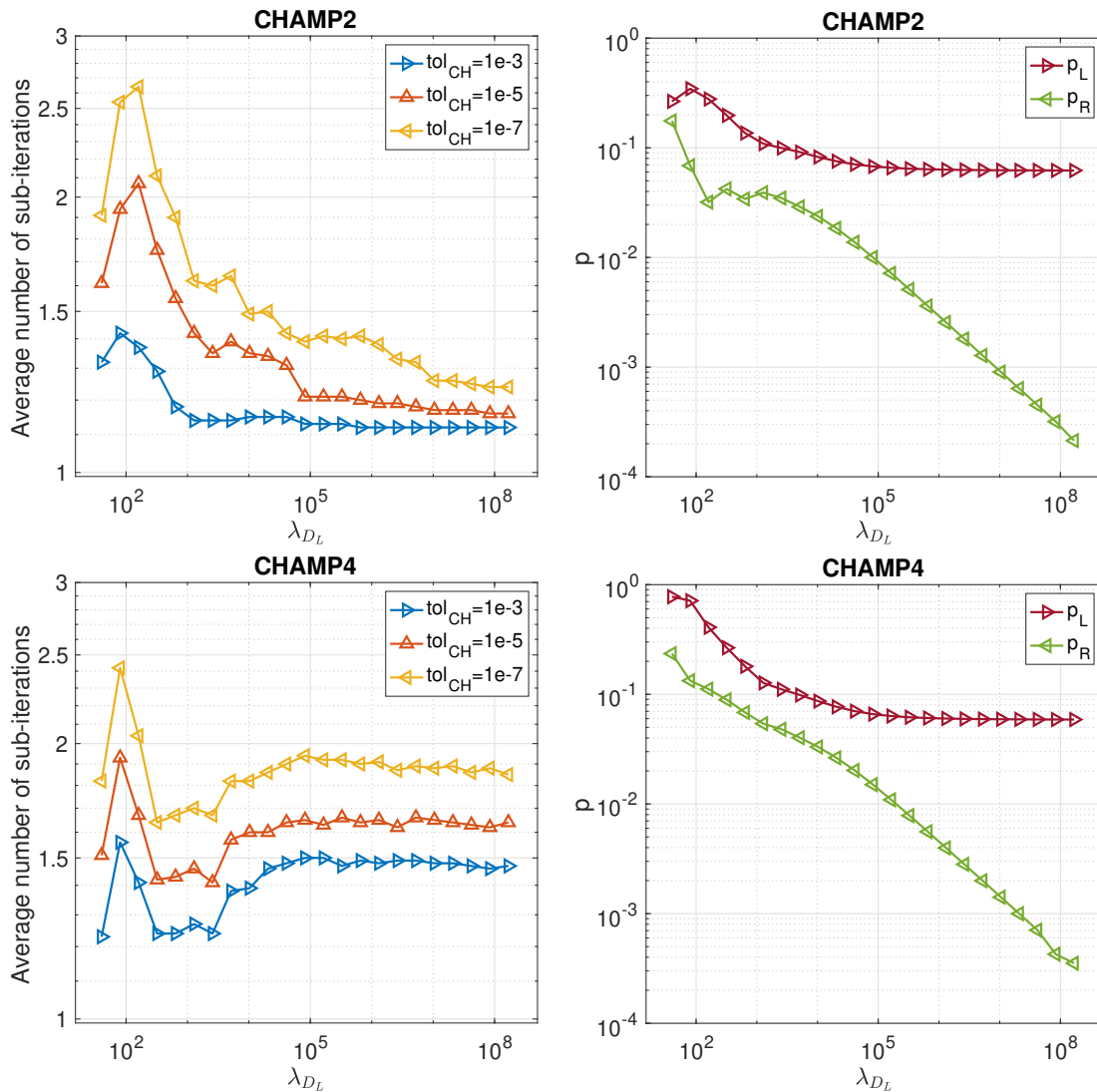


Figure 2.20: Adaptive CHAMP algorithm. Left: average number of sub-iterations as a function of λ_{DL} for different CHAMP tolerance. Right: optimal weighting parameters p_L and p_R for different λ_{DL} .

2.9.5 Four-Disks-in-a-Square Geometry

The un-iterated CHAMP time-stepping algorithm described in Section 2.4 is implemented here on a multi-domain CHT problem, with a geometry configuration consisting of four solid disks embedded in a square. As illustrated in the left of Figure 2.21, the four-disk geometry consists of five subdomains, which are denoted by Ω_m , $m = 1, 2, 3, 4, 5$. The interfaces between various sub-domains are labeled as $l_{1,5}$, $l_{2,5}$, $l_{3,5}$ and $l_{4,5}$, respectively. The composite grid for this geometry, denoted by $G_d^{(j)}$, consist of a total of thirteen compo-

ment grids, each with grid spacing chosen to approximately equal $\Delta s^{(j)} = 1/(40j)$. A large background Cartesian grid covers the region $[-1.5, 1.5]^2$ exterior to the disks, while smaller Cartesian grids cover the interior of each disk. The disks have a radius of $r_c = 0.4$, and the centers of the disks are separated by a distance of 1.2. Annular grids lie adjacent to the inside and outside of the four circular interfaces. A coarse version of the composite grid used here is presented in the middle of Figure 2.21, and an enlarged view of the component grids is shown in the right of Figure 2.21.

Table 2.16: Material coefficients and coupling parameters used for the four-disks-in-a-box problem.

Four disks in a box.				
domain	D	K	p_L	p_R
disk 1	1.4	0.2	1.37e-01	1.79e-01
disk 2	1.5	0.1	8.12e-02	3.13e-01
disk 3	1.2	0.4	7.20e-02	3.29e-01
disk 4	1.3	0.3	5.34e-02	3.73e-01
outer square 5	1.0	0.5		

The exact solution used in the problem is the trigonometric manufactured solution, given by

$$T_m = \cos(f_x x) \cos(f_y y) \cos(f_t t), \quad (2.147)$$

with $f_x = f_y = f_t = 2\pi$ for $m = 1, 2, 3, 4, 5$. The material coefficients and the coupling parameters p_L, p_R used for each subdomain are given in Table 2.16. Solutions are computed using $\Delta t = 0.01$ to a final time $t_{\text{nal}} = 0.5$ using the second and fourth-order accurate schemes, and the un-iterated CHAMP time-stepping algorithm is implemented. Here the optimal weighting parameters are chosen using the methods described in Section 2.6.2. The maximum error at each grid resolution and the estimated convergence rate computed at t_{nal} are shown in Table 2.17. A contour plot of solution at $t_{\text{nal}} = 0.5$ is presented in the middle of Figure 2.22, with the plot on the right showing the error at $t_{\text{nal}} = 0.5$. The maximum error as a function of grid spacing Δs in a log-log plot is shown in the left of Figure 2.22, and the slope of the curves agree with the second or fourth-order reference lines.

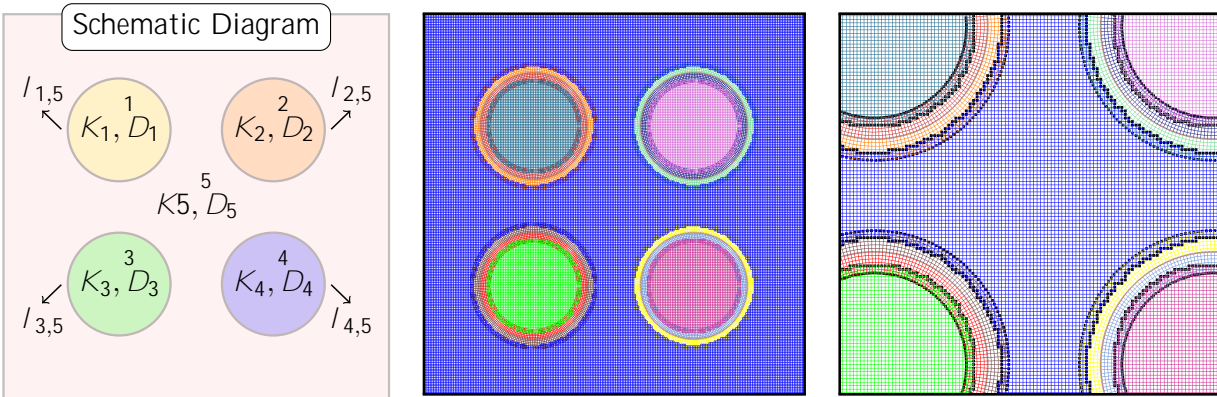


Figure 2.21: Four disks in a box. Left: a schematic diagram showing five sub-domains. Middle: a sample overset grid used for the calculations. Right: amplified grid showing different components of the overset grid.

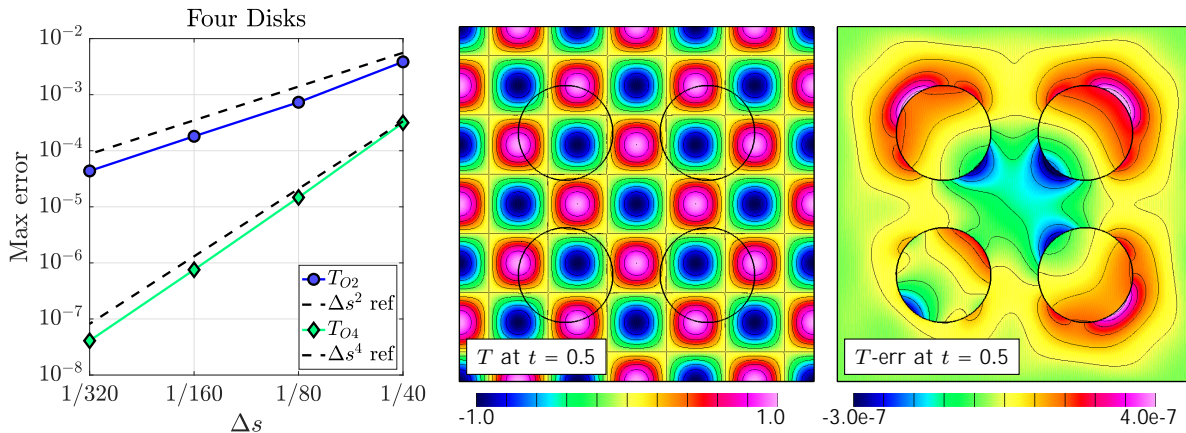


Figure 2.22: Four disks in a box results. Left: max-norm errors at $t_{\text{nal}} = 0.5$ using CHAMP2 and CHAMP4 scheme. Middle: CHAMP4 solution at $t_{\text{nal}} = 0.5$ on grid $G^{(4)}$. Right: error at $t_{\text{nal}} = 0.5$ on the same grid.

2.10 Conclusions

A high-order accurate partitioned algorithm for solving coupled conjugate heat transfer problems with the diffusion equation is developed. A simplified model problem involving two rectangular sub-domain with a vertical interface is constructed. The governing equations are the diffusion equation with the usual interface matching conditions involving continuity of temperature and heat flux, together with the boundary and initial conditions. The new CHAMP interface condition is considered to be of mixed type, with a weighted combination of a generalized Dirichlet condition and a generalized Neumann condition. These conditions are derived based on a Taylor series expansion of the temperature and heat flux in each

Table 2.17: A convergence study for a multi-domain problem using the adaptive CHAMP algorithm.

Four disks in a box.							
		CHAMP2 results			CHAMP4 results		
j	Δs	max error	ratio	rate	max error	ratio	rate
1	2.50e 02	3.85e 03			3.16e 04		
2	1.25e 02	7.32e 04	5.26	2.29	1.47e 05	21.50	4.64
4	6.25e 03	1.81e 04	4.04	2.01	7.54e 07	19.50	4.42
8	3.13e 03	4.36e 06	4.15	2.04	4.09e 08	18.44	4.29

subdomain, and an effective domain overlap is included by expanding the solution at a distance equal to the overlap width about the interface. Additional compatibility conditions are derived using the original interface conditions and governing equations. These conditions, together with the usual matching conditions are used to replace terms in the Taylor series expansion to form the CHAMP Dirichlet and Neumann operator. These operators are combined together using the weighting parameters to form the new CHAMP conditions. Detailed analysis are given to show the convergence of the CHAMP sub-time step iterations, and the exact form of the iteration amplification factor is also provided. The weighting parameters can be determined by solving a min-max problem derived from the iteration amplification factor following the optimized Schwarz approach. When no sub-iteration is taken, the so-called un-iterated time-stepping scheme is proved to be stable and accurate with a p th-order accurate CHAMP condition. For the case when a large time step is taken, a new adaptive variable sub-iteration CHAMP algorithm is developed, where the number of sub-iteration is chosen based on a measure of the convergence of the CHAMP conditions at each time step. For solution that reaches steady state, the fourth-order accurate adaptive algorithm only require approximately two sub-iterations for very large time-steps. Finally, spatial and temporal accuracy of the un-iterated time-stepping scheme is verified by numerical simulations to problems with different material coefficients on various geometries. The new algorithm is proved to be stable and accurate without sub-time step iteration for a wide range of material parameters.

CHAPTER 3

HIGH-ORDER ACCURATE PARTITIONED SCHEMES FOR CONJUGATE HEAT TRANSFER WITH ADVECTION-DIFFUSION EQUATIONS

3.1 A Brief Introduction

In this chapter, a high-order accurate partitioned scheme for solving conjugate heat transfer problems with advection-diffusion equations is developed. The derivation of the CHAMP coupling conditions follows similar lines of logic to the presentation in [75], although with significant modifications necessitated by the inclusion of the advection terms and extension to higher order.

The remainder of this chapter is organized as follows. In Section 3.2 the model problem and governing equations are introduced. In Section 3.3 a general approach to derive a p^{th} -order accurate CHAMP condition is presented. A brief description of the interface discretization and a complete CHT algorithm for the model problem are given in Section 3.4. In Section 3.5.1 the CHAMP sub-time step iteration is analyzed according to the Godunov–Ryabenkii theory normal-mode analysis. A sufficient condition for the second-order accurate CHAMP iteration to converge is derived in Section 3.5.2. In Section 3.5.3, the stability of the uniterated CHAMP time-stepping scheme is studied. In Section 3.6 the method is applied to curvilinear domains. Results from numerical simulations are presented in Section 3.7 and some concluding remarks are given in Section 3.8.

3.2 Governing Equations and Model Problem

Consider the solution to a CHT problem on a physical domain Ω which is a disjoint union of sub-domains Ω_m for $m = 1, 2, \dots, N_m$, each representing a region occupied by a given material. An example is depicted in Figure 3.1. The initial-boundary-value-problem

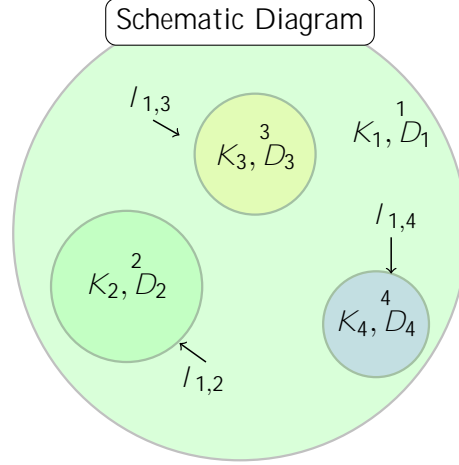


Figure 3.1: An example of a conjugate heat transfer problem. The entire domain consists of four sub-regions, one large disk with material properties (K_1, D_1) and three smaller disks with material properties (K_2, D_2) , (K_3, D_3) and (K_4, D_4) respectively. The interfaces between various domains are labeled with $l_{1,2}$, $l_{1,3}$, $l_{1,4}$.

for the temperature $T = T(\mathbf{x}, t)$ is

$$\partial_t(\rho CT) + r \cdot (\rho CT \mathbf{u}) = r \cdot (KrT) + f(\mathbf{x}, t), \quad \mathbf{x} \in \Omega, \quad (3.1a)$$

$$BT = g(\mathbf{x}, t), \quad \mathbf{x} \in \partial\Omega, \quad (3.1b)$$

$$[T]_I = 0, \quad \mathbf{x} \in I, \quad (3.1c)$$

$$[(K\partial_n T - \rho CT \mathbf{n} \cdot \mathbf{u})]_I = 0, \quad \mathbf{x} \in I, \quad (3.1d)$$

$$T(\mathbf{x}, 0) = T^{\text{IC}}(\mathbf{x}), \quad \mathbf{x} \in \Omega, \quad (3.1e)$$

where $\rho = \rho(\mathbf{x})$ is the density, $C = C(\mathbf{x})$ is the specific heat at constant pressure, $K = K(\mathbf{x})$ is the thermal conductivity, and $\mathbf{u} = \mathbf{u}(\mathbf{x}, t)$ is the advection velocity. Equations (3.1c) and (3.1d) denote the interface matching conditions where \mathbf{n} denotes the unit normal that points in the direction from domain m_1 to domain m_2 , and $\partial_n = \mathbf{n} \cdot \nabla$ denotes the normal derivative. The operator B in (3.1b) is the boundary condition operator on physical boundaries (e.g. Dirichlet, Neumann or Robin), while $T^{\text{IC}}(\mathbf{x})$ is the initial condition. Equation (3.1d) is derived from the conservation form of the advection-diffusion equation, which includes an additional advective heat flux term to ensure the total heat flux is conserved at the interface. Note that the heat equation in (3.1a) includes a forcing function (a given heat source)

denoted by $f(\mathbf{x}, t)$. It is also possible to include forcing functions in the interface matching conditions, as needed, for a chosen heat flow model, but such source terms have not been considered here¹.

For the purposes of this thesis, ρ , C and K are taken to be constants in each sub-domain Ω_m . Furthermore $\mathbf{r} \cdot \mathbf{u} = 0$ is assumed on each sub-domain as the primary interest is in applications involving incompressible flows. Letting T_m and \mathbf{u}_m denote the temperature and velocity restricted to domain Ω_m , then T_m satisfies the advection-diffusion equation

$$\partial_t T_m + \mathbf{u}_m \cdot \nabla T_m = D_m \Delta T + f(\mathbf{x}, t), \quad \mathbf{x} \in \Omega_m, \quad (3.2)$$

where

$$D_m \stackrel{\text{def}}{=} \frac{K_m}{\rho_m C_m}, \quad (3.3)$$

is the thermal diffusivity.

The CHT problem (3.1) is solved using a partitioned scheme in which the temperature is updated sequentially in each sub-domain using an implicit time-stepping method that is restricted to the sub-domain (see Algorithm 7). Implicit BDF schemes are used, which, at p^{th} -order accuracy, take the form

$$\sum_{j=0}^p \alpha_j T_m^{n+1-j} = \beta_0 W_m(T_m^{n+1}), \quad (3.4)$$

where T_m^n denotes the approximate solution at time t^n and

$$W_m \stackrel{\text{def}}{=} D_m \Delta + \mathbf{u}_m \cdot \nabla, \quad (3.5)$$

denotes the advection-diffusion operator. Constants α_j and β_0 for $p = 2, 4, 6$ are given in Table 2.1; values for other orders of accuracy can be found in [1]. The partitioned scheme requires interface and boundary conditions; the form of these interface conditions is our primary concern. In general, for the scheme to be stable and accurate, sub-iterations may be required to update the solution at each time-step. Let $T_m^{(j)}$ denote the j^{th} iterate for

¹Forcing functions are included later to for the purpose of constructing exact solutions to verify the accuracy of numerical schemes for the system using the method of manufactured solutions.

T_m^{n+1} , $j = 0, 1, 2, \dots$. As derived in Section 3.3, the p^{th} -order accurate CHAMP interface condition between the active domain $m = L$ and $m = R$ takes the form of an optimized Schwarz condition, involving a generalized Neumann operator \mathbf{N}_{LR} and generalized Dirichlet operator \mathbf{D}_{LR} ,

$$\left(\mathbf{N}_{LR} + \mathbf{S}_L \mathbf{D}_{LR}\right) T_L^{(j)}(\mathbf{x}) = \left(\partial_{n,R} + \mathbf{S}_L\right) T_R^{(j-1)}(\mathbf{x} + h_R \mathbf{n}_R), \quad \mathbf{x} \in \Gamma_{LR}. \quad (3.6)$$

Here \mathbf{N}_{LR} and \mathbf{D}_{LR} are differential operators of order p , \mathbf{S}_L is a differential operator that provides a weighted combination of \mathbf{N}_{LR} and \mathbf{D}_{LR} , $\partial_{n,R}$ is the normal derivative to the interface in the direction of the outward normal, \mathbf{n}_R , to the right domain, and h_R represents the grid spacing on domain R , normal to the interface Γ_{LR} . One key ingredient of the CHAMP conditions, indicated in (3.6), is the evaluation of the RHS at a distance h_R from the interface, thus introducing an effective overlap into the interface conditions; non-zero overlaps are well known to improve the convergence of Schwarz iterations.

3.3 Derivation of the CHAMP Operators for a p th-Order Accurate Scheme

In this section, the general form of the CHAMP interface conditions is derived for the model problem given in (3.1). Consider the solution of the IBVP (3.1) on a domain consisting of two adjacent rectangles with a material interface at $x = 0$. The CHAMP Dirichlet and Neumann operators for the advection-diffusion equation are defined in a similar fashion to those for the diffusion equation derived in Section 2.3.3. Define \mathbf{u}^D to be the velocity scaled by the thermal diffusivity,

$$\mathbf{u}_m^D = [u_m^D, v_m^D] \stackrel{\text{def}}{=} \frac{\mathbf{u}_m}{D_m}, \quad m = L, R, \quad (3.7)$$

and write the advection-diffusion equation in terms of the operator H_m and \mathbf{u}_m^D ,

$$\partial_t T_m = H_m T_m \stackrel{\text{def}}{=} D_m (\Delta - (\mathbf{u}_m^D \cdot \nabla)) T_m. \quad (3.8)$$

The compatibility interface conditions are based on time-derivatives of the basic interface conditions (3.1c) and (3.1d),

$$[\partial_t^q T]_I = 0, \quad (3.9a)$$

$$[\partial_t^q (K(\partial_x T - u^D T))]_I = 0, \quad (3.9b)$$

which leads to the following compatibility interface conditions

$$[H^q T]_I = 0, \quad q = 0, 1, 2, \dots, \quad (3.10a)$$

$$\left[K \left\{ \partial_x H^q T - \sum_{j=0}^q \binom{q}{j} (\partial_t^j u^D) H^{q-j} T \right\} \right]_I = 0, \quad q = 0, 1, 2, \dots \quad (3.10b)$$

As for the case of the diffusion equation, (3.10) is used to define x -derivatives of T_R on the interface in terms of x and y -derivatives of T_L ,

$$\partial_x^j T_R(0, y) = L_j^{\text{ad}} T_L(0, y). \quad (3.11)$$

For example, L_j^{ad} for $j = 0, 1, 2, 3$ are

$$L_0^{\text{ad}} \stackrel{\text{def}}{=} I, \quad (3.12a)$$

$$L_1^{\text{ad}} \stackrel{\text{def}}{=} (K_{LR} u_L^D + u_R^D) I + K_{LR} \partial_x, \quad (3.12b)$$

$$\begin{aligned} L_2^{\text{ad}} \stackrel{\text{def}}{=} & (K_{LR} u_L^D u_R^D + (u_R^D)^2) I + (D_{LR} u_L^D + K_{LR} u_R^D) \partial_x \\ & + (D_{LR} v_L^D + v_R^D) \partial_y + D_{LR} \partial_x^2 + (D_{LR} - 1) \partial_y^2, \end{aligned} \quad (3.12c)$$

$$\begin{aligned} L_3^{\text{ad}} \stackrel{\text{def}}{=} & c_{3,I} + c_{3,x} \partial_x + c_{3,y} \partial_y + c_{3,xx} \partial_x^2 + c_{3,yy} \partial_y^2 \\ & + c_{3,xy} \partial_x \partial_y + c_{3,xxx} \partial_x^3 + c_{3,xyy} \partial_x \partial_y^2, \end{aligned} \quad (3.12d)$$

where

$$c_{3,I} = \partial_y^2 u_L^D K_{LR} + \partial_x u_R^D u_R^D + v_R^D \partial_y u_R^D \quad (u_R^D)^2 u_L^D K_{LR} \quad v_R^D \partial_y u_L^D K_{LR} \quad (3.13a)$$

$$\partial_x u_R^D u_L^D K_{LR} + (u_R^D)^3 + (K_{LR} \partial_t u_L^D + \partial_t u_R^D) / D_R \quad \partial_y^2 u_R^D,$$

$$c_{3,x} = D_{LR} K_{LR} (u_L^D)^2 \quad D_{LR} K_{LR} \partial_x u_L^D \quad 2D_{LR} u_L^D u_R^D + K_{LR} (u_R^D)^2 + K_{LR} \partial_x u_R^D, \quad (3.13b)$$

$$c_{3,y} = D_{LR} K_{LR} u_L^D v_L^D \quad D_{LR} K_{LR} \partial_x v_L^D \quad 2D_{LR} u_R^D v_L^D \quad (3.13c)$$

$$K_{LR} u_L^D v_R^D + 2K_{LR} \partial_y u_L^D + 2u_R^D v_R^D \quad 2\partial_y u_R^D + \partial_x v_R^D,$$

$$c_{3,xx} = 2D_{LR} K_{LR} u_L^D + 2D_{LR} u_R^D, \quad (3.13d)$$

$$c_{3,xy} = D_{LR} K_{LR} v_L^D + K_{LR} v_R^D, \quad (3.13e)$$

$$c_{3,yy} = D_{LR} K_{LR} u_L^D + 2D_{LR} u_R^D + K_{LR} u_L^D \quad 2u_R^D, \quad (3.13f)$$

$$c_{3,xxx} = D_{LR} K_{LR}, \quad (3.13g)$$

$$c_{3,xyy} = D_{LR} K_{LR} \quad K_{LR}. \quad (3.13h)$$

The expressions for larger j are computed with a symbolic algebra package such as Maple. A sample algorithm for deriving a 4th-order accurate CHAMP condition is provided in Algorithms 5 and 6. The CHAMP Dirichlet and Neumann operators for the advection-diffusion equation are defined using the operators L_j^{ad} in the Taylor expansions (2.27). This result is summarized in the following Theorem.

Theorem 6 *The CHAMP Dirichlet and Neumann operators for the advection-diffusion equation for a p th-order accurate scheme are*

$$\mathbf{D}_{LR}^{\text{ad},(p)} T_L(0) \stackrel{\text{def}}{=} \sum_{j=0}^p \frac{h_R^j}{j!} L_j^{\text{ad}} T_L(0), \quad (3.14a)$$

$$\mathbf{N}_{LR}^{\text{ad},(p)} T_L(0) \stackrel{\text{def}}{=} \sum_{j=0}^{p-1} \frac{h_R^j}{j!} L_{j+1}^{\text{ad}} T_L(0), \quad (3.14b)$$

where the operators L_j^{ad} are constructed from the compatibility interface conditions (3.10) following the procedure outlined above. The expressions for L_j^{ad} , $j = 0, 1, 2, 3$ are given in (3.12).

Algorithm 5: A sample MAPLE code that defines x -derivatives of T_R for advection-diffusion equations.

```

alias (TL = TL(x,y)): alias (TR = TR(x,y)):
alias (uL = uL(x,y)): alias (uR = uR(x,y)):

# Define Operators
HL := w -> (diff(w,x$2)+diff(w,y$2))-uL diff(w,x)-vL diff(w,y):
HR := w -> (diff(w,x$2)+diff(w,y$2))-uR diff(w,x)-vR diff(w,y):

# Primary temperature interface condition
TempIC := TL-TR:
TR_x[0] := solve(TempIC=0,TR):

# Primary flux interface condition
fluxIC := KLR diff(TL,x) - uL KLR TL - diff(TR,x) + uR TR:
TR_x[1] := solve(fluxIC=0,diff(TR,x)):

# First temperature compatibility condition
TempIC_t := DLR HL(TL) - HR(TR):
TR_x[2] := solve(TempIC_t=0,diff(TR,x$2)):

# First flux compatibility condition
fluxIC_t :=subs([TL= DLR HL(TL),TR=HR(TR)], fluxIC):
TR_x[3] := solve(fluxIC_t=0, diff(TR,x$3)):

# Second temperature compatibility condition
TempIC_tt := subs([TL= DLR HL(TL),TR=HR(TR)], TempIC_t):
TR_x[4] := solve(TempIC_tt=0, diff(TR,x$4)):

```

Algorithm 6: A sample MAPLE code that forms the fourth-order accurate CHAMP conditions for advection-diffusion equations.

```

DLCHAMP:=0: DRCHAMP:=0: NLCHAMP:=0: NRCHAMP:=0:
for i from 0 by 1 to 4 do
  for j from i by -1 to 0 do
    TR_x[i] := subs([diff(TR,[y$j])=diff(TL,[y$j]),
                      diff(TR,[x$j-1])=TR_x[j-1]), TR_x[i]):
    TL_x[i] := subs([diff(TL,[y$j])=diff(TR,[y$j]),
                      diff(TL,[x$j-1])=TL_x[j-1]), TL_x[i]):
  end do:
  DLCHAMP += hR^i/(i!) TR_x[i]:
  DRCHAMP += (-hL)^i/(i!) TL_x[i]:
  if not i=0 then
    NLCHAMP += (hR)^(i-1)/((i-1)!) TR_x[i]:
    NRCHAMP += (-hL)^(i-1)/((i-1)!) TL_x[i]:
  end if:
end do:

CHAMP_Left := NLCHAMP + SL DLCHAMP:
CHAMP_Right := NRCHAMP - SR DRCHAMP:

```

3.4 The Partitioned Conjugate Heat Transfer Algorithm Using CHAMP Conditions

As is typical in a partitioned approach, the solvers used to evolve the temperature in each domain are decoupled from all other domains. To complete a time step an approximate numerical interface conditions is applied, and the temperature in each domain is then provisionally advanced in time. Satisfaction of the interface matching conditions (3.1c)–(3.1d) is then ensured using an iterative technique, where each iteration involves a time update of the temperature in each domain.

Algorithm 7 presents the basic partitioned CHT solver for a problem with two domains. On each domain the discrete approximation to the temperature, $T_{m,i} = T(\mathbf{x}_i, t^n)$,

Algorithm 7: CHAMP partitioned conjugate heat transfer solver for advection-diffusion equations.

```

1: AdvectionDiffusionSolver( $\Omega, t_{final}$ )
2:  $t = 0, n = 0$ ;
3:  $T_m^0(\mathbf{x}) = T_k^{IC}(\mathbf{x}), \quad \mathbf{x} \in \Omega_k, \quad k = L, R;$  ▷ Initial conditions
4: Evaluate past time values as needed by BDF schemes.
5: // Time stepping loop
6: while  $t < t_{final}$  do
7:    $F_k(\mathbf{x}) = \sum_{j=1}^p \alpha_j T_m^{n-j}(\mathbf{x}), \quad \mathbf{x} \in \Omega_k, \quad k = L, R;$  ▷ Assign RHS for BDF scheme
8:    $T_R^{(0)} = \sum_{i=1}^{p+1} \binom{p+1}{i} (-1)^{i+1} T_R^{n+1-i};$  ▷ Extrapolate in time for initial guess
9:   for  $j = 1, \dots, N_{si}$  do ▷ Sub-time-step iterations
10:    // Solve for  $T_L^{(j)}$  given  $T_R^{(j-1)}$ :
11:     $T_L^{(j)} - \beta_0 \Delta t (D_L \Delta + \mathbf{u}_L \cdot \nabla) T_L^{(j)} = F_L, \quad \mathbf{x} \in \Omega_L;$ 
12:     $(\mathbf{N}_{LR} + \mathbf{S}_L \mathbf{D}_{LR}) T_L^{(j)}(\mathbf{x}) = (\partial_n + \mathbf{S}_L) T_R^{(j-1)}(\mathbf{x} + h_R \mathbf{n}_{LR}), \quad \mathbf{x} \in \Gamma; \quad \triangleright$  CHAMP
13:     $B_L(T_L^{(j)}) = g(\mathbf{x}, t + \Delta t), \quad \mathbf{x} \in \partial\Omega_L; \quad \triangleright$  Physical BCs.
14:    // Solve for  $T_R^{(j)}$  given  $T_L^{(j)}$ :
15:     $T_R^{(j)} - \beta_0 \Delta t (D_R \Delta + \mathbf{u}_R \cdot \nabla) T_R^{(j)} = F_R, \quad \mathbf{x} \in \Omega_R;$ 
16:     $(\mathbf{N}_{RL} + \mathbf{S}_R \mathbf{D}_{RL}) T_R^{(j)}(\mathbf{x}) = (\partial_n + \mathbf{S}_R) T_L^{(j)}(\mathbf{x} + h_L \mathbf{n}_{RL}), \quad \mathbf{x} \in \Gamma; \quad \triangleright$  CHAMP
17:     $B_R(T_R^{(j)}) = g(\mathbf{x}, t + \Delta t), \quad \mathbf{x} \in \partial\Omega_R; \quad \triangleright$  Physical BCs.
18:     $error^{(j)} = \max_{\Gamma} \{|T_L^{(j)} - T_R^{(j)}|\};$  ▷ Error in iteration
19:    If  $|error^{(j)} - error^{(j-1)}| < tol$  then break; ▷ Converged
20:  end for
21:   $T_k^{n+1} = T_k^{(j)}, \quad k = L, R;$  ▷ Solution at new time
22:   $t = t + \Delta t, n = n + 1;$ 
23: end while

```

is advanced in time using a backward differentiation formula (BDF) given in (3.4), with W defined in (3.5). The superscript in T_m without the parenthesis indicate the time level, and the superscript with the parenthesis indicates the number of sub-iterations. Solutions are initialized at $t = 0$ using the initial condition. At each time-step, $F_m(\mathbf{x})$ is defined to be a linear combination of the discrete temperature values at past time steps in the BDF scheme for each subdomain. To initialize the CHAMP iteration, an initial guess $T_R^{(0)}$ for the temperature in the right domain is needed. Here a p th-order accurate extrapolation formula is used to obtain a temperature value for the right domain from past time values. The solution is then advanced in a segregated fashion with sub-time-step iterations used as

needed. Physical boundary conditions are approximated to p^{th} -order accuracy,

$$B_{ph} T_{m,\mathbf{i}}^{n+1} = g(\mathbf{x}_i, t^{n+1}), \quad (3.15)$$

together with appropriate numerical boundary conditions.

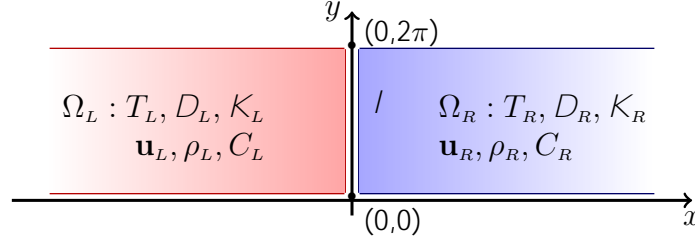


Figure 3.2: The geometry for the model problems. The solution is assumed to be 2π -periodic in the y -direction.

3.5 Analysis of the CHAMP Schemes

In this section, the CHAMP scheme is analyzed by considering a model problem consisting of two rectangular domains that meet at a vertical interface located at $x = 0$. The geometry of the model problem is shown in Figure 3.2. The problem arises by considering a general curved interface, as shown in Figure 1.3, and looking at a small region about some point on the interface, choosing coordinates that are normal and tangential to the interface and retaining the most important terms. The result is a problem involving a semi-infinite domain on the left, $\Omega_L = (-\infty, 0) \times [0, 2\pi]$, adjacent to a semi-infinite domain on the right, $\Omega_R = (0, \infty) \times [0, 2\pi]$. The problem is taken to be periodic in the y -direction and the solution with an initial condition of compact support is assumed to have bounded L_2 -norm. The resulting IBVP is then

$$\partial_t T_m + (\mathbf{u}^c \cdot \nabla) T_m = D_m \Delta T_m, \quad \mathbf{x} \in \Omega_m, \quad (3.16a)$$

$$[T]_l = 0, \quad y \in (0, 2\pi), \quad (3.16b)$$

$$[K \partial_x T - u^c \rho C T]_l = 0, \quad y \in (0, 2\pi), \quad (3.16c)$$

$$T_m(x, y + 2\pi, t) = T_m(x, y, t), \quad \mathbf{x} \in \Omega_m, \quad (3.16d)$$

$$k T_m k_2 < 1, \quad (3.16e)$$

$$T_m(\mathbf{x}, 0) = T_m^{\text{IC}}(\mathbf{x}), \quad \mathbf{x} \in \Omega_m, \quad (3.16f)$$

where $m = L, R$ indicates the left or right sub-domain, and the velocity $\mathbf{u}^c = (u^c, v^c)$ is constant. Expanding the solution in a Fourier series in y

$$T_m(\mathbf{x}, t) = \sum_{k=-1}^1 \hat{T}_m(x, k, t) e^{iky}, \quad (3.17)$$

gives a one-dimensional CHT problem, which is parameterized by the wave number k in the y -direction,

$$\partial_t \hat{T}_L + (u^c \partial_x - ikv^c) \hat{T}_L = D_m (\partial_x^2 - k^2) \hat{T}_L, \quad x \in (-1, 0), \quad (3.18a)$$

$$\partial_t \hat{T}_R + (u^c \partial_x - ikv^c) \hat{T}_R = D_m (\partial_x^2 - k^2) \hat{T}_R, \quad x \in (0, 1), \quad (3.18b)$$

$$[\hat{T}]_{x=0} = 0, \quad (3.18c)$$

$$[K \partial_x \hat{T} - u^c \rho C \hat{T}]_{x=0} = 0, \quad (3.18d)$$

$$k \hat{T}_m(x, k, t) k_2 < 1, \quad (3.18e)$$

$$\hat{T}_m(x, 0) = \hat{T}_m^{\text{IC}}(x). \quad (3.18f)$$

Temporal discretization uses the BDF scheme given in (3.4), with W denoting the advection diffusion operator defined in (3.5). Replacing the standard interface jump conditions with the equivalent CHAMP interface conditions leads to the IBVP CHT problem

$$\left[I - \Delta t \beta_0 (D_L (\partial_x^2 - k^2) - (u^c \partial_x - ikv^c)) \right] \hat{T}_L^{n+1} = \sum_{j=1}^p \alpha_j \hat{T}_L^{n-j} \stackrel{\text{def}}{=} F_L^n, \quad (3.19a)$$

$$\left[I - \Delta t \beta_0 (D_R (\partial_x^2 - k^2) - (u^c \partial_x - ikv^c)) \right] \hat{T}_R^{n+1} = \sum_{j=1}^p \alpha_j \hat{T}_R^{n-j} \stackrel{\text{def}}{=} F_R^n, \quad (3.19b)$$

$$\left(\mathbf{N}_{LR}[\partial_x, ik] + \mathbf{S}_L \mathbf{D}_{LR}[\partial_x, ik] \right) \hat{T}_L^{n+1}(0) = \left(\partial_x + \mathbf{S}_L \right) \hat{T}_R^{n+1}(+h), \quad (3.19c)$$

$$\left(\mathbf{N}_{RL}[\partial_x, ik] + \mathbf{S}_R \mathbf{D}_{RL}[\partial_x, ik] \right) \hat{T}_R^{n+1}(0) = \left(\partial_x + \mathbf{S}_R \right) \hat{T}_L^{n+1}(-h), \quad (3.19d)$$

$$k \hat{T}_m^{n+1} k_2 < 1, \quad (3.19e)$$

$$\hat{T}_m^0(x) = \hat{T}_m^{\text{IC}}(x), \quad (3.19f)$$

where $\mathbf{N}_{LR}[\partial_x, ik]$, $\mathbf{D}_{LR}[\partial_x, ik]$, $\mathbf{N}_{RL}[\partial_x, ik]$ and $\mathbf{D}_{RL}[\partial_x, ik]$ are the linearized and Fourier transforms of the CHAMP Dirichlet and Neumann operators formed by replacing ∂_y with ik and \mathbf{u} by \mathbf{u}^c .

Equation (3.19) is solved in a partitioned fashion following Algorithm 7. This involves a potential sub-time-step iteration, whose convergence is studied in Section 3.5.1. The analysis of the un-iterated time-stepping scheme is then studied in Section 3.5.3.

3.5.1 Model Problem Analysis of the CHAMP Iteration

The analysis of the CHAMP sub-time-step iteration for the advection-diffusion problem is now considered. In Section 2.6.1, the iteration was found to converge for all physically relevant values of the parameters for the diffusion-only case. For the advection-diffusion problem, the velocity at the interface needs to satisfy certain conditions in order for the iteration to converge. Derivation of the convergence factor for a p^{nd} -order accurate scheme is presented first, followed by a detailed analysis of a 2^{nd} -order accurate scheme to show these conditions.

Let $\hat{T}_m^{(j)}$ and \hat{T}_m^{n+1} denote the j^{th} iterate in the fixed-point iteration to compute \hat{T}_L^{n+1} and \hat{T}_R^{n+1} in (3.19). The fixed-point iteration is given by

$$\left[I - \Delta t \beta_0 (D_L(\partial_x^2 - k^2) - (u^c \partial_x + ikv^c)) \right] \hat{T}_L^{(j)} = F_L^n, \quad x \in (-1, 0), \quad (3.20a)$$

$$\left(\mathbf{N}_{LR}[\partial_x, ik] + \mathbf{S}_L \mathbf{D}_{LR}[\partial_x, ik] \right) \hat{T}_L^{(j)}(0) = \left(-\partial_x + \mathbf{S}_L \right) \hat{T}_R^{(j-1)}(h), \quad (3.20b)$$

$$k \hat{T}_L^{(j)} k_2 < 1, \quad (3.20c)$$

$$\left[I - \Delta t \beta_0 (D_R(\partial_x^2 - k^2) - (u^c \partial_x + ikv^c)) \right] \hat{T}_R^{(j)} = F_R^n, \quad x \in (0, 1), \quad (3.20d)$$

$$\left(\mathbf{N}_{RL}[\partial_x, ik] + \mathbf{S}_R \mathbf{D}_{RL}[\partial_x, ik] \right) \hat{T}_R^{(j)}(0) = \left(\partial_x + \mathbf{S}_R \right) \hat{T}_L^{(j)}(-h), \quad (3.20e)$$

$$k \hat{T}_R^{(j)} k_2 < 1, \quad (3.20f)$$

with an initial guess for $\hat{T}_R^{(0)}$ obtained by extrapolating the past temperature values in time. The errors $\hat{E}_m^{(j)} = \hat{T}_m^{(j)} - \hat{T}_m^{n+1}$, $m = L, R$ satisfy the same equations with $F_m^n = 0$. Therefore, $\hat{T}_m^{(j)}$ is now interpreted as an error with F_m^n taken to be zero in (3.20).

The spatial approximations used to discretize the CHAMP Dirichlet and Neumann operators are taken to be p^{th} -order accurate, while the order of accuracy in time is left open. The general solution of (3.20) subject to the far-field boundary conditions (and with $F_m^n = 0$)

is given as

$$\hat{T}_L^{(j)}(x, k) = c^L A^j e^{\xi_L x}, \quad (3.21a)$$

$$\hat{T}_R^{(j)}(x, k) = c^R A^j e^{-\xi_R x}, \quad (3.21b)$$

where

$$\xi_L \stackrel{\text{def}}{=} +\frac{\tilde{u}_L^D}{2} + \sqrt{\frac{1}{\beta_0 D_L \Delta t} + k^2 + \frac{(\tilde{u}_L^D)^2}{4} + ik\tilde{v}_L^D}, \quad (3.22a)$$

$$\xi_R \stackrel{\text{def}}{=} -\frac{\tilde{u}_R^D}{2} + \sqrt{\frac{1}{\beta_0 D_R \Delta t} + k^2 + \frac{(\tilde{u}_R^D)^2}{4} + ik\tilde{v}_R^D}, \quad (3.22b)$$

with \tilde{u}_L^D , \tilde{v}_L^D , \tilde{u}_R^D and \tilde{v}_R^D given by

$$\tilde{u}_m^D \stackrel{\text{def}}{=} \frac{u_m^c}{D_m}, \quad \tilde{v}_m^D \stackrel{\text{def}}{=} \frac{v_m^c}{D_m}, \quad m = L, R, \quad (3.23)$$

and the root ξ_m chosen such that $\text{Re}(\xi_m) > 0$. Substituting (3.21) into the CHAMP interface equations leads to an equation for the iteration amplification factor A which is summarized in the following theorem.

Theorem 7 (CHAMP iteration, advection-diffusion) *The iteration amplification factor when using p^{th} -order accurate spatial approximations to the CHAMP interface conditions for the advection-diffusion equations is*

$$A_{CI} = \frac{(\xi_R + \mathbf{S}_L) e^{-\xi_R h}}{(\mathbf{N}_{RL}^{(p)}[\xi_R, ik] + \mathbf{S}_R \mathbf{D}_{RL}^{(p)}[\xi_R, ik])} \frac{(\xi_L + \mathbf{S}_R) e^{-\xi_L h}}{(\mathbf{N}_{LR}^{(p)}[\xi_L, ik] + \mathbf{S}_L \mathbf{D}_{LR}^{(p)}[\xi_L, ik])}, \quad (3.24)$$

where the Dirichlet and Neumann operators $\mathbf{D}_{RL}^{(p)}$, $\mathbf{N}_{RL}^{(p)}$, etc., are given in (3.14) and where ξ_L and ξ_R are defined in (3.22).

The formula (3.24) for A can be written in non-dimensional form using

$$p_L \stackrel{\text{def}}{=} h\mathbf{S}_L, \quad p_R \stackrel{\text{def}}{=} h\mathbf{S}_R, \quad z_m \stackrel{\text{def}}{=} \xi_m h, \quad \kappa \stackrel{\text{def}}{=} k h, \quad \hat{u}_m^D \stackrel{\text{def}}{=} \tilde{u}_m^D h, \quad \hat{v}_m^D \stackrel{\text{def}}{=} \tilde{v}_m^D h, \quad (3.25)$$

and

$$z_L \stackrel{\text{def}}{=} \frac{\hat{u}_L^D}{2} + \sqrt{\frac{1}{\beta_0 \lambda_{DL}} + \kappa^2 + \frac{(\hat{u}_L^D)^2}{4} + i\kappa(\hat{v}_L^D)}, \quad (3.26a)$$

$$z_R \stackrel{\text{def}}{=} \frac{\hat{u}_R^D}{2} + \sqrt{\frac{1}{\beta_0 \lambda_{DR}} + \kappa^2 + \frac{(\hat{u}_R^D)^2}{4} + i\kappa(\hat{v}_R^D)}. \quad (3.26b)$$

Note that the velocities in (3.26) are scaled by h , and so $(\hat{u}_m^D, \hat{v}_m^D) \rightarrow 0$ as $h \rightarrow 0$. The implication of this is that the convergence of the CHAMP iteration for the advection-diffusion model approaches that of the diffusion-only model as the grid is refined. At second-order accuracy, for example, the symbols of the Dirichlet and Neumann operators are

$$\begin{aligned} \mathbf{D}_{RL}^{(2)} = & \frac{1}{2} z_L^2 D_{LR} + (K_{LR} \frac{1}{2} \hat{u}_L^D D_{LR} + \frac{1}{2} K_{LR} \hat{u}_R^D) z_L + (\frac{1}{2} D_{LR} + \frac{1}{2}) \kappa^2 \\ & + (\frac{1}{2} i \hat{v}_L^D D_{LR} + \frac{1}{2} i \hat{v}_R^D) \kappa + 1 \quad \hat{u}_L^D K_{LR} + \hat{u}_R^D + \frac{1}{2} (K_{LR} \hat{u}_L^D + \hat{u}_R^D) \hat{u}_R^D, \end{aligned} \quad (3.27a)$$

$$\begin{aligned} h \mathbf{N}_{RL}^{(2)} = & z_L^2 D_{LR} + (D_{LR} \hat{u}_L^D + K_{LR} \hat{u}_R^D + K_{LR}) z_L + (D_{LR} + 1) \kappa^2 + \hat{u}_R^D \\ & + (i \hat{v}_L^D D_{LR} + i \hat{v}_R^D) \kappa \quad \hat{u}_L^D K_{LR} + (K_{LR} \hat{u}_L^D + \hat{u}_R^D) \hat{u}_R^D. \end{aligned} \quad (3.27b)$$

Optimal values for the parameters p_L and p_R can be found in the same way as described for the diffusion equation in Section 2.6.1.

Figures 3.3 and 3.4 shows the behavior of A_{CI} and the corresponding optimal (p_L, p_R) of the CHAMP iteration for the advection-diffusion model for various choices of the velocities. For the case with no advection, the A_{CI} curve is symmetric about $K_{LR} = 1$, and also attains the maximum there (see Figure 2.6), so the hardest problem corresponds to the case when there is no jump in the material parameters across the interface. For the case $[\hat{u}_L^D, \hat{v}_L^D] = [0.7, 0]$, $[\hat{u}_R^D, \hat{v}_R^D] = [0.1, 0]$ the maximum in the curves shifts slightly to the right, while for $[\hat{u}_L^D, \hat{v}_L^D] = [0.5, .1]$, $[\hat{u}_R^D, \hat{v}_R^D] = [0.1, 0.1]$ there is a slight shift to the left. Figure 3.4 shows more results for the advection-diffusion amplification factor A_{CI} for different values of the time-stepping parameter λ_{DL} . All of the curves are slightly shifted toward right, and as λ_{DL} increases, the curve becomes flatter, and the largest value A_{CI} achieved also increases. For all of the cases presented, the value for A_{CI} with advection is smaller than the case with no advection.

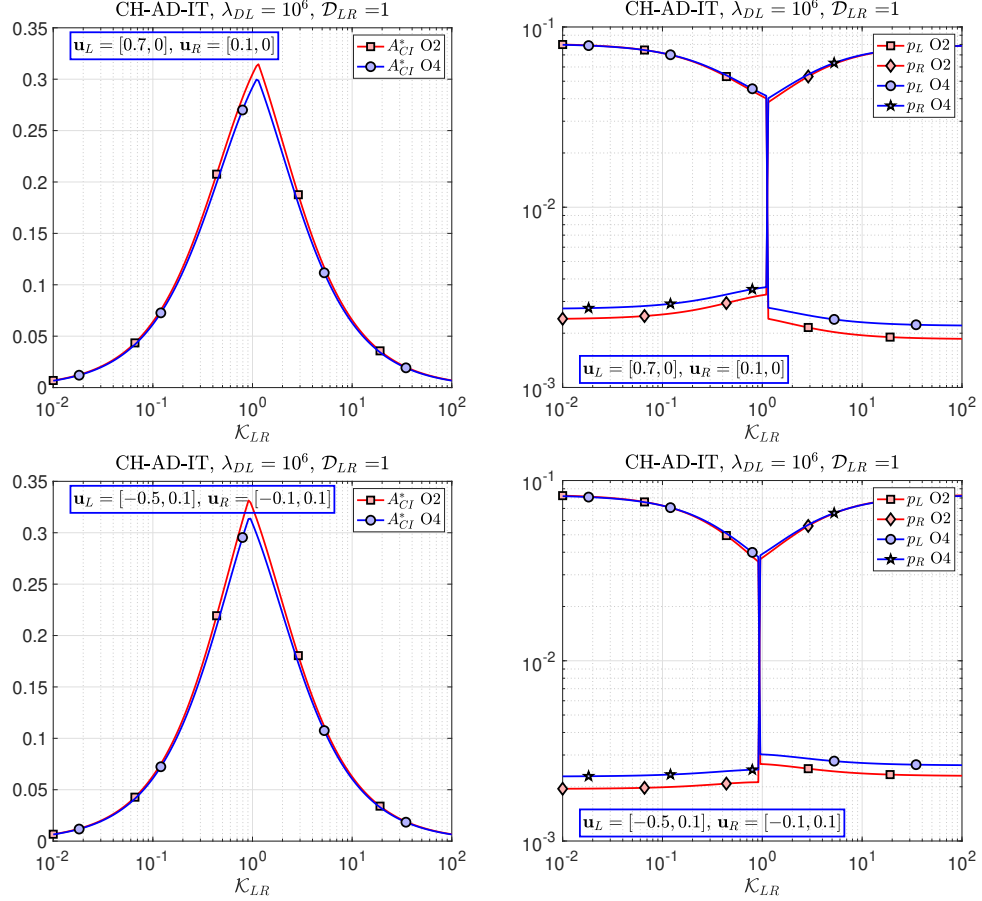


Figure 3.3: CHAMP iteration for advection-diffusion: A_{CI} and corresponding optimal p_L and p_R for orders 2 and 4 ($h = 10^{-3}$) with various choices of material parameters $K_{LR} = \frac{K_L}{K_R}$, $D_{LR} = \frac{D_L}{D_R}$, $\lambda_{DL} = \frac{tD_L}{h^2}$.

3.5.2 Constraints on Velocities for the CHAMP Conditions

In this section, a detailed analysis is presented to investigate the convergence of the CHAMP iteration for the case $p = 2$. The 2nd-order accurate CHAMP operators are given in (3.27). If \hat{u}_m^D and \hat{v}_m^D are zero, then the iteration amplification factor reduces to the one for the diffusion equation, and it has been shown that there always exists parameters p_L and p_R such that $A_{CI} < 1$ and the iteration converges [75]. When \hat{u}_m^D and \hat{v}_m^D are not zero, using the relation

$$D_{LR}z_L^2 \quad \kappa^2(D_{LR} \quad 1) \quad D_{LR}\hat{u}_L^D z_L = z_R^2 + \hat{u}_R^D z_R, \quad (3.28a)$$

$$D_{RL}z_R^2 \quad \kappa^2(D_{RL} \quad 1) + D_{RL}\hat{u}_L^D z_R = z_L^2 \quad \hat{u}_L^D z_L, \quad (3.28b)$$

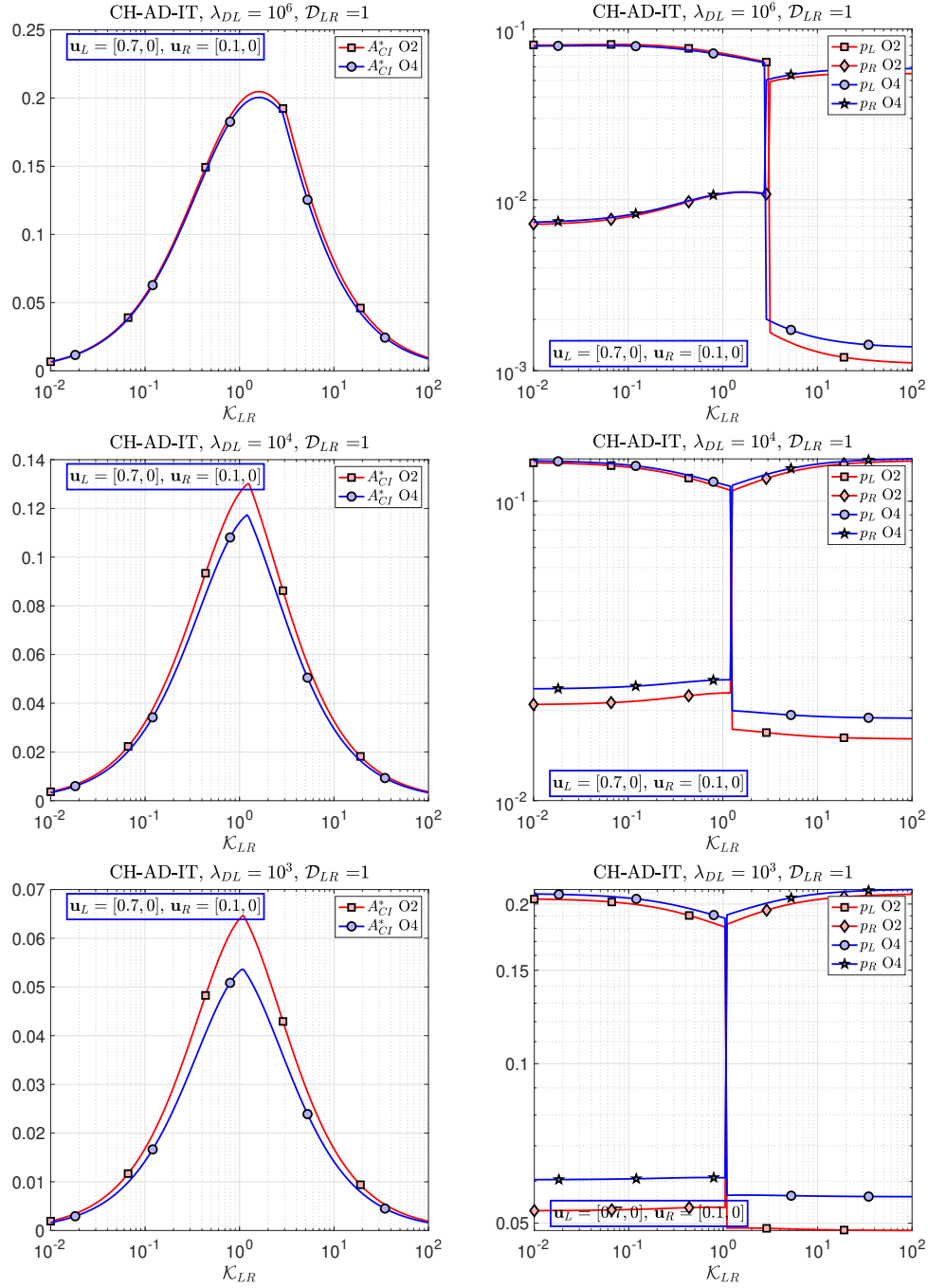


Figure 3.4: CHAMP iteration for advection-diffusion: A_{CI} and corresponding optimal p_L and p_R for orders 2 and 4 ($h = 10^{-2}$) for various choices of material parameters $K_{LR} = \frac{K_L}{K_R}$, $D_{LR} = \frac{D_L}{D_R}$, $\lambda_{DL} = \frac{tD_L}{h^2}$. Here λ_{DL} are chosen to be 10^6 , 10^4 and 10^3 .

the iteration amplification factor A_{CI} for the case $p = 2$ can be written as

$$A_{CI} = \frac{(z_R + p_L) e^{-z_R} (z_L + p_R) e^{-z_L}}{(M_{z_L, z_R, \hat{u}_L^D, \hat{u}_R^D, K_{LR}})(N_{z_L, z_R, \hat{u}_L^D, \hat{u}_R^D, K_{LR}})}, \quad (3.29)$$

where

$$\begin{aligned} M_{z_L, z_R, \dots} &= K_{LR} z_L (1 + \hat{u}_R^D) + (\hat{u}_R^D - K_{LR} \hat{u}_L^D) (1 + \hat{u}_R^D) + z_R (\hat{u}_R^D + z_R) \\ &+ \hat{\mathbf{S}}_L \left(1 + K_{LR} z_L \left(1 + \frac{1}{2} \hat{u}_R^D \right) + (\hat{u}_R^D - K_{LR} \hat{u}_L^D) \left(1 + \frac{1}{2} \hat{u}_R^D \right) + \frac{1}{2} z_R (\hat{u}_R^D + z_R) \right), \end{aligned} \quad (3.30a)$$

$$\begin{aligned} N_{z_L, z_R, \dots} &= K_{RL} z_R (1 + \hat{u}_L^D) + (\hat{u}_L^D - K_{RL} \hat{u}_R^D) (1 + \hat{u}_L^D) + z_L (\hat{u}_L^D + z_L) \\ &+ \hat{\mathbf{S}}_R \left(1 + K_{RL} z_R \left(1 + \frac{1}{2} \hat{u}_L^D \right) + (\hat{u}_L^D - K_{RL} \hat{u}_R^D) \left(1 + \frac{1}{2} \hat{u}_L^D \right) + \frac{1}{2} z_L (\hat{u}_L^D + z_L) \right). \end{aligned} \quad (3.30b)$$

The CHAMP condition can be separated into a pure Dirichlet portion and a pure Neumann portion. The Neumann portion, for example can be obtained by setting both $p_L = p_R = 0$, to get

$$\mathbf{N}_{LR} T_L^{(j)}(\mathbf{x}) = \partial_{n,L} T_R^{(j-1)}(\mathbf{x} + h_R \mathbf{n}_L), \quad \mathbf{x} \in \Gamma_{LR}, \quad (3.31a)$$

$$\mathbf{N}_{LR} T_R^{(j)}(\mathbf{x}) = \partial_{n,L} T_L^{(j)}(\mathbf{x} - h_L \mathbf{n}_L), \quad \mathbf{x} \in \Gamma_{LR}, \quad (3.31b)$$

and the remaining Dirichlet portion has the form

$$\mathbf{D}_{LR} T_L^{(j)}(\mathbf{x}) = T_R^{(j-1)}(\mathbf{x} + h_R \mathbf{n}_L), \quad \mathbf{x} \in \Gamma_{LR}, \quad (3.32a)$$

$$\mathbf{D}_{LR} T_R^{(j)}(\mathbf{x}) = T_L^{(j)}(\mathbf{x} - h_L \mathbf{n}_L), \quad \mathbf{x} \in \Gamma_{LR}. \quad (3.32b)$$

The corresponding amplification factors are denoted as $A_{CI}^{(2),D}$ and $A_{CI}^{(2),N}$ respectively. For the Dirichlet portion, the numerator of $A_{CI}^{(2),D}$ is denoted by $\mathbf{N}(A_{CI}^{(2),D})$ and expressed as

$$\mathbf{N}(A_{CI}^{(2),D}) = e^{-z_R - z_L}. \quad (3.33)$$

Since z_L, z_R are chosen so that they always have a positive real part, the magnitude of $\mathbf{N}(A_{CI}^{(2),D})$ is always less than or equal to 1, i.e.

$$|\mathbf{N}(A_{CI}^{(2),D})| = |e^{-z_R - z_L}| \leq 1. \quad (3.34)$$

The denominator of $A_{CI}^{(2),D}$ is denoted by $D(A_{CI}^{(2),D})$ and has the form

$$D(A_{CI}^{(2),D}) \stackrel{\text{def}}{=} \begin{pmatrix} 1 + K_{LR}z_L(1 + \frac{1}{2}\hat{u}_R^D) + (\hat{u}_R^D & K_{LR}\hat{u}_L^D)(1 + \frac{1}{2}\hat{u}_R^D) + \frac{1}{2}z_R(\hat{u}_R^D + z_R) \\ (1 + K_{RL}z_R(1 - \frac{1}{2}\hat{u}_L^D) + (\hat{u}_L^D & K_{RL}\hat{u}_R^D)(\frac{1}{2}\hat{u}_L^D - 1) + \frac{1}{2}z_L(z_L - \hat{u}_L^D)) \end{pmatrix} \quad (3.35)$$

For the CHAMP schemes containing only the Dirichlet portion to converge, the magnitude of the iteration amplification factor must be less than 1, i.e.

$$|A_{CI}^{(2),D}| < 1, \quad (3.36)$$

which requires

$$|D(A_{CI}^{(2),D})| > 1. \quad (3.37)$$

Since \hat{u}_m^D , $m = L, R$ are velocities scaled by grid spacing h , it is reasonable to assume their magnitudes are small. Under such assumption, the condition in (3.37) holds when \hat{u}_m^D , $m = L, R$, satisfies

$$\hat{u}_L^D - K_{LR}\hat{u}_R^D < 0. \quad (3.38)$$

The inequality in (3.38) poses a constraint on the scaled velocities \hat{u}_m^D , $m = L, R$. Changing back to dimensional quantities gives

$$\frac{u_L}{D_L} - K_{LR}\frac{u_R}{D_R} < 0, \quad (3.39a)$$

which can be simplified to

$$(C_R - C_L)u_R > 0, \quad (3.39b)$$

where C_m , $m = L, R$ are the specific heats of the materials. Equation (3.39b) shows that the convergence of the sub-time step iteration depends on the relative sizes of the heat capacity and velocities. The condition in (3.38) provides a sufficient condition for the CHAMP iteration to converge for the case involving only the Dirichlet portion. Similar results can be

obtained by analyzing the iteration amplification factor corresponding to the pure Neumann portion, both the details are suppressed here.

3.5.3 Analysis of the Un-iterated CHAMP Time-stepping Scheme

In this section, the stability of the un-iterated CHAMP time-stepping scheme for the model problem in (3.19) is analyzed. At each time step, the CHAMP scheme requires iterations so that the interface matching conditions in (3.1c)–(3.1d) can be satisfied. Each iteration involves an implicit solve of the temperature in each subdomain, and as a result, it is desirable to formulate a scheme that uses as few iterations as possible. For the case when no sub-iterations are taken, the CHAMP time-stepping scheme becomes the so-called the un-iterated CHAMP time-stepping scheme (as indicated before). The analysis in this section aims to show that the CHAMP scheme, with no sub-time step iteration, is stable for a wide range of material properties.

Algorithm 8: Un-iterated CHAMP time-stepping algorithm for advection-diffusion equation.

- 1: $t = 0, n = 0;$
 - 2: $T_m^0(\mathbf{x}) = T_m^{\text{IC}}(\mathbf{x}), \quad \mathbf{x} \in \Omega_m, \quad m = L, R;$ ▷ Initial conditions
 - 3: Evaluate past time values as needed by BDF schemes.
 - 4: *// Time stepping loop*
 - 5: **for** $t = 1, \dots, t_{\text{final}}$ **do**
 - 6: $F_m(\mathbf{x}) = \sum_{\ell=1}^p \alpha_\ell T_m^{n+1-\ell}(\mathbf{x}), \quad \mathbf{x} \in \Omega_m, \quad m = L, R;$ ▷ Assign RHS for BDF scheme
 - 7: $T_R^{(0)} = \sum_{i=1}^{p+1} \binom{p+1}{i} (-1)^{i+1} T_R^{n+1-i};$ ▷ Extrapolate in time for initial guess
 - 8: *// Solve for T_L^{n+1} given $T_R^{(0)}$:*
 - 9: $T_L^{n+1} - \beta_0 \Delta t (D_L \Delta + \mathbf{u}_L \cdot \nabla) T_L^{n+1} = F_L, \quad \mathbf{x} \in \Omega_L;$
 - 10: $(\mathbf{N}_{LR} + \mathbf{S}_L \mathbf{D}_{LR}) T_L^{n+1}(\mathbf{x}) = (\partial_n + \mathbf{S}_L) T_R^{(0)}(\mathbf{x} + h_R \mathbf{n}_{LR}), \quad \mathbf{x} \in \Gamma;$ ▷ CHAMP
 - 11: $B_L(T_L^{n+1}) = g(\mathbf{x}, t + \Delta t), \quad \mathbf{x} \in \partial\Omega_L;$ ▷ Physical BCs.
 - 12: *// Solve for T_R^{n+1} given T_L^{n+1} :*
 - 13: $T_R^{n+1} - \beta_0 \Delta t (D_R \Delta + \mathbf{u}_R \cdot \nabla) T_R^{n+1} = F_R, \quad \mathbf{x} \in \Omega_R;$
 - 14: $(\mathbf{N}_{RL} + \mathbf{S}_R \mathbf{D}_{RL}) T_R^{n+1}(\mathbf{x}) = (\partial_n + \mathbf{S}_R) T_L^{n+1}(\mathbf{x} + h_L \mathbf{n}_{RL}), \quad \mathbf{x} \in \Gamma;$ ▷ CHAMP
 - 15: $B_R(T_R^{n+1}) = g(\mathbf{x}, t + \Delta t), \quad \mathbf{x} \in \partial\Omega_R;$ ▷ Physical BCs.
 - 16: $t = t + \Delta t, n = n + 1;$
 - 17: **end for**
-

The time-step update to determine \hat{T}_L^{n+1} and \hat{T}_R^{n+1} is given by

$$\hat{T}_R^{(0)} = \text{extrapolate}(\hat{T}_R^n, \hat{T}_R^{n-1}, \dots), \quad (3.40a)$$

$$\left[I \quad \Delta t \beta_0 (D_L (\partial_x^2 - k^2) \quad (u_L^c \partial_x \quad ikv_L^c)) \right] \hat{T}_L^{n+1} = F_L^n, \quad x \in (-1, 0), \quad (3.40b)$$

$$\left(\hat{\mathbf{N}}_{LR} + \mathbf{S}_L \hat{\mathbf{D}}_{LR} \right) \hat{T}_L^{n+1}(0) = \left(\partial_x + \mathbf{S}_L \right) \hat{T}_R^{(0)}(+h), \quad (3.40c)$$

$$k \hat{T}_L^{n+1} k_2 < 1, \quad (3.40d)$$

$$\left[I \quad \Delta t \beta_0 (D_R (\partial_x^2 - k^2) \quad (u_R^c \partial_x \quad ikv_R^c)) \right] \hat{T}_R^{n+1} = F_R^n, \quad x \in (0, 1), \quad (3.40e)$$

$$\left(\hat{\mathbf{N}}_{RL} + \mathbf{S}_R \hat{\mathbf{D}}_{RL} \right) \hat{T}_R^{n+1}(0) = \left(\partial_x + \mathbf{S}_R \right) \hat{T}_L^{n+1}(-h), \quad (3.40f)$$

$$k \hat{T}_R^{n+1} k_2 < 1, \quad (3.40g)$$

with an initial guess for $\hat{T}_R(0)$ obtained by extrapolation in time with $(p+1)$ -order extrapolation formula

$$\hat{T}_R^{(0)} = \text{extrapolate}(\hat{T}_R^n, \hat{T}_R^{n-1}, \dots) = \sum_{\ell=1}^{p+1} \binom{p+1}{\ell} (-1)^{\ell+1} \hat{T}_R^{n+1-\ell}. \quad (3.41)$$

and a BDF scheme in time. A sample algorithm is given in Algorithm 8. The analysis follows similar steps to those for the diffusion equation derived in Section 2.6.2. A GKS normal mode analysis is carried out with the assumption that the IVP is stable, and the normal mode solutions in each domain has the form

$$\hat{T}_L^n = A^n e^{\xi_L x}, \quad \hat{T}_R^n = A^n e^{-\xi_R x}, \quad (3.42)$$

where A is the time-stepping amplification factor for both domains. Substitute the solution ansatz into (3.40b) gives the characteristic polynomial

$$\xi_m^2 + \frac{u_m^c}{D_m} \xi_m + \left(\frac{ikv_m^c}{D_m} - k^2 - \frac{1}{\Delta t D_m} \frac{\sum_{\mu=0}^p \alpha_\mu A^{p-\mu}}{\beta_0} \right) = 0. \quad (3.43)$$

Two possible roots for ξ_L and ξ_R are expressed as

$$\xi_L = +\frac{u_L^c}{2D_L} \sqrt{\left(\frac{u_L^c}{2D_L}\right)^2 + \frac{1}{\Delta t D_L} \frac{\sum_{\mu=0}^p \alpha_{\mu} A^{p-\mu}}{\beta_0} + k^2} - \frac{ikv_L^c}{D_L}, \quad (3.44a)$$

$$\xi_R = \frac{u_R^c}{2D_R} \sqrt{\left(\frac{u_R^c}{2D_R}\right)^2 + \frac{1}{\Delta t D_R} \frac{\sum_{\mu=0}^p \alpha_{\mu} A^{p-\mu}}{\beta_0} + k^2} - \frac{ikv_R^c}{D_R}. \quad (3.44b)$$

The scheme is stable provided that there are no nontrivial solutions to the homogeneous equations (3.40a)–(3.40g) with $|jAj| > 1$. For nonzero u_m^c and v_m^c , values for ξ_m are always complex, and solutions of ξ_m contain one root with a positive real part and the other root with a negative real part. Satisfaction of the far-field boundary conditions in (3.40g) removes one of the two roots in (3.44), which leads to the following solutions

$$\hat{T}_L^n = c_L A^n e^{\xi_L x}, \quad \hat{T}_R^n = c_R A^n e^{-\xi_R x}, \quad (3.45)$$

where the principal branch of the square root in (3.44) is chosen to have a positive real part of ξ_m .

The same notation for $\mathbf{D}_{LR}^{(p)}[\partial_x, \partial_y]$ and $\mathbf{N}_{LR}^{(p)}[\partial_x, \partial_y]$ is used to denote the p^{th} -order CHAMP Dirichlet and Neumann operators. The Fourier transformed CHAMP operators can be written as $\mathbf{D}_{LR}^{(p)}[\partial_x, ik]$, $\mathbf{N}_{LR}^{(p)}[\partial_x, ik]$, where the y -derivatives have been replaced by multiples of ik .

Substituting the solution in (3.45) into the CHAMP interface conditions and using the extrapolation formula (3.41) yields

$$\begin{aligned} & c^L A^{n+1} \left(\mathbf{N}_{LR}^{(p)}[\xi_L, ik] + \mathbf{S}_L \mathbf{D}_{LR}^{(p)}[\xi_L, ik] \right) \\ & = c^R \left\{ \sum_{\ell=1}^{p+1} \binom{p+1}{\ell} (-1)^{\ell+1} A^{n+1-\ell} \right\} (\xi_R + \mathbf{S}_L) e^{-\xi_R h}, \end{aligned} \quad (3.46a)$$

$$c^R A^{n+1} \left(\mathbf{N}_{RL}^{(p)}[\xi_R, ik] + \mathbf{S}_R \mathbf{D}_{RL}^{(p)}[\xi_R, ik] \right) = c^L A^{n+1} (\xi_L + \mathbf{S}_R) e^{\xi_L h}. \quad (3.46b)$$

Equations (3.46) give two equations for two unknowns c^L and c^R . Non-trivial solutions exist

only if the determinant of the corresponding matrix equation is zero. This implies

$$\begin{aligned} & A \left(\mathbf{N}_{LR}^{(p)}[\xi_L, ik] + \mathbf{S}_L \mathbf{D}_{LR}^{(p)}[\xi_L, ik] \right) \left(\mathbf{N}_{RL}^{(p)}[\xi_R, ik] + \mathbf{S}_R \mathbf{D}_{RL}^{(p)}[\xi_R, ik] \right) \\ &= \left(\xi_L + \mathbf{S}_R \right) e^{\xi_L h} \left(\xi_R + \mathbf{S}_L \right) e^{-\xi_R h} \left\{ \sum_{\ell=1}^{p+1} \binom{p+1}{\ell} (1)^{\ell+1} A^{-\ell} \right\}, \end{aligned} \quad (3.47)$$

which leads to the following result.

Theorem 8 *The p^{th} -order accurate un-iterated CHAMP time-stepping scheme for the advection-diffusion equation is stable provided there are no solutions to $G(A) = 0$ with $|Aj| > 1$, where*

$$\begin{aligned} G(A) \stackrel{\text{def}}{=} & \frac{A^{p+1}}{\sum_{\ell=1}^{p+1} \binom{p+1}{\ell} (1)^{\ell+1} A^{-\ell}} \\ & \frac{\left(\xi_L + \mathbf{S}_R \right) e^{\xi_L h}}{\left(\mathbf{N}_{LR}^{(p)}[\xi_L, ik] + \mathbf{S}_L \mathbf{D}_{LR}^{(p)}[\xi_L, ik] \right)} \frac{\left(\xi_R + \mathbf{S}_L \right) e^{-\xi_R h}}{\left(\mathbf{N}_{RL}^{(p)}[\xi_R, ik] + \mathbf{S}_R \mathbf{D}_{RL}^{(p)}[\xi_R, ik] \right)}, \end{aligned} \quad (3.48)$$

where $\xi_L(A)$ and $\xi_R(A)$ are defined by (3.44) with $\text{Re}(\xi_m) > 0$. This must be true for all $kh \in [\pi, \pi]$.

Using the same non-dimensional parameters defined in (3.25), z_L and z_R are now given by

$$z_L \stackrel{\text{def}}{=} \frac{\hat{u}_L^D}{2} + \sqrt{\frac{1}{\Delta t D_L} \frac{\sum_{\mu=0}^p \alpha_{\mu} A^{p-\mu}}{\beta_0} + \kappa^2 + \frac{(\hat{u}_L^D)^2}{4} + i\kappa (\hat{v}_L^D)}, \quad (3.49a)$$

$$z_R \stackrel{\text{def}}{=} \frac{\hat{u}_R^D}{2} + \sqrt{\frac{1}{\Delta t D_R} \frac{\sum_{\mu=0}^p \alpha_{\mu} A^{p-\mu}}{\beta_0} + \kappa^2 + \frac{(\hat{u}_R^D)^2}{4} + i\kappa (\hat{v}_R^D)}. \quad (3.49b)$$

which yields a non-dimensional $G(A) = G(A; K_{LR}, \mathbf{D}_{LR}, \lambda_{DL}, \kappa, p_L, p_R, z_L, z_R, \hat{u}_L^D, \hat{u}_R^D, \hat{v}_L^D, \hat{v}_R^D)$ given by

$$\begin{aligned} G(A) = & \frac{A^{p+1}}{\sum_{\ell=1}^{p+1} \binom{p+1}{\ell} (1)^{\ell+1} A^{-\ell}} \\ & \frac{\left(z_L + p_L \right) e^{z_L}}{\left(\mathbf{N}_{LR}^{(p)}[z_L] + p_L \mathbf{D}_{LR}^{(p)}[z_L] \right)} \frac{\left(z_R + p_R \right) e^{-z_R}}{\left(\mathbf{N}_{RL}^{(p)}[z_R] + p_R \mathbf{D}_{RL}^{(p)}[z_R] \right)}. \end{aligned} \quad (3.50)$$

The detailed expressions of $G(A)$ for the time-stepping amplification factor can be computed using a symbolic algebra package such as Maple. A sample algorithm for computing A for a second-order accurate CHAMP scheme is provided in Algorithm 9.

Algorithm 9: A sample MAPLE code that computes $G(A)$ for the time-stepping amplification factor of the advection-diffusion equation.

```
# CHAMP_Left and CHAMP_Right are pre-computed CHAMP conditions .

J:=Complex(0,1):
# Fourier transform the CHAMP conditions
CHAMP_Left_Fourier:=subs([hR=1,diff(UL,r2)=-J kappa,
    diff(UL,r2$2)=-kappa^2,
    diff(diff(UL,r1),r2)=-J kappa diff(UL,r1)], CHAMP_Left):
CHAMP_Right_Fourier:=subs([hL=1,diff(UR,r2)=-J kappa,
    diff(UR,r2$2)=-kappa^2,
    diff(diff(UR,r1),r2)=-J kappa diff(UR,r1)], CHAMP_Right):

# Substitute in solution ansatz
CHAMP_Left_s:=subs([UL=1,diff(UL,r1)=zL,diff(UL,r1$2)=zL^2],
    CHAMP_LeftL):
CHAMP_Right_s:=subs([UR=1,diff(UR,r1)=-zR,diff(UR,r1$2)=zR^2],
    CHAMP_RightL):

A_Denominator:=CHAMP_RightLF CHAMP_LeftLF:
A_Numerator:=(zL-pR) (1-zR) (-zR+pL) (1-zL)

G_A:=A^3/(3 A^2-3 A+1)-A_Denominator/A_Numerator:
```

3.6 The CHAMP Interface Conditions on Curvilinear Grids

In this section, how the governing equations and interface conditions are implemented on a curvilinear grid is described. To solve problems on complex geometry, one can make use of overset grids [17]. Overset grids consist of a set of overlapping structure grids. Each component grid may be Cartesian or curvilinear. A curvilinear grid is defined by a smooth

mapping

$$\mathbf{x} = \mathbf{G}(\mathbf{r}), \quad (3.51)$$

from the parameter space $\mathbf{r} \in [0, 1]^{n_d}$ to physical space \mathbf{x} .

The governing equations are first transformed to the parameter-space coordinates \mathbf{r} using the mapping method which uses of the chain rule to convert \mathbf{x} -derivatives to \mathbf{r} -derivatives. For example, using the summation convention,

$$\frac{\partial T(\mathbf{x})}{\partial x_i} = \frac{\partial r_k}{\partial x_i} \frac{\partial T(\mathbf{r})}{\partial r_k}, \quad (3.52)$$

$$\frac{\partial^2 T(\mathbf{x})}{\partial x_i \partial x_j} = \frac{\partial r_k}{\partial x_i} \frac{\partial r_l}{\partial x_j} \frac{\partial^2 T(\mathbf{r})}{\partial r_k \partial r_l} + \left(\frac{\partial}{\partial x_j} \frac{\partial r_j}{\partial x_i} \right) \frac{\partial T(\mathbf{r})}{\partial r_j}. \quad (3.53)$$

In curvilinear coordinates the Laplacian operator is written as

$$\Delta_{\mathbf{r},m} = \sum_{i,j} c_{ij}^m(\mathbf{r}^m) \partial_{r_i}^m \partial_{r_j}^m + \sum_i c_i^m(\mathbf{r}^m) \partial_{r_i}^m, \quad (3.54)$$

where

$$c_{ij}^m = \sum_k (\partial_{x_k} r_i^m) (\partial_{x_k} r_j^m), \quad (3.55a)$$

$$c_i^m = \sum_k \partial_{x_k} \partial_{x_k} r_i^m. \quad (3.55b)$$

Discrete approximations to these equations are formed using centred finite differences in parameter space.

Now consider deriving the CHAMP Dirichlet and Neumann operators on curvilinear grids defined by the mappings, $\mathbf{x} = \mathbf{G}_m(\mathbf{r}^m)$, $m = L, R$. The the normal derivative on side m , denoted by $\partial_{n,m}$, (here the normal \mathbf{n}_L is used from the left-side since the primary focus is on deriving the CHAMP condition for the left side) is written as

$$\partial_{n,m} = \mathbf{n}_L \cdot \nabla_{\mathbf{x},m} = \sum_i b_i^m(\mathbf{r}^m) \partial_{r_i}^m, \quad m = L, R, \quad (3.56a)$$

where

$$b_i^m \stackrel{\text{def}}{=} (\mathbf{n}_L \cdot \mathbf{r}_{\mathbf{x},m}) r_i^m = \sum_k n_{L,k} \frac{\partial r_i^m}{\partial x_k}, \quad m = L, R. \quad (3.56b)$$

The p^{th} -order accurate CHAMP interface conditions on curvilinear grids are written as

$$\left(\mathbf{N}_{LR}^{c,(p)} + \mathbf{S}_L \mathbf{D}_{LR}^{c,(p)} \right) T_L^{(j)}(\mathbf{r}^L) = \left(\partial_{n,R} + \mathbf{S}_L \right) T_R^{(j-1)}(\mathbf{r}^R - \Delta r^R), \quad (\mathbf{r}^L, \mathbf{r}^R) \in I_r, \quad (3.57)$$

where \mathbf{r}^L is a point in parameter space on the left interface, \mathbf{r}^R is the corresponding point on the right interface and Δr^R is the grid spacing in parameter space on the right grid. The sign for $\mathbf{r}^R - \Delta r^R$ in (3.57) is chosen so that the point is the first grid line inside the grid. Note that \mathbf{S}_L should be non-negative for well-posedness. To simplify the following discussion let us assume that the interface on the right grid occurs at $r_1^R = 0$ (left side) or $r_1^R = 1$ (right side). To ease notation let

$$h_R \stackrel{\text{def}}{=} \Delta r_1^R. \quad (3.58)$$

As for the Cartesian case, $T_R(h_R, r_2^R)$ and $\partial_{r_1^R} T_R(h_R, r_2^R)$ are expanded in Taylor series about points on the interface at $r_1^R = 0$,

$$T_R(h_R, r_2^R) = \sum_{j=0}^p \frac{h_R^j}{j!} \partial_{r_1^R}^j T_R(0, r_2^R) + O(h_R^{p+1}), \quad (3.59a)$$

$$\partial_x T_R(h_R, r_2^R) = \sum_{j=0}^{p-1} \frac{h_R^j}{j!} \partial_{r_1^R}^{j+1} T_R(0, r_2^R) + O(h_R^p). \quad (3.59b)$$

Expressions for the r_1^R -derivatives of T_R on the interface are derived in terms of derivatives of T_L on the interface. These derivatives will be denoted by the differential operators L_j^c ,

$$\partial_{r_1^R}^j T_R(\mathbf{r}^R) \stackrel{\text{def}}{=} L_j^c T_L(\mathbf{r}^L), \quad j = 0, 1, 2, \dots, \quad (\mathbf{r}^L, \mathbf{r}^R) \in I_r. \quad (3.60)$$

From the continuity of temperature on the interface we have that L_0^c is just the identity,

$$L_0^c = I. \quad (3.61)$$

To derive an expression for L_1^c we start from the jump condition on the heat flux

$$K_R(\partial_{n,R} \quad \mathbf{n}_L \quad \mathbf{u}_L^D) T_R(\mathbf{r}^R) = K_L(\partial_{n,L} \quad \mathbf{n}_L \quad \mathbf{u}_R^D) T_L(\mathbf{r}^L), \quad (\mathbf{r}^L, \mathbf{r}^R) \geq l_r, \quad (3.62)$$

which upon re-arrangement gives an expression for the r_1 -derivative of T_R on the interface in terms of derivatives of T_L ,

$$\begin{aligned} \partial_{r_1^R} T_R(\mathbf{r}^R) &= \frac{1}{b_1^R} \left\{ K_{LR} \partial_{n,L} + \mathbf{n}_L \cdot (\mathbf{u}_L^D \cdot K_{LR} \mathbf{u}_R^D) \sum_{i \neq 1} b_i^R \partial_{r_i^R} \right\} T_L(\mathbf{r}^L) \\ &\stackrel{\text{def}}{=} L_1^c T_L(\mathbf{r}^L), \quad (\mathbf{r}^L, \mathbf{r}^R) \geq l_r. \end{aligned} \quad (3.63)$$

To derive an expression for $\partial_{r_1^R}^2 T_R$ on the interface, the compatibility jump condition (3.10a) with $q = 1$ is used,

$$D_R(\Delta_{\mathbf{r},R} \quad \mathbf{u}_R^D \quad r_{\mathbf{x},R}) T_R(\mathbf{r}^R) = D_L(\Delta_{\mathbf{r},L} \quad \mathbf{u}_L^D \quad r_{\mathbf{x},L}) T_L(\mathbf{r}^L), \quad (\mathbf{r}^L, \mathbf{r}^R) \geq l_r, \quad (3.64)$$

which can be re-arranged to give

$$\begin{aligned} c_{11}^R \partial_{r_1^R}^2 T_R(\mathbf{r}^R) &= D_{LR}(\Delta_{\mathbf{r},L} \quad \mathbf{u}_L^D \quad r_{\mathbf{x},L}) T_L(\mathbf{r}^L) + \mathbf{u}_R^D \cdot r_{\mathbf{x},R} T_R(\mathbf{r}^R) \\ &\quad \sum_{i,j \neq 1,1g} c_{ij}^R \partial_{r_i^R} \partial_{r_j^R} T_R(\mathbf{r}^R) - \sum_i c_i^R \partial_{r_i^R} T_R(\mathbf{r}^R). \end{aligned} \quad (3.65)$$

Terms involving T_R on the right-side of (3.65) are now replaced with terms involving T_L , making use of L_0^c and L_1^c . The advection term on the right, for example, can be re-written as

$$\begin{aligned} (\mathbf{u}_R^D \cdot r_{\mathbf{x},R}) T_R(\mathbf{r}^R) &= d_1^R \partial_{r_1^R} T_R(\mathbf{r}^R) + d_2^R \partial_{r_2^R} T_R(\mathbf{r}^R) \\ &= d_1^R L_1^c T_L(\mathbf{r}^L) + d_2^R \partial_{r_2^R} T_L(\mathbf{r}^L), \quad (\mathbf{r}^L, \mathbf{r}^R) \geq l_r, \end{aligned} \quad (3.66)$$

where

$$d_i^R \stackrel{\text{def}}{=} \sum_k \mathbf{u}_{R,k}^D \frac{\partial r_i^R}{\partial x_k}. \quad (3.67)$$

Some further manipulations leads to an expression for $\partial_{r_1^R}^2 T_R$ on the interface

$$\begin{aligned} \partial_{r_1^R}^2 T_R(\mathbf{r}^R) &= \frac{1}{c_{11}^R} \left\{ \mathbf{D}_{LR}(\Delta_{\mathbf{r},L} \quad \mathbf{u}_L^D \quad r_{\mathbf{x},L}) + d_1^R L_1^c + d_1^R \partial_{r_2^R} \right. \\ &\quad \left(c_{12}^R + c_{21}^R \right) \partial_{r_2^R} L_1^c \quad c_{22}^R \partial_{r_2^R} \partial_{r_2^R} \\ &\quad \left. c_1^R L_1^c \quad c_2^R \partial_{r_2^R} \right\} T_L(\mathbf{r}^L), \\ &\stackrel{\text{def}}{=} L_2^c T_L(\mathbf{r}^L), \quad (\mathbf{r}^L, \mathbf{r}^R) \supseteq l_r. \end{aligned} \quad (3.68)$$

This process can be continued to find L_j^c , $j = 3, 4, \dots$

To define the p^{th} -order accurate CHAMP interface conditions, one starts from the expression for the mixed derivative of $T_R(\mathbf{r}^R \quad \Delta r^R)$

$$\left(\partial_{n,R} + \mathbf{S}_L \right) T_R(\mathbf{r}^R \quad \Delta r^R) = \left(b_1^R(\mathbf{r}^R) \partial_{r_1^R} \quad b_2^R(\mathbf{r}^R) \partial_{r_2^R} + \mathbf{S}_L \right) T_R(\mathbf{r}^R \quad \Delta r^R), \quad (3.69)$$

where b_i^R are the coefficients associated with the normal derivative (3.56). Substituting the Taylor series (3.59) into (3.69) gives an expression involving derivatives of T_R on the interface. These derivatives of T_R are converted into derivatives of T_L using the operators L_j^c and this leads to

$$\begin{aligned} \left(\partial_{n,R} + \mathbf{S}_L \right) T_R(\mathbf{r}^R \quad \Delta r^R) &= \left(b_1^R(\mathbf{r}^R) \mathbf{N}_{LR}^{r,(p)} \right. \\ &\quad \left. b_2^R(\mathbf{r}^R) \left\{ (\partial_{r_2^R} \mathbf{D}_{LR}^{r,(p)}) + \mathbf{D}_{LR}^{r,(p)} \partial_{r_2^R} \right\} + \mathbf{S}_L \mathbf{D}_{LR}^{r,(p)} \right) T_L(\mathbf{r}^L), \end{aligned} \quad (3.70)$$

where the parameter space Dirichlet and Neumann-like operators are defined by

$$\mathbf{D}_{LR}^{r,(p)} T_L(\mathbf{r}^L) \stackrel{\text{def}}{=} \sum_{\ell=0}^p \frac{h_R^\ell}{\ell!} L_\ell^c T_L(\mathbf{r}^L), \quad (\mathbf{r}^L, \mathbf{r}^R) \supseteq l_r, \quad (3.71a)$$

$$\mathbf{N}_{LR}^{r,(p)} T_L(\mathbf{r}^L) \stackrel{\text{def}}{=} \sum_{\ell=0}^{p-1} \frac{h_R^\ell}{\ell!} L_{\ell+1}^c T_L(\mathbf{r}^L) \quad (\mathbf{r}^L, \mathbf{r}^R) \supseteq l_r. \quad (3.71b)$$

Note that the following relationship has been used

$$\begin{aligned}
\partial_{r_2^R} T_R(\mathbf{r}^R \quad \Delta r^R) &= \partial_{r_2^R} \mathbf{D}_{LR}^{r,(p)} T_L(\mathbf{r}^L), \\
&= \partial_{r_2^R} \sum_{\ell=0}^p \frac{h_R^\ell}{\ell!} L_\ell^c(r_2^R) T_L(\mathbf{r}^L), \\
&= \sum_{\ell=0}^p \frac{h_R^\ell}{\ell!} \partial_{r_2^R} (L_\ell^c(r_2^R)) T_L(\mathbf{r}^L) + L_\ell^c(r_2^R) \partial_{r_2^R} T_L(\mathbf{r}^L), \\
&= \left\{ (\partial_{r_2^R} \mathbf{D}_{LR}^{r,(p)}) + \mathbf{D}_{LR}^{r,(p)} \partial_{r_2^R} \right\} T_L(\mathbf{r}^L).
\end{aligned} \tag{3.72}$$

These results are summarized in the following Theorem.

Theorem 9 *The p^{th} -order accurate CHAMP interface condition for the diffusion equation on curvilinear grids is*

$$\left(\mathbf{N}_{LR}^{c,(p)} + \mathbf{S}_L \mathbf{D}_{LR}^{c,(p)} \right) T_L(\mathbf{r}^L) = \left(\partial_{n,R} + \mathbf{S}_L \right) T_R(\mathbf{r}^R \quad \Delta r^R), \quad (\mathbf{r}^L, \mathbf{r}^R) \geq l_r, \tag{3.73a}$$

with

$$\mathbf{D}_{LR}^{c,(p)} T_L(\mathbf{r}^L) \stackrel{\text{def}}{=} \sum_{\ell=0}^p \frac{(\Delta r_1^R)^\ell}{\ell!} L_\ell^c T_L(\mathbf{r}^L), \tag{3.74a}$$

$$\mathbf{N}_{LR}^{c,(p)} T_L(\mathbf{r}^L) \stackrel{\text{def}}{=} \sum_{\ell=0}^{p-1} \frac{(\Delta r_1^R)^\ell}{\ell!} \left(b_1^R(\mathbf{r}^R) L_{\ell+1}^c \quad b_2^R(\mathbf{r}^R) \partial_{r_2^R} L_\ell^c \right) T_L(\mathbf{r}^L), \tag{3.74b}$$

where the operators L_ℓ^c are constructed from the compatibility interface conditions (3.10) following the procedure outlined above, and where b_i^R are the coefficients associated with the normal derivative (3.56). The choice of sign in Δr_1^R depends on whether the interface occurs at $r_1^R = 0$ (plus) or $r_1^R = 1$ (minus).

3.7 Numerical Results

In this section, computational results are presented to verify the accuracy and stability of the CHAMP time-stepping schemes. The results presented in this section are solved using either a second-order or fourth-order accurate CHAMP scheme. Both spatial and temporal discretization are done to second or fourth-order on a uniform grid, and the implicit BDF2 or BDF4 scheme is chosen to discretize the solution in time, with difference formulae chosen to

match the order of accuracy of the spatial discretization of the governing equations. Centered finite differences are used in the approximations of all terms in the governing equations and the CHAMP interface conditions since the problems considered here are assumed to be diffusion dominated². In Section 3.7.1, numerical solutions of the time dependent CHT problems with domains consisting of two adjacent rectangles and two concentric annuli are presented to verify the fourth-order spatial and temporal accuracy of the un-iterated CHAMP time-scheme. An exact solution can be worked out for the problem involving two adjacent rectangles, and this is done in Section 3.7.1.1. For problem involving two concentric annuli, an exact solution is not known for the case when the advective velocities are non-zero, and so a semi-analytical solution is used as discussed in Section 3.7.1.2. In Section 3.7.2 computations are performed for problems involving more complicated geometries. A rotated square-square geometry and a stretched square-square geometry are presented in Sections 3.7.2.1 and 3.7.2.2 to verify the accuracy of the CHAMP scheme using the method of manufactured solutions. In Sections 3.7.2.3 and 3.7.2.4, simulations are performed on curvilinear domains with more complex mapping functions.

3.7.1 Verification with Exact Solutions for Time Dependent Problems

In this section, the spatial and temporal accuracy of a fourth-order accurate un-iterated CHAMP time-stepping scheme is verified using exact solutions of time dependent CHT problems with advection-diffusion equations. Computations are first performed on a double-square domain in Section 3.7.1.1 and then on a double-annulus domain in Section 3.7.1.2, with various material parameters and advection velocities chosen to demonstrate the stability properties of the CHAMP scheme.

3.7.1.1 *Adjacent Rectangles*

Consider the exact solution to the time-dependent CHT problem for a region consisting of two adjacent rectangles. The left and right domains are denoted as $\Omega_L = [x_a, 0] \quad [y_a, y_b]$

²Upwind differences can also be considered for the advection terms, as needed, for advection-dominated problems, but such problems are not considered in this thesis.

and $\Omega_R = [0, x_b] \cup [y_a, y_b]$ respectively. The time dependent CHT problem is given by

$$\partial_t T_m + u_m \partial_x T_m + v_m \partial_y T_m = D_m \Delta T_m, \quad \text{for } \mathbf{x} \in \Omega_m, \quad m = L, R, \quad (3.75a)$$

$$[T]_l = 0, \quad \text{for } y \in [y_a, y_b], \quad x = 0, \quad (3.75b)$$

$$[K(\partial_x T - \frac{1}{D} u T)]_l = 0, \quad \text{for } y \in [y_a, y_b], \quad x = 0, \quad (3.75c)$$

$$T_L(x_a, y, t) = 0, \quad T_R(x_b, y, t) = 0, \quad \text{for } y \in [y_a, y_b], \quad (3.75d)$$

$$T_m(x, y, 0) = T_m^{\text{IC}}(x, y), \quad \text{for } \mathbf{x} \in \Omega_m, \quad m = L, R, \quad (3.75e)$$

where $m = L, R$ indicates the left or right domain and the velocity in each domain, $\mathbf{u}_m = [u_m, v_m]^T$, is assumed to be constant. Solutions are assumed to be periodic in y . An exact solution can be found of the form

$$T_m(x, y, t) = e^{-s^2 t} \hat{T}(x) e^{iky}, \quad m = L, R, \quad (3.76)$$

where s is an eigenvalue and k is chosen so that $k(y_b - y_a) = 2\pi\mu$ for an integer μ . Solutions for \hat{T}_m take the form

$$\hat{T}_m = A_m e^{r_m^+ x} + B_m e^{r_m x} \quad (3.77)$$

where r_m is defined as

$$r_m = \frac{u_m}{2D_m} \sqrt{\frac{u_m^2}{4D_m^2} + k^2 + \frac{s^2}{D_m} - \frac{ikv_m}{D_m}}, \quad m = L, R. \quad (3.78)$$

and A_m and B_m are chosen so that the boundary and interface conditions are satisfied. Substituting the solution ansatz into the boundary conditions and matching conditions at the interface leads to a homogeneous system in terms of the constants A_L, B_L, A_R, B_R and

the eigenvalue s , given by

$$\begin{pmatrix} 1 & 1 & 1 & 1 \\ K_L r_L^+ & u_L \frac{K_L}{D_L} & K_L r_L & u_L \frac{K_L}{D_L} & K_R r_R^+ + u_R \frac{K_R}{D_R} & K_R r_R + u_R \frac{K_R}{D_R} \\ e^{r_L^+ x_a} & & e^{r_L x_a} & & 0 & 0 \\ 0 & & 0 & & e^{r_R^+ x_b} & e^{r_R x_b} \end{pmatrix} A = 0, \quad (3.79)$$

with

$$A = \begin{pmatrix} A_L \\ B_L \\ A_R \\ B_R \end{pmatrix}. \quad (3.80)$$

Non-trivial solutions exist if the determinant of the coefficient matrix in (3.79) is zero, and this leads to a determinant condition for s . For a given μ that defines the wave number k in the y direction, there is an infinite set of real roots s . Once the eigenvalues are found, nontrivial values for the coefficients A_L , B_L , A_R and B_R can be found in the nullspace of the (singular) coefficient matrix. For solutions that are complex, only the real part or the imaginary part are used for the exact solution. Table 3.1 gives selected eigenvalues and corresponding coefficients for some choices of the materials parameters. Here A_L is normalized to equal to 1, with other coefficients scaled accordingly.

Table 3.1: Selected eigenvalues s and coefficients for two selected cases on double-rectangle domain.

Adjacent Rectangles							
Case 1: $D_L = 1$, $K_L = 10$, $D_R = 10$, $K_R = 1$, $\mathbf{u}_L = [1, 2]^T$, $\mathbf{u}_R = [3, 4]^T$.							
ν	s	A_L	B_L	A_R	B_R		
1	1.325	0.759i	1	$0.587 + 0.023i$	$0.129 + 0.055i$	0.934	0.186i
Case 2: $D_L = 1$, $K_L = 1$, $D_R = 1$, $K_R = 1$, $\mathbf{u}_L = [1, 1]^T$, $\mathbf{u}_R = [1, 1]^T$.							
ν	s	A_L	B_L	A_R	B_R		
0	0.707	1	$0.540 + 0.842i$	0.416	0.909i	$0.540 + 0.842i$	

Computations are performed on a domain defined by $x_a = -\pi$, $x_l = 0$, $x_b = \pi$, $y_a = 0$ and $y_b = 2\pi$. The grids used for this domain are two Cartesian grids with a target grid-spacing chosen to be approximately $\Delta s^{(j)} = \pi/(15j)$ for a resolution factor j , $j = 1, 2, 4$. The grid is denoted by $G_{dr}^{(j)}$. A sample rectangular grid is given in the left of Figure 3.5. Table 3.2 presents a grid refinement study for selected material parameters and advection velocities using both the second-order and fourth-order accurate un-iterated CHAMP time-stepping scheme. The initial data to this problem is obtained from the exact solutions, along with the past temperature values required by the multi-step schemes. The coefficients and the eigenvalues for the exact solutions used here are given in Table 3.1. The scheme is run with $\Delta t = \Delta s$ to a final time $t_{\text{nal}} = 5$. Contour plots of the solution and corresponding error at $t_{\text{nal}} = 5$ using the fourth-order CHAMP scheme for Case 1 in Table 3.2 are shown in the middle and right of Figure 3.5. For the CHAMP2 case, the error decreases by a factor of 4 as the grid size decreases by a factor of 2, indicating a 2nd-order convergence rate of the tested scheme. For the CHAMP4 case, the error decreases by a factor of 16 as the mesh spacing decreases by a factor of 2, which indicates a 4th-order convergence rate.

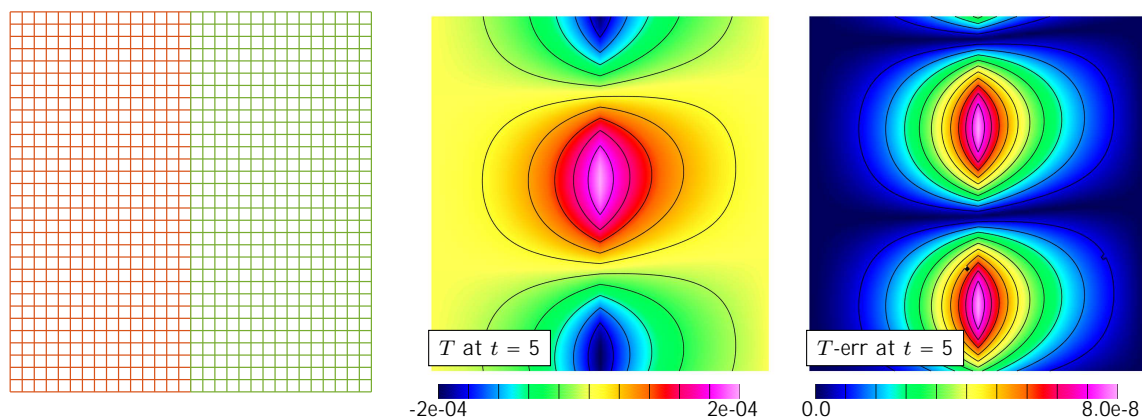


Figure 3.5: Double-rectangle results. Left: a sample grid for the double-rectangle geometry. Middle: BDF4 solution at $t_{\text{nal}} = 5$ for Case 1 on grid $G^{(4)}$. Right: error at $t_{\text{nal}} = 5$ on grid $G^{(4)}$ for the same case.

3.7.1.2 Concentric Annuli

In this section, the accuracy of the CHAMP scheme is verified for time-dependent CHT problems on a domain consisting of two concentric annuli. The exact analytical solution to

Table 3.2: A convergence study for the double-rectangle problem using the time-dependent exact solution with selected thermal parameters.

Adjacent Rectangles									
Case 1: $\nu = 1$, $D_L = 1$, $K_L = 10$, $D_R = 10$, $K_R = 1$, $\mathbf{u}_L = [1, 2]^T$, $\mathbf{u}_R = [3, 4]^T$.									
CHAMP2 results: $t_{\text{nal}} = 5$, max-iteration = 1.									
j	Δs	λ_{DL}	max error left	ratio	rate	max error right	ratio	rate	
1	2.09e 01	4.77e+00	2.228e 04			2.251e 04			
2	1.01e 01	9.87e+00	4.333e 05	5.14	2.36	4.355e 05	5.17	2.37	
4	5.07e 02	1.97e+01	9.323e 06	4.65	2.22	9.346e 06	4.66	2.22	
CHAMP4 results: $t_{\text{nal}} = 5$, max-iteration = 1.									
j	Δs	λ_{DL}	max error left	ratio	rate	max error right	ratio	rate	
1	2.09e 01	4.77e+00	3.049e 05			3.087e 05			
2	1.01e 01	9.87e+00	1.477e 06	20.64	4.37	1.489e 06	20.73	4.37	
4	5.07e 02	1.97e+01	7.872e 08	18.76	4.23	7.906e 08	18.84	4.24	
Case 2: $\nu = 0$, $D_L = 1$, $K_L = 1$, $D_R = 1$, $K_R = 1$, $\mathbf{u}_L = [1, 1]^T$, $\mathbf{u}_R = [1, 1]^T$.									
CHAMP2 results: $t_{\text{nal}} = 5$, max-iteration = 1.									
j	Δs	λ_{DL}	max error left	ratio	rate	max error right	ratio	rate	
1	2.09e 01	4.77e+00	1.322e 05			9.143e 06			
2	1.01e 01	9.87e+00	3.203e 06	4.13	2.05	2.582e 06	3.54	1.82	
4	5.07e 02	1.97e+01	7.946e 07	4.03	2.01	6.939e 07	3.72	1.90	
CHAMP4 results: $t_{\text{nal}} = 5$, max-iteration = 1.									
j	Δs	λ_{DL}	max error left	ratio	rate	max error right	ratio	rate	
1	2.09e 01	4.77e+00	3.765e 07			7.024e 07			
2	1.01e 01	9.87e+00	2.04e 08	18.37	4.20	3.435e 08	20.45	4.35	
4	5.07e 02	1.97e+01	1.238e 09	16.55	4.05	1.978e 09	17.37	4.12	

this problem is unavailable, and instead a semi-exact solution is derived.

For the double-annulus problem, the initial boundary value problem in polar coordi-

nates for the advection diffusion equation is

$$\partial_t T_m + u_m^r \partial_r T_m + \frac{u_m^\theta}{r} \partial_\theta T_m = D_m \left(\frac{1}{r} (r \partial_r T_m)_r + \frac{1}{r^2} \partial_\theta^2 T_m \right), \quad \mathbf{x} \in \Omega_m, \quad (3.81a)$$

$$[T]_l = 0, \quad \theta \in [0, 2\pi), \quad (3.81b)$$

$$\left[\mathcal{K} \partial_r T \quad u^r \frac{\mathcal{K}}{D} T \right]_l = 0, \quad \theta \in [0, 2\pi), \quad (3.81c)$$

$$T_L(r_a, \theta, t) = 0, \quad T_R(r_b, \theta, t) = 0, \quad \theta \in [0, 2\pi), \quad (3.81d)$$

$$T_m(r, \theta, 0) = T_m^{\text{IC}}(r, \theta), \quad \mathbf{x} \in \Omega_m, \quad (3.81e)$$

where $m = L, R$ and u_m^r, u_m^θ are the radial and circumferential components of the velocity, $\mathbf{u} = u_m^r \hat{\mathbf{r}} + u_m^\theta \hat{\boldsymbol{\theta}}$. Provided $u_m^r = u_m^r(r)$ and $u_m^\theta = u_m^\theta(r)$ are functions of r alone, separable solutions can be found of the form

$$T_m(r, \theta, t) = e^{-s^2 t} \phi_m(r) e^{i\nu\theta}, \quad (3.82)$$

where ν is an integer, s is an eigenvalue and $\phi_m(r)$ is an eigenfunction. Substituting the ansatz (3.82) into (3.81) leads to a one-dimensional eigenvalue problem for s and $\phi_m(r)$, given by

$$r^2 \partial_{rr} \phi_m + \left(r \frac{r^2 u_m^r}{D_m} \right) \partial_r \phi_m + \left(\nu^2 + \frac{i\nu r u_m^\theta}{D_m} \right) \phi_m = \frac{s}{D_m} r^2 \phi_m. \quad (3.83)$$

This eigenvalue problem is solved using a finite difference approximation with sufficient accuracy to be considered as an *exact* solution. Table (3.3) provides some values for the eigenvalues s for different material parameters for the domain with $r_a = 1$, $r_l = 2$ and $r_b = 3$.

Simulations are run using both the second-order and fourth-order accurate un-iterated CHAMP scheme on a double-annulus domain defined by $r_a = 1$, $r_b = 3$, $r_l = 2$. The mapping function is given in (2.126), and the grid for the calculation of T_L uses $\alpha = 1$, $\beta = 2$ and $\omega = 2\pi$, while the grid for the calculation of T_R uses $\alpha = 3$, $\beta = 2$, and $\omega = 2\pi$. The grid for this particular mapping function is denoted by $G_{\text{da}}^{(j)}$, with resolution factor j , $j = 1, 2, 4$. A target mesh spacing $\Delta s^{(j)} = 1/(10j)$ is chosen in both the radial and circumferential direction. A sample double-annulus domain is given in the left of Figure 3.6.

Table 3.3: Selected eigenvalues s_ν of the exact solutions for three selected cases on double-annulus domain.

Concentric Annuloi	
Case 1: $D_L = 1, K_L = 10, D_R = 10, K_R = 1.$ $\mathbf{u}_L = [1, 2], \mathbf{u}_R = [3, 4].$	
ν	s
2	1.694 0.693i
Case 2: $D_L = 1, K_L = 10, D_R = 10, K_R = 1.$ $\mathbf{u}_L = [0.1, 0.2], \mathbf{u}_R = [0.3, 0.4].$	
ν	s
2	1.859 0.0639i

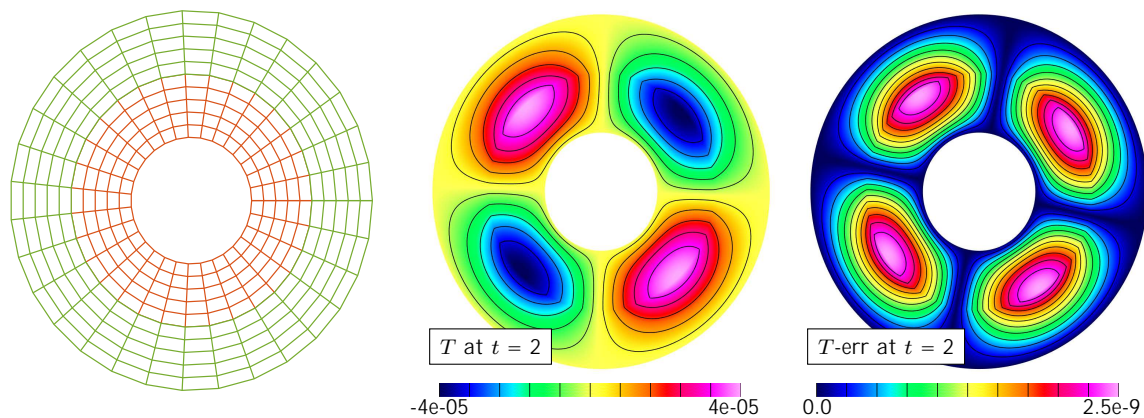


Figure 3.6: Double-annulus results. Left: a sample grid for the double-annulus geometry. Middle: BDF4 solution at $t_{\text{nal}} = 2$ for Case 2 on grid $G^{(4)}$. Right: error at $t_{\text{nal}} = 2$ on grid $G^{(4)}$ for the same case.

Different thermal coefficients and advection velocities are chosen and the scheme is tested with just one sub-iteration at each time step. Maximum error and the estimated convergence rate at $t_{\text{nal}} = 2$ are shown in Table 3.4. Solution and error contours at t_{nal} for Case 2 in Table 3.4 using the fourth-order accurate CHAMP scheme are presented in the middle and right of Figure 3.6. For all the case tested, the ratio between errors in nearby resolutions are approximately equal to 16 or 4, which indicates a fourth-order or second-order convergence rate.

Table 3.4: A convergence study for the double-annulus problem using the time-dependent exact solution with selected thermal parameters.

Concentric Annuli										
Case 1: $\nu = 2$, $D_L = 1$, $K_L = 10$, $D_R = 10$, $K_R = 1$, $\mathbf{u}_L = [1, 2]^T$, $\mathbf{u}_R = [3, 4]^T$.										
CHAMP2 results: $t_{\text{nal}} = 2$, max-iteration = 1.										
j	Δs	λ_{DL}	max error left	ratio	rate	max error right	ratio	rate		
1	1.00e 01	1.00e+01	1.068e 04			1.096e 04				
2	5.00e 02	2.00e+01	2.226e 05	4.80	2.26	2.252e 05	4.87	2.28		
4	2.50e 02	4.00e+01	5.161e 06	4.31	2.11	5.191e 06	4.34	2.12		
CHAMP4 results: $t_{\text{nal}} = 2$, max-iteration = 1.										
j	Δs	λ_{DL}	max error left	ratio	rate	max error right	ratio	rate		
1	1.00e 01	1.00e+01	7.565e 06			7.758e 06				
2	5.00e 02	2.00e+01	3.646e 07	20.75	4.37	3.697e 07	20.98	4.39		
4	2.50e 02	4.00e+01	2.006e 08	18.17	4.18	2.021e 08	18.29	4.19		
Case 2: $\nu = 2$, $D_L = 1$, $K_L = 10$, $D_R = 10$, $K_R = 1$, $\mathbf{u}_L = [0.1, 0.2]^T$, $\mathbf{u}_R = [0.3, 0.4]^T$.										
CHAMP2 results: $t_{\text{nal}} = 2$, max-iteration = 1.										
j	Δs	λ_{DL}	max error left	ratio	rate	max error right	ratio	rate		
1	1.00e 01	1.00e+01	1.131e 05			e 05				
2	5.00e 02	2.00e+01	2.503e 06	4.52	2.18	2.519e 06	4.56	2.19		
4	2.50e 02	4.00e+01	5.879e 07	4.26	2.09	5.892e 07	4.27	2.10		
CHAMP4 results: $t_{\text{nal}} = 2$, max-iteration = 1.										
j	Δs	λ_{DL}	max error left	ratio	rate	max error right	ratio	rate		
1	1.00e 01	1.00e+01	1.049e 06			1.077e 06				
2	5.00e 02	2.00e+01	4.751e 08	22.08	4.46	4.799e 08	22.44	4.49		
4	2.50e 02	4.00e+01	2.549e 09	18.64	4.22	2.557e 09	18.77	4.23		

3.7.2 Verification Using Manufactured Solutions on Various Geometries

In this section, the accuracy of the un-iterated CHAMP scheme is verified using the method of manufactured solutions. The manufactured solutions used have the form

$$T_m = a_m \sin(f_{m,x}x + \phi_{m,x}) \sin(f_{m,y}y + \phi_{m,y}) \sin(f_{m,t}t), \quad (3.84)$$

where $f_{m,x}$, $\phi_{m,x}$, $f_{m,y}$, $\phi_{m,y}$ and $f_{m,t}$ are constants chosen later. Computations are performed for various domain geometries using Cartesian grids and curvilinear grids, some of

which being non-orthogonal. The calculations assume Dirichlet boundary conditions on all boundaries. Sections 3.7.2.1 and 3.7.2.2 present computational results for the CHAMP scheme on domains consisting of two squares that are either rotated or sheared. Problems with curvilinear domains are considered in Sections 3.7.2.3 and 3.7.2.4.

3.7.2.1 Rotated Squares

The first geometry considers the same configuration described in Section 2.9.3.1, where the domain consists of two adjacent squares that are both rotated about the bottom left corner. The mapping function for this configuration was given in (2.140). The grid for this particular mapping function is denoted by $G_{\text{dr},r}^{(j)}$ with a resolution factor j given by $j = 2, 4, 8$. A sample grid is presented in the left of Figure 3.7 with the parameters chosen to be $\theta_0 = 3\pi/4$, $\beta_0 = 1$ for the left grid and $\theta_0 = 3\pi/4$, $\beta_0 = 0$ for the right grid.

Table 3.5: Constants in manufactured solutions used for rotated-square geometry.

a_L	$f_{L,x}$	$f_{L,y}$	$\phi_{L,x}$	$\phi_{L,y}$	$f_{L,t}$	a_R	$f_{R,x}$	$f_{R,y}$	$\phi_{R,x}$	$\phi_{R,y}$	$f_{R,t}$
0.8	1.2	0.3	1.2	1.1	0.6	0.6	1.5	1.7	0.4	0.8	0.6

Numerical simulations are performed using different thermal coefficients and advection velocities, and solutions are run to a final time $t_{\text{nal}} = 0.1$ using both the second-order accurate and fourth-order accurate un-iterated CHAMP schemes. Parameters in the manufactured solutions are presented in Table 3.5. The maximum error in the discrete solution and the estimated convergence rate at t_{nal} for different grid resolutions are given in Table 3.6. The solution and error contours at t_{nal} for Case 1 computed using the fourth-order accurate CHAMP scheme on the finest grid are shown in Figure 3.7. Convergence plots showing errors as a function of mesh spacing Δs are presented in Figure 3.8. The slopes for each curve agrees with their reference lines, which indicates second-order accuracy for CHAMP2 and fourth-order accuracy for CHAMP4.

3.7.2.2 Sheared Squares

The second geometry considers a domain involving two adjacent squares that are both sheared in the same direction. The mapping function for this geometry was given in (2.141), where α_0 determines the displacement of the points in a fixed direction, β_0 is a constant and

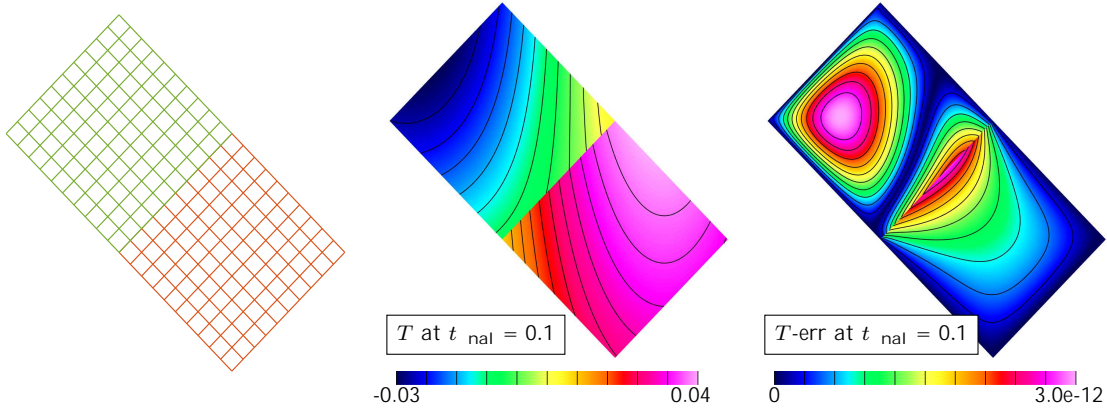


Figure 3.7: Rotated-square results. Left: a sample grid for a rotated-square geometry. Middle: BDF4 solution at $t_{\text{nal}} = 0.1$ for Case 1 on grid $G^{(8)}$. Right: error at $t_{\text{nal}} = 2$ on grid $G^{(8)}$ for the same case.

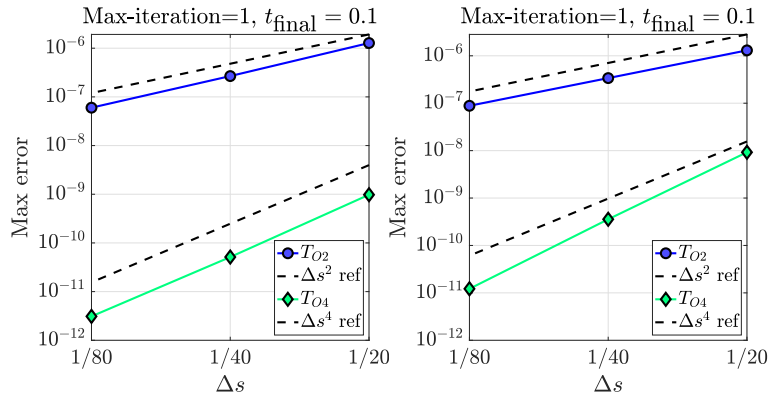


Figure 3.8: Convergence plots for rotated-square geometry. Left: max-norm errors as a function of mesh spacing for Case 1 at $t_{\text{nal}} = 0.1$. Right: max-norm errors as a function of mesh spacing for Case 2 at $t_{\text{nal}} = 0.1$.

$\mathbf{r} = [r_1, r_2]^T$ are the coordinates in the computational domain. The physical grid is denoted by $G_{\text{dr},s}^{(j)}$ with resolution factor j chosen to be $j = 2, 4, 8$. A coarse version of the grid used in the computation is presented in Figure 3.9 with parameters chosen to be $\alpha_0 = 1$ and $\beta_0 = 1$ for the left grid and $\alpha_0 = 1$ and $\beta_0 = 0$ for the right grid. Parameters in the manufactured solutions are given in Table 3.7.

Numerical simulations are performed using both the second-order and fourth-order accurate un-iterated CHAMP schemes for different material parameters and advection velocities. The maximum error in the discrete solution and corresponding convergence rates for

Table 3.6: A convergence study for the un-iterated CHAMP scheme on a rotated-square domain using the trigonometric manufactured solution with various choices of material parameters.

Rotated Squares									
Case 1: $D_L = 1, D_R = 1, K_L = 1, K_R = 1, \mathbf{u}_L = [1, 1]^T, \mathbf{u}_R = [1, 1]^T$.									
CHAMP2 results: $t_{\text{nal}} = 0.1, \text{max-iteration} = 1$.									
j	Δs	λ_{DL}	max error left	ratio	rate	max error right	ratio	rate	
2	5.00e 02	2.00e+00	4.169e 07			1.277e 06			
4	2.50e 02	4.00e+00	1.476e 07	2.82	1.50	2.675e 07	4.77	2.25	
8	1.25e 02	8.00e+00	4.476e 08	3.30	1.72	5.998e 08	4.46	2.16	
CHAMP4 results: $t_{\text{nal}} = 0.1, \text{max-iteration} = 1$.									
j	Δs	λ_{DL}	max error left	ratio	rate	max error right	ratio	rate	
2	5.00e 02	2.00e+00	9.773e 10			8.505e 10			
4	2.50e 02	4.00e+00	5.128e 11	19.06	4.25	5.078e 11	16.75	4.07	
8	1.25e 02	8.00e+00	2.917e 12	17.58	4.14	3.099e 12	16.38	4.03	
Case 2: $D_L = 0.9, D_R = 9.6, K_L = 7.3, K_R = 0.5, \mathbf{u}_L = [0.2, 0.4]^T, \mathbf{u}_R = [0.8, 0.7]^T$.									
CHAMP2 results: $t_{\text{nal}} = 0.1, \text{max-iteration} = 1$.									
j	Δs	λ_{DL}	max error left	ratio	rate	max error right	ratio	rate	
2	5.00e 02	1.80e+00	9.844e 07			1.302e 06			
4	2.50e 02	3.60e+00	2.427e 07	4.06	2.02	3.387e 07	3.84	1.94	
8	1.25e 02	7.20e+00	5.911e 08	4.11	2.04	8.826e 08	3.84	1.94	
CHAMP4 results: $t_{\text{nal}} = 0.1, \text{max-iteration} = 1$.									
j	Δs	λ_{DL}	max error left	ratio	rate	max error right	ratio	rate	
2	5.00e 02	1.80e+00	4.162e 10			9.235e 09			
4	2.50e 02	3.60e+00	1.698e 11	24.51	4.62	3.566e 10	25.90	4.69	
8	1.25e 02	7.20e+00	7.291e 13	23.29	4.54	1.218e 11	29.26	4.87	

different grid resolutions are computed at $t_{\text{nal}} = 0.1$ and listed in Table 3.8. Contour plots of the solution and error for Case 1 are presented in the middle and right plots of Figure 3.9. The convergence plots in Figure 3.10 confirm second-order or fourth-order convergence rates of the two CHAMP schemes for all of the cases tested.

Table 3.7: Constants in manufactured solutions used for sheared-square geometry.

a_L	$f_{L,x}$	$f_{L,y}$	$\phi_{L,x}$	$\phi_{L,y}$	$f_{L,t}$	a_R	$f_{R,x}$	$f_{R,y}$	$\phi_{R,x}$	$\phi_{R,y}$	$f_{R,t}$
0.5	1.4	0.1	1.7	1.1	0.8	0.6	1.6	0.2	0.5	0.6	0.8

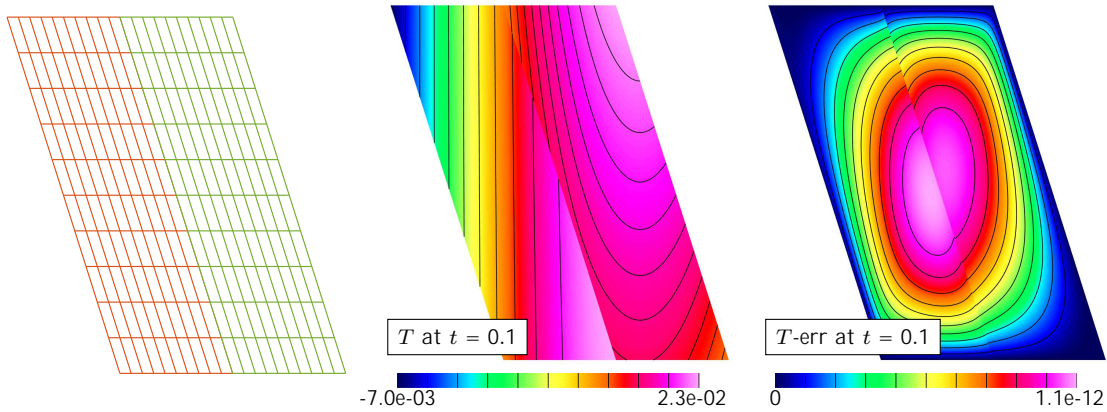


Figure 3.9: Stretched-square results. Left: a sample grid for a stretched-square geometry. Middle: BDF4 solution at $t_{\text{nal}} = 0.1$ on grid $G^{(8)}$ for Case 1. Right: error at $t_{\text{nal}} = 0.1$ on grid $G^{(8)}$ for the same case.

3.7.2.3 Wavy Geometry with Orthogonal Grid at Interface

The next example considers a curvilinear domain consisting of curved boundaries defined by cosine functions. For this mapping the grid lines at the interface are orthogonal locally, but not orthogonal elsewhere. The mapping function is given as

$$\mathbf{x} = \mathbf{G}_{\text{dw},c}(\mathbf{r}) = (1 - r_2)\mathbf{C}_{\text{top}}(r_1) + r_2\mathbf{C}_{\text{bot}}(r_1), \quad (3.85)$$

where $\mathbf{r} = [r_1, r_2]^T$ are the coordinates in the computational space, and the boundary functions $\mathbf{C}_{\text{top}}(r_1)$ and $\mathbf{C}_{\text{bot}}(r_1)$ were given previously in (2.143). A sample curvilinear grid with $a_1 = 1$, $a_2 = 1$, $b_1 = 1$ and $\delta_0 = 1$ for the left sub-domain and $a_1 = 1$, $a_2 = 1$, $b_1 = 0$ and $\delta_0 = 1$ for the right sub-domain is illustrated in Figure 3.11. For this setup, the curvilinear grid is denoted by $G_{\text{dw},c}^{(j)}$ with the resolution factor j chosen to be $j = 2, 4, 8$. Parameters in the manufactured solutions are given in Table 3.9.

Different thermal coefficients and advection velocities are chosen to test both the second-order and fourth-order accurate un-iterated CHAMP time-stepping scheme, and the

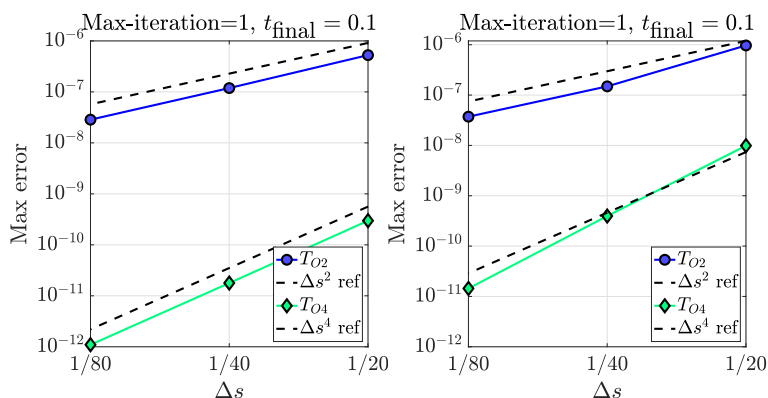


Figure 3.10: Convergence plots for stretched-square geometry. Left: max-norm errors as a function of mesh spacing for Case 1 at $t_{\text{nal}} = 0.1$. Right: max-norm errors as a function of mesh spacing for Case 2 at $t_{\text{nal}} = 0.1$.

maximal error in the discrete solutions at $t_{\text{nal}} = 0.1$ are given in Table 3.10. The solution and error contours at t_{nal} for Case 2 on the finest grid are plotted in Figure 3.11. Figure 3.12 plots the max-norm error as a function of mesh spacing for various cases presented in Table 3.9. The grid refinement study shows that the CHAMP scheme, with no sub-iterations, is stable and second or fourth-order accurate for the given choices of the parameters

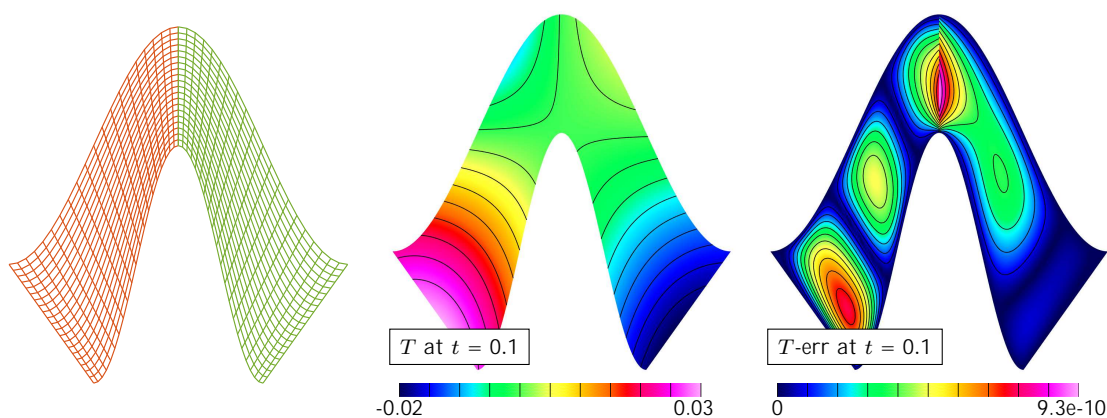


Figure 3.11: Wiggled domain results. Left: a sample grid for a wiggled geometry. Middle: BDF4 solution at $t_{\text{nal}} = 0.1$ on grid $G^{(8)}$ for Case 2. Right: error at $t_{\text{nal}} = 0.1$ on grid $G^{(8)}$ for the same case.

Table 3.8: A convergence study for the un-iterated CHAMP scheme on a stretched-square domain using the trigonometric manufactured solution with various choices of material parameters.

Stretched Squares									
Case 1: $D_L = 1, D_R = 1, K_L = 1, K_R = 1, \mathbf{u}_L = [1, 1]^T, \mathbf{u}_R = [1, 1]^T$.									
CHAMP2 results: $t_{\text{nal}} = 0.1, \text{max-iteration} = 1$.									
j	Δs	λ_{DL}	max error left	ratio	rate	max error right	ratio	rate	
2	5.00e 02	2.00e+00	4.032e 07			5.262e 06			
4	2.50e 02	4.00e+00	1.086e 07	3.71	1.89	1.188e 07	4.43	2.15	
8	1.25e 02	8.00e+00	2.831e 08	3.84	1.94	2.852e 08	4.17	2.06	
CHAMP4 results: $t_{\text{nal}} = 0.1, \text{max-iteration} = 1$.									
j	Δs	λ_{DL}	max error left	ratio	rate	max error right	ratio	rate	
2	5.00e 02	2.00e+00	2.974e 10			2.506e 10			
4	2.50e 02	4.00e+00	1.779e 11	16.72	4.06	1.629e 11	15.39	3.94	
8	1.25e 02	8.00e+00	1.097e 12	16.22	4.02	1.044e 12	15.60	3.96	
Case 2: $D_L = 0.9, D_R = 9.6, K_L = 7.3, K_R = 0.5, \mathbf{u}_L = [0.2, 0.4]^T, \mathbf{u}_R = [0.8, 0.7]^T$.									
CHAMP2 results: $t_{\text{nal}} = 0.1, \text{max-iteration} = 1$.									
j	Δs	λ_{DL}	max error left	ratio	rate	max error right	ratio	rate	
2	5.00e 02	1.80e+00	3.354e 07			9.664e 07			
4	2.50e 02	3.60e+00	8.200e 08	4.09	2.03	1.488e 07	6.49	2.70	
8	1.25e 02	7.20e+00	2.034e 08	4.03	2.01	3.719e 08	4.00	2.00	
CHAMP4 results: $t_{\text{nal}} = 0.1, \text{max-iteration} = 1$.									
j	Δs	λ_{DL}	max error left	ratio	rate	max error right	ratio	rate	
2	5.00e 02	1.80e+00	5.332e 10			9.874e 09			
4	2.50e 02	3.60e+00	3.577e 11	14.91	3.90	3.956e 10	24.96	4.64	
8	1.25e 02	7.20e+00	2.546e 12	14.05	3.81	1.441e 11	27.45	4.78	

3.7.2.4 Wavy Geometry with Non-Orthogonal Grid at Interface

The last example considers a completely non-orthogonal grid consisting of domains with boundary curves defined by sine functions. The mapping function for this case is given by

$$\mathbf{x} = \mathbf{G}_{\text{dw},s}(\mathbf{r}) = (1 - r_2)\mathbf{C}_{\text{top}}(r_1) + r_2\mathbf{C}_{\text{bot}}(r_1) \quad (3.86)$$

Table 3.9: Constants in manufactured solutions used for wiggled geometry.

a_L	$f_{L,x}$	$f_{L,y}$	$\phi_{L,x}$	$\phi_{L,y}$	$f_{L,t}$	a_R	$f_{R,x}$	$f_{R,y}$	$\phi_{R,x}$	$\phi_{R,y}$	$f_{R,t}$
0.9	0.7	0	0	0.5	0.8	0.8	0.4	0	0	0.5	0.8

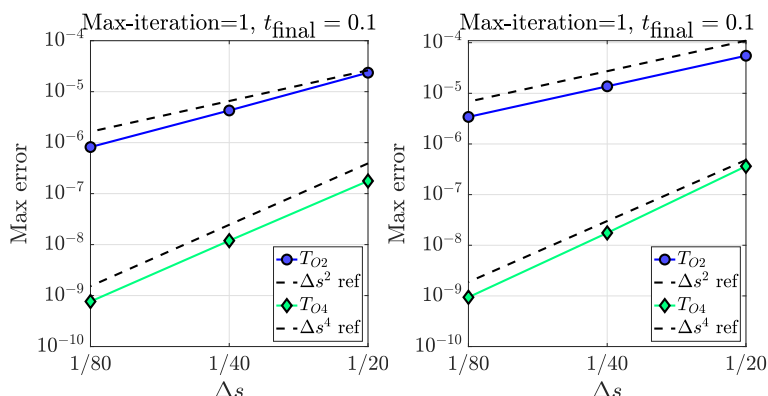


Figure 3.12: Convergence plots for a wiggled geometry. Left: max-norm errors as a function of mesh spacing for Case 1 at $t_{\text{nal}} = 0.1$. Right: max-norm errors as a function of mesh spacing for Case 2 at $t_{\text{nal}} = 0.1$.

where the boundary functions $\mathbf{C}_{\text{top}}(r_1)$ and $\mathbf{C}_{\text{bot}}(r_1)$ are given in (2.145a). The grid presented in Figure 3.13 with $a_1 = 0.2$, $a_2 = 0.3$, $b_1 = 1$ and $\delta_0 = 1$ for the left sub-domain and $a_1 = 0.2$, $a_2 = 0.3$, $b_1 = 0$ and $\delta_0 = 1$ for the right sub-domain is a coarse version of the grid used in the computation. The curvilinear grid for this particular mapping function is denoted by $\mathcal{G}_{\text{dw},s}^{(j)}$ with $j = 2, 4, 8$.

Parameters for the manufactured solution are given in Table 3.9. Both the second-order and fourth-order accurate un-iterated CHAMP schemes are tested for problems with various thermal parameters and advection velocities, and the schemes are run to a final time $t_{\text{nal}} = 0.1$. Maximal discrete errors and the convergence rates are computed at t_{nal} and given in Table 3.11, and the results confirm second-order and fourth-order convergence. The solution and error contours at t_{nal} for Case 1 using the fourth-order accurate CHAMP scheme on the finest grid are plotted in Figure 3.13. The results show that the fourth-order accurate CHAMP scheme converges faster and gives much smaller errors than the second-order accurate CHAMP when same number of grid points are used in the computation.

Table 3.10: A convergence study for the un-iterated CHAMP scheme on a wiggled domain defined by the cos function using the trigonometric manufactured solution with various choices of material parameters.

Cosine Curve									
Case 1: $D_L = 1, D_R = 1, K_L = 1, K_R = 1, \mathbf{u}_L = [1, 1]^T, \mathbf{u}_R = [1, 1]^T$.									
CHAMP2 results: $t_{\text{nal}} = 0.1, \text{max-iteration} = 1$.									
j	Δs	λ_{DL}	max error left	ratio	rate	max error right	ratio	rate	
2	5.00e 02	2.00e+00	2.355e 05			7.953e 06			
4	2.50e 02	4.00e+00	4.277e 06	5.51	2.46	1.211e 06	6.57	2.72	
8	1.25e 02	8.00e+00	8.193e 07	5.22	2.38	3.597e 07	3.37	1.75	
CHAMP4 results: $t_{\text{nal}} = 0.1, \text{max-iteration} = 1$.									
j	Δs	λ_{DL}	max error left	ratio	rate	max error right	ratio	rate	
2	5.00e 02	2.00e+00	1.770e 07			1.020e 07			
4	2.50e 02	4.00e+00	1.194e 08	14.82	3.89	4.363e 09	23.37	4.55	
8	1.25e 02	8.00e+00	7.650e 10	15.61	3.96	2.125e 10	20.53	4.36	
Case 2: $D_L = 0.9, D_R = 9.6, K_L = 7.3, K_R = 0.5, \mathbf{u}_L = [0.2, 0.4]^T, \mathbf{u}_R = [0.8, 0.7]^T$.									
CHAMP2 results: $t_{\text{nal}} = 0.1, \text{max-iteration} = 1$.									
j	Δs	λ_{DL}	max error left	ratio	rate	max error right	ratio	rate	
2	5.00e 02	1.80e+00	5.521e 05			1.800e 05			
4	2.50e 02	3.60e+00	1.375e 05	4.02	2.01	8.803e 06	2.04	1.03	
8	1.25e 02	7.20e+00	3.420e 06	4.02	2.01	2.792e 06	3.15	1.66	
CHAMP4 results: $t_{\text{nal}} = 0.1, \text{max-iteration} = 1$.									
j	Δs	λ_{DL}	max error left	ratio	rate	max error right	ratio	rate	
2	5.00e 02	1.80e+00	1.815e 07			3.632e 07			
4	2.50e 02	3.60e+00	1.196e 08	15.17	3.92	1.752e 08	20.73	4.37	
8	1.25e 02	7.20e+00	7.685e 10	15.57	3.96	9.402e 10	18.64	4.22	

3.8 Conclusions

A high-order accurate partitioned algorithm for solving coupled conjugate heat transfer problems with advection diffusion equation is developed. Analysis are presented for a simplified model problem consists of two rectangular domains with a planer interface located at $x = 0$. The interface conditions are the usual temperature continuity equations, together with a flux interface condition that involves additional advective terms. The CHAMP conditions for the advection-diffusion equation are derived similarly as those for the diffusion

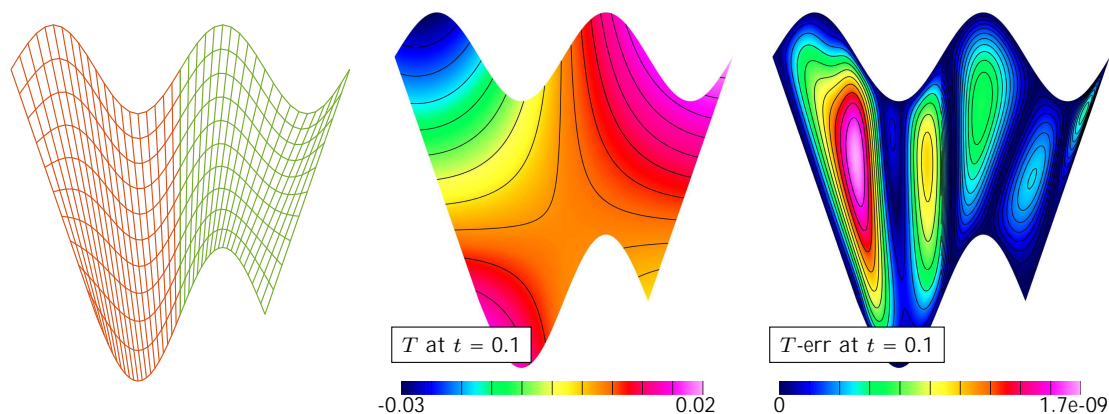


Figure 3.13: Wiggled domain results. Left: a sample grid for a wiggled geometry. Middle: BDF4 solution at $t_{\text{nal}} = 0.1$ on grid $G^{(8)}$ for Case 1. Right: error at $t_{\text{nal}} = 0.1$ on grid $G^{(8)}$ for the same case.

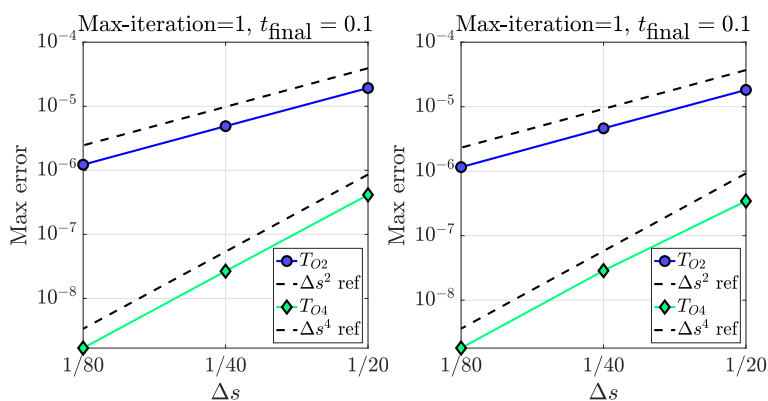


Figure 3.14: Convergence plots for a wiggled geometry. Left: max-norm errors as a function of mesh spacing for Case 1 at $t_{\text{nal}} = 0.1$. Right: max-norm errors as a function of mesh spacing for Case 2 at $t_{\text{nal}} = 0.1$.

equations, in which a Taylor series expansion is used to derive a generalized Dirichlet operator and a generalized Neumann operator using the matching conditions and additional compatibility conditions. These operators are combined together using the weighting operators following the optimized Schwarz approach to form the complete CHAMP conditions. The coupling parameters are determined by solving an optimization problem based on the iteration amplification, and some sample values for the optimal choices are given to show the effects of different material coefficients. The CHAMP iteration is found to converge for all material parameters provided that the velocities in each sub-domain satisfy certain jump

Table 3.11: A convergence study for the un-iterated CHAMP scheme on a wiggled domain defined by the sin function using the trigonometric manufactured solution with various choices of material parameters.

Sine Curve									
Case 1: $D_L = 1, D_R = 1, K_L = 1, K_R = 1, \mathbf{u}_L = [1, 1]^T, \mathbf{u}_R = [1, 1]^T$.									
CHAMP2 results: $t_{\text{nal}} = 0.1, \text{max-iteration} = 1$.									
j	Δs	λ_{DL}	max error left	ratio	rate	max error right	ratio	rate	
2	5.00e 02	2.00e+00	1.927e 05			6.140e 06			
4	2.50e 02	4.00e+00	4.890e 06	3.94	1.98	1.536e 06	4.00	2.00	
8	1.25e 02	8.00e+00	1.225e 06	3.99	2.00	4.038e 07	3.80	1.93	
CHAMP4 results: $t_{\text{nal}} = 0.1, \text{max-iteration} = 1$.									
j	Δs	λ_{DL}	max error left	ratio	rate	max error right	ratio	rate	
2	5.00e 02	2.00e+00	4.140e 07			1.663e 07			
4	2.50e 02	4.00e+00	2.664e 08	15.54	3.96	9.615e 09	17.30	4.11	
8	1.25e 02	8.00e+00	1.679e 09	15.86	3.99	6.045e 10	15.90	3.99	
Case 2: $D_L = 0.9, D_R = 9.6, K_L = 7.3, K_R = 0.5, \mathbf{u}_L = [0.2, 0.4]^T, \mathbf{u}_R = [0.8, 0.7]^T$.									
CHAMP2 results: $t_{\text{nal}} = 0.1, \text{max-iteration} = 1$.									
j	Δs	λ_{DL}	max error left	ratio	rate	max error right	ratio	rate	
2	5.00e 02	1.80e+00	1.820e 05			9.003e 06			
4	2.50e 02	3.60e+00	4.617e 06	3.94	1.98	2.640e 06	3.41	1.77	
8	1.25e 02	7.20e+00	1.156e 06	3.99	2.00	6.838e 07	3.86	1.95	
CHAMP4 results: $t_{\text{nal}} = 0.1, \text{max-iteration} = 1$.									
j	Δs	λ_{DL}	max error left	ratio	rate	max error right	ratio	rate	
2	5.00e 02	1.80e+00	4.458e 07			3.441e 07			
4	2.50e 02	3.60e+00	2.866e 08	15.55	3.96	1.952e 08	17.63	4.14	
8	1.25e 02	7.20e+00	1.806e 09	15.87	3.99	1.181e 09	16.52	4.05	

conditions. A complete time-stepping algorithm is given, and a detailed analysis is carried out for the case where no sub-iteration is taken at each time-step. The CHAMP scheme was shown to be fourth order accurate in space and time using the method of manufactured solutions. Numerical results on different computational domains suggests that the CHAMP scheme is stable and accurate with just one implicit solve in each domain for a wide range of CHT problems.

CHAPTER 4

CONCLUSIONS AND FUTURE WORK

In this thesis, a high-order accurate partitioned algorithm for solving conjugate heat transfer problems is developed and analyzed. The new method, called the CHAMP scheme, consists of a weighted combination of a generalized Dirichlet condition and a generalized Neumann condition, which are derived based on Taylor series expansions of the temperature and heat flux in each sub-domain at a distance equal to the overlap width about the interface. The CHAMP condition is first analyzed as a fixed point iteration for a particular time step, where the interface conditions are applied for each domain sequentially with a fixed number of iterations, usually determined by the residual of the temperature at the interface. A normal mode analysis is carried out to determine the convergence factor for the inner-iteration loop, which provides an objective function that can be used to choose the optimal weights in the CHAMP conditions. If the advective terms are turned off, then the CHAMP iteration for the diffusion equation is guaranteed to converge for any choice of material parameters, regardless of the grid spacing or the time step. With advective terms turned on, the convergence of the iteration depends on the relative size of the heat capacity in each sub-domain. Computation shows that for both cases, the iteration converges rapidly when the optimal weighting parameters are chosen.

Performing sub-iterations could be time-consuming and costly. Thus one generally wants to do as few iterations as possible. Analysis of the un-iterated CHAMP scheme shows that, when using an implicit time-stepping method, the CHAMP scheme, with just one implicit solve for the solution in each sub-domain, is stable and accurate for a wide range of material properties. A detailed discussion is given to verify the order of accuracy of a fourth-order accurate un-iterated CHAMP scheme. In addition, it can also be proved that for the un-iterated time-stepping scheme to be p th-order accurate, a $p + 1$ extrapolation formula must be used at each time step to initialize the CHAMP iterations. The analysis also explains why the Taylor series expansion for deriving the CHAMP conditions is truncated at certain orders.

The CHAMP conditions are also derived for general curvilinear domains. The governing equations and the interface conditions in Cartesian coordinates are first transformed into the parameter space coordinates using the chain rule. The CHAMP Dirichlet and Neu-

mann operators are derived similarly using Taylor series expansion about the points on the interface. The general forms of the CHAMP operators are given at the end.

Based on the observations from the iteration and time-stepping analysis, an adaptive CHAMP algorithm is proposed to leverage the difficulties of the un-iterated scheme when a large time step is taken during the implementation. The new algorithm chooses the number of sub-iterations adaptively based on a measure of the convergence of the CHAMP conditions and a chosen tolerance at each time step and was proven to be stable and accurate when a large time step is taken for given problems.

The accuracy of a fourth-order accurate CHAMP scheme is verified first by computing numerical solutions to some CHT problems where the exact solution is known. Two steady-state problems with a double-square domain and a double-annulus domain are constructed to verify the spatial accuracy of the CHAMP scheme. A time-dependent CHT problem on a double-rectangle domain is presented next, and the numerical solutions show good agreement with the analytical solutions. Another time-dependent CHT problem on an annulus-annulus domain is also presented. For the case where the advective terms are non-zero, the exact solution is unavailable, and a numerical 'exact solution' is derived using an eigenvalue solver. This exact solution is then used in computations to provide error and convergence analysis. Finally, the method of manufactured solution is used to check the accuracy of the CHAMP scheme. The scheme was shown to be fourth-order accurate in space and time using the method of manufactured solutions when applied to domains with different geometries. In particular, a curvilinear domain with non-orthogonal coordinates at the interface is presented. Results from numerical simulations show good agreement with the theory and analysis.

Current work focuses on the CHAMP condition for advection-diffusion equations and is restricted to a simple two-dimensional model problem with a uniform grid and equal grid spacing. In practice, one can have non-uniform grids for each sub-domain so that the grid lines do not necessarily match on either side of the interface. One can also have disparate time scales for solutions in each sub-domain. In addition, the CHAMP scheme could be applied to problems involving more complex physical situations. For example, one may extend CHAMP to general numerical solvers for problems involving the interaction between incompressible flow and rigid solids, heated solids, etc., or to problems for which one material is in thermal contact with two (or more) materials so that all three (or more) materials can

meet at points on the interface. Finally, one may consider deriving CHAMP for problems involving a moving interface, which is common in phase change problems. These topics could be explored in the future.

REFERENCES

- [1] *Backward Differentiation Formula*,
https://en.wikipedia.org/wiki/Backward_differentiation_formula (accessed 03 May 2022).
- [2] Y. ACHDOU, P. LE TALLEC, F. NATAF, AND M. VIDRASCU, *A domain decomposition preconditioner for an advection–diffusion problem*, *Comput. Methods Appl. Mech. Engrg.*, 184 (2000), pp. 145–170,
[https://doi.org/10.1016/S0045-7825\(99\)00227-3](https://doi.org/10.1016/S0045-7825(99)00227-3).
- [3] S. BADIA, F. NOBILE, AND C. VERGARA, *Fluid–structure partitioned procedures based on Robin transmission conditions*, *J. Comput. Phys.*, 227 (2008), pp. 7027–7051,
<https://doi.org/10.1016/j.jcp.2008.04.006>.
- [4] J. BANKS, W. HENSHAW, AND D. SCHWENDEMAN, *An analysis of a new stable partitioned algorithm for FSI problems. Part I: Incompressible flow and elastic solids*, *J. Comput. Phys.*, 269 (2014), pp. 108–137,
<https://doi.org/10.1016/j.jcp.2014.03.006>.
- [5] J. BANKS, W. HENSHAW, AND D. SCHWENDEMAN, *An analysis of a new stable partitioned algorithm for FSI problems. Part II: Incompressible flow and structural shells*, *J. Comput. Phys.*, 268 (2014), pp. 399–416,
<https://doi.org/10.1016/j.jcp.2014.03.004>.
- [6] J. BANKS, W. HENSHAW, D. SCHWENDEMAN, AND Q. TANG, *A stable partitioned FSI algorithm for rigid bodies and incompressible flow. Part I: Model problem analysis*, *J. Comput. Phys.*, 343 (2017), pp. 432–468,
<https://doi.org/10.1016/j.jcp.2017.01.015>.
- [7] J. BANKS, W. HENSHAW, D. SCHWENDEMAN, AND Q. TANG, *A stable partitioned FSI algorithm for rigid bodies and incompressible flow. Part II: General formulation*, *J. Comput. Phys.*, 343 (2017), pp. 469–500,
<https://doi.org/10.1016/j.jcp.2017.04.064>.

- [8] J. BANKS, W. HENSHAW, D. SCHWENDEMAN, AND Q. TANG, *A stable partitioned FSI algorithm for rigid bodies and incompressible flow in three dimensions*, J. Comput. Phys., 373 (2018), pp. 455–492, <https://doi.org/10.1016/j.jcp.2018.06.072>.
- [9] J. BANKS, W. HENSHAW, AND B. SJÖGREEN, *A stable FSI algorithm for light rigid bodies in compressible flow*, J. Comput. Phys., 245 (2013), pp. 399–430, <https://doi.org/10.1016/j.jcp.2013.02.050>.
- [10] P. T. BAUMAN, R. STOGNER, G. F. CAREY, K. W. SCHULZ, R. UPDADHYAY, AND A. MAURENTE, *Loose-coupling algorithm for simulating hypersonic flows with radiation and ablation*, J. Spacecr. Rockets, 48 (2011), pp. 72–80, <https://doi.org/10.2514/1.50588>.
- [11] L. BENNANI, P. TRONTIN, R. CHAUVIN, AND P. VILLEDIEU, *A non-overlapping optimized Schwarz method for the heat equation with non linear boundary conditions and with applications to de-icing*, Comput. Math., 80 (2020), pp. 1500–1522, <https://doi.org/10.1016/j.camwa.2020.07.017>.
- [12] D. BENNEQUIN, M. J. GANDER, L. GOUARIN, AND L. HALPERN, *Optimized Schwarz waveform relaxation for advection reaction diffusion equations in two dimensions*, Numer. Math., 134 (2015), pp. 513–567, <https://doi.org/10.1007/s00211-015-0784-8>.
- [13] P. BIRKEN, K. J. QUINT, S. HARTMANN, AND A. MEISTER, *A time-adaptive fluid-structure interaction method for thermal coupling*, Comput. Vis. Sci., 13 (2010), pp. 331–340, <https://doi.org/10.1007/s00791-010-0150-4>.
- [14] P. E. BJØRSTAD AND O. B. WIDLUND, *Iterative methods for the solution of elliptic problems on regions partitioned into substructures*, SIAM J. Numer. Anal., 23 (1986), pp. 1097–1120, <https://doi.org/10.1137/0723075>.
- [15] E. BLAYO, L. HALPERN, AND C. JAPHET, *Optimized Schwarz waveform relaxation algorithms with nonconforming time discretization for coupling convection-diffusion problems with discontinuous coefficients*, in Domain Decomposition Methods in Science and Engineering XVI, O. B. Widlund and D. E. Keyes, eds., Springer, Berlin, Heidelberg, 2007, pp. 267–274.

- [16] X. CHEN AND P. HAN, *A note on the solution of conjugate heat transfer problems using SIMPLE-like algorithms*, *Int. J. Heat Fluid Flow*, 21 (2000), pp. 463–467, [https://doi.org/10.1016/s0142-727x\(00\)00028-x](https://doi.org/10.1016/s0142-727x(00)00028-x).
- [17] G. CHESHIRE AND W. HENSHAW, *Composite overlapping meshes for the solution of partial differential equations*, *J. Comput. Phys.*, 90 (1990), pp. 1–64, [https://doi.org/10.1016/0021-9991\(90\)90196-8](https://doi.org/10.1016/0021-9991(90)90196-8).
- [18] R. COSTA, J. M. NÓBREGA, S. CLAIN, AND G. J. MACHADO, *Very high-order accurate polygonal mesh finite volume scheme for conjugate heat transfer problems with curved interfaces and imperfect contacts*, *Comput. Methods Appl. Mech. Eng.*, 357 (2019), 112560, <https://doi.org/10.1016/j.cma.2019.07.029>.
- [19] J. DEGROOTE, K.-J. BATHE, AND J. VIERENDEELS, *Performance of a new partitioned procedure versus a monolithic procedure in fluid–structure interaction*, *Comput. Struct.*, 87 (2009), pp. 793–801, <https://doi.org/10.1016/j.compstruc.2008.11.013>.
- [20] V. DOLEAN, F. NATAF, AND S. LANTERI, *Construction of interface conditions for solving the compressible Euler equations by non-overlapping domain decomposition methods*, *Internat. J. Numer. Methods Fluids*, 40 (2002), pp. 1485–1492, <https://doi.org/10.1002/flid.406>.
- [21] O. DUBOIS, *Optimized Schwarz methods with robin conditions for the advection-diffusion equation*, in *Domain Decomposition Methods in Science and Engineering XVI*, O. B. Widlund and D. E. Keyes, eds., Springer, Berlin, Heidelberg, 2007, pp. 181–188.
- [22] F. DUCHAINE, A. CORPRON, L. PONS, V. MOUREAU, F. NICLOUD, AND T. POINSOT, *Development and assessment of a coupled strategy for conjugate heat transfer with Large Eddy Simulation: Application to a cooled turbine blade*, *Int. J. Heat Fluid Flow*, 30 (2009), pp. 1129–1141, <https://doi.org/10.1016/j.ijheatfluidflow.2009.07.004>.
- [23] R. R. EL KHOURY, M. ERRERA, K. EL KHOURY, AND M. NEMER, *Efficiency of coupling schemes for the treatment of steady state fluid-structure thermal interactions*,

- Int. J. Therm. Sci., 115 (2017), pp. 225–235,
<https://doi.org/10.1016/j.ijthermalsci.2017.02.001>.
- [24] M. ERRERA, R. MORETTI, Y. BACHELIER, AND T. SOUBRIÉ, *Stable and optimal interface treatment for partitioned conjugate heat transfer problems*, in Proceedings of the AIAA Scitech 2019 Forum, American Institute for Aeronautics and Astronautics, San Diego, CA, 2019, <https://doi.org/10.2514/6.2019-1561>.
- [25] M.-P. ERRERA AND S. CHEMIN, *Optimal solutions of numerical interface conditions in fluid–structure thermal analysis*, J. Comput. Phys., 245 (2013), pp. 431–455,
<https://doi.org/10.1016/j.jcp.2013.03.004>.
- [26] M.-P. ERRERA AND F. DUCHAINE, *Comparative study of coupling coefficients in Dirichlet–Robin procedure for fluid–structure aerothermal simulations*, J. Comput. Phys., 312 (2016), pp. 218–234, <https://doi.org/10.1016/j.jcp.2016.02.022>.
- [27] M.-P. ERRERA, M. LAZAREFF, J.-D. GARAUD, T. SOUBRIÉ, C. DOUTA, AND T. FEDERICI, *A coupling approach to modeling heat transfer during a full transient flight cycle*, Int. J. Heat Mass Transf., 110 (2017), pp. 587–605,
<https://doi.org/10.1016/j.ijheatmasstransfer.2017.03.048>.
- [28] M.-P. ERRERA, R. MORETTI, J. MAYEUR, M. GELAIN, L. TESSÉ, J.-M. LAMET, AND E. LAROCHE, *A numerical predictive model for conjugate heat transfer with radiation*, Int. J. Heat Mass Transf., 160 (2020), 120155,
<https://doi.org/10.1016/j.ijheatmasstransfer.2020.120155>.
- [29] M.-P. ERRERA, R. MORETTI, R. SALEM, Y. BACHELIER, T. ARRIVÉ, AND M. NGUYEN, *A single stable scheme for steady conjugate heat transfer problems*, J. Comput. Phys., 394 (2019), pp. 491–502,
<https://doi.org/10.1016/j.jcp.2019.05.036>.
- [30] M.-P. ERRERA AND G. TURPIN, *Temporal multiscale strategies for conjugate heat transfer problems*, JCSMD, 1 (2013), pp. 89–98,
<https://doi.org/10.1166/jcsmd.2013.1005>.
- [31] J. A. ESFAHANI AND J. ALINEJAD, *Lattice Boltzmann simulation of viscous-fluid flow and conjugate heat transfer in a rectangular cavity with a heated moving wall*,

- Thermophys. Aeromechanics., 20 (2013), pp. 613–620,
<https://doi.org/10.1134/s0869864313050084>.
- [32] M. E. EWING, T. S. LAKER, AND D. T. WALKER, *Numerical modeling of ablation heat transfer*, J. Thermophys. Heat Transf., 27 (2013), pp. 615–632,
<https://doi.org/10.2514/1.t4164>.
- [33] M. J. GANDER, *Optimized Schwarz methods*, SIAM J. Numer. Anal., 44 (2006), pp. 699–731, <https://doi.org/10.1137/s0036142903425409>.
- [34] M. J. GANDER AND O. DUBOIS, *Optimized Schwarz methods for a diffusion problem with discontinuous coefficient*, Numer. Algorithms, 69 (2014), pp. 109–144,
<https://doi.org/10.1007/s11075-014-9884-2>.
- [35] M. J. GANDER AND L. HALPERN, *Optimized Schwarz waveform relaxation methods for advection reaction diffusion problems*, SIAM J. Numer. Anal., 45 (2007), pp. 666–697, <https://doi.org/10.1137/050642137>.
- [36] M. J. GANDER, L. HALPERN, AND M. KERN, *A Schwarz waveform relaxation method for advection-diffusion-reaction problems with discontinuous coefficients and non-matching grids*, in Domain Decomposition Methods in Science and Engineering XVI, O. B. Widlund and D. E. Keyes, eds., Springer, Berlin, Heidelberg, 2007, pp. 283–290.
- [37] M. J. GANDER, F. MAGOULÈS, AND F. NATAF, *Optimized Schwarz methods without overlap for the Helmholtz equation*, SISC, 24 (2002), pp. 38–60,
<https://doi.org/10.1137/s1064827501387012>.
- [38] M. J. GANDER AND A. M. STUART, *Space-time continuous analysis of waveform relaxation for the heat equation*, SIAM J. Sci. Comput., 19 (1998), pp. 2014–2031,
<https://doi.org/10.1137/s1064827596305337>.
- [39] M. J. GANDER AND T. VANZAN, *Heterogeneous optimized Schwarz methods for second order elliptic PDEs*, SISC, 41 (2019), pp. A2329–A2354,
<https://doi.org/10.1137/18m122114x>.

- [40] M. GARBEY AND D. TROMEUR-DERVOU, *On some Aitken-like acceleration of the Schwarz method*, Internat. J. Numer. Methods Fluids, 40 (2002), pp. 1493–1513, <https://doi.org/10.1002/fl d.407>.
- [41] M. GELAIN, M.-P. ERRERA, AND O. GICQUEL, *Assessment and numerical validation of a normal mode stability analysis for conjugate heat transfer*, Int. J. Heat Mass Transf., 191 (2022), 122794, <https://doi.org/10.1016/j.ijheatmasstransfer.2022.122794>.
- [42] L. GERARDO-GIORDA AND F. NATAF, *Optimized Schwarz methods for unsymmetric layered problems with strongly discontinuous and anisotropic coefficients*, J. Numer. Math., 13 (2005), pp. 265–294, <https://doi.org/10.1515/156939505775248338>.
- [43] M. B. GILES, *Stability analysis of numerical interface conditions in fluid-structure thermal analysis*, Internat. J. Numer. Methods Fluids, 25 (1997), pp. 421–436, [https://doi.org/10.1002/\(SICI\)1097-0363\(19970830\)25:4<421::AID-FLD557>3.0.CO;2-J](https://doi.org/10.1002/(SICI)1097-0363(19970830)25:4<421::AID-FLD557>3.0.CO;2-J).
- [44] G. GIMENEZ, M. ERRERA, D. BAILLIS, Y. SMITH, AND F. PARDO, *A coupling numerical methodology for weakly transient conjugate heat transfer problems*, Int. J. Heat Mass Transf., 97 (2016), pp. 975–989, <https://doi.org/10.1016/j.ijheatmasstransfer.2016.02.037>.
- [45] S. K. GODUNOV AND V. S. RYABENKI, *Theory of Difference Schemes - An Introduction*, North-Holland Publishing Company, Amsterdam, Netherlands, 1964, <https://ui.adsabs.harvard.edu/abs/1964tdsa.book.....G>.
- [46] M. GÖRTZ AND P. BIRKEN, *On the convergence rate of the Dirichlet-Neumann iteration for coupled Poisson problems on unstructured grids*, in Finite Volumes for Complex Applications IX - Methods, Theoretical Aspects, Examples, R. Klöforn, E. Keilegavlen, F. A. Radu, and J. Fuhrmann, eds., Springer International Publishing, Cham, Switzerland, 2020, pp. 355–363.
- [47] S. GUO, Y. FENG, AND W.-Q. TAO, *Deviation analysis of loosely coupled quasi-static method for fluid-thermal interaction in hypersonic flows*, Comput. Fluids, 149 (2017), pp. 194–204, <https://doi.org/10.1016/j.compfluid.2017.03.017>.

- [48] L. HE AND M. L. G. OLDFIELD, *Unsteady conjugate heat transfer modeling*, J. Turbomach., 133 (2010), 031022, <https://doi.org/10.1115/1.4001245>.
- [49] M. HEIL, *An efficient solver for the fully coupled solution of large-displacement fluid–structure interaction problems*, Comput. Methods Appl. Mech. Engrg., 193 (2004), pp. 1–23, <https://doi.org/10.1016/j.cma.2003.09.006>.
- [50] W. D. HENSHAW, *A fourth-order accurate method for the incompressible Navier-Stokes equations on overlapping grids*, J. Comput. Phys., 113 (1994), pp. 13–25, <https://doi.org/10.1006/j.cph.1994.1114>.
- [51] W. D. HENSHAW AND K. K. CHAND, *A composite grid solver for conjugate heat transfer in fluid–structure systems*, J. Comput. Phys., 228 (2009), pp. 3708–3741, <https://doi.org/10.1016/j.jcp.2009.02.007>.
- [52] W. D. HENSHAW AND D. W. SCHWENDEMAN, *Moving overlapping grids with adaptive mesh refinement for high-speed reactive and non-reactive flow*, J. Comput. Phys., 216 (2006), pp. 744–779, <https://doi.org/10.1016/j.jcp.2006.01.005>.
- [53] A. HESELHAUS, *A hybrid coupling scheme and stability analysis for coupled solid/fluid turbine blade temperature calculations*, in Proceedings of Turbo Expo: Power for Land, Sea, and Air, The American Society of Mechanical Engineers, Stockholm, Sweden, 1998, <https://doi.org/10.1115/98-GT-088>.
- [54] T.-T.-P. HOANG, *Fully implicit local time-stepping methods for advection-diffusion problems in mixed formulations*, Comput. Math. with Appl., 118 (2022), pp. 248–264, <https://doi.org/10.1016/j.camwa.2022.05.022>.
- [55] T.-T.-P. HOANG, J. JAFFRÉ, C. JAPHET, M. KERN, AND J. E. ROBERTS, *Space-time domain decomposition methods for diffusion problems in mixed formulations*, SIAM J. Numer. Anal., 51 (2013), pp. 3532–3559, <https://doi.org/10.1137/130914401>.
- [56] C. JAPHET AND F. NATAF, *The best interface conditions for domain decomposition methods : absorbing boundary conditions*, in Absorbing Boundaries and Layers, Domain Decomposition Methods, I. L. Tourrette, ed., Nova Science Publishers, New York, NY, 2003, p. 348–373, <https://ti.nyurl.com/4n56r8h6>.

- [57] B. JOHN, P. SENTHILKUMAR, AND S. SADASIVAN, *Applied and theoretical aspects of conjugate heat transfer analysis: a review*, Arch. Comput. Methods Eng., 26 (2018), pp. 475–489, <https://doi.org/10.1007/s11831-018-9252-9>.
- [58] O. JOSHI AND P. LEYLAND, *Stability analysis of a partitioned fluid–structure thermal coupling algorithm*, J. Thermophys. Heat Transf., 28 (2014), pp. 59–67, <https://doi.org/10.2514/1.t4032>.
- [59] D. KAMINSKI AND C. PRAKASH, *Conjugate natural convection in a square enclosure: effect of conduction in one of the vertical walls*, Int. J. Heat Mass Transf., 29 (1986), pp. 1979–1988, [https://doi.org/10.1016/0017-9310\(86\)90017-7](https://doi.org/10.1016/0017-9310(86)90017-7).
- [60] V. KAZEMI-KAMYAB, A. VAN ZUIJLEN, AND H. BIJL, *A high order time-accurate loosely-coupled solution algorithm for unsteady conjugate heat transfer problems*, Comput. Methods Appl. Mech. Engrg., 264 (2013), pp. 205–217, <https://doi.org/10.1016/j.cma.2013.05.021>.
- [61] V. KAZEMI-KAMYAB, A. VAN ZUIJLEN, AND H. BIJL, *Analysis and application of high order implicit Runge–Kutta schemes for unsteady conjugate heat transfer: A strongly-coupled approach*, J. Comput. Phys., 272 (2014), pp. 471–486, <https://doi.org/10.1016/j.jcp.2014.04.016>.
- [62] V. KAZEMI-KAMYAB, A. H. VAN ZUIJLEN, AND H. BIJL, *Accuracy and stability analysis of a second-order time-accurate loosely coupled partitioned algorithm for transient conjugate heat transfer problems*, Internat. J. Numer. Methods Fluids, 74 (2013), pp. 113–133, <https://doi.org/10.1002/flid.3842>.
- [63] S. KUTLUAY, A. BAHADIR, AND A. ÖZDEŞ, *The numerical solution of one-phase classical Stefan problem*, J. Comput. Appl. Math., 81 (1997), pp. 135–144, [https://doi.org/10.1016/s0377-0427\(97\)00034-4](https://doi.org/10.1016/s0377-0427(97)00034-4).
- [64] E. LELARSMEE, A. RUEHLI, AND A. SANGIOVANNI-VINCENTELLI, *The waveform relaxation method for time-domain analysis of large scale integrated circuits*, IEEE Trans. Comput.-Aided Des. Integr. Circuits Syst., 1 (1982), pp. 131–145, <https://doi.org/10.1109/tcad.1982.1270004>.

- [65] L. LI, C. CHEN, R. MEI, AND J. F. KLAUSNER, *Conjugate heat and mass transfer in the lattice Boltzmann equation method*, Phys. Rev. E, 89 (2014), 043308, <https://doi.org/10.1103/physreve.89.043308>.
- [66] Q. LI, P. LIU, AND G. HE, *Fluid–solid coupled simulation of the ignition transient of solid rocket motor*, Acta Astronaut., 110 (2015), pp. 180–190, <https://doi.org/10.1016/j.actaastro.2015.01.017>.
- [67] J. LINDSTRÖM AND J. NORDSTRÖM, *A stable and high-order accurate conjugate heat transfer problem*, J. Comput. Phys., 229 (2010), pp. 5440–5456, <https://doi.org/10.1016/j.jcp.2010.04.010>.
- [68] A. LUIKOV, *Conjugate convective heat transfer problems*, Int. J. Heat Mass Transf., 17 (1974), pp. 257–265, [https://doi.org/10.1016/0017-9310\(74\)90087-8](https://doi.org/10.1016/0017-9310(74)90087-8).
- [69] Y. MADAY AND F. MAGOULÈS, *Non-overlapping additive schwarz methods tuned to highly heterogeneous media*, C. R. Math., 341 (2005), pp. 701–705, <https://doi.org/10.1016/j.crma.2005.09.032>.
- [70] Y. MADAY AND F. MAGOULÈS, *Optimized Schwarz methods without overlap for highly heterogeneous media*, Comput. Methods Appl. Mech. Eng., 196 (2007), pp. 1541–1553, <https://doi.org/10.1016/j.cma.2005.05.059>.
- [71] F. MAGOULÈS AND R. PUTANOWICZ, *Optimal convergence of non-overlapping schwarz methods for the helmholtz equation*, J. Comput. Acoust., 13 (2005), pp. 525–545, <https://doi.org/10.1142/S0218396X05002748>.
- [72] B. C. MANDAL, *A time-dependent Dirichlet-Neumann method for the heat equation*, in Domain Decomposition Methods in Science and Engineering XXI, J. Erhel, M. J. Gander, L. Halpern, G. Pichot, T. Sassi, and O. Widlund, eds., Springer International Publishing, Cham, Switzerland, 2014, pp. 467–475, https://doi.org/10.1007/978-3-319-05789-7_44.
- [73] V. MARTIN, *An optimized Schwarz waveform relaxation method for the unsteady convection diffusion equation in two dimensions*, Appl. Numer. Math., 52 (2005), pp. 401–428, <https://doi.org/10.1016/j.apnum.2004.08.022>.

- [74] MATLAB, *9.8.0.1380330 (R2020a)*, The MathWorks Inc., Natick, Massachusetts, 2020.
- [75] F. MENG, J. BANKS, W. HENSHAW, AND D. SCHWENDEMAN, *A stable and accurate partitioned algorithm for conjugate heat transfer*, *J. Comput. Phys.*, 344 (2017), pp. 51–85, <https://doi.org/10.1016/j.jcp.2017.04.052>.
- [76] B. A. MILLER AND J. J. MCNAMARA, *Loosely coupled time-marching of fluid-thermal-structural interactions with time-accurate CFD*, in *Proceedings of the 56th AIAA/ASCE/AHS/ASC Structures, Structural Dynamics, and Materials Conference*, American Institute for Aeronautics and Astronautics, Kissimmee, FL, 2015, <https://doi.org/10.2514/6.2015-0686>.
- [77] A. MONGE AND P. BIRKEN, *On the convergence rate of the Dirichlet–Neumann iteration for unsteady thermal fluid–structure interaction*, *Comput. Mech.*, 62 (2017), pp. 525–541, <https://doi.org/10.1007/s00466-017-1511-3>.
- [78] A. MONGE AND P. BIRKEN, *Towards a time adaptive Neumann–Neumann waveform relaxation method for thermal fluid-structure interaction*, in *Domain Decomposition Methods in Science and Engineering XXV*, R. Haynes, S. MacLachlan, X.-C. Cai, L. Halpern, H. H. Kim, A. Klawonn, and O. Widlund, eds., Springer International Publishing, Cham, Switzerland, 2020, pp. 466–473, https://doi.org/10.1007/978-3-030-56750-7_54.
- [79] R. MORETTI, M.-P. ERRERA, V. COUAILLIER, AND F. FEYEL, *Stability, convergence and optimization of interface treatments in weak and strong thermal fluid-structure interaction*, *Int. J. Therm. Sci.*, 126 (2018), pp. 23–37, <https://doi.org/10.1016/j.ijthermalsci.2017.12.014>.
- [80] A. MOSTAFAVI AND A. JAIN, *Analytical modeling of conjugate heat transfer between a bed of phase change material and laminar convective flow*, *Int. J. Heat Mass Transf.*, 183 (2022), 122180, <https://doi.org/10.1016/j.ijheatmasstransfer.2021.122180>.

- [81] X. PAN, C. LEE, AND J.-I. CHOI, *Efficient monolithic projection method for time-dependent conjugate heat transfer problems*, J. Comput. Phys., 369 (2018), pp. 191–208, <https://doi.org/10.1016/j.jcp.2018.05.010>.
- [82] M. PARHIZI AND A. JAIN, *Analytical modeling and optimization of phase change thermal management of a Li-ion battery pack*, Appl. Therm. Eng., 148 (2019), pp. 229–237, <https://doi.org/10.1016/j.applthermaleng.2018.11.017>.
- [83] T. PERELMAN, *On conjugated problems of heat transfer*, Int. J. Heat Mass Transf., 3 (1961), pp. 293–303, [https://doi.org/10.1016/0017-9310\(61\)90044-8](https://doi.org/10.1016/0017-9310(61)90044-8).
- [84] B. ROE, A. HASELBACHER, AND P. H. GEUBELLE, *Stability of fluid–structure thermal simulations on moving grids*, Internat. J. Numer. Methods Fluids, 54 (2007), pp. 1097–1117, <https://doi.org/10.1002/flid.1416>.
- [85] B. ROE, R. JAUMAN, A. HASELBACHER, AND P. H. GEUBELLE, *Combined interface boundary condition method for coupled thermal simulations*, Internat. J. Numer. Methods Fluids, 57 (2008), pp. 329–354, <https://doi.org/10.1002/flid.1637>.
- [86] F.-X. ROUX AND J.-D. GARAUD, *Domain decomposition methodology with robin interface matching conditions for solving strongly coupled fluid-Structure problems*, Int. J. Multiscale Comput. Eng., 7 (2009), pp. 29–38, <https://doi.org/10.1615/intjmultcompeng.v7.i1.50>.
- [87] R. SALEM, M. ERRERA, AND J. MARTY, *Adaptive diffusive time-step in conjugate heat transfer interface conditions for thermal-barrier-coated applications*, Int. J. Therm. Sci., 145 (2019), 106048, <https://doi.org/10.1016/j.ijthermalsci.2019.106048>.
- [88] S. SCHOLL, B. JANSSENS, AND T. VERSTRAETE, *Stability of static conjugate heat transfer coupling approaches using Robin interface conditions*, Comput. Fluids, 172 (2018), pp. 209–225, <https://doi.org/10.1016/j.compfluid.2018.06.016>.
- [89] D. SERINO, J. BANKS, W. HENSHAW, AND D. SCHWENDEMAN, *A stable added-mass partitioned (AMP) algorithm for elastic solids and incompressible flow*, J. Comput. Phys., 399 (2019), 108923, <https://doi.org/10.1016/j.jcp.2019.108923>.

- [90] B. F. SMITH, *Domain decomposition methods for partial differential equations*, in *Parallel Numerical Algorithms*, D. E. Keyes, A. Sameh, and V. Venkatakrisnan, eds., Springer, Dordrecht, Netherlands, 1997, pp. 225–243, https://doi.org/10.1007/978-94-011-5412-3_8.
- [91] D. L. SONDAK AND D. J. DORNEY, *Simulation of coupled unsteady flow and heat conduction in turbine stage*, *J. Propuls. Power*, 16 (2000), pp. 1141–1148, <https://doi.org/10.2514/2.5689>.
- [92] E. SOUSA, *Stability analysis of difference methods for parabolic initial value problems*, *SIAM J. Sci. Comput.*, 26 (2005), pp. 45–66, <https://doi.org/10.1007/s10915-004-4799-z>.
- [93] E. SOUSA, *High-order methods and numerical boundary conditions*, *Comput. Methods Appl. Mech. Engrg.*, 196 (2007), pp. 4444–4457, <https://doi.org/10.1016/j.cma.2007.04.015>.
- [94] T. VERSTRAETE AND S. SCHOLL, *Stability analysis of partitioned methods for predicting conjugate heat transfer*, *Int. J. Heat Mass Transf.*, 101 (2016), pp. 852–869, <https://doi.org/10.1016/j.ijheatmasstransfer.2016.05.041>.
- [95] WIKIPEDIA CONTRIBUTORS, *Additive Schwarz Method*, https://en.wikipedia.org/wiki/Additive_Schwarz_method (accessed 21 June 2022).
- [96] L. YUE, Z. CHAI, L. WANG, AND B. SHI, *A lattice Boltzmann model for the conjugate heat transfer*, *Int. J. Heat Mass Transf.*, 165 (2021), 120682, <https://doi.org/10.1016/j.ijheatmasstransfer.2020.120682>.
- [97] S. ZHANG, F. CHEN, AND H. LIU, *Time-adaptive, loosely coupled strategy for conjugate heat transfer problems in hypersonic flows*, *J. Thermophys. Heat Transf.*, 28 (2014), pp. 635–646, <https://doi.org/10.2514/1.t4278>.
- [98] Q.-L. ZHAO, Z.-L. SUN, C. TONG, AND X.-D. CHAI, *Numerical stability analysis for fluid structure conjugate heat transfer on moving interface*, *J. Northeast. Univ.*, 37 (2016), p. 222 – 226, <https://doi.org/10.3969/j.issn.1005-3026.2016.02.016>.

APPENDIX A

PROOF OF LEMMA 1

In this appendix, Lemma 1 in section 2.6.2 is proved for the case where $p = 4$. The form of ξ_m for a 4th-order accurate scheme is given as

$$\xi_m = \sqrt{\frac{1}{D_m \Delta t} \frac{25A^4 - 48A^3 + 36A^2 - 16A + 3}{12A^4} + k^2}, \quad m = L, R. \quad (\text{A.1})$$

The complete Lemma 1 is reproduced below.

Lemma 1. *Consider ξ_m and A satisfying (A.1). If ξ_m is pure imaginary, then $|jA| \leq 1$. Furthermore $|jA| = 1$ only when $\xi_m = 0$ and $k = 0$, in which case $A = 1$ is a simple root.*

Proof. Let ξ_m be pure imaginary, i.e. $\xi_m = i\alpha, \alpha \in \mathbb{R}$. Equation (A.1) can be written as a polynomial of degree two in A ,

$$\begin{aligned} \alpha^2 &= \frac{1}{D_m \Delta t} \frac{25A^4 - 48A^3 + 36A^2 - 16A + 3}{12A^4} + k^2, \\ 25A^4 - 48A^3 + 36A^2 - 16A + 3 &= ((\alpha^2 - k^2)D_m \Delta t) 12A^4, \\ (25 - c)A^4 - 48A^3 + 36A^2 - 16A + 3 &= 0, \end{aligned}$$

with

$$c = 12(\alpha^2 + k^2)D_m \Delta t.$$

It follows that $c \geq 0$ and $c = 0$ iff $\alpha = k = 0$, in which case $A = 1$ or $A = \frac{1}{3}$ or $A = 0.27 - 0.49i$. Otherwise if $c < 0$ then we want to show $|jA| < 1$. One can use the theory of Schur and von Neumann polynomials.

Let

$$\phi_4(A) = (25 - c)A^4 - 48A^3 + 36A^2 - 16A + 3. \quad (\text{A.2})$$

To show $|jA| < 1$ for $c < 0$, it is equivalent of showing the polynomial (A.2) is a simple von Neumann polynomial. We make repeated use of the definition of simple von Neumann

polynomials, which gives

$$\begin{aligned} \phi_4(A) &= (25 - c) - 48A + 36A^2 - 16A^3 + 3A^4, \\ j\phi_4(0)j &= (25 - c)^2, \quad j\phi_4(0)j = 3^2. \end{aligned}$$

To satisfy condition for a simple von Neumann polynomial, one must have

$$9 < (25 - c)^2.$$

This is satisfied for $c < 0$. One then looks for polynomials of degree $p = 1$,

$$\begin{aligned} \phi_3(A) &= \frac{\phi_4(0)\phi_4(z) - \phi_4(0)\phi_4(z)}{z}, \\ &= ((25 - c)^2 - 9)A^3 + (48(c - 24))A^2 + (36(25 - c) - 108)A + (16(c - 25) + 144), \end{aligned}$$

which leads to

$$\phi_3(A) = ((25 - c)^2 - 9) + (48(c - 24))A + (36(25 - c) - 108)A^2 + (16(c - 25) + 144)A^3,$$

and one must have

$$\begin{aligned} j\phi_3(0)j < j\phi_3(0)j \quad & \Rightarrow \quad (16(c - 25) + 144)^2 < ((25 - c)^2 - 9)^2, \\ & \Rightarrow \quad c > 33 + \sqrt{\frac{10}{217}} \quad \text{or} \quad c < 33 - \sqrt{\frac{10}{217}}. \end{aligned}$$

This is also satisfied for $c < 0$. Next we look at polynomials of degree $p = 2$,

$$\begin{aligned} \phi_2(A) &= \frac{\phi_3(0)\phi_3(z) - \phi_3(0)\phi_3(z)}{z}, \\ &= (c^2 - 66c + 872)(c^2 - 34c + 360)A^2 + 48(c - 22)(c^2 - 40c + 480)A \\ &\quad - 12(3c^3 - 152c^2 + 2588c - 16080), \end{aligned}$$

and

$$\begin{aligned} \phi_2(0) &= -12(3c^3 - 152c^2 + 2588c - 16080), \\ \phi_2(0) &= (c^2 - 66c + 872)(c^2 - 34c + 360). \end{aligned}$$

This yields

$$|\phi_2(0)| < |\phi_2(0)|,$$

$$) \quad c > 84.04 \quad \text{or} \quad c < 12.22 \quad \text{or} \quad 22 < c < 28,$$

which is also satisfied for $c < 0$. Finally one has

$$\begin{aligned} \phi_1(A) &= \frac{\phi_2(0)\phi_2(z) - \phi_2(0)\phi_2(z)}{z}, \\ &= (c - 22)(c^3 - 114c^2 + 2792c - 23040)(c - 28)(c^3 - 36c^2 + 644c - 4320)A \\ &\quad + 48(c - 22)(c^2 - 40c + 480)(c - 28)(c^3 - 36c^2 + 644c - 4320), \end{aligned}$$

and

$$\begin{aligned} \phi_1(0) &= 48(c - 22)(c^2 - 40c + 480)(c - 28)(c^3 - 36c^2 + 644c - 4320), \\ \phi_1(0) &= (c - 22)(c^3 - 114c^2 + 2792c - 23040)(c - 28)(c^3 - 36c^2 + 644c - 4320), \end{aligned}$$

which yields

$$|\phi_1(0)| < |\phi_1(0)|,$$

$$) \quad c > 128 \quad \text{or} \quad c < 0 \quad \text{or} \quad 33 - \frac{\rho}{217} < c < 33 + \frac{\rho}{217}.$$

This is also satisfied for $c < 0$. Thus $\phi_4(A)$ is shown to be a simple Von Neumann polynomial, so all its roots $|A|$ must be less than 1. The proof is completed.

APPENDIX B

DERIVATION OF THE INTERFACE PROJECTION

In section 2.4, a formula for computing the convergence rate of the CHAMP iteration is introduced based on a residual calculation. The residual of the temperature and the heat flux at the interface, however, do not necessarily converge to zero at each time step for the CHAMP scheme, as the CHAMP scheme does not solve the original jump condition exactly. If the scheme is un-iterated, the difference between the temperature of the interface could be substantial. Therefore a projection might be needed to make sure the temperature is continuous across the interface. In this section, a formula for projection is derived based on the one-dimensional similarity solutions for the coupled heat equations. The one-dimensional heat equation on a single domain is given by

$$T_t = DT_{xx}, \quad (\text{B.1})$$

where D is the constant thermal diffusivity of that domain, and T is the simply the temperature. The transformation

$$x = \frac{m}{\tau^\alpha}, \quad t = \frac{n}{\tau^\beta}, \quad T = \frac{H}{\tau^\gamma}, \quad (\text{B.2})$$

is introduced here and the PDE is invariant under the transformation (B.2) given that $\beta - \gamma = 2\alpha - \gamma$, (i.e. $\beta = 2\alpha$). One can then look for solution of the form

$$T(x, t) = t^{\gamma/\beta} f(\eta) \quad \text{for} \quad \eta = \frac{x}{t^{\alpha/\beta}} = \frac{x}{t^{\alpha/2}}, \quad (\text{B.3})$$

and the PDE (B.1) becomes

$$\frac{\gamma}{\beta} f(\eta) - \frac{1}{2} \eta f''(\eta) - D f''(\eta) = 0, \quad (\text{B.4})$$

i.e. the PDE has been reduced to a variable-coefficient ODE.

Now consider 1-D coupled heat equations consists of a left and right domain with $x = 0$ to

be the interface, the problem becomes

$$T_{L,t} = D_L T_{L,xx}, \quad T_{R,t} = D_R T_{R,xx}, \quad (\text{B.5})$$

where D_m is the constant thermal diffusivities for the left and right domain. The boundary and interface conditions are given by

$$fT_L(x,t)j < 1 \text{ as } x \neq 1, \quad fT_R(x,t)j < 1 \text{ as } x \neq 1, \quad (\text{B.6a})$$

$$T_L(0,t) = T_R(0,t), \quad K_L \partial_x T_L(0,t) = K_R \partial_x T_R(0,t), \quad (\text{B.6b})$$

with initial conditions

$$T_L(x,0) = u_L, \quad T_R(x,0) = u_R. \quad (\text{B.7})$$

Using the same transformation (B.2) with $a_L, a_R, b_L, b_R, c_L, c_R$ to be the constants on left and right domains respectively, equation (B.5) can be reduced to two ODEs,

$$q_L f_L(\eta) - \frac{1}{2} \eta f_L^\theta(\eta) - D_L f_L^{\theta\theta}(\eta) = 0, \quad (\text{B.8a})$$

$$q_R f_R(\eta) - \frac{1}{2} \eta f_R^\theta(\eta) - D_R f_R^{\theta\theta}(\eta) = 0, \quad (\text{B.8b})$$

where $q_L = \frac{c_L}{b_L}$, $q_R = \frac{c_R}{b_R}$, $\eta = \frac{x}{t}$ and

$$T_L(x,t) = t^{q_L} f_L(\eta) \quad (\text{B.9a})$$

$$T_R(x,t) = t^{q_R} f_R(\eta) \quad (\text{B.9b})$$

Substitute solutions (B.9a) into interface conditions (B.6a) yields

$$t^{q_L} f_L(0) = t^{q_R} f_R(0), \quad K_L t^{q_L} \frac{1}{2} f_L^\theta(0) = K_R t^{q_R} \frac{1}{2} f_R^\theta(0). \quad (\text{B.10})$$

Since $f_L(0), f_R(0)$ are both constants, one must have

$$q_L = q_R. \quad (\text{B.11})$$

Substitute solutions (B.9a) into the initial conditions (B.7) gives

$$(t)^{q_L} j_{t=0} f_L(\eta) = u_L, \quad (t)^{q_R} j_{t=0} f_R(\eta) = u_R. \quad (\text{B.12})$$

Since u_L, u_R are both constants, the above equations hold only if

$$q_L = q_R = 0, \quad (\text{B.13})$$

which gives

$$f_L(\eta) = u_L, \quad f_R(\eta) = u_R. \quad (\text{B.14})$$

Then the ODEs become

$$\frac{1}{2}\eta f_L''(\eta) + D_L f_L''(\eta) = 0, \quad (\text{B.15a})$$

$$\frac{1}{2}\eta f_R''(\eta) + D_R f_R''(\eta) = 0, \quad (\text{B.15b})$$

which can be integrated twice to get the general solutions to this problem,

$$f_L(\eta) = C_1(D_L\pi)^{1/2} \operatorname{erf}\left(\frac{\eta}{\sqrt{4D_L}}\right) + C_2, \quad (\text{B.16})$$

$$f_R(\eta) = C_3(D_R\pi)^{1/2} \operatorname{erf}\left(\frac{\eta}{\sqrt{4D_R}}\right) + C_4. \quad (\text{B.17})$$

Substitute into the interface conditions at $\eta = 0$ gives

$$c_2 = c_4, \quad (\text{B.18})$$

$$K_L C_1 = K_R C_3. \quad (\text{B.19})$$

Using the initial condition (B.14), one obtains

$$C_1(D_L\pi)^{1/2} + C_2 = u_L, \quad (\text{B.20})$$

$$C_3(D_R\pi)^{1/2} + C_4 = u_R. \quad (\text{B.21})$$

Solving for C_1, C_2, C_3, C_4 yields

$$C_1 = \frac{(u_R \quad u_L)}{\rho \frac{\overline{D}_L}{\pi} \left(\frac{K_L \rho \overline{D}_R}{K_R \rho \overline{D}_L} + 1 \right)}, \quad (\text{B.22a})$$

$$C_2 = u_L + \frac{(u_R \quad u_L)}{\frac{K_L \rho \overline{D}_R}{K_R \rho \overline{D}_L} + 1} = C_4, \quad (\text{B.22b})$$

$$C_3 = \frac{(u_R \quad u_L)}{\rho \frac{\overline{D}_L}{\pi} \left(\frac{\rho \overline{D}_R}{\rho \overline{D}_L} + \frac{K_R}{K_L} \right)}. \quad (\text{B.22c})$$

At interface $x = 0$, $\eta = 0$ and $f_L = f_R = c_2$. This gives

$$f_L(0) = f_R(0) = u_L + \frac{(u_R \quad u_L)}{\frac{K_L \rho \overline{D}_R}{K_R \rho \overline{D}_L} + 1} = \frac{u_L K_L \rho \overline{D}_R + u_R K_R \rho \overline{D}_L}{K_L \rho \overline{D}_R + K_R \rho \overline{D}_L} \quad (\text{B.23a})$$

which determines the weights for the left and right solutions at the interface. This formula can be applied at each time-step to make sure the temperature matches at the interface.

APPENDIX C

A POWER-METHOD-LIKE APPROACH FOR COMPUTING COMPLEX AMPLIFICATION FACTORS

To verify the theory for the CHAMP iteration and time-stepping method, one wants to solve the problem numerically and estimate the largest amplification factor. When the amplification factor A is a real number, the traditional power method can be used to estimate A using two successive iterates. However, when the amplification factor A is a complex number, but the numerical solution is real valued, a modified approach to compute A is needed and this approach is described here.

Consider a sequence of real-valued numerical solutions $\mathbf{u}^n \in \mathbb{R}^N$ that arise from some algorithm (such as a BDF scheme) involving real matrices, $B_j \in \mathbb{R}^{N \times N}$,

$$\mathbf{u}^{n+1} = \sum_{j=0}^q B_j \mathbf{u}^{n-j}. \quad (\text{C.1})$$

Here N denotes the total number of grid points, for example. Mode solutions take the form

$$\mathbf{u}^n = A^n \mathbf{w}, \quad (\text{C.2})$$

where A and \mathbf{w} are eigenvalues and eigenvectors of the polynomial eigenvalue problem,

$$\left[A^{n+1} I - \sum_{j=0}^q A^{n-j} B_j \right] \mathbf{w} = 0. \quad (\text{C.3})$$

Suppose one wishes to find the eigenvalue A with largest modulus. Furthermore suppose that A is complex with non-zero real and imaginary parts. In terms of the real vectors \mathbf{u}^n the mode solution can be written as the real part³ of $A^n \mathbf{w}$

$$\mathbf{u}^n = \frac{1}{2} (A^n \mathbf{w} + \bar{A}^n \bar{\mathbf{w}}). \quad (\text{C.4})$$

³To make \mathbf{u}^n always be the real part and not, say the imaginary part, one can scale \mathbf{w} by the appropriate complex scalar.

It follows from (C.4) that \mathbf{u}^{n+1} is a linear combination of \mathbf{u}^n and \mathbf{u}^{n-1} .

$$\mathbf{u}^{n+1} = a_1 \mathbf{u}^n + a_2 \mathbf{u}^{n-1}, \quad (\text{C.5})$$

for some $a_j \in \mathbb{R}$ independent of n . To see this, substitute (C.4) into (C.5) to find that (C.5) is true provided A satisfies the quadratic equation

$$A^2 = a_1 A + a_2. \quad (\text{C.6})$$

If A has non-zero real and imaginary parts then this last condition uniquely determines a_1 and a_2 . Conversely, if one knows a_j then one can find A (and \bar{A}). Therefore, to find A one can equivalently find a_1 and a_2 .

Consider, then, finding approximations to a_j given a three consecutive vectors in the sequence \mathbf{u}^n . This can be written as

$$U^{n+1} = U^n A, \quad (\text{C.7})$$

where $U^n \in \mathbb{R}^{N \times 2}$ and $A \in \mathbb{R}^{2 \times 2}$ are given by

$$U^n = \begin{bmatrix} \mathbf{u}^n & \mathbf{u}^{n-1} \end{bmatrix}, \quad A = \begin{bmatrix} a_1 & 1 \\ a_2 & 0 \end{bmatrix}. \quad (\text{C.8})$$

Note that the eigenvalues of A are A and \bar{A} . If $N = 2$, so that U^n was a square 2×2 matrix, then one could solve (C.7) for $A = (U^n)^{-1} U^{n+1}$ and compute A . If $N > 2$ let

$$U^n = QR^n, \quad (\text{C.9})$$

$$U^{n+1} = QR^{n+1}, \quad (\text{C.10})$$

denote the reduced QR factorizations of U^n and U^{n+1} where $Q \in \mathbb{R}^{N \times 2}$ and $R^n \in \mathbb{R}^{2 \times 2}$. Note that the same Q has been used for both factorizations, which follows from (C.5). Now (C.7) becomes

$$QR^{n+1} = QR^n A. \quad (\text{C.11})$$

This is an over-determined set of equations for A . To estimate A we can perform a Galerkin projection by multiplying by Q ,

$$QQR^{n+1} = QR^n A. \quad (\text{C.12})$$

Since $QQ = I_{2 \times 2}$ the result can be solved for A ,

$$A = (R^n)^{-1}R^{n+1} = (R^n)^{-1}QU^{n+1}. \quad (\text{C.13})$$

The eigenvalues of A then form our approximations for A and \bar{A} .

Summary. To estimate the complex amplification factor A (that is largest in magnitude) from three iterates \mathbf{u}^{n+1} , \mathbf{u}^n and \mathbf{u}^{n-1} , first compute the reduced QR factorization of the matrix U^n

$$U^n = \left[\mathbf{u}^n \mid \mathbf{u}^{n-1} \right] = QR^n. \quad (\text{C.14})$$

Secondly form the matrix $A \in \mathbb{R}^{2 \times 2}$ from

$$A = (R^n)^{-1}QU^{n+1}. \quad (\text{C.15})$$

The eigenvalues of A are estimates for A and \bar{A} .